Development of dynamic column breakthrough for multicomponent adsorption equilibrium and diffusion

by

Nicholas Stiles Wilkins

A thesis submitted in partial fulfillment of the requirements for the degree of

Doctor of Philosophy

in

Chemical Engineering

Department of Chemical and Materials Engineering
University of Alberta

Abstract

Pressure and temperature swing adsorption processes are increasingly being designed and optimized computationally. The reliability of these predictions are highly dependent on the quality of the experimental equilibrium and kinetic data used in these simulations. Consistent experimental methodology is fundamental to obtain accurate data. The main aims of this thesis are to provide multicomponent adsorption equilibrium and kinetic data on various adsorbents, to provide recommendations to improve experimental methodology, and finally to use this data for pressure swing adsorption design and optimization. Dynamic column breakthrough is extensively studied in this thesis. This method involves a column packed with an adsorbent of interest that can measure multicomponent equilibrium and kinetics, as well as column dynamics. This thesis examines all three of these aspects in dynamic column breakthrough. A few highlights are described below.

The equilibrium loading of each species in a multicomponent mixture can be calculated from a dynamic column breakthrough experiment. This is most commonly done with a ternary gas mixture for a binary equilibrium measurement: the column is initialized with an inert gas (such as helium), and then replaced with a binary mixture of adsorbates. After the experiment is finished, a transient mass balance can be solved to yield an equilibrium loading for each species in the mixture. However, a ternary adsorption breakthrough experiment (two adsorbates and one inert) on a highly selectively system, will often yield erroneous equilibrium data for the weaker component. This is in part due to the measurement of effluent flow, and part due to the long experimental times that accumulate error in the transient mass balance.

It was found that a desorption breakthrough experiment, performed after a desired multicomponent adsorption experiment, yielded more accurate data with less associated error for the weaker species. This is due to the relatively short experimental time for the weaker component to desorb, minimizing the accumulation of error in the mass balance. The stronger component can be calculated from the adsorption breakthrough experiment. The combined elution profile yields the binary equilibrium data at a given composition, temperature and total pressure. The error associated with the adsorption mass balance of the weaker component can also be bypassed by performing true binary experiments without an inert (only the two adsorbates of interest). These experiments are performed by saturating the column with one adsorbate of interest, and then performing an adsorption breakthrough experiment with a binary mixed-adsorbate system. This methodology still requires two sets of experiments to obtain a single binary pairing, but avoids error due to roll-up.

Dynamic column breakthrough is usually performed with tens to hundreds of grams of adsorbent. This sample size creates a large signal change in the effluent mole flow measurement, reduces loading variation from heterogeneous samples, and minimizes effects due to the extra-column volume. However, nothing in the transient mass balance excludes measurement on milligram sized samples. This thesis provides recommendations to build a milligram-scale dynamic column breakthrough apparatus to obtain accurate and precise unary and binary equilibrium data. While some aspects of milligram-scale experimentation are complicated, overall the milligram-scale operation offered many more benefits. These included shorter experimental times, near-isothermal operation, a much simpler effluent flow calibration, as well as being able to test as-synthesized and crystalline adsorbents. This apparatus was tested with mixtures of dry gases on various adsorbent materials. This thesis provides quantitative data for unary and binary adsorption equilibrium, and qualitative trends for multicomponent kinetics, from dynamic column breakthrough experiments on milligram quantities of adsorbent.

Preface

This thesis focuses mostly on the use of dynamic column breakthrough as a technique to measure multicomponent adsorption equilibrium and diffusion. Two chapters do not explicitly follow this theme. The first is chapter 5, which involves the measurement of diffusion into zeolite 4A and Ba-RPZ using constant volume uptake experiments. The results of chapter 5 were fundamental for the study in the following chapter, which involves the kinetic breakthrough of methane and nitrogen on the same materials. The second is chapter 7, which involves machine-learning aided optimization of a metal-organic framework for the separation of methane from nitrogen. This work was entirely computational, and was performed during the intermittent laboratory closures of the COVID-19 pandemic. Nomenclature will be included at the end of each chapter in this thesis due small definitional changes between the chapters.

A minor amount of data included in this thesis was originally published in my M.Sc. thesis [1]. This data is limited only to Chapter 2; these are the adsorption equilibrium and isosteric heat data for CO_2 and N_2 in Fig. 2.3, and the 15 and 50 mol% CO_2/He breakthrough curves in Fig. 2.4(**a**). The major findings in Chapter 2 were found, and published, after the M.Sc. thesis was defended.

This thesis was partly funded by the Natural Sciences and Engineering Research Council (NSERC) Discovery grant, the Canada Foundation for Innovation, the Canada First Excellence fund through the University of Alberta Future Energy Systems, NSERC and Benchmark International (Edmonton) through the NSERC-Alliance program, Alberta Innovates through the Campus Alberta Small Business Engagement (CASBE) grant and Compute Canada. This thesis is compiled as a paper-based the-

sis. Therefore, some minor elements may be repeated between chapters, such as the methodology and modeling of dynamic column breakthrough experiments. Arvind Rajendran and Steven M. Kuznicki were the supervisory authors of this thesis. Arvind Rajendran was involved in conceptualization, formal analysis and manuscript composition. Steven M. Kuznicki was involved in conceptualization and provided the Ba-RPZ sample (through his company Extraordinary Adsorbents Inc.) used in this thesis.

Chapter 1 is an introduction to the topic of adsorption-based separations, adsorption equilibrium and diffusion, and the main experimental technique of this thesis: dynamic column breakthrough.

Chapter 2 of this thesis was published by N. S. Wilkins and Arvind Rajendran as "Measurement of competitive CO_2 and N_2 adsorption on zeolite 13X for post-combustion CO_2 capture" in *Adsorption* [2]. In this paper, N. S. Wilkins was responsible for experimental design and simulation, formal analysis and original manuscript composition. Arvind Rajendran contributed formal analysis and edited the manuscript.

Chapter 3 of this thesis was published by N. S. Wilkins, James A. Sawada and Arvind Rajendran as "Measurement of competitive CO_2 and H_2O adsorption on zeolite 13X for post-combustion CO_2 capture" in *Adsorption* [3]. In this paper, N. S. Wilkins was responsible for experimental design and simulation, formal analysis and original manuscript composition. James A. Sawada contributed with experimental design and edited the manuscript. Arvind Rajendran contributed formal analysis and edited the manuscript.

Chapter 4 of this thesis was published by N. S. Wilkins, James A. Sawada and Arvind Rajendran as "Quantitative microscale dynamic column breakthrough apparatus for measurement of unary and binary adsorption equilibria on milligram quantities of adsorbent" in *Industrial & Engineering Chemistry Research* [4]. In this paper, N. S. Wilkins was responsible for conceptualization, experimental design, for-

mal analysis and original manuscript composition. James A. Sawada contributed with conceptualization, experimental design and edited the manuscript. Arvind Rajendran contributed formal analysis and edited the manuscript.

Chapter 5 of this thesis was published by N. S. Wilkins, James A. Sawada and Arvind Rajendran as "Diffusion of CH_4 and N_2 in barium-exchanged reduced pore zorite (Ba-RPZ) and zeolite 4A" in *Industrial & Engineering Chemistry Research* [5]. In this paper, N. S. Wilkins was responsible for experimental design and simulation, formal analysis and original manuscript composition. James A. Sawada contributed with experimental design and edited the manuscript. Arvind Rajendran contributed formal analysis and edited the manuscript.

Chapter 6 of this thesis is a currently unpublished work on kinetic dynamic column breakthrough experiments. This chapter builds on the work in Chapters 4 and 5.

Chapter 7 of this thesis was published by N. S. Wilkins, Kasturi Nagesh Pai and Arvind Rajendran as "Optimization of pressure-vacuum swing adsorption processes for nitrogen rejection from natural gas streams using a nitrogen selective metal organic framework" in the *Canadian Journal of Chemical Engineering* [6]. In this paper, N. S. Wilkins was responsible for experimental design and simulation, formal analysis and original manuscript composition. Kasturi Nagesh Pai and Arvind Rajendran contributed formal analysis and edited the manuscript.

Chapter 8 contains a summary of the major conclusions of this thesis and offers some insight into possible future work.

"And mage and sailor are not so far apart; both work with the powers of sky and sea, and bend great winds to the uses of their hands, bringing near what was remote."

- Ursula K. Le Guin (in The Farthest Shore)

To my family and friends

Alla mia famiglia ed i miei amici

Acknowledgments

I want to express my sincere gratitude to my thesis supervisors, Arvind Rajendran and Steven M. Kuznicki, who gave me the opportunity to pursue my doctoral studies here at the University of Alberta. My individual meetings and discussions with Arvind were immensely helpful. When I got stuck on a particular problem, he often helped me step out of my tunnel-vision, by encouraging me to look at the problem more broadly, or by suggesting possible experiments. Arvind made me feel as an equal collaborator in our projects. He also gave me the freedom to pursue research tangents that resulted in interesting studies (or parts of studies) included in this thesis. I finally thank Arvind for his patience, throughout both my M.Sc. and Ph.D. programs. I would like to thank Dr. Kuznicki for our discussions and his helpful insights into the chemistry of the materials we studied.

I would also like to express my deep gratitude to Jim Sawada, who was a co-author in many of the studies included in this thesis. Jim was instrumental in many of the experimental aspects of our studies; either by building the experimental apparatuses or through discussions on apparatus construction, and on the methodology of experiments. Jim has instilled into me the idea to not trust experimental results without overwhelming evidence. Our discussions on material chemistry were also extremely helpful, and deepened my understanding of adsorbents.

I would like to thank Shamsuzzaman Farooq for our discussions on dynamic column breakthrough and constant volume diffusion experiments. His insights aided my understanding greatly of both subjects.

I am grateful for the opportunity to work with the International Adsorption So-

ciety (IAS). During the COVID-19 pandemic, Arvind got me involved with the IAS Education Committee to organize webinars and online poster conferences. It has been a great experience working with David, Isabel, Juliana, Nicholas and Valentina. I am also thankful to Daniel Siderius who was an immense help with many IAS activities.

I would also like to thank my current and former colleagues: Ali, Ashwin, Bhubesh, Gokul, Gywn, Johan, Lauren, Libardo, Nagesh, Omid, Parinaz, Rafael, Ravi, Sripradha, Sunny, Tai, Vishal, and Yoga, for playing boardgames and good discussions. It was especially fun traveling during and after conferences with Tai, Nagesh and Gokul.

I want to thank Ilaria who has been there for me, through everything. Thank you for your patience and love. Grazie per tutto, e ti amo. Anche ringrazio a Gloria e Paolo per tutto.

Finally, I want to thank Mom, Dad, Riley, Taylor and Momoo. Your constant love and support has made this thesis much easier to write.

Table of Contents

List of Tables

List of Figures

List of Symbols

Constants

R	universal gas constant	8.314 Pa m^3 mol^{-1} K^{-1}

Latin

$\bar{t}$	dimensionless time	-
$\bar{t}$	mean retention time (Chapter 4)	s
ΔH	heat of adsorption	J mol^{-1}
ΔU	internal energy of adsorption	J mol^{-1}
A	adsorption surface area	m^2
b	adsorption equilibrium constant for site 1	m^3 mol^{-1}
c	concentration	mol m^{-3}
C_p	specific heat capacity	J mol^{-1} K^{-1}
D	diffusivity	m^2 s^{-1}
d	adsorption equilibrium constant for site 2	m^3 mol^{-1}
D_c	micropore diffusivity	s^{-1}
E	energy consumption	kWh_e tonne of CO_2 $captured^{-1}$
E_a	activation energy	J mol^{-1}
f	function	-
H	dimensionless Henry constant	-

h	heat transfer coefficient	$\mathrm{W\ m^{-2}\ K^{-1}}$
I	TCD signal	mV
J	objective function	-
K	Henry constant	$\mathrm{m^3\ mol^{-1}\ kg^{-1}}$
K	thermal conductivity	$\mathrm{W\ m^{-1}\ K^{-1}}$
k	barrier constant (Chapter 5)	$\mathrm{s^{-1}}$
k	mass transfer coefficient	$\mathrm{s^{-1}}$
L	ZLC parameter (Chapter 4)	-
L	dual-resistance parameter (Chapter 5)	-
L	length	m
m	adsorbent mass	kg
n	moles	mol
P	total pressure	bar
p	partial pressure	bar
q	solid phase loading	$\mathrm{mol\ kg^{-1}}$
$Q(t)$	effluent volumetric flow	$\mathrm{m^3\ s^{-1}}$
q^*	equilibrium solid phase loading	$\mathrm{mol\ kg^{-1}}$
Q_{in}	inlet volumetric flow	$\mathrm{m^3\ s^{-1}}$
r	radius	m
R_{p}	particle radius	m
T	temperature	K
t	time	s
V	volume	$\mathrm{m^3}$

v	interstitial velocity	m s^{-1}
x	solid phase fraction	-
$y(t)$	effluent mole fraction	-
y_{in}	inlet mole fraction	-
z	axial direction	m
Prod	productivity	mol i m^{-3} s^{-1}
Pu	purity	mol%
Rec	recovery	%

Greek

α	selectivity	-
β	modified DSL nonlinearity constant	kg mol^{-1}
δ	uncertainty	-
ϵ	void fraction	-
η	vacuum pump efficiency	-
γ	uncertain variable	-
μ	viscosity	Pa s^{-1}
π	spreading pressure	Pa
ρ	density	kg m^{-3}
τ	tortuosity	-
θ	fractional loading	-

Abbreviations & Acronyms

ADS adsorption.

ANN artificial neural networks.

BPR back pressure regulator.

CBMC configurational-bias Monte Carlo.

CCS carbon capture and storage.

CMS carbon molecular sieve.

CSS cyclic steady state.

DCB dynamic column breakthrough.

DES desorption.

DOE department of energy.

DSL dual-site Langmuir isotherm.

EES equal energy site DSL model.

ETS Engelhard titanosilicate.

EVAC evacuation.

FP feed pressurization.

GC gas chromatograph.

HFZ halogen free zorite.

HPVA high pressure volumetry apparatus.

IAST ideal adsorbed solution theory.

IET isotope exchange technique.

KPSA kinetic pressure swing adsorption.

LDF linear driving force.

LHS Latin hypercube sampling.

LPP light product pressurization.

LR light reflux.

MFC mass flow controller.

MFM mass flow meter.

MOF metal-organic framework.

MS mass spectrometer.

MSB magnetic suspension balance.

NSGA II non-sorting genetic algorithm II.

ODE ordinary differential equation.

PN perfect negative pairing.

PP perfect positive pairing.

PSA pressure-swing adsorption.

PT pressure transducer.

PVSA pressure-vacuum-swing adsorption.

RH relative humidity.

RHM relative humidity meter.

ROA rate of adsorption.

RPZ reduced pore zorite.

SEM scanning electron microscopy.

SSL single-site Langmuir model.

TC thermocouple.

TCD thermal conductivity detector.

TGA thermogravimetric analysis.

UES unequal energy site DSL model.

VCR vacuum coupling radiation.

VEMC Virial excess mixing coefficient.

VSA vacuum-swing adsorption.

ZLC zero-length column.

Chapter 1

Introduction

1.1 Adsorptive Separation Processes

Separations are important processes in the chemical industry; accounting for about half of all industrially consumed energy, and about 10 to 15% of all energy consumed in the United States [7]. Many separation techniques are used industrially, depending on the materials and phases in the separation [8]. Pressure, and temperature, swing adsorption (P/TSA) both can be used to separate mixtures of gases from each other using a solid, porous material called an adsorbent [9]. Both utilize a packed bed filled with an adsorbent that is able to selectively adsorb gases into its micropores. Many industrial processes employ adsorption to separate gases from each other. A few examples are: air separation [10], air pre-purification [11], biogas separation [12], carbon capture [13], hydrogen purification [14], desiccation [15] and nitrogen rejection [16, 17]. Adsorptive gas separations are appealing for many reasons, the main being lower energy costs for small-to-medium scale separations and the ability to change P/TSA process configuration easily [7, 18]. Adsorptive separations also can purify gases to 100 mol%, although this generally is not required in bulk gas separations.

Physically, adsorption is the process of an adsorbate (a particular gas molecule) creating a weak physical bond with an adsorbent. These weak physical bonds are reversible, and the affinity of an adsorbate to an adsorbent depends on the adsorbate-adsorbent pairing. This reversibility allows adsorbed gas molecules to be desorbed

and then re-adsobed in a cyclic process, with no damage or chemical change to the adsorbent. This affinity can induce a separation, and is the principle behind pressure and temperature swing adsorption. The pressure is cycled between a high and low value to adsorb and desorb a mixed gas in a pressure swing adsorption process. For temperature swing adsorption, the temperature is cycled between a low and high value to adsorb and desorb a mixed gas. The selective uptake of one gas over another is due to both adsorption equilibrium and kinetics, with the diffusion of the gas into the adsorbent micropores dictating whether the separation is either an 'equilibrium' or 'kinetically' controlled separation.

It is becoming more common to design and optimize P/TSA processes computationally. This is often done by modeling a packed bed as a one-dimensional column and solving the coupled mass and energy balances as a set of discretized partial differential equations [19]. These simulations require many inputs to predict true process behavior. These inputs include column dimensions (length, inner and outer diameter, material), fluid properties (density, viscosity, thermal conductivity), operating conditions (pressure, inlet velocity, temperature, gas composition) and adsorbent material properties (density, voidage, particle size), as well as adsorbent thermodynamic and kinetic information. The last two quantities are usually referred to adsorption equilibrium and kinetics (or diffusion), and are the focus of many studies in the literature due to their importance in P/TSA process design. Measuring these quantities accurately and precisely is one of the objectives of this thesis. The next sections will introduce the key data necessary for successful P/TSA process simulation: adsorption equilibrium and diffusion.

1.1.1 Adsorption Equilibrium

The affinity of an adsorbate to an adsorbent is quantified through adsorption equilibrium data and the isotherm. This data is also referred to as an equilibrium loading. An isotherm is a function of the form: $q_i^* = f(p_i)$, that models the equilibrium loading

of gas i (q_i^*) on the adsorbent as a function of the partial pressure of gas i (p_i) at a given temperature, T. Adsorption equilibrium data and isotherms are extremely useful in simulated P/TSA process design and optimization, where an isotherm can be used as an approximation or prediction of adsorbate equilibrium. The isotherm model acts as the adsorbent in the simulation, predicting the affinity of a particular gas to the adsorbent at a given temperature and pressure.

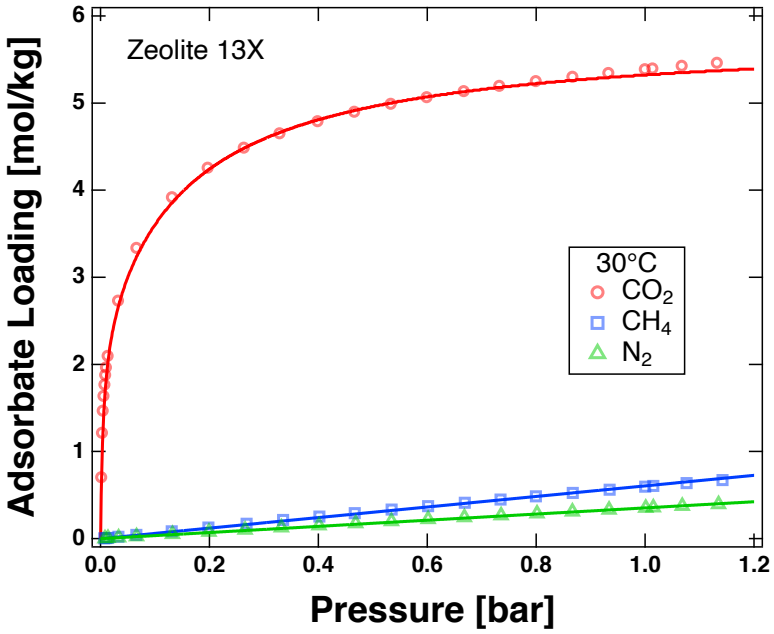

Figure 1.1: Single-component equilibrium of CO_2, CH_4 and N_2 on zeolite 13X at 30°C. Experimentally collected adsorption equilibrium data is shown as markers and lines denote the isotherm model fits.

An example set of experimental equilibrium data and isotherm fits for CO_2, CH_4 and N_2 on the adsorbent zeolite 13X is shown in Fig. 1.1. This data is at a single temperature (30°C) over a range of total pressure (from $\approx$ 5 mbar to 1.2 bar absolute) on the x-axis. The y-axis is the adsorbate loading, the affinity of the adsorbate to the adsorbent, in moles adsorbate trapped per kilogram of adsorbent (mol/kg). As seen in Fig. 1.1, when pressure increases from vacuum to 1.2 bar, the affinity of CO_2, CH_4 and N_2 increases on zeolite 13X. At vaccuum, there is no adsorption of any gas into zeolite 13X. At any given pressure, the adsorption affinity of CO_2 is stronger than CH_4

and N_2, with N_2 having the weakest affinity to zeolite 13X. Generally, the affinity of a particular adsorbate to an adsorbent increases as the strength of the physical bond increases; from van der Waals forces (quadrupole and dipole interactions) to hydrogen bonding. These differences in affinity can be exploited to separate mixtures of CO_2, CH_4 and N_2, generally by pressurizing and depressurizing the mixed gas.

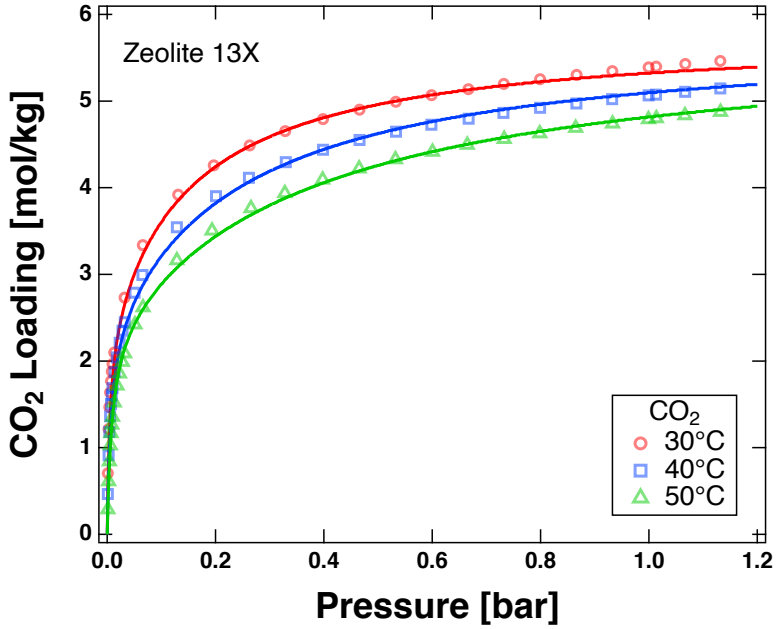

Figure 1.2: Single-component equilibrium of CO_2 on zeolite 13X at 30, 40 and 50°C. Experimentally collected adsorption equilibrium data is shown as markers and lines denote the isotherm model fits.

Heating and cooling the adsorbent can also induce a separation. Figure 1.2 shows the adsorption equilibrium of CO_2 on zeolite 13X at 30, 40 and 50°C. As the temperature of the adsorbate-adsorbent system increases from 30 to 50°C, the amount of carbon dioxide adsorbed decreases per kilogram of zeolite 13X. In other words, since adsorption is an exothermic process the affinity of the adsorbate lowers as the temperature increases [18]. Again, these differences in temperature can induce a separation. It is critical to ensure that the isotherm accurately describes the measured equilibrium data over a range of pressures and temperatures, so that a simulation can accurately predict adsorption equilibrium.

It is important to note that the data in Fig. 1.1 (or Fig. 1.2) is currently for a single gas, either CO_2, CH_4 or N_2, in equilibrium with zeolite 13X without any effects of other gases that could be in a hypothetical mixture. It is possible to perform P/TSA process design and optimization with only single-component isotherms. However, unary equilibrium (such as shown in Fig. 1.1) will usually not be representative of the affinity of a gas toward an adsorbent when two or more gases co-adsorb into the adsorbent. This is true for almost all gas-phase separations of interest (excluding those with helium or hydrogen). Unary equilibrium is still very important, but multicomponent adsorption equilibrium must also be understood in order to predict potential separation performance [2]. Predictive multicomponent isotherms models are required for accurate process simulation. Multicomponent adsorption equilibrium can be predicted with single-component isotherm models fitted to experimental data. This could be as an isotherm extension, such as the extended Langmuir isotherm, or with ideal adsorbed solution theory [20, 21]. However, it needs to be stressed that these are just predictions of multicomponent behavior, and generally do not predict the correct multicomponent equilibrium. These predictions must be verified with experimentally collected multicomponent equilibrium data to ensure accurate process simulation.

A common way to represent experimental binary adsorption equilibrium data is through a phase diagram at a specific temperature and total pressure. An example of a phase diagram for CH_4/N_2 mixtures on zeolite 13X is shown in Fig. 1.3. All data in this figure is collected at 0.95 bar and 30°C. The x-axis is the composition of CH_4 (y_{CH_4}) in the CH_4/N_2 mixture, with one minus the CH_4 composition equaling the N_2 composition ($1 - y_{CH_4} = y_{N_2}$). The y-axis is the equilibrium loading in mol/kg of each component (either CH_4 or N_2) in the mixture. As an example, for $y_{CH_4} = 0.25$ ($y_{N_2} = 0.75$), the equilibrium loadings for CH_4 and N_2 in the mixture are 0.143 and 0.261 mol/kg, respectively.

Phase diagrams are an excellent way to check that a proposed predictive isotherm

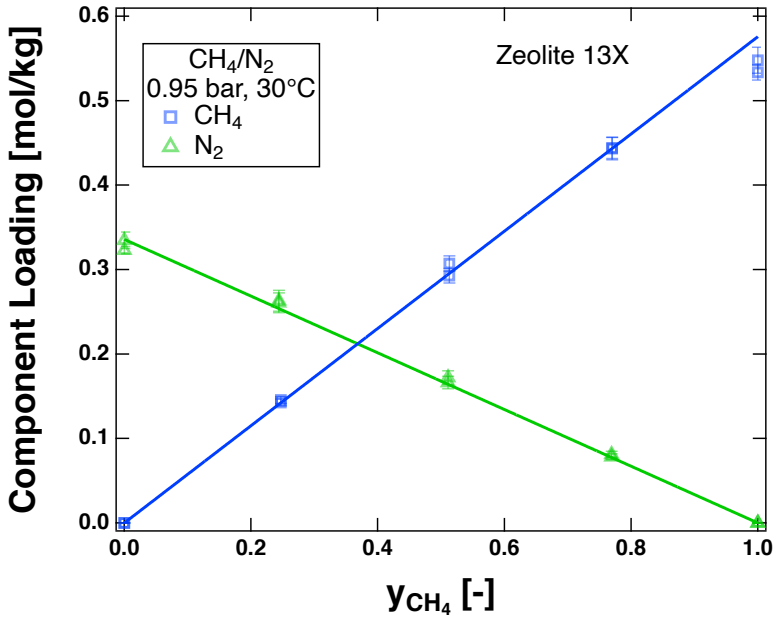

Figure 1.3: Binary equilibrium of CH_4 and N_2 on zeolite 13X at 0.95 bar and 30°C. Experimentally collected adsorption equilibrium data is shown as markers and lines denote the predictive isotherm model.

model qualitatively fits the experimentally collected multicomponent equilibrium data. The continuous lines in Fig. 1.3 are all at 0.95 bar and 30°C while allowing y_{CH_4} to vary, producing the binary isotherms at these conditions. Similar to unary equilibrium, the adsorbate loading would increase at a greater total pressure or a lower temperature. Multiple phase diagrams at different combinations of temperature and pressure would be ideal to determine an isotherm model's predictivity [21]. However, multicomponent adsorption equilibrium data can be time consuming to collect experimentally, sometimes taking multiple days for a single pair of binary equilibrium loadings [3]. Due to this, most studies include only a few phase diagrams at the most relevant process conditions, or simply assume a multicomponent isotherm model from unary data. More work must be done to improve the methodology and speed of multicomponent equilibrium data measurement.

1.1.2 Diffusion in Adsorbent Materials

To this point, only adsorption equilibrium has been discussed. Another important aspect of adsorptive separations is kinetics; essentially, how long it takes for an adsorbate to reach equilibrium with the adsorbent [22]. Accurate mass transfer kinetics are particularly important to estimate gas purity in P/TSA process simulations [23]. For equilibrium controlled P/TSA separations, this is generally limited to rapid-cycling [23] and near-pure gas purifications [24].

Adsorptive separations can also exploit a difference in gas diffusion through the adsorbent micropores [18]. Gas diffusivities are typically due to the size of a particular gas molecule compared to the pore size of the adsorbent it is diffusing through. A common example is the separation of CH_4 from N_2 using the adsorbent zeolite 4A (NaA zeolite). Methane and nitrogen have a kinetic diameter of approximately 3.80 and 3.64 Å, respectively [22]. Zeolite 4A has a pore diameter of approximately 4.0 Å [25]. This results in a greater resistance to CH_4 adsorption than to N_2 adsorption [26]. The diffusion of a gas, either in the bulk fluid or into an adsorbent, is quantified by its diffusivity (in s^{-1}). The diffusivity of a particular gas into an adsorbent decreases as the gas's relative size increases with respect to the adsorbate pore size. If two molecules have vastly different diffusivities, there is a potential to separate them kinetically, such as CH_4 and N_2 on zeolite 4A. This is done by selectively adsorbing the gas that can more quickly diffuse into the adsorbent. For kinetically controlled adsorptive separations, process simulation usually will require more rigorous uptake models [27]. This is further complicated by the fact that diffusion within the adsorbent micropores and surface-barrier diffusion cannot be predicted with correlations [22]. For these systems, experimental diffusivity measurements are required for accurate process simulation.

Many different techniques exist to measure gas diffusion in nanoporous materials [22]. One common way to measure macroscopic gas diffusion is with a volumetric

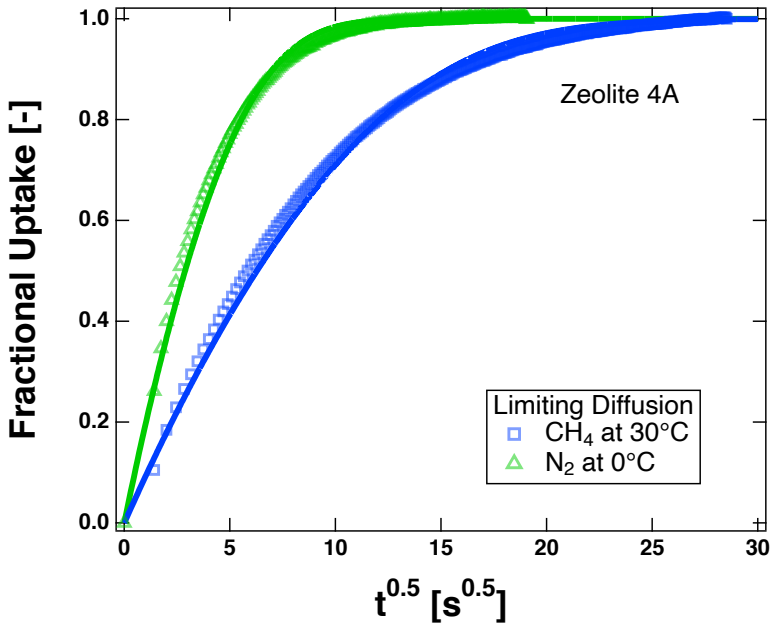

Figure 1.4: Volumetric uptake experiments for N_2 and CH_4 on zeolite 4A at 0 and 30°C, respectively. Experimentally collected adsorption equilibrium data is shown as markers and lines denote the diffusion uptake models.

uptake experiment. These experiments can then be regressed with an appropriate diffusion model to obtain an estimate of the gas diffusivity. A typical example is shown in Fig. 1.4 with N_2 and CH_4 on zeolite 4A. These examples are provided at the limiting diffusivity of both gases, which essentially means the diffusion into the adsorbent is as slow as it can possibly be at the measured temperature. The x-axis denotes the time, specifically the square root of the time in seconds. The y-axis is the fractional uptake, a dimensionless mass uptake where zero is the initial adsorbate-adsorbent equilibrium, and one is the final adsorbate-adsorbent equilibrium. The path between zero and one fractional loading allows us to qualitatively see the resistance of a particular gas molecule into the adsorbent. As seen in Fig. 1.4, CH_4 diffuses into zeolite 4A more slowly than N_2. Since CH_4 takes a longer time to equilibrate than N_2 there is a possibility to separate the gases from each other kinetically. Diffusional resistance decreases as the temperature increases, and usually as the quantity of adsorbed gas increases. To model the entire region of diffusivity for a particular

separation, uptake curves must be made at the temperatures and equilibrium loadings of interest. These models can then be incorporated into a P/TSA process simulator to predict process performance.

1.1.3 Dynamic Column Breakthrough

There are many different experimental methods to measure adsorption equilibrium and diffusion [28, 29]. One that will be extensively used in this thesis is dynamic column breakthrough (DCB). This technique is especially useful since it can be used to calculate multicomponent adsorption equilibrium and diffusion, as well as provide column dynamics to validate P/TSA process simulations [30]. Dynamic column breakthrough is a technique that utilizes a packed bed filled with an adsorbent of interest. Mixtures of adsorbing gas and inert gas can be introduced to the column to measure a dynamic response, in gas composition, temperature and flow, at the outlet of the column. These signals (flow, composition and temperature) are combined to solve a transient mass balance after the experiment has reached an equilibrium. An example schematic is shown in Fig. 1.5. The adsorbent packed bed is downstream of a bank of mass flow controllers that control a desired flowrate of mixed adsorbing gas into the packed bed. Downstream of the packed bed, the effluent volumetric flow and gas composition is measured. These experiments are performed at a constant temperature, typically in a convection oven or circulating fluid bath.

Two categories of DCB experiments exist: adsorption and desorption breakthrough experiments. For an adsorption breakthrough experiment, the adsorbent packed bed is initially saturated with an inert gas at equilibrium and under a constant flow of the inert gas. In Fig. 1.5, this would be the Gas 1 mass flow controller flowing an inert gas through the valve to the bed. At some time, a mixed adsorbing gas (Gas 2) is introduced to the column to displace the equilibrated inert gas. The effluent composition and flow is measured. For a desorption breakthrough experiment, the adsorbent packed bed is initially saturated with a mixed adsorbing gas at equilibrium and un-

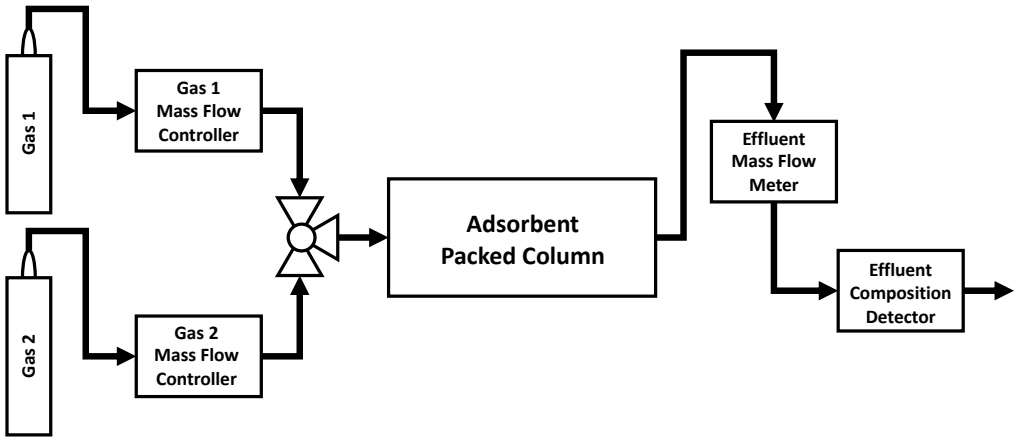

Figure 1.5: A simple schematic of a dynamic column breakthrough apparatus.

der a constant flow of the mixed adsorbing gas (Gas 2). At some time, an inert gas (Gas 1) is introduced to the column to displace the equilibrated mixed adsorbing gas. The effluent flow and composition data collected from both experiments can be used to solve a transient mass balance for the equilibrium loadings. The adsorption and desorption experiments are considered complete once the composition of the inlet gas is observed at the outlet, the effluent flow equals the inlet flow, and the temperature of the packed bed returns to the bath temperature. These experiments are essentially a simplified P/TSA process step, where the column starts at one equilibrium and is perturbed to establish a new equilibrium. Due to the nature of these experiments, they are also extremely useful as a validation for P/TSA process simulations.

A typical adsorption/desorption breakthrough experiment on zeolite 13X is shown in Fig. 1.6 at 30°C. This was for a 100 mol% step change in N_2, when the bed was initially in equilibrium with 100 mol% helium. The mole fraction of N_2 and flow at the column effluent are shown in Fig. 1.6(**a**) and (**c**) for the adsorption experiment. The red markers in Fig. 1.6(**a**) denote the composite experiment, which is the signal resulting from the blank response and the adsorbent packed bed. The blank is the response of all the fluid volume outside of the column, and given by the blue curve. At time equal to zero, the valve is switched from 5.3 sccm of He (Gas 1) to 5.3 sccm

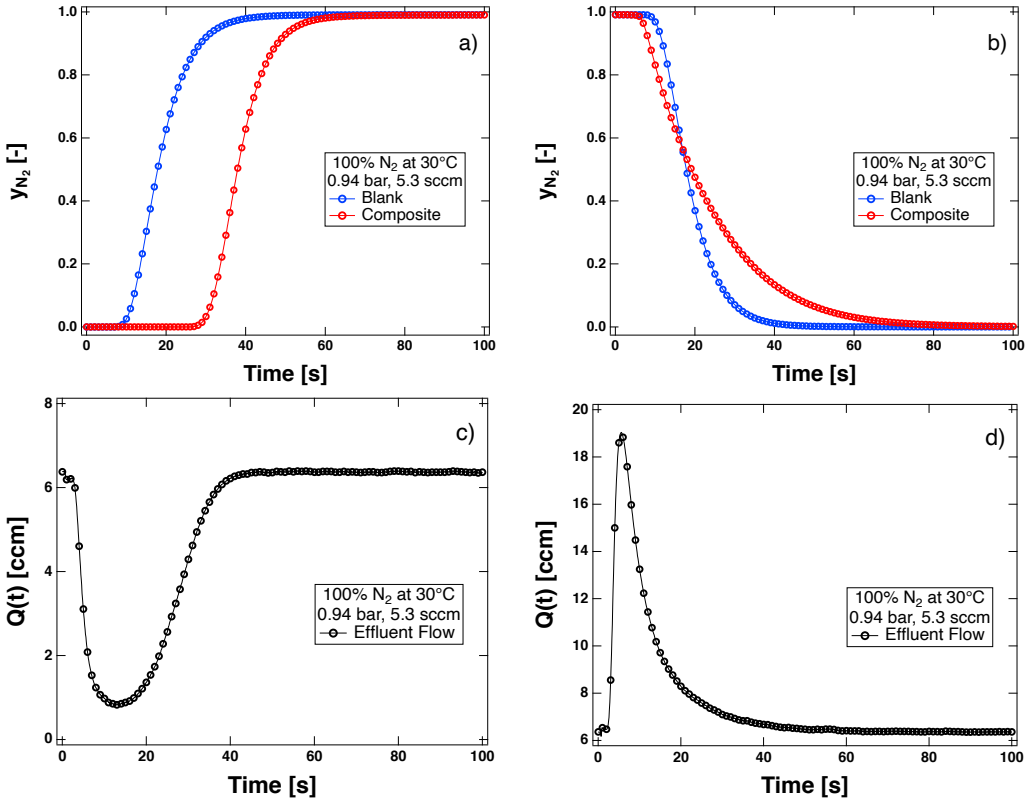

Figure 1.6: Single-component N_2/He adsorption and desorption dynamic column breakthrough experiments for 100 mol% N_2 in He on zeolite 13X at 0.94 bar and 30°C. The top row shows the (**a**) adsorption and (**b**) desorption curves. The corresponding effluent flow curves for (**c**) adsorption and (**d**) desorption are shown below the mole fraction responses.

of N_2 (Gas 2). When N_2 breaks through the packed bed in Fig. 1.6(**a**) (N_2 is observed at the column effluent), the mole fraction changes as a dispersed square wave, often called a shock. This lag in composition, when compared to the blank experiment, signifies that N_2 has adsorbed into the column. The corresponding effluent flow in Fig. 1.6(**c**) initially shows a decrease in flow as N_2 adsorbs into the bed; the effluent flow returns to the inlet flow after N_2 fully saturates the bed, and establishes a new equilibrium. The effluent flow drops because N_2 is adsorbing into the adsorbent and is removed from the bulk fluid traveling through the column. When the effluent flow returns to the inlet flow, and 100 mol% N_2 is observed at the outlet, the adsorption breakthrough experiment is complete.

A desorption experiment is run after the adsorption experiment. Figure 1.6(**b**) and (**d**) show the effluent composition and flow, respectively. In this case, the bed initially is in equilibrium with 100 mol% N_2. At time equal to zero, the valve is flipped to 5.3 sccm of He to sweep the adsorbed N_2 out of the column. Since N_2 was previously adsorbed into the adsorbent, the effluent flow in Fig. 1.6(**d**) increases initially to a value greater than the inlet flow. In other words, the effluent flow is greater than the inlet flow. Over time, the flow-spike reaches a maximum and then decreases back to the inlet value. At the same time, the effluent N_2 composition in Fig. 1.6(**b**) decreases to zero. When the N_2 composition reaches zero, and the effluent flow returns to the inlet flow, the desorption experiment is complete.

As previously mentioned, dynamic column breakthrough offers many benefits in the measurement of multicomponent equilibrium and diffusion. The desired equilibrium gas composition, temperature and pressure can be specified before an adsorption or desorption experiment is performed. This allows phase diagrams, like the one presented in Fig. 1.3, to be constructed with relatively few experiments. A breakthrough experiment also provides heat and mass transfer information through the spread of the breakthrough curve [30]. Since breakthrough experiments are a simplified step of a P/TSA process, they are also ideal to validate P/TSA process simulations and ensure accurate process performance predictions. However, there are also many challenges to obtain consistent quantitative data using dynamic column breakthrough. One of the biggest challenges is the estimation of effluent flow, which is required to obtain equilibrium data [31]. This is the 'effluent mass flow meter' in Fig. 1.5. Most mass flow meters are functions of flow and gas composition. These quantities change simultaneously during a breakthrough experiment. In limited circumstances, the effluent flow can be assumed constant, but this assumption will often lead to erroneous data [32, 33]. As seen in Figs. 1.6(**c**) and (**d**), there is a significant change in effluent flow for the adsorption and desorption breakthrough experiments. It also can be difficult to measure low-affinity adsorbates using the technique [2, 34]. This

difficulty is linked to the estimation of effluent flow [31], signal-noise from the mass flow meter, and the accumulation of error in the calculation of equilibrium loading [30]. For quantitative work, large adsorbent sample sizes are often used to minimize dead volume contributions and the pressure-drop, and to increase the resolution of data collected. However, this excludes testing on crystalline, as-synthesized or rare adsorbents. Testing small adsorbent sample sizes will become increasing important as more novel materials, such as metal-organic and covalent-organic frameworks, are synthesized, and considered for P/TSA processes. These challenges can be addressed, and overcome, with an appropriate apparatus and experimental protocol.

1.2 Motivation

Increasing need for multicomponent adsorption equilibrium and kinetic data. As mentioned earlier, pressure and temperature swing adsorption processes are increasingly being designed and optimized computationally [35, 36]. The predicted process performance of these simulations are highly dependent on the quality of data that is fed to them. In terms of adsorption equilibrium, this means repeatable, accurate and precise data, to fit a reliable isotherm model [37]. Ideally, this also includes multicomponent equilibrium data to check any predictive multicomponent isotherm, or to test if the adsorbate-adsorbent pairing follows ideal adsorbed solution theory. Often, a multicomponent isotherm model is assumed in P/TSA process simulations, which can lead to erroneous simulation results [2]. This is coupled with the fact that experimental multicomponent data can be difficult to measure, and often requires custom-built hardware [29]. Some databases of multicomponent adsorption equilibrium data exist, but this data is limited [38, 39]. The same is true for kinetic data. Again, repeatable, accurate and precise diffusional data is required to assume a mass transport model in a process simulator. Inaccuracies in these estimates, or an incorrect mass transport model, can also lead to erroneous simulation results [23, 27]. Again, collecting the necessary data required to perform P/TSA process design and

optimization is often time-consuming, and can be experimentally challenging [40]. The lack of fundamental data can only be expected to increase over time with the increasing number of novel materials that are being synthesized, some of which will be considered for adsorptive separations. This is also true for many heavily studied systems where very little multicomponent data exists, such as humid post-combustion carbon capture on zeolite 13X [41].

Need for consistent, repeatable and improved experimental protocol. A further problem is the need to have good experimental techniques and well explained experimental protocols to obtain repeatable, accurate and precise adsorption equilibrium and kinetic data. This does not necessarily mean creating new techniques to measure adsorption equilibrium and kinetics, but to fully understand and improve the current techniques so we can apply them to their greatest potential. This also includes understanding the benefits and limitations of a particular technique, as well as ways to assess the quality of the collected data to obtain more repeatable, accurate and precise data. The misuse of these techniques can lead to low quality data, which can lead to poor simulated process predictions.

Dynamic column breakthrough is particularly important for the prediction capability of P/TSA process simulations, since the simulator must be validated with a series of breakthrough experiments. It is also an excellent method to construct multicomponent phase-diagrams and check a proposed multicomponent isotherm model. However, there are also many limitations that have been discussed in the literature. The technique is considered slow, mostly stemming from adsorbent regeneration between experiments [29]. This is also partially a dimensional problem, a smaller column will require less time to regenerate. As mentioned earlier, quantitative work is generally performed with large sample sizes (tens to hundreds of grams) to tackle other problems, such as dead volume, pressure-drop, and sample homogeneity [30]. It should be mentioned though that nothing precludes sub-gram sample sizes in breakthrough experiments, they just bring their own challenges. Improving the estimation

of effluent flow is also a significant challenge. A large amount of error is introduced in a breakthrough experiment due to the simultaneous change in effluent composition and flow [31]. Estimating the equilibrium loadings of low-affinity adsorbates in single, and multicomponent, experiments also remains a challenge [34]. This is partially due to effluent flow inaccuracies, but also due to the accumulation of error in the breakthrough mass balances. Many of these challenges can be addressed with novel protocol and instrumentation.

1.3 Objectives

The main objective of this thesis is to improve existing methods to obtain high quality adsorption equilibrium and kinetic data. The hope is that these methods and data can be helpful in simulated P/TSA process design and optimization. A secondary objective is to determine how this data, and assumptions made with this data, can influence process simulation and optimization. The vast majority of this thesis will focus on improving and modifying dynamic column breakthrough to collect high quality data and column dynamics. These studies are performed with adsorbate-adsorbent systems, and adsorbent sample sizes that have been classically difficult to quantify to highlight their potential uses. These aims are investigated in the following chapters in this thesis:

- The nonideal competitive adsorption of CO_2 and N_2 on zeolite 13X was studied with dynamic column breakthrough experiments to propose ways to reduce measurement error, suggestions to measure low-affinity adsorbate equilibrium, and to provide insight into the effect of an incorrect multicomponent isotherm on pressure swing adsorption process performance.

- The previous study was extended using a highly nonideal competitive mixture of CO_2 and H_2O on zeolite 13X. The previously proposed dynamic column breakthrough techniques were successfully employed and a multicomponent equilib-

rium model for competitive CO_2/H_2O was developed.

- A microscale dynamic column breakthrough apparatus was developed to measure multicomponent adsorption equilibrium and column dynamics on milligram-sized samples. Experimental protocol suggestions are made to obtain repeatable, accurate and precise equilibrium data quickly for low and high-affinity adsorbates on milligram-sized adsorbent samples. These experiments were also designed to bypass the challenging effluent flow calibration.

- The diffusion of CH_4 and N_2 into two small-pore adsorbents, Ba-RPZ and zeolite 4A, was quantified and the diffusion mechanisms were determined. Models for the change of diffusivity with temperature and concentration are provided and used to validate uptake simulations.

- The microscale dynamic column breakthrough apparatus was used to study the kinetic breakthrough of CH_4 and N_2 mixtures on Ba-RPZ and zeolite 4A. The near-isothermal operation of the microscale dynamic column breakthrough apparatus was shown to be especially beneficial for kinetic breakthrough experiments.

- A vanadium-based metal organic framework was computationally evaluated and optimized with machine-learning techniques for nitrogen rejection in raffinate pressure swing adsorption cycles.

1.4 Structure of the Thesis

This paper-based thesis is structured into six main chapters and a conclusion. The abstracts of these chapters are given below:

Chapter 2 discusses the competitive adsorption of CO_2 and N_2 on zeolite 13X. Single component CO_2 and N_2 equilibrium loadings were measured and reported on zeolite 13X. The CO_2 equilibrium data was fit to a dual-site Langmuir (DSL)

isotherm. The equilibrium data for N_2 was fit using four isotherm schemes: two single site Langmuir isotherms, the DSL with the equal energy sites, and the DSL with unequal energy site pairings. Adsorption breakthrough experiments were able to provide accurate data for CO_2 competitive adsorption, while failing to provide reliable N_2 data. It was shown that desorption experiments from a bed fully saturated with the desired composition provides a better estimate of the competitive N_2 loading. The impact of the chosen adsorption isotherm model on process performance was evaluated by simulating a 4-step vacuum swing adsorption process to concentrate CO_2 from dry post-combustion flue gas. The results show that the purity, recovery, energy and productivity are affected by the choice of the competitive adsorption isotherm.

Chapter 3 discusses the competitive adsorption of CO_2 and H_2O on zeolite 13X. The adsorption isotherms of water on zeolite 13X were measured. The equilibrium data was fit to a dual-site Langmuir isotherm. A series of single component H_2O dynamic column breakthrough experiments were measured on zeolite 13X. These breakthrough experiments were modeled and simulated with our built in-house adsorption simulator. The simulator predicted composition and thermal breakthrough behavior well for all single component experiments. Competitive CO_2/H_2O breakthrough experiments were then performed.. The collected equilibrium data showed up to a 98% loading reduction for CO_2 (compared to the single component loading) for $\approx 2\%$ RH while H_2O showed no reduction compared to its single component loading. The binary equilibrium isotherms were described by an explicit water-loading adjusted dual-site Langmuir isotherm.

Chapter 4 describes a microscale dynamic column breakthrough (μDCB) apparatus with the ability to measure unary and binary adsorption equilibrium on a milligram-scale quantity of adsorbent. The μDCB is a low cost system that can be constructed through minor modifications of a commercial gas chromatograph and uses a thermal conductivity detector. The small scale of the apparatus allows for the rapid collection

of dynamic column breakthrough experiments. The mass balances for adsorption and desorption experiments were derived along with a description of the blank. The μDCB apparatus was tested with 238.9 mg of zeolite 13X and 180.2 mg of activated carbon with single-component N_2/He and CH_4/He adsorption and desorption measurements. The measured equilibrium data agreed well with volumetrically collected data. These measurements are both accurate and precise. Multicomponent adsorption was also studied on zeolite 13X and activated carbon for CH_4/N_2 and CO_2/CH_4 mixtures. This data was compared with ideal adsorbed solution theory, extended dual-site Langmuir calculations and the literature.

Chapter 5 discusses a barium-exchanged reduced pore zorite (Ba-RPZ), which is a titanosilicate molecular sieve that is able to separate CH_4 from N_2 based on their relative molecular sizes. A detailed study of N_2 and CH_4 adsorption equilibrium and diffusion on Ba-RPZ was completed using low and high-pressure volumetry. Adsorption equilibrium data for CH_4 and N_2 on Ba-RPZ was collected. Constant volume uptake experiments were conducted to estimate the diffusivities of CH_4 and N_2. Similar experiments were carried out with zeolite 4A to validate the methods used in this study. On the one hand, the transport of N_2 in Ba-RPZ was found to be controlled by diffusion in the micropores. On the other hand, the transport of CH_4 in Ba-RPZ was described by a dual-resistance model, including a barrier resistance and micropore diffusional resistance. Both the barrier and micropore diffusion coefficients demonstrated concentration dependence. While the micropore diffusion constant followed Darken's relationship, the barrier resistance did not. A concentration-dependent dual-resistance diffusion model for methane was constructed and validated using experimental data across a range of pressures and temperatures. The concentration-dependent dual-resistance model was able to describe the complex diffusion behavior methane displays as it progressed from the dual-resistance controlled region to the micropore-controlled region of the isotherm. The calculated CH_4/N_2 kinetic selectivity of Ba-RPZ was shown to be significantly larger than the current benchmark

material for CH_4/N_2 separation.

Chapter 6 discusses the qualitative kinetic breakthrough of CH_4 and N_2 on two small pore adsorbents: zeolite 4A and Ba-RPZ. These experiments were performed with the micro dynamic column breakthrough apparatus. Unary equilibrium loadings for N_2 were measured on both materials and are consistent with independently collected equilibrium data from a volumetric apparatus. Unary CH_4 experiments were also collected on both materials. For zeolite 4A, the single component CH_4 breakthrough experiments confirmed the phenomena observed in Chapter 5. The CH_4 breakthrough curves reached equilibrium faster at higher temperatures (70°C) than at lower temperatures (30°C). All compositions studied at a given temperature yielded the same diffusivity. The methane uptake on Ba-RPZ was too slow (the signal was too weak) to draw many conclusions. There was a change in diffusivity with concentration at a given temperature. However, the composition signal was too small to differentiate the change in diffusivity as a function of temperature. Binary CH_4/N_2 experiments were also performed. For zeolite 4A, the same CH_4 diffusivities were obtained as in a unary experiment. For Ba-RPZ, binary CH_4/N_2 diffusivities were inconclusive. The binary CH_4 diffusivity appears similar to the unary CH_4 diffusivity, but this likely is due to limitations in our current hardware.

Chapter 7 discusses a process optimization study on a newly discovered vanadium(II/III) metal-organic framework (MOF), $V_2Cl_{2.8}$(btdd), that is selective to N_2 over CH_4. Process optimizations were performed to determine the performance of this MOF to reach pipeline transport purity of 96 mol% CH_4 purity. Two cycles were considered: the basic 3-step cycle and the Skarstrom cycle. First, the 3-step cycle was considered with a wide range of operating conditions. A detailed process model in tandem with machine learning-aided optimization was employed to determine the optimal set of operating conditions. The 3-step cycle was unable to meet the 96 mol% CH_4 purity requirement in most cases studied. However, the Skarstrom cycle was able to meet the 96 mol% CH_4 purity requirement in all cases studied. The maximum re-

covery, at a purity of 96 mol%, was at 84.2% for the Skarstrom cycle with a methane feed composition of 80 mol% at 50°C and an adsorption pressure of 100 kPa. For the Skarstrom cycle, at a feed temperature of 50°C, an adsorption pressure of 100 kPa and a feed methane composition of 92 mol%, the productivity could be as high as 21.18 tonnes per day CH_4 m^{-3} at a recovery of 85.1%.

Finally, in Chapter 8, a summary of the significant results are detailed with recommendations for possible future work.

Chapter 2

Measurement of competitive CO_2 and N_2 adsorption on zeolite 13X for post-combustion CO_2 capture

2.1 Introduction

Anthropogenic CO_2 emissions are driving climate change [42]. One proposed solution to mitigate CO_2 emissions is carbon capture and storage (CCS) from point sources such as power plants. CCS is the process of capturing and concentrating CO_2, before the flue gas is released to the environment, and storing it underground. One method to capture CO_2 is through post-combustion carbon capture, or capturing the CO_2 after the fuel is burned for power [43, 44]. Although liquid absorption is the current method of choice for the CO_2 capture step, it suffers from high parasitic energy requirements and solvent degradation [45]. Adsorption using solid adsorbents has been suggested as a possible alternative to capture CO_2 from the effluent gas stream [46]. In a traditional power plant, fuel and air are fed to a furnace and combusted to yield primarily H_2O and CO_2. The N_2 and excess O_2 from air remains unreacted. On a dry basis, after the desulphurization step, the flue gas is a mixture of $\approx 12-15$ mol% CO_2 and the rest being N_2 and O_2 [43].

Many adsorbents are being studied for their potential use in CO_2 capture from

This chapter was originally published as: N. S. Wilkins and A. Rajendran, "Measurement of competitive CO_2 and N_2 adsorption on zeolite 13X for post-combustion CO_2 capture," *Adsorption*, vol. 25, no. 2, pp. 115-133, 2019

large point sources [47, 48]. Among them, zeolite 13X is considered the benchmark adsorbent for post-combustion carbon capture, not only due to its large selectivity of CO_2 over N_2, but also because it is cheap and currently used in other commercial separations. Many process-scale studies point to the fact that zeolite 13X is capable of reaching the U.S. Department of Energy (US-DOE) targets for CO_2 purity and recovery [19, 41]. Further, the efficacy of zeolite 13X for the separation of CO_2 and N_2 at post-combustion conditions has been demonstrated at pilot plant scales [41, 49, 50]. Krishnamurthy *et al.* reported cycles that achieved high purity ($\approx 95\%$) and high recovery ($\approx 90\%$) from a feed containing 15 mol% CO_2 [41]. The separation mechanism of CO_2 and N_2 on zeolite 13X is based on differences in the equilibrium adsorption of these gases. Therefore, it is critical to obtain the adsorption isotherms for the adsorbent. CO_2 and N_2 adsorption on zeolite 13X is well studied. Several reports exist and data can be easily obtained from public databases [41, 51–54]. In some of the recent literature, specifically those dealing with metal-organic frameworks (MOFs), it is increasingly common only to see only reports of CO_2 adsorption, while ignoring measurement of N_2 adsorption. Recent studies have pointed out that measuring N_2 isotherms on the same sample is critical for reliable process simulations [55–57].

Understanding and quantifying competitive adsorption is critical for process design [58]. However, it is surprising to note the lack of experimental studies that report the competitive adsorption of CO_2 and N_2 on such a common material as zeolite 13X [34, 54, 59]. The lack of competitive data at low pressures (< 1 bar), i.e., conditions at which most processes for post-combustion CO_2 capture are optimal, is glaring. Most process modeling studies have been performed with the assumption that single component isotherms can be used either with the ideal adsorbed solution theory or the competition can be described by simple extensions of the single component models [50, 60]. Further, the impact of such assumptions on predicting process performance is not well studied. These outstanding issues provide the motivation for the current

work where the main aim is to measure low pressure isotherms of CO_2 and N_2 on the same zeolite 13X sample, quantify the competition by measuring competitive loadings and proposing an explicit competitive isotherm validated with dynamic column breakthrough experiments, and to demonstrate the importance of proper characterization of competitive adsorption on process performance.

As previously mentioned only a few papers have studied the competition of CO_2 and N_2 on the same sample of zeolite 13X [34, 54, 59]. Hefti *et al.* studied single and multicomponent CO_2 and N_2 mixtures on zeolite 13X at 1.2, 3.0 and 10.0 bar total pressures at 25°C and 45°C using a magnetic suspension balance [54]. The CO_2/N_2 mixtures in Hefti *et al.* are primarily at relatively high N_2 and low CO_2 concentrations to study the non-ideality of the mixture on zeolite 13X [54]. Hefti *et al.* found the extended Sips equilibrium model fit the competitive data reasonably although under-predicting the competition [54]. Purdue used the experimentally collected competitive CO_2/N_2 equilibrium data from Hefti *et al.* to study the competition of CO_2, N_2 and H_2O on zeolite 13X using grand-canonical Monte Carlo (GCMC) simulations [59]. Purdue was able to confirm the data that was collected by Hefti *et al.* at 25°C and predicted the CO_2/N_2 competitive loadings at 50°C and 70°C [59]. Avijegon *et al.* measured competitive loadings of CO_2, N_2 and CH_4 mixtures on zeolite 13X using dynamic column breakthrough experiments [34]. Avijegon *et al.* measured multicomponent loadings by sending a step input of adsorbing gas into an activated zeolite 13X bed and solving the transient mass balance [34]. The authors were able to easily measure the CO_2 competitive loadings, but were not able to measure the N_2 loadings with certainty, particularly at low N_2 concentrations in their binary CO_2/N_2 mixtures; the experimental uncertainty was larger than the calculated N_2 loadings [34]. This clearly highlighted the challenges of measuring the loading of the lighter component in a binary mixture, especially in a case where competition is very strong.

In this paper, the single component isotherms of CO_2 and N_2 are measured using two techniques: volumetry and gravimetry. The competition between CO_2 and N_2

is studied through dynamic column breakthrough adsorption and desorption experiments. Single and multicomponent equilibrium data for N_2 and CO_2 are reported for temperatures and pressures around post-combustion process conditions on zeolite 13X. These experiments were described with a detailed model and a suitable competitive isotherm that describes both the competitive loadings and the dynamic column breakthrough profiles. Some key challenges faced during the measurement of strongly competitive species are elaborated and ways to overcome those challenges are discussed. Finally, the importance of competitive behavior is illustrated using process studies. Specifically, the choice of a competitive equilibrium description and its effect on the predictions of process performance.

2.2 Materials and Methods

Zeolite 13X (Z10-02ND) was obtained from Zeochem (Uetikon am See, Switzerland). This particular zeolite 13X has a stronger affinity and higher CO_2 loading compared to another material that has been reported by Krishnamurthy *et al.* but, it is similar to the one that was studied by Hefti *et al.* [41, 54]. The zeolite 13X particles are spherical and have a diameter between 0.8 and 1.2 mm. The Langmuir and BET surface areas, and the internal pore volume of zeolite 13X were measured with a volumetric liquid N_2 isotherm at -196°C using a Micromeritics ASAP 2020 (Norcross, GA, USA). The Langmuir and BET surface areas were measured to be 859 ± 2 m^2/g and 575 ± 21 m^2/g, respectively. The internal pore volume was determined to be 2.995×10^{-7} m^3/g. All gases in this study (99.999% He, 99.998% CO_2, 99.999% N_2) were obtained from Praxair Canada.

Single component adsorption isotherms for CO_2 and N_2 were measured using volumetry and gravimetry. Single and multicomponent adsorption equilibrium and column dynamics were measured with dynamic column breakthrough adsorption and desorption experiments. In all cases, the focus was on measurements at low pressures (< 1 bar). At these conditions, the fluid phase density is significantly lower than

the adsorbed phase density; therefore the measured loadings can be treated as the absolute amount adsorbed [51, 61]

2.2.1 Volumetry

Volumetric isotherms for CO_2 and N_2 were measured with a Micromeritics ASAP 2020 (Norcross, GA, USA). The Micromeritics system can measure adsorption equilibrium between 1 mbar up to 1.2 bar. Volumetric equilibrium data is measured by dosing an initially evacuated chamber, filled with some adsorbent, with known volumes of gas. The resulting change in pressure is proportional to the amount of gas adsorbed. Prior to each volumetric isotherm experiment, the sample was regenerated for 12 hours under vacuum at 350°C. The volumetric system has a loading accuracy of $< 0.15\%$ of the reading and pressure accuracy of $< 1.3 \times 10^{-7}$ mbar. A sample mass of ≈ 200 mg was used for these experiments.

2.2.2 Gravimetry

Gravimetric isotherms for CO_2 and N_2 were measured with a Rubotherm Type E10 (Bochum, Germany) magnetic suspension balance (MSB). The MSB can measure from 0.2 bar up to 50 bar. The gravimetric equilibrium loading is measured by placing ≈ 2 grams of adsorbent on the MSB and measuring the mass change as a function of the pressure [51]. Prior to each gravimetric isotherm experiment, the sample was regenerated under vacuum at 350°C for 12 hours. Before the CO_2 and N_2 isotherm measurements, experiments using He were performed to measure the skeletal volume of the adsorbent. Helium was assumed to be non-adsorbing. This assumption is reasonable since only low pressure data (< 5 bar) was targeted [62].

2.2.3 Dynamic Column Breakthrough Experiments

The dynamic column breakthrough (DCB) apparatus used in this study is shown in Fig. 2.1. The mass flow controllers control the flow of the gasses. Controllers for

"gas 1" and "gas 2" were purchased from Parker/Porter (Hatfield, PA, USA) with a maximum flowrate of 5 SLPM, while the controller for "gas 3" was purchased from Alicat Scientific (Tucson, AZ, USA) and can control the flow up to 500 sccm. The outlet mass flow meter (Parker/Porter, Hatfield, PA) can measure up to 1 SLPM. The heart of the system is a stainless steel column (Swagelok 304L-HDF2-40) with a packed length of 6.4 cm and a diameter of 2.82 cm containing 23.02 g of adsorbent. One thermocouple (Omega Engineering, Laval, QC, Canada) was kept 5.2 cm from the column inlet. The inlet pressure and pressure drop were measured using a pressure transducer and differential pressure gauge, respectively (GE Druck, Billerica, MA, USA). The gas composition at the column outlet was measured with a mass spectrometer (Pfeiffer Vacuum OmniStar GSD 320, Asslar, Germany) that was calibrated before each experiment with known gas compositions. All necessary quantities were recorded in a data acquisition system built using LabView. The temperature in the lab was maintained at $\approx 22°C$. Before every breakthrough experiment, the column was regenerated at 350°C under 350 sccm of helium for 12 hours. All breakthrough experiments were performed at $\approx$ 22°C and $\approx$ 0.97 bar total pressure. Since the extra-column volume of the DCB apparatus was 0.6 mL (which is 1.5% of the column volume), no correction procedures were used to treat the breakthrough profiles [63]. Blank experiments showed that the average spread (from 5% to 95% signal of the step response) in the dead volume was small $\approx 0.3\,\bar{t}$, which is negligible compared to the spread of the adsorption and desorption experiments.

For an adsorption breakthrough experiment, at time $t < 0$ a carrier gas flowed through the column. At $t = 0$, a step signal of pure or mixed gas was sent through the column. The outlet compositions, inlet and outlet flows, pressure, pressure drop and temperature were recorded in a data acquisition system. This step signal continues for some time until the compositions and thermal breakthroughs were completed. For a desorption experiment, at time $t < 0$ a single or multicomponent adsorbing gas flows through the column until the column is saturated with the feed. At $t = 0$, a

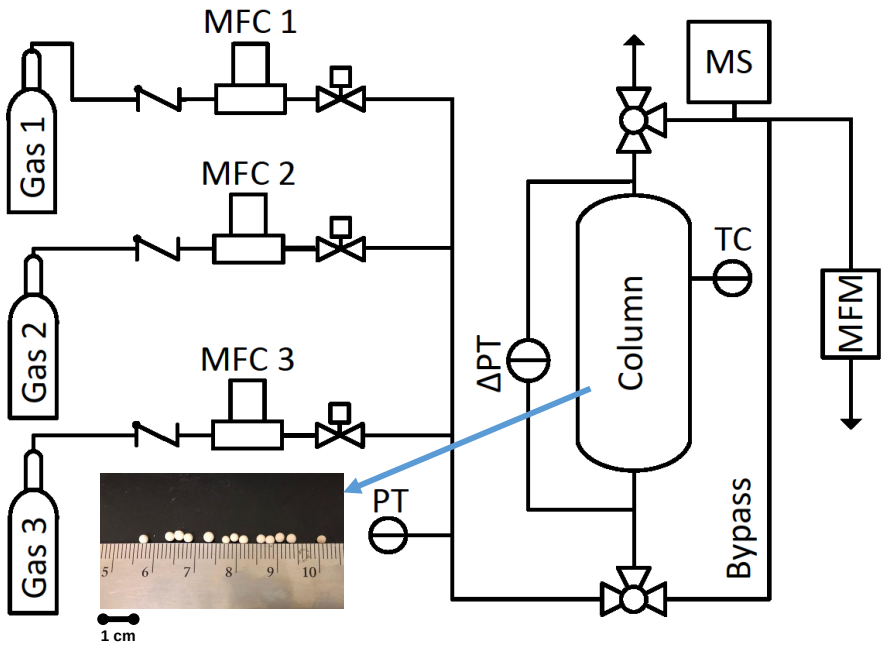

Figure 2.1: Schematic of the dynamic column breakthrough apparatus. MFC = mass flow controller, MFM = mass flow meter, MS = mass spectrometer, PT = pressure transducer, ΔPT = differential pressure transducer and TC = thermocouple. The Z10-02ND zeolite 13X sample is also shown with a ruler for scale.

step signal of inert gas is sent through the column. The pressure drop in the system was < 0.02 bar and is therefore considered negligible.

Prior to each experiment, flow and composition calibrations were performed. The effluent composition detected in the MS was calibrated using gas cylinders of known compositions. The effluent mass flow meter was calibrated first using pure CO_2, N_2 and He by setting an inlet flow on one of the mass flow controllers, and measuring the real outlet flow and the mass flow meter signal. Then, different mixtures of CO_2, N_2 and He were made at different flowrates to build a calibration curve of real flow as a function of the effluent compositions and the mass flow meter signal.

2.3 Modeling

2.3.1 Dynamic Column Breakthrough Simulation

The adsorption dynamics of the column were modeled based on the following assumptions:

1. The gas phase is ideal. The experiments were all performed at low pressures so the ideal gas assumption is justified.

2. The column is one-dimensional and there are no radial gradients for concentration or temperature.

3. An axially dispersed plug flow model adequately describes the flow through the column.

4. The ambient temperature is uniform. This was confirmed by measurements in the laboratory. The variation over a single experiment was $< 0.5°C$.

5. Darcy's law adequately describes the pressure drop in the column. The flowrates were low and the measured pressure drop was small (< 0.02 bar).

6. The solid and gas phases achieve thermal equilibrium instantaneously.

7. The adsorbent and bed properties are uniform throughout the column.

8. The linear driving force (LDF) model adequately describes the solid phase mass transfer rate. The LDF coefficient was calculated from the expression for molecular diffusion in the macropores. This mechanism has been demonstrated to be the controlling mechanism for CO_2 in zeolite 13X [64].

With these assumptions, the gas phase mass balance, which accounts for dispersive, convective and adsorptive effects within the column, is given by:

$$\frac{\partial c_i}{\partial t} = \frac{\partial}{\partial z}\left(cD_{\mathrm{L}}\frac{\partial y_i}{\partial z} + c_i v\right) - \frac{1-\epsilon}{\epsilon}\frac{\partial q_i}{\partial t} \tag{2.1}$$

For the independent variables, z is the axial length and t is the time. For the dependent variables, c is the total gas phase concentration, while c_i, y_i and q_i are the fluid phase concentration, the fluid phase mole fraction and the solid phase loading of component i, v is the interstitial velocity, ϵ is the bed void fraction and D_{L} is the axial dispersion coefficient. If the ideal gas law is assumed, c in Eqn. 2.1 can be expanded. For an ideal gas, using $c = P/RT$, where P is the pressure, R is the universal gas constant and T is the temperature. The component mass balance can be written as:

$$\frac{\partial y_i}{\partial t} + \frac{y_i}{P}\frac{\partial P}{\partial t} - \frac{y_i}{T}\frac{\partial T}{\partial t} = D_{\mathrm{L}}\frac{T}{P}\frac{\partial}{\partial z}\left(\frac{P}{T}\frac{\partial y_i}{\partial z}\right) - \frac{T}{P}\frac{\partial}{\partial z}\left(\frac{y_i P}{T}v\right) - \frac{RT}{P}\frac{1-\epsilon}{\epsilon}\frac{\partial q_i}{\partial t} \tag{2.2}$$

If all component mass balances are summed, the overall mass balance can be written as:

$$\frac{1}{P}\frac{\partial P}{\partial t} - \frac{1}{T}\frac{\partial T}{\partial t} = -\frac{T}{P}\frac{\partial}{\partial z}\left(\frac{P}{T}v\right) - \frac{RT}{P}\frac{1-\epsilon}{\epsilon}\sum_{i=1}^{n_{\mathrm{comp}}}\frac{\partial q_i}{\partial t} \tag{2.3}$$

Mass transfer in the solid phase is described by the linear driving force model:

$$\frac{\partial q_i}{\partial t} = k_i(q_i^* - q_i) \tag{2.4}$$

where q^* is the equilibrium loading and k_i is LDF coefficient. The equilibrium loading, q^* can be represented by a suitable adsorption isotherm:

$$q^* = q^*(y, P, T) \tag{2.5}$$

The LDF coefficient is a lumped parameter which, for the case of a system that is controlled by molecular diffusion in the macropores, is described as:

$$k_i = \frac{15\epsilon_{\mathrm{p}}D_{\mathrm{p}}}{r_{\mathrm{p}}^2}\frac{c_i}{q_i^*} \tag{2.6}$$

where ϵ_{p} is the particle void fraction, r_{p} is the particle radius and and D_{p} is the macropore diffusivity, which is a function of molecular diffusion, D_{m} (calculated from the Chapman-Enskog equation) and the adsorbent tortuosity, τ [18, 65].

$$D_{\mathrm{p}} = \frac{D_{\mathrm{m}}}{\tau} \tag{2.7}$$

Darcy's law describes the axial pressure drop across the column:

$$-\frac{\partial P}{\partial z} = \frac{150}{4}\frac{1}{r_{\mathrm{p}}^2}\left(\frac{1-\epsilon}{\epsilon}\right)^2 \mu v \tag{2.8}$$

where μ is the gas phase viscosity, which is assumed to be constant during the process. The column energy balance includes thermal effects due to conduction through the column wall, convection along the bed and adsorption:

$$\left[\frac{1-\epsilon}{\epsilon}(\rho_{\mathrm{s}} C_{\mathrm{p,s}} + C_{\mathrm{p,a}} \sum_{i=1}^{n_{\mathrm{comp}}} q_i)\right]\frac{\partial T}{\partial t} = \frac{K_z}{\epsilon}\frac{\partial^2 T}{\partial z^2} - \frac{C_{\mathrm{p,g}}}{R}\frac{\partial}{\partial z}(vP) - \frac{C_{\mathrm{p,g}}}{R}\frac{\partial P}{\partial t}$$
$$- \frac{1-\epsilon}{\epsilon} C_{\mathrm{p,a}} T \sum_{i=1}^{n_{\mathrm{comp}}} \frac{\partial q_i}{\partial t} + \frac{1-\epsilon}{\epsilon}\sum_{i=1}^{n_{\mathrm{comp}}}\left[(-\Delta H_i)\frac{\partial q_i}{\partial t}\right] - \frac{2h_{\mathrm{in}}}{\epsilon r_{\mathrm{in}}}(T - T_{\mathrm{w}}) \tag{2.9}$$

where ρ_{s} is the particle density, $C_{\mathrm{p,s}}$ is the solid heat capacity, $C_{\mathrm{p,g}}$ is the fluid heat capacity, $C_{\mathrm{p,a}}$ is the adsorbed phase heat capacity, K_z is the thermal conductivity of the gas, ΔH_i is the heat of adsorption of component i, h_{in} is the internal heat transfer coefficient, r_{in} is the internal radius of the column and T_{w} is the column wall temperature. The energy balance on the column wall is written as:

$$\rho_{\mathrm{w}} C_{\mathrm{p,w}}\frac{\partial T_{\mathrm{w}}}{\partial t} = K_{\mathrm{w}}\frac{\partial^2 T_{\mathrm{w}}}{\partial z^2} + \frac{2r_{\mathrm{in}}h_{\mathrm{in}}}{r_{\mathrm{out}}^2 - r_{\mathrm{in}}^2}(T - T_{\mathrm{w}}) - \frac{2r_{\mathrm{out}}h_{\mathrm{out}}}{r_{\mathrm{out}}^2 - r_{\mathrm{in}}^2}(T_{\mathrm{w}} - T_{\mathrm{amb}}) \tag{2.10}$$

where ρ_{w} is the density of the column wall, $C_{\mathrm{p,w}}$ is the heat capacity of the column wall, K_{w} is the thermal conductivity of the column wall, r_{out} is the external radius of the column wall, h_{out} is the external heat transfer coefficient and T_{amb} is the ambient temperature outside of the column

The axial dispersion coefficient, D_{L}, is a lumped parameter that is a combination of the molecular diffusion, D_{m}, and turbulent mixing which can be written as [18]:

$$D_{\mathrm{L}} = 0.7 D_{\mathrm{m}} + v r_{\mathrm{p}} \tag{2.11}$$

The model equations were discretized in the axial direction using a finite volume scheme employing a WENO flux limiter. The column was discretized into 30 finite volumes. The resulting set of ordinary differential equations (ODE) were solved using *ode15s*, an explicit inbuilt MATLAB ODE solver. The details are explained in earlier publications [19, 66].

2.3.2 Mass Balance Calculations

Since there is no reaction within the column, the following molar balance can be written for the case of an adsorption experiment [67].

$$n_{\text{acc}} = n_{\text{in}} - n_{\text{out}} \tag{2.12}$$

The accumulation, n_{acc}, is the difference between the moles entering the column, n_{in}, and the moles leaving the column, n_{out}. Part of the accumulation is in the solid phase and the remaining amount is in the fluid. Assuming that the ideal gas law is valid, at the end of a DCB experiment the individual terms can be written as:

$$m_{\text{ads}} q_i^* + \frac{y_{i,\text{in}} P_{\text{avg}}}{RT_{\text{in}}} \left(V_{\text{b}} \epsilon + V_{\text{d}} \right) = \int_0^{t_{\text{ads}}} \left(\frac{y_{\text{i,in}} P_{\text{ave}} Q_{\text{in}}}{RT_{\text{in}}} \right) dt - \int_0^{t_{\text{ads}}} \left(\frac{y_{i,\text{out}} P_{\text{ave}} Q_{\text{out}}}{RT_{\text{out}}} \right) dt \tag{2.13}$$

In Eqn. 2.13, Q is the actual gas volumetric flowrate, V_{b} is the total bed volume, V_{d} is the extra-column volume, sometimes called the dead volume, and q_i^* is the averaged equilibrium loading. Solving Eqn. 2.13 for q_i^* yields the equilibrium loading for the adsorbent for the particular set of conditions [67]. In all experiments performed, the pressure drop across the column was negligible (< 0.02 bar), therefore the average column pressure was used, $P_{\text{ave}} = \frac{P_{\text{in}} + P_{\text{out}}}{2} \approx P$. Note that Eqn. 2.13 can be used to measure the competitive loadings in multicomponent mixtures provided that independent equations are written for each of the components in the experiment. The measured q_i^* provides the loading corresponding to the partial pressures of each species, $y_{\text{in}} P_{\text{ave}}$ and temperature, T. Note that it is important that the experiment proceeds as long as its required for both the composition and thermal breakthroughs to occur.

For the case of a desorption experiment with an inert feed, the mass balance can be written as:

$$n_{\text{acc}} = n_{\text{out}} \tag{2.14}$$

Again, assuming that the ideal gas law is valid, at the end of a desorption experiment

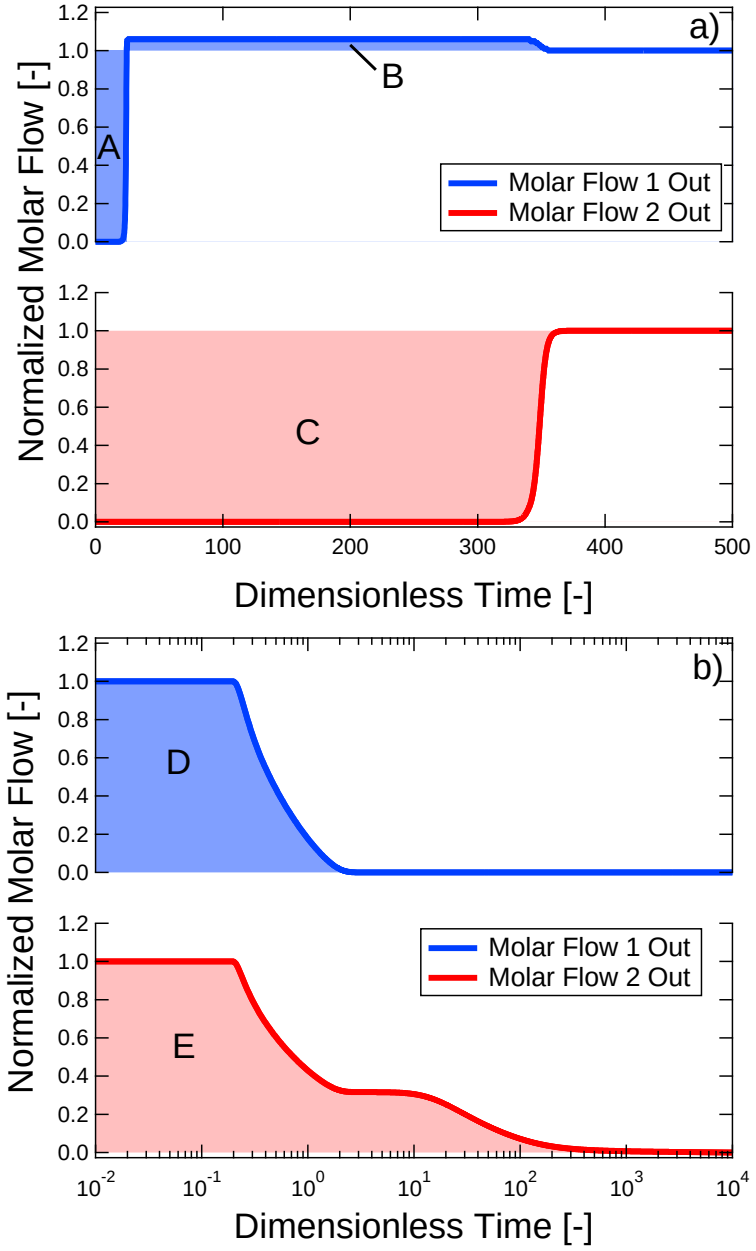

Figure 2.2: A graphical representation of the solid and fluid phase accumulations for (**a**) adsorption and (**b**) desorption of a hypothetical binary mixture. The molar flows have been normalized to the component inlet flow rate so that 1 represents the molar feed flowrate. For adsorption, component 1 and 2 have an accumulation of $[\boldsymbol{A} - \boldsymbol{B}]$ and $\boldsymbol{C}$, respectively. For desorption, component 1 and 2 have an accumulation of $\boldsymbol{D}$ and $\boldsymbol{E}$, respectively.

the individual terms can be written as:

$$m_{\text{ads}} q_i^* + \frac{y_{i,\text{in}} P_{\text{avg}}}{RT_{\text{in}}} \left(V_{\text{b}} \epsilon + V_{\text{d}} \right) = \int_0^{t_{\text{des}}} \left(\frac{y_{i,\text{out}} P_{\text{ave}} Q_{\text{out}}}{RT_{\text{out}}} \right) dt \tag{2.15}$$

where q_i^* is the solid phase loading at $t = 0$. In this situation it is important to wait until the column is both saturated with the desired feed and thermally equilibrated before flow is switched to the sweep gas. Also, it is important to perform these experiments where the ΔP across the column is low to satisfy the condition that q_i^* is uniform across the column.

The fluid and solid accumulation of a given component can be determined graphically from the addition or subtraction of shaded areas in Fig. 2.2. For a single component system, let us just consider component 2 in Fig. 2.2. For adsorption, the accumulation is area $\boldsymbol{C}$; for desorption, the accumulation is area $\boldsymbol{E}$. For a hypothetical mixture of component 1 and 2 (both components normalized with their component feed molar flowrates for the sake of simplicity), it is important to consider the breakthrough curves for both components. As seen in Fig. 2.2(**a**), for a period of time the outlet molar flow of component 1 is greater than its flowrate at the inlet. This is referred to as the "roll-up" and is crucial to determine the competitive equilibrium loading of component 1. The roll-up is the amount of component 1 that is forced out of the column due to adsorptive competition with component 2. For the desorption, the equivalent of the roll-up is now found as a plateau in the component 2 profile. Summarizing, in a binary adsorption experiment the accumulation for components 1 and 2 are the areas $[\boldsymbol{A} - \boldsymbol{B}]$ and $\boldsymbol{C}$, respectively. For the same mixture, the desorptive accumulation for components 1 and 2 are areas $\boldsymbol{D}$ and $\boldsymbol{E}$, respectively.

2.4 Experimental Results

2.4.1 Single Component Equilibrium

Volumetric and gravimetric equilibrium data of CO_2 and N_2 were measured and reported in Fig. 2.3. The results indicate that the adsorption affinity of CO_2 is greater

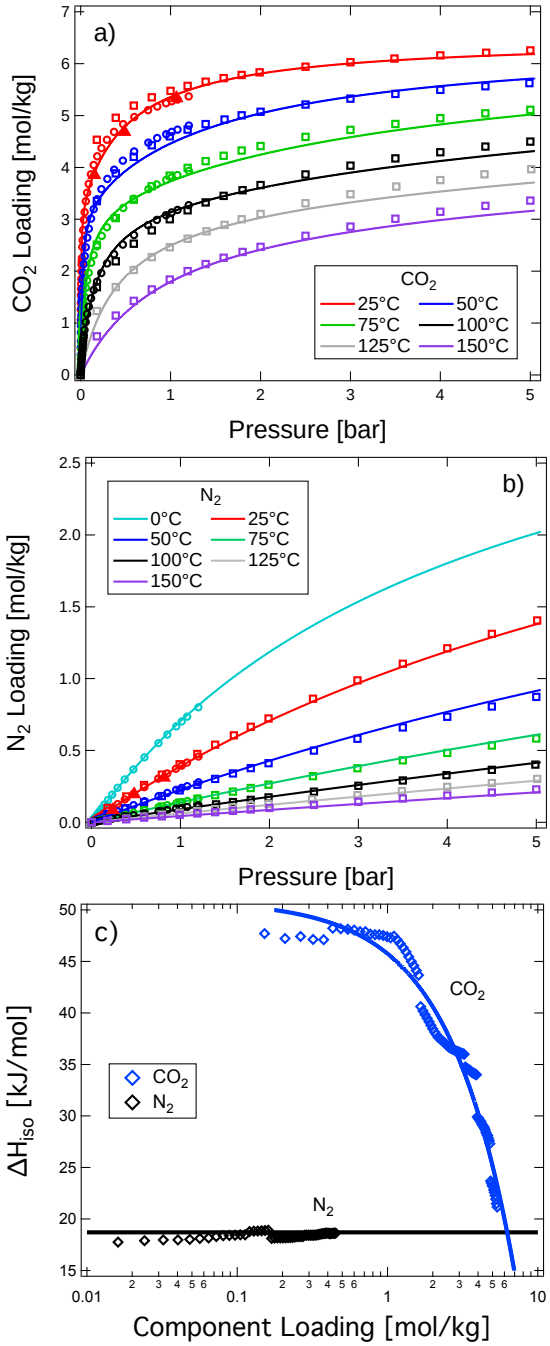

Figure 2.3: Single component adsorption equilibrium on zeolite 13X for (**a**) CO_2 and (**b**) N_2, symbols represent experimentally measured data and the lines represent isotherm fits. Volumetric data are circles, gravimetric data are squares and dynamic column breakthrough experiments are triangles. The lines shown here for N_2 correspond to the EES model. (**c**) Measured (symbols) and fitted (lines) isosteric heats for CO_2 and N_2.

than N_2, with N_2 having a fairly linear isotherm, while CO_2 is nonlinear at the same temperature. Note that the data from the volumetric and gravimetric systems were consistent and can be reliably combined if there is a need to obtain data over a wide range of pressures.

The isosteric heat of adsorption, ΔH_{iso} was calculated using the Clausius-Clapeyron equation:

$$\left[\frac{\partial \ln(p_i)}{\partial(1/T)}\right]_{q_i^*} = -\frac{\Delta H_{\text{iso}}}{R} \tag{2.16}$$

ΔH_{iso} is related to ΔU by

$$\Delta U = \Delta H_{\text{iso}} + RT \tag{2.17}$$

Fig. 2.3(**c**) shows the calculated values ΔH_{iso} for CO_2 and N_2. These values were calculated from 25 to 100°C and 1 mbar to 1.2 bar using the volumetric experiments. It is clear that N_2 and CO_2 show different trends as a function of loading. On the one hand, although there is a minor variation, the isosteric heat of N_2 does not change much over the loading range. This suggests that for N_2, zeolite 13X is practically energetically homogenous [68, 69]. On the other hand, the isosteric heat of CO_2 decreases as the loading increases. The calculated CO_2 isosteric heats are in agreement with values found by Dirar and Loughlin [70]. At low CO_2 loadings, the isosteric heat is very high (≈ 47 kJ/mol) and low (≈ 20 kJ/mol) at high CO_2 loadings. This suggests that CO_2 adsorbs onto high energy sites at low pressures (low loadings) and once they are saturated, low energy sites are occupied at high pressures (high loadings) [68]. The ΔH_{iso} of CO_2 (in J/mol) was fit to an empirical linear equation for simulation purposes as a function of q_{CO_2} (in mol/kg):

$$\Delta H_{\text{iso},CO_2} = -5156 q_{CO_2} + 50.907 \times 10^3 \tag{2.18}$$

2.4.2 Single Component Breakthrough Experiments

Single component CO_2 and N_2 breakthrough experiments were performed at ≈ 0.98 bar and ≈ 22°C. A summary of the breakthrough experiments is shown in Table 2.1.

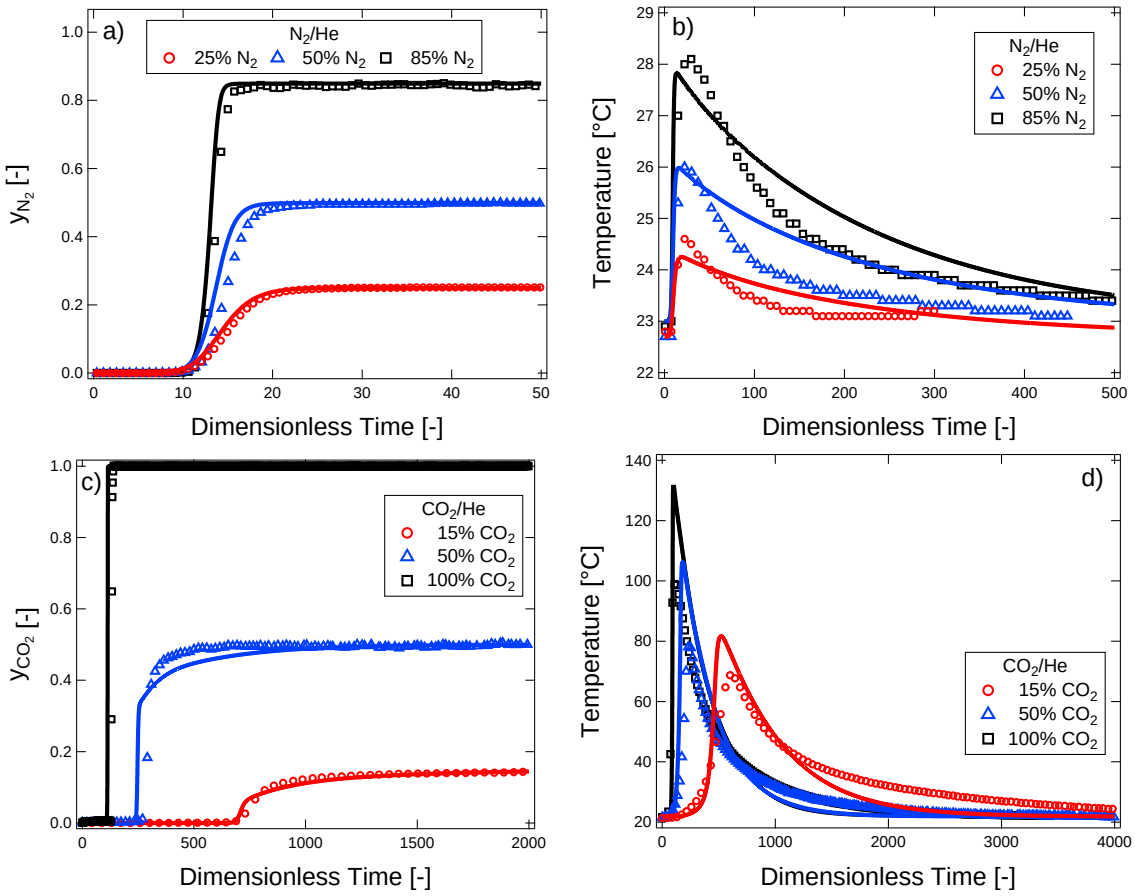

Figure 2.4: Single component N_2 [(**a**) and (**b**)] and CO_2 [(**c**) and (**d**)] composition and temperature breakthrough curves on zeolite 13X at $\approx 22°C$. The carrier gas for all cases was He. Experiments are the symbols and lines are from simulations using the EES model. The temperature is measured at $z = 0.8L$.

For all breakthrough experiments, He was used as a carrier gas. The results are reported in dimensionless time, $\bar{t}$, which is calculated as $\bar{t} = tv/L$, where t is the experimental time, v is the interstitial velocity at the column inlet and L is the packed length.

The results of the single-component N_2 breakthrough experiments at 25, 50 and 85 mol% N_2 are shown in Fig. 2.4(**a**). All the experimental breakthrough curves exit at $\bar{t} \approx 10$. The observation that the average retention time (corresponding to the first moment) is nearly independent of concentration indicates the linearity of the N_2 isotherm. The temperature histories show a similar trend, they all reach their peaks at about the same time. The slight difference in breakthrough times between the different feed compositions corresponds to the change in velocity associated with the adsorption of N_2 along the packed bed length. The maximum temperature reached increases with increasing N_2 feed composition. The N_2 loadings from the DCB experiments (triangles), calculated using Eqn. 2.13, compare well with static equilibrium experiments (circles and squares) as shown in Fig. 2.3(**b**) and reported in Table 2.1.

The results of the single component CO_2 adsorption breakthrough experiments at 15, 50 and 100 mol% CO_2 are shown in Fig. 2.4. The composition breakthrough is shown in Fig. 2.4(**c**) while the temperature history is shown in Fig. 2.4(**d**). As expected for Type 1 isotherms, the breakthrough time increases as the feed composition of CO_2 reduces [71]. The composition breakthrough shows the classical shock transition starting from $y_{CO_2} = 0$. The smooth transition to the feed composition can be attributed to the non-isothermal nature of the process. The high heat of adsorption can be seen from the maximum temperatures (up to 100°C) observed in these experiments. It is worth noting that the thermal wave propagates slower when the composition is lower; this is different than the case of N_2 where all the thermal waves propagate at approximately the same speed. Finally, the CO_2 loading was calculated from Eqn. 2.13 and is shown in Fig. 2.3(**a**) as triangles. It is clear that the loadings match well with those from the batch experiments. The consistency in loadings

Table 2.1: A summary of all adsorption and desorption experiments. For the adsorption experiments, the columns "Gas", y_{CO_2} and y_{N_2} refer to the feed, while for the desorption experiments they indicate the conditions at which the column was initially saturated. The value [0] means that $q^*_{N_2}$ was calculated to be negative and they are represented as 0 to provide a meaningful result. Note that $y_{CO_2} + y_{N_2} + y_{He} = 1$.

.

Experiment Type	Gas	Q_{in} [ccm]	T [°C]	P [bar]	y_{CO_2} [-]	y_{N_2} [-]	$q^*_{CO_2}$ [mol/kg]	$q^*_{N_2}$ [mol/kg]
Adsorption	N_2/He	350	22.7	0.96	-	0.25	-	8.53×10^{-2}
	N_2/He	351	23.0	0.96	-	0.50	-	0.195
	N_2/He	350	23.0	0.96	-	0.85	-	0.311
	CO_2/He	700	21.8	1.02	0.15	-	3.854	-
	CO_2/He	315	21.9	0.97	0.50	-	4.685	-
	CO_2/He	350	22.1	1.07	1.00	-	5.501	-
	CO_2/N_2	500	23.1	1.06	0.05	0.95	2.909	[0]
	CO_2/N_2	498	22.9	1.05	0.10	0.90	3.461	[0]
	CO_2/N_2	300	22.0	1.02	0.15	0.85	3.833	[0]
	CO_2/N_2	201	23.5	0.95	0.50	0.50	4.814	[0]
	CO_2/N_2	202	21.6	0.98	0.75	0.25	5.375	[0]
	CO_2/N_2/He	400	24.4	1.04	0.05	0.45	3.090	[0]
	CO_2/N_2/He	400	23.8	1.00	0.10	0.40	3.498	[0]
	CO_2/N_2/He	400	23.9	1.03	0.25	0.25	4.200	[0]
	CO_2/N_2/He	400	23.7	1.02	0.40	0.10	4.708	[0]
Desorption	CO_2/N_2	50	22.6	0.97	0.05	0.95	-	0.1445
	CO_2/N_2	50	22.1	0.97	0.10	0.90	-	0.0811
	CO_2/N_2	50	23.1	0.97	0.15	0.85	-	0.0801
	CO_2/N_2	50	23.8	0.97	0.50	0.50	-	0.0362
	CO_2/N_2	50	23.8	0.96	0.75	0.25	-	0.0200
	CO_2/N_2/He	50	24.4	0.95	0.05	0.45	-	0.0281
	CO_2/N_2/He	50	23.9	0.95	0.10	0.40	-	0.0192
	CO_2/N_2/He	50	24.6	0.96	0.25	0.25	-	0.0186
	CO_2/N_2/He	50	24.1	0.97	0.40	0.10	-	0.0082

between the three experiments (volumetry, gravimetry and dynamic column breakthrough) confirm that the zeolite sample is reasonably consistent and reproducible.

2.4.3 Binary Adsorption Breakthrough Experiments

After the single component breakthroughs were completed, competitive adsorption CO_2/N_2 breakthroughs were measured. Experiments were performed with CO_2/N_2 compositions of: 15/85, 50/50 and 75/25 mol% CO_2/N_2 mixtures at $T = 22°C$, $P = 0.98$ bar and $Q_{in} = 350$ ccm. A summary of all the competitive breakthrough experiments are shown in Table 2.1 and the adsorption breakthrough curves are shown in Fig. 2.5. As seen from the breakthrough curves, N_2 breaks through very early and the outlet composition of N_2 reaches 100 mol%. This classic "roll-up" effect is well known and has been reported for competitive systems obeying Type 1 isotherms. The CO_2 breakthrough is similar to the single component runs. The temperature history shown in Fig. 2.5(**c**) shows the presence of a small peak at very low values of $\bar{t}$ which corresponds to the heat generated by N_2 adsorption. The temperature rise due to CO_2 adsorption is more prominent. Note that the experiments were run for a prolonged period of time until the temperature front fully broke through and the column was returned to the surrounding temperature. This is essential to perform the transient mass balance to measure the competitive loadings.

The competitive loadings of CO_2 and N_2 were calculated from the adsorption breakthrough profiles using Eqn. 2.13. The competitive CO_2 loadings were measured with high reliability and are reported in Fig. 2.6 and Table 2.1. However, the N_2 equilibrium loadings could not be accurately calculated from the competitive breakthrough experiments. The N_2 loadings calculated with this method yielded negative values, which are physically unrealistic. Some of the experiments were repeated to check for reproducibility. Although the breakthrough curves showed excellent reproducibility, the unrealistic N_2 loadings persisted. Similar results have been reported in the literature [34]. This was partially due to the sensitivities and accuracies for the mass flow

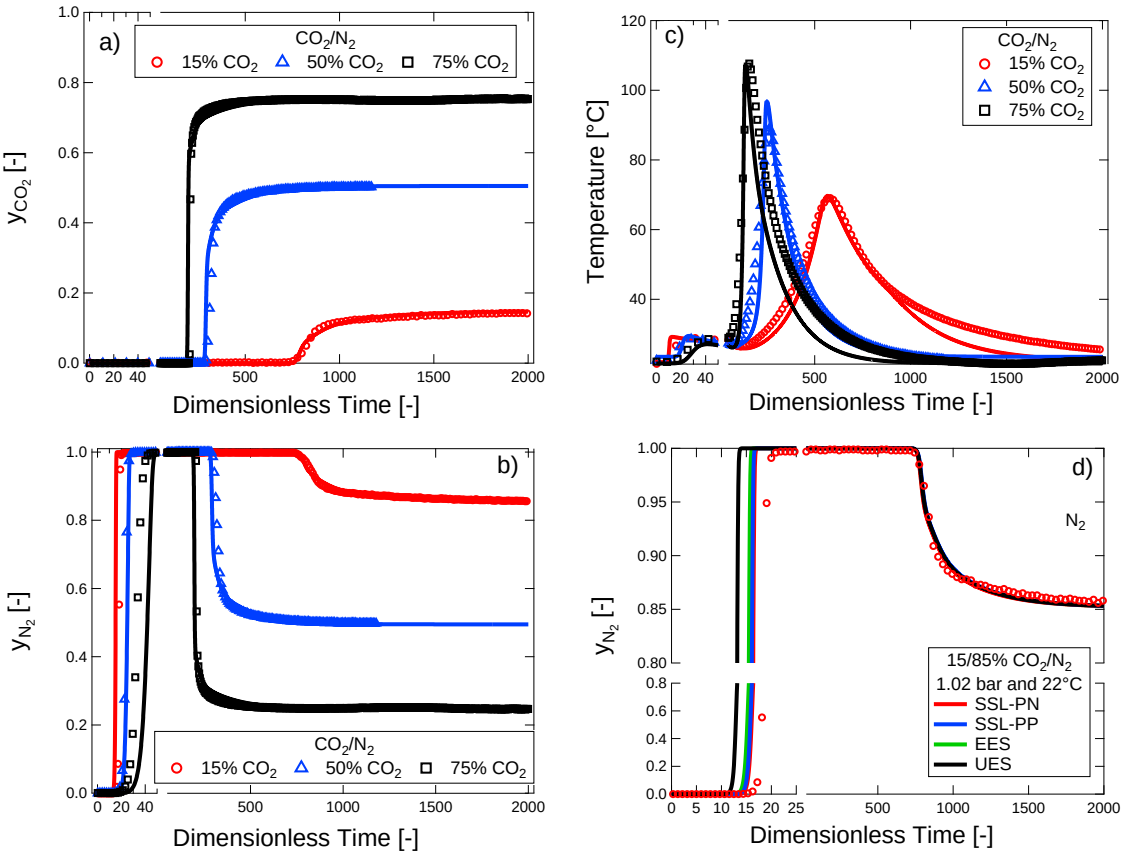

Figure 2.5: Competitive (**a**) CO_2 and (**b**) N_2 composition and temperature (**c**) breakthrough profiles on zeolite 13X. The competitive CO_2/N_2 breakthrough experiments are at 15/85, 50/50 and 25/75 mol% mixtures of CO_2 and N_2. Symbols are the experimental measurements and lines are the simulations from UES parameters. (**d**) Comparison of the calculations by the different fitting procedures with the experimental breakthrough curve for N_2.

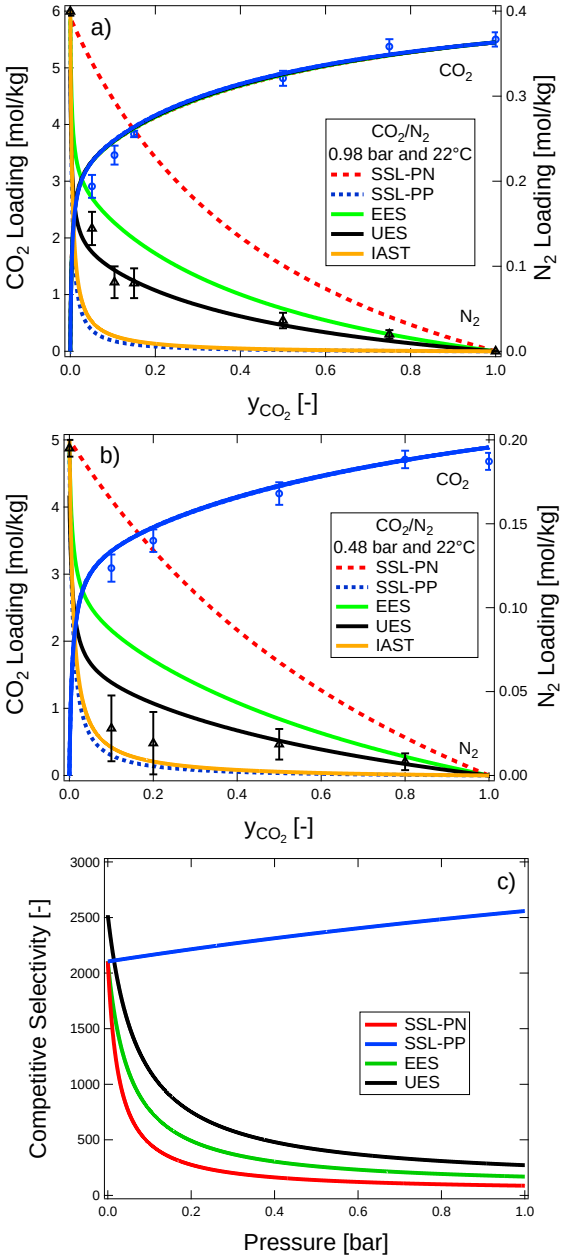

Figure 2.6: Competitive CO_2 (circles) and N_2 (triangles) equilibrium loadings from dynamic column breakthrough and desorption experiments on zeolite 13X at a total pressure of 0.98 (**a**) and 0.48 (**b**) bar at 22°C. CO_2 is shown in blue and N_2 is shown in black. The different equilibrium fitting procedures are shown with IAST predictions. (**c**) Calculated competitive CO_2/N_2 selectivities for a 15/85 mol% mixture as a function of total pressure at 25°C. The error bars show the 95% confidence intervals of each measurement.

controllers (±2 sccm), mass flow meter (±1 sccm) and primary flow calibrator (±2 ccm). However, the largest uncertainty was the accumulated error that is associated with the relatively long breakthrough time of CO_2 ($\bar{t} > 120$) to the fast N_2 breakthrough time ($\bar{t} = 10$). This uncertainty accumulates for the entire experimental time, from $\bar{t} = 10$ to at least $\bar{t} = 120$. Due to these problems, the integration of Eqn. 2.13 often yielded unrealistic negative N_2 loadings. Fig. 2.2(**a**) shows a qualitative picture of Eqn. 2.13. As discussed earlier, for the case of CO_2 the shaded region ***C*** represents the amount of CO_2 present in the column, while for N_2 this amount of is given by [***A*** − ***B***]. As it can be seen in Fig. 2.2(**a**), the areas ***A*** and ***B*** can be very similar and since the compositions and flows are measured with a finite accuracy, the calculated N_2 loadings are rather unreliable. This could possibly explain why Avijegon *et al.* measured negligible (≈ 0) loadings for the competitive adsorption of N_2 in mixtures of CO_2 and N_2 at ≈ 1 bar [34]. This analysis suggests that adsorption breakthrough experiments could result in unreliable measurements for the lighter component, when the competition between the two species is very strong. Note that such issues are not faced when gases of comparable affinities were used as seen from our previous studies with O_2 and Ar on Ag-ETS-10 where the selectivity is 1.5 [66].

2.4.4 Binary Desorption Breakthrough Experiments

The adsorption breakthrough experiments provided inconclusive data for competitive N_2 adsorption. Therefore, it was decided to consider desorption experiments. The hypothesis was that in the desorption experiments, the area proportional to the accumulated amount corresponds to ***D*** in Fig. 2.2 (**b**), which is obtained in a short time that prevents the accumulation of error. It should be noted that for a system where the competitive loading is small, it is likely that the desorption is over in a very short time. Hence, in order to overcome this, we also decided to perform the desorption experiments at much lower flows. The experiments were done by first performing a breakthrough experiment with a given mixture of CO_2, N_2 and He. After the break-

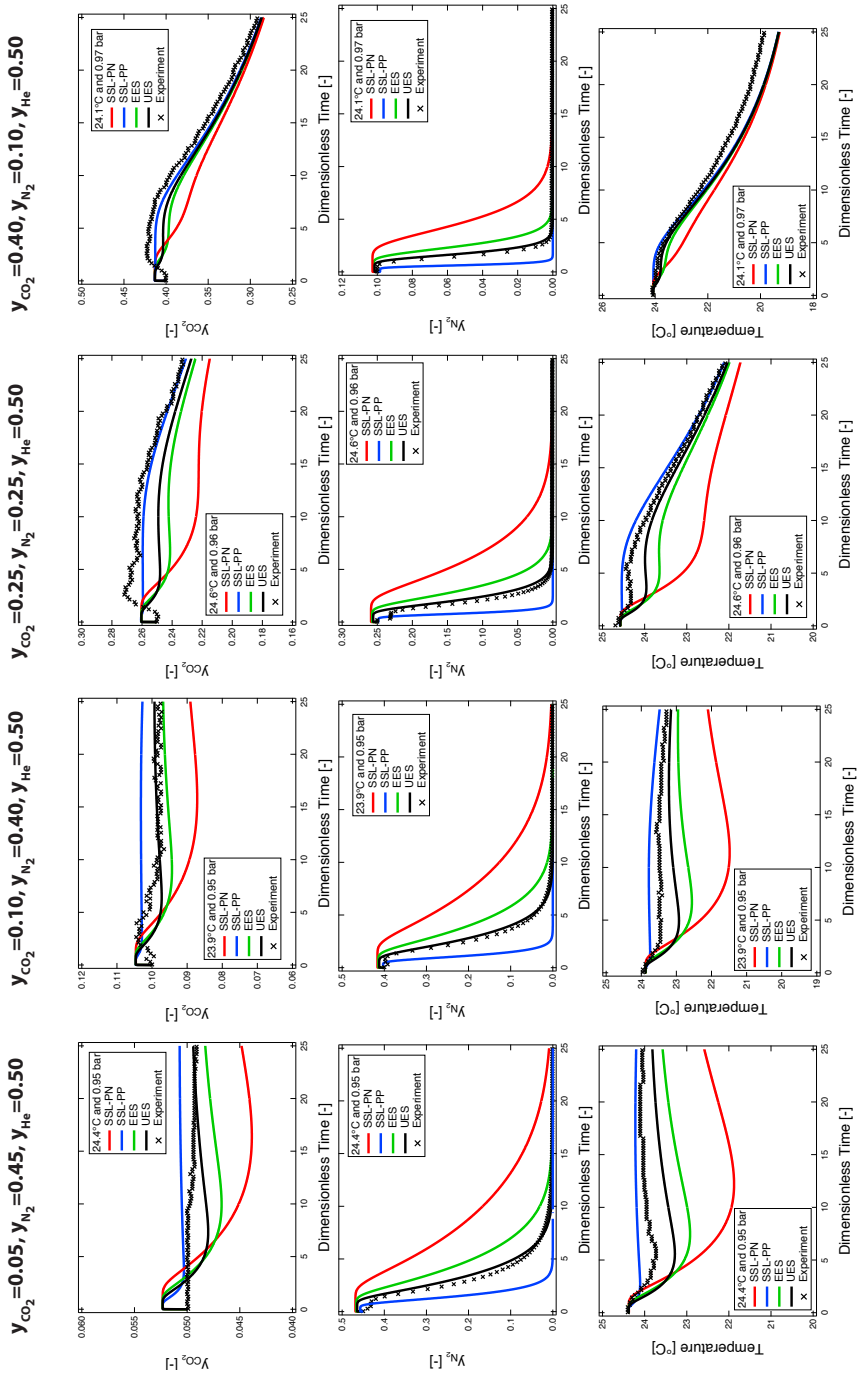

Figure 2.7: Competitive CO_2/N_2 composition (left columns) and temperature (right column) desorption profiles on zeolite 13X at $\approx 22°C$ and 0.48 bar. Experiments are the markers and simulations are the various lines. These experiments were diluted with 50 mol% He during adsorption. The initial compositions are provided at the top of each column of figures. Temperature is measured at $z = 0.8L$. Desorption was performed using a sweep of He at 50 ccm.

through was complete, the adsorbing gas was switched to 50 ccm of He. Two types of experiments were performed. The first set of experiments involved saturating the bed with different compositions of CO_2 and N_2, and desorbing it with He. In the second set of experiments, the column was saturated with a mixture of He, CO_2 and N_2, and later desorbed with He. Various experiments were performed by fixing the He composition at 50 mol% while changing the relative proportion of CO_2 and N_2. Since He can be considered a non-adsorbing gas, these experiments allowed us to explore competition at lower concentrations ($P = 0.48$ bar).

The details of the experiments are provided in Table 2.1. The competitive desorption composition and temperature profiles for the case where a mixture of CO_2/N_2 and He were saturated at the beginning of the experiment are shown in Fig. 2.7. Similar plots for the case where the column was saturated with mixtures of CO_2 and N_2 are provided in the supporting information. As seen from Fig. 2.7, N_2 desorbs very quickly compared to CO_2. In this case the qualitative desorption profiles are shown in Fig. 2.2(**b**). Since the experiment was performed at low flows, it resulted in a reliable estimation of the N_2 competitive loadings that are plotted in Fig. 2.6. Owing to the strong CO_2 isotherm, the desorption can take an unusually long time and the experiments were not extended beyond $\bar{t} \approx 500$. Accordingly, competitive CO_2 loadings were not measured from the desorption experiments. In order to calculate the competitive N_2 loading, Eqn. 2.15 was integrated between $\bar{t} = 0$ to 500. The measured competitive N_2 loadings are shown in Fig. 2.6. It can be seen that these experiments provided physically realistic, meaningful, N_2 loadings compared to the adsorption breakthrough experiments. It is also worth noting that the N_2 loadings obtained from the desorption experiments compare well with those reported by Hefti *et al.* [54].

2.5 Parameter Estimation and Modeling Results

2.5.1 Isotherm Parameter Estimation

Several isotherm models have been proposed in the literature to describe the equilibrium of CO_2 and N_2 on zeolite 13X. The goal in this study is to consider forms that are easy to describe and have a straightforward, explicit extension to competitive forms so that they can be used for large-scale simulation and optimization. Recently, Purdue has discussed the use of a dual-site model to describe CO_2 isotherms to reliably represent CO_2 adsorption on zeolite 13X [59]. The variation of the isosteric heat with loading lends itself to support this argument; that CO_2 adsorbs to a heterogenous surface. Further, Farmahini *et al.* also demonstrated the ability of the dual-site Langmuir model to describe single component isotherms of CO_2 and N_2 [57]. The DSL model for a binary mixture is expressed as:

$$q_i^* = \frac{q_{\mathrm{b},i}^{\mathrm{sat}} b_i c_i}{1 + b_1 c_1 + b_2 c_2} + \frac{q_{\mathrm{d},i}^{\mathrm{sat}} d_i c_i}{1 + d_1 c_1 + d_2 c_2} \tag{2.19}$$

where $q_{\mathrm{b}}^{\mathrm{sat}}$ and $q_{\mathrm{d}}^{\mathrm{sat}}$ are the saturation capacities of the two sites b and d, respectively. The equilibrium constants b_i and d_i are dependent on temperature as described by:

$$b_i = b_{0,i} \exp\left(\frac{-\Delta U_{\mathrm{b},i}}{RT}\right) \tag{2.20}$$

$$d_i = d_{0,i} \exp\left(\frac{-\Delta U_{\mathrm{d},i}}{RT}\right) \tag{2.21}$$

where $\Delta U_{\mathrm{b},i}$ and $\Delta U_{\mathrm{d},i}$ are the internal energies of adsorption to sites b and d, respectively. The sites "b" and "d" represent the strong and the weak sites, respectively.

Determining the correct isotherm parameters is critical. Several ways have been proposed to estimate the parameters. Farmahini *et al.* recently discussed a few ways of fitting the CO_2 and N_2 isotherms [57]. In their study three methods were proposed. The first two involved fitting CO_2 isotherms first, then setting the saturation capacity of N_2 for both sites to be identical to that of CO_2 and then fitting the b and d constants to different constraints. The third involved a more detailed fit considering the Henry's

Table 2.2: Dual-site Langmuir isotherm parameters for pure components on zeolite 13X.

Gas	Model	$q_{\mathrm{b}}^{\mathrm{sat}}$ [mol/kg]	b_0 [m^3/mol]	$-\Delta U_{\mathrm{b}}$ [kJ/mol]	$q_{\mathrm{d}}^{\mathrm{sat}}$ [mol/kg]	d_0 [m^3/mol]	$-\Delta U_{\mathrm{d}}$ [kJ/mol]
CO_2	DSL	3.257	2.09×10^{-7}	42.67	3.240	1.06×10^{-7}	32.21
N_2	SSL	6.497	2.15×10^{-6}	16.23	0	0	0
N_2	EES	3.257	2.13×10^{-6}	16.25	3.240	2.13×10^{-6}	16.25
N_2	UES	3.257	7.96×10^{-7}	18.86	3.240	6.94×10^{-7}	17.76

constant of both components and low temperature isotherms. In the current work we adapt an approach similar to Farmahini *et al.* First, the DSL model is fitted to the experimentally measured CO_2 isotherms. The parameters, namely $q_{\mathrm{b,CO_2}}^{\mathrm{sat}}$, $q_{\mathrm{d,CO_2}}^{\mathrm{sat}}$, $b_{0,\mathrm{CO_2}}$, $d_{0,\mathrm{CO_2}}$, $\Delta U_{\mathrm{b,CO_2}}$ and $\Delta U_{\mathrm{d,CO_2}}$, were fitted simultaneously using the data points between 0 and 1.2 bar for the temperatures 25 to 100°C. The goal was to obtain an accurate fit for the range of pressures where the model will be used. The parameters are listed in Table 2.2. As can be seen, the ΔU values, for the two sites corresponds approximately to the upper and lower bounds of the ΔH_{iso} shown in Fig. 2.3(**c**) (note the relationship between ΔH_{iso} and ΔU is given by Eqn. 2.17). Four different procedures were used to estimate the parameters for the N_2 isotherm:

Single Site Langmuir (SSL) The single site Langmuir isotherm fitting procedure (SSL) is the first approach. The SSL uses a single site Langmuir isotherm by forcing $q_{\mathrm{N_2}}^{\mathrm{sat}} = q_{\mathrm{b,CO_2}}^{\mathrm{sat}} + q_{\mathrm{d,CO_2}}^{\mathrm{sat}}$ and then fitting $b_{0,\mathrm{N_2}}$ and $\Delta U_{\mathrm{b,N_2}}$ to the experimental data. Variations of this approach have been used in the literature [41, 50]. The implicit assumption here is that the adsorbent is homogenous with respect to N_2. The volumetric single-component data between $P = 0$ to 1.2 bar and $T = 25$ to 100°C were used for the fitting procedure. Parameters obtained by this fitting method are shown in Table 2.2. Note that the ΔU obtained nicely corresponds to the ΔH_{iso} shown in Fig. 2.3(**c**). Since the DSL model was used to describe the CO_2 isotherms, there are two possible ways to combine the SSL parameters for N_2 to describe the

competitive behavior. The SSL perfect positive (SSL-PP) fitting procedure refers to the case where the SSL parameters are paired with the b site of the CO_2 and for the SSL perfect negative (SSL-PN), the SSL parameters of N_2 are paired with the d site [21]. Note that the values of equilibrium constants and ΔU for the two approaches are, as expected, the same. What changes is just the pairing with the CO_2 isotherm.

Dual Site Langmuir with Equal Energy Sites (EES): In this case N_2 is considered to be distributed between two equal energy sites (hence EES) with the saturation capacity of each site identical to that of CO_2 [57]. In other words, the following conditions are enforced:

$$q^{\text{sat}}_{\text{b,N}_2} = q^{\text{sat}}_{\text{b,CO}_2} \tag{2.22}$$

$$q^{\text{sat}}_{\text{d,N}_2} = q^{\text{sat}}_{\text{d,CO}_2} \tag{2.23}$$

$$b_{0,\text{N}_2} = d_{0,\text{N}_2} \tag{2.24}$$

$$\Delta U_{\text{b,N}_2} = \Delta U_{\text{d,N}_2} \tag{2.25}$$

Note that while Eqns. 2.22 and 2.23 are required to obtain the thermodynamically consistent form of a DSL isotherm [57, 72], Eqns. 2.24 and 2.25 enforce a condition that N_2 sees a homogenous surface. Variations of this approach have been used in the literature [57, 73]. The volumetric single-component data between $P = 0$ to 1.2 bar and $T = 25$ to 100°C were used for the fitting procedure and the parameters are provided in in Table 2.2.

Dual Site Langmuir with Unequal Energy Sites (UES): In this case the restriction of equal energy sites (Eqns. 2.24 and 2.25) is removed. The sorbent is considered to posses unequal energy sites (UES) also for N_2. Only the constraints described in Eqns. 2.22 and 2.23 are enforced. For this case, the competitive N_2 loadings were also considered to fit the model. In other words the objective function that is used to fit the parameters now includes both the data from the volumetric

experiments and the binary data from the breakthrough experiments. Naturally, the relaxation of the equal energy requirements and the use of the binary data should provide this approach an advantage over the others. The fitting parameters are shown in Table 2.2. As can be seen in Table 2.2, the estimated values of ΔU_{b} and ΔU_{d} vary by $\approx 6\%$, indicating that that the two sites are of comparable energy. While this fitting procedure provides a better estimate of the binary data, it underpredicts the single-component data up to $\approx 15\%$. This compromise was necessary in order to fit the binary data in an explicit form.

IAST: Ideal adsorbed solution theory (IAST) was used as a comparison for these models. IAST was developed by Myers and Prausnitz to describe ideal adsorption competition on an adsorbent [20]. This approach provides a method to calculate competitive loadings based on single-component isotherms. The method to calculate the competitive loadings using the IAST is provided in the supporting information.

2.5.2 Comparison of Isotherm Parameter Estimation Approaches

Fig. 2.6 shows the calculated competitive loadings of CO_2 and N_2 as a function of CO_2 composition at a total pressure of 0.98 and 0.48 bar at 22°C. It can be seen that the competitive CO_2 loadings are essentially unaffected by the type of competitive isotherm chosen. However, the N_2 loading is significantly impacted by the competitive model. The SSL-PP model, where N_2 competes with the strong site of CO_2, predicts the lowest N_2 loading, while the SSL-PN, where N_2 competes with the weak site of CO_2, predicts the highest N_2 loading. The EES and UES fitting procedures predict intermediate N_2 loadings. The EES predicts a slightly higher loading compared to the UES fitting procedure. IAST for all N_2 isotherms predicts competition very close to the SSL-PP fitting procedure. It is important to note that the IAST calculations under-predict the observations by Hefti *et al.* [54].

The competitive selectivity, α_{CO_2,N_2}, for a mixture is calculated using:

$$\alpha_{CO_2,N_2} = \frac{q^*_{CO_2}(y_{CO_2})}{q^*_{N_2}(y_{N_2})} \frac{y_{N_2}}{y_{CO_2}} \tag{2.26}$$

The competitive selectivities were determined as a function of total pressure for all four fitting procedures for a mixture of 15/85 mol% CO_2/N_2, i.e., corresponding to a typical feed composition of a post-combustion CO_2 capture plant, and are shown in Fig 2.6(**c**). The selectivities of SSL-PN, EES and UES follow the expected trend, i.e., where α decreases as the pressure increases. Specifically, in this case, the selectivity drops from $\approx$ 2000-2500 to 100-300. The selectivities calculated by the the three procedures decrease in the following order UES>EES>SSL-PN. However, the SSL-PP fitting procedure provides a physically unrealistic picture where α increases with pressure. This is due to the weak adsorption of N_2 in the SSL-PP fitting procedure, which affects the high-energy sites that get filled at low pressures. At high pressures, the low energy sites start to dominate and there is virtually no competition from N_2 on these sites. Hence, at higher pressures the SSL-PP likely will overpredict the performance of zeolite 13X

2.5.3 Breakthrough Simulation Parameter Estimation

Parameters for the experiments and simulations are provided in Table 2.3. The bulk density of the adsorbent, ρ_{bulk}, was measured by weighing a volume of adsorbent from a graduated cylinder after the particles had been well packed. The bulk void fraction, ϵ, was taken from the literature for a column of well-packed spherical particles [74]. The particle void fraction, ϵ_p, the specific heat capacity of the adsorbent, $C_{p,s}$, the specific heat capacity of the column wall, $C_{p,w}$, the thermal conductivity of the wall, K_w, the column density, ρ_w and the tortuosity, τ, were assumed to be the same as in Haghpanah *et al.*, which used a similar zeolite 13X sample and a stainless steel column [19]. The specific heat capacity of the gas mixtures, $C_{p,g}$ were taken as standard values for each different gas mixture; these values were obtained using the

Table 2.3: Adsorption and desorption simulation parameters for zeolite 13X.

Parameter	Value	Source
Column Properties		
adsorbent mass, m_{ads} [g]	23.02	measured
column length, L [m]	6.4×10^{-2}	measured
inner column diameter, d_{in} [m]	2.82×10^{-2}	manufacturer
outer column diameter, d_{out} [m]	3.18×10^{-2}	measured
column void fraction, ϵ	0.4	assumed
particle void fraction, ϵ_{p}	0.35	assumed
tortuosity, τ	3	assumed
Properties and Constants		
universal gas constant, R [m^3 Pa mol^{-1} K^{-1}]	8.314	standard value
adsorbent particle density, ρ_{p} [kg m^{-3}]	961.7	assumed
column wall density, ρ_{w} [kg m^{-3}]	7800	standard value
specific heat capacity of the gas, $C_{\text{p,g}}$ [J mol^{-1} K^{-1}]	1600 (N_2/He)	NIST database
	1440 (CO_2/He)	
	922 (CO_2/N_2)	
specific heat capacity of the adsorbed phase, $C_{\text{p,a}}$ [J mol^{-1} K^{-1}]	$C_{p,g}$	assumed
specific heat capacity of the adsorbent, $C_{\text{p,s}}$ [J mol^{-1} K^{-1}]	856	assumed
specific heat capacity of the column wall, $C_{\text{p,w}}$ [J mol^{-1} K^{-1}]	502.0	standard value
fluid viscosity, μ [kg m^{-1} s^{-1}]	1.812×10^{-5}	standard value
molecular diffusion, D_{m} [m s^{-2}]	1.6×10^{-5}	Chapman-Enskog
effective gas thermal conductivity, K_z [W m^{-1} K^{-1}]	0.19	fitted
thermal conductivity of column wall, K_{w} [W m^{-1} K^{-1}]	16.0	standard value
internal heat transfer coefficient, h_{in} [W m^{-2} K^{-1}]	11.0	fitted
external heat transfer coefficient, h_{out} [W m^{-2} K^{-1}]	10.0	fitted

NIST REFPROP v9.1 database [75]. The specific heat capacity of the adsorbed phase, $C_{p,a}$, was assumed to be the same as $C_{p,g}$ since no information was known about $C_{p,a}$. The molecular diffusion, D_m, for all mixtures was found using the Chapman-Enskog equation [8]. The internal and external heat transfer coefficients, h_{in} and h_{out}, and the effective gas thermal conductivity, K_z, were determined via an optimization to match the thermal breakthrough profiles of the single component CO_2 DCB experiments; this procedure was done to ensure the thermal breakthrough profiles were matched since N_2 releases less energy during adsorption.

2.5.4 Single Component Adsorption Simulations

After the experimental DCB adsorption and desorption experiments were performed and quantified, they were simulated using the different fitting procedures. For all of the adsorption experiments, the EES fitting procedure is shown as the simulation unless otherwise specified. The single component CO_2 and N_2 DCB adsorption experiments are shown in Fig. 2.4. From Fig. 2.4(**b**), the temperature profiles are matched reasonably, but the temperature decay after the adsorptive heat front passed the thermocouple is faster in the experiment than in the simulation; overall, the temperature difference between the experiment and the simulation is within 1°C. For the CO_2 experiments, the comparison of the simulated and experimental temperature histories is good. The CO_2 breakthrough experiments were at two different flowrates. The 15% CO_2 experiment was carried out at 700 ccm while the 50 and 100 mol% CO_2 experiments were at 315 and 350 ccm, respectively. This was due to limitations of the flow controllers utilized in the breakthrough apparatus. The value of h_{in} reported in Table 2.3 was determined by an optimization to fit all of the CO_2 experiments. The composition breakthrough simulations agree with the experiments for both CO_2 and N_2.

2.5.5 Binary Adsorption Simulations

Fig. 2.5 shows that the simulated breakthrough curves for CO_2 predict the experimental measurements well. This is highlighted in Fig. 2.5(**d**), where all four fitting procedures are shown for the 15/85 mol% experiment. IAST was not simulated since the computational effort is large and it is very similar to the SSL-PP fitting procedure. In the case of N_2, for the duration of the entire experiment, all the fitting procedures seem to predict the curves very well. Upon zooming into the earlier breakthrough, all four methods predict an earlier breakthrough, with the UES predicting a much earlier breakthrough compared to the others. Further, focussing on the end of the roll-up, it is practically impossible to differentiate between the different calculations. From a simulation perspective, it is challenging to identify which of the isotherm fitting procedure should be selected for N_2 from just the binary adsorption experiments.

2.5.6 Binary Desorption Simulations

The desorption curves were simulated for the various fitting procedures and the profiles are shown in Fig. 2.7 (See supporting information for more comparisons). The comparisons of the N_2 desorption breakthrough and the prediction of the temperature profiles together shows clearly the distinction between the various fitting procedures. The SSL-PP (blue lines) predicts the least amount of N_2 loading and therefore leaves the column very quickly. This is reflected in the temperature profiles with essentially no change in temperature during the N_2 desorption. The SSL-PN (red lines) predicts the greatest competitive N_2 loading and takes the longest to desorb N_2. In this case, the largest change in temperature for N_2 desorption is seen. The EES (green lines) fitting procedure provides a good predictive description of the CO_2/N_2 competition; these predictions fall between the SSL-PP and SSL-PN fitting procedures. The UES (black lines) clearly shows an excellent prediction of the curves for the cases of N_2, CO_2 and temperature, especially the excellent match of the CO_2 composition profiles. Here again, the UES fitting procedure shows a better prediction compared to

the other fitting procedures.

2.6 Effect of Isotherm Parameters on Process Performance

In the previous sections the importance of describing the CO_2/N_2 competition was elaborated. It is important to understand the impact of these descriptions on the process performance. For this we consider a 4-step VSA cycle with LPP, a VSA configuration that has been used extensively to compare post-combustion CO_2 capture adsorbents [13, 55, 60].

The 4-step VSA cycle configuration studied is shown in Fig. 2.8. It consists of an adsorption step, a co-current blowdown, an counter-current evacuation and finally a light product pressurization using part of the collected raffinate from the ADS step [13]. A description of the cycle steps is found below.

Adsorption (ADS): Feed gas enters the column at $z = 0$ at a given T and P_{H}. The heavy product (CO_2) adsorbs into the adsorbent, while the light product (N_2) leaves the $z = L$ end of the column.

Blowdown (BLO): The feed end of the column ($z = 0$) is closed and a vacuum is pulled from the raffinate end of the column ($z = L$). The pressure changes from P_{H} to an intermediate pressure, P_{I}, in this step. This removes most of the N_2 within the column, increasing the concentration of CO_2.

Evacuation (EVAC): The raffinate end of the column ($z = L$) is closed and the feed end ($z = 0$) is opened and a deeper vacuum is pulled. The pressure changes from P_{I} to the lowest pressure in the cycle, P_{L}. This step concentrates CO_2 at the feed end and collects it as the heavy product.

Light Product Pressurization (LPP): This step takes part of the ADS light product and reintroduces it to the column in a reverse pressurization from $z = L$ while the feed end of the column ($z = 0$) is closed. This enriches the raffinate end of the column with N_2 and sharpens the CO_2 front, and forces CO_2 towards the feed

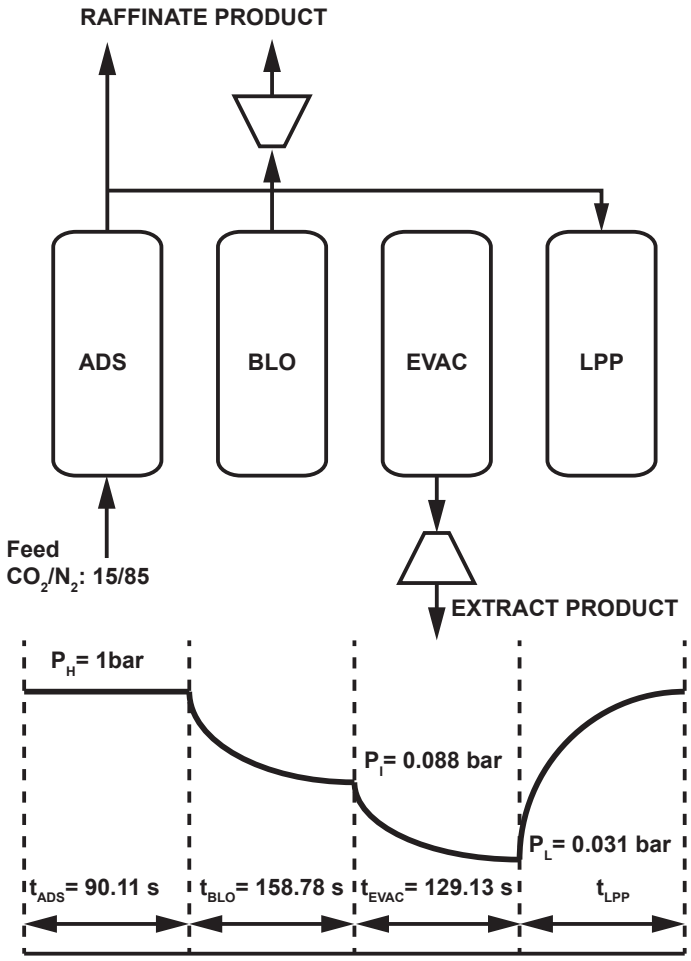

Figure 2.8: The schematic of the 4-step cycle with light product pressurization. The values of the various operating parameters used for the study is also shown.

end of the column.

The key process performance indicators are defined as follows:

$$\text{Purity}, Pu = \frac{n_{\text{CO}_2,\text{EVAC}}}{n_{\text{CO}_2,\text{EVAC}} + n_{\text{N}_2,\text{EVAC}}} \tag{2.27}$$

$$\text{Recovery}, Re = \frac{n_{\text{CO}_2,\text{EVAC}}}{n_{\text{CO}_2,\text{ADS}}} \tag{2.28}$$

$$\text{Energy}, En = \frac{E_{\text{ADS}} + E_{\text{BLO}} + E_{\text{EVAC}}}{n_{\text{CO}_2,\text{EVAC}}} \tag{2.29}$$

where each of E_{ADS}, E_{BLO} and E_{EVAC} are calculated using

$$E = \frac{1}{\eta}\frac{\gamma}{\gamma - 1}\int_{t=0}^{t=t_{\mathrm{step}}} QP\left[\left(\frac{1}{P}\right)^{\frac{(\gamma-1)}{\gamma}} - 1\right] dt \tag{2.30}$$

where $\eta = 0.72$ is the efficiency of the vacuum pump and γ is the ratio of the heat capacities.

To determine the effect of N_2 on process performance, a set of process conditions were used to simulate the SSL-PP, SSL-PN, EES and UES fitting procedures in the 4-step LPP cycle for a 15/85 mol% CO_2/N_2 feed at 25°C and 1 bar. The parameters were taken from Rajagopalan *et al.* and are $t_{\mathrm{ADS}} = 90.11$ s, $t_{\mathrm{BLO}} = 158.78$ s, $t_{\mathrm{EVAC}} = 129.13$ s, $P_{\mathrm{I}} = 0.088$ bar, $P_{\mathrm{L}} = 0.031$ bar and $v_{\mathrm{in}} = 0.37$ m/s. The column and adsorbent parameters where taken from Haghpanah *et al.* and are shown in the Supporting Information [19]. For each case, the column was considered to be initially saturated with N_2 at 1 bar pressure. The single column switches from one step to the others in a periodic fashion. The LPP step is implemented by storing the output of the adsorption step in a data buffer and using it to pressurize the column. The blowdown step removes the N_2 to purify the bed, while the evacuation recovers the CO_2 from the bed. This was continued until the process reached cyclic steady state.

The impact of the fitting procedures for describing the N_2 isotherm is shown in Fig. 2.9. The purity/recovery values shown in Fig. 2.9(**a**) indicate that as the competitive loading of N_2 increases in the order SSL-PP, UES, EES, SSL-PN (from left to right in Fig. 2.9), the CO_2 purity decreases, while its recovery increases. The change is small for both purity and recovery ($< 3\%$) between the SSL-PP, UES and EES fitting procedures, but significantly larger for the SSL-PN fitting procedure ($\approx 6.5\%$). Fig. 2.9(**b**) shows that an increase in $q^*_{N_2}$ increases the parasitic energy. The change between the DSL fitting procedures is significantly larger for the energy predictions; when compared to UES fitting procedure the change is between 9 to 40%. Fig. 2.9(**b**) also shows how much energy is used in each of the constituent steps. The parasitic energy in the adsorption step is marginal and stays relatively the same. The evacua-

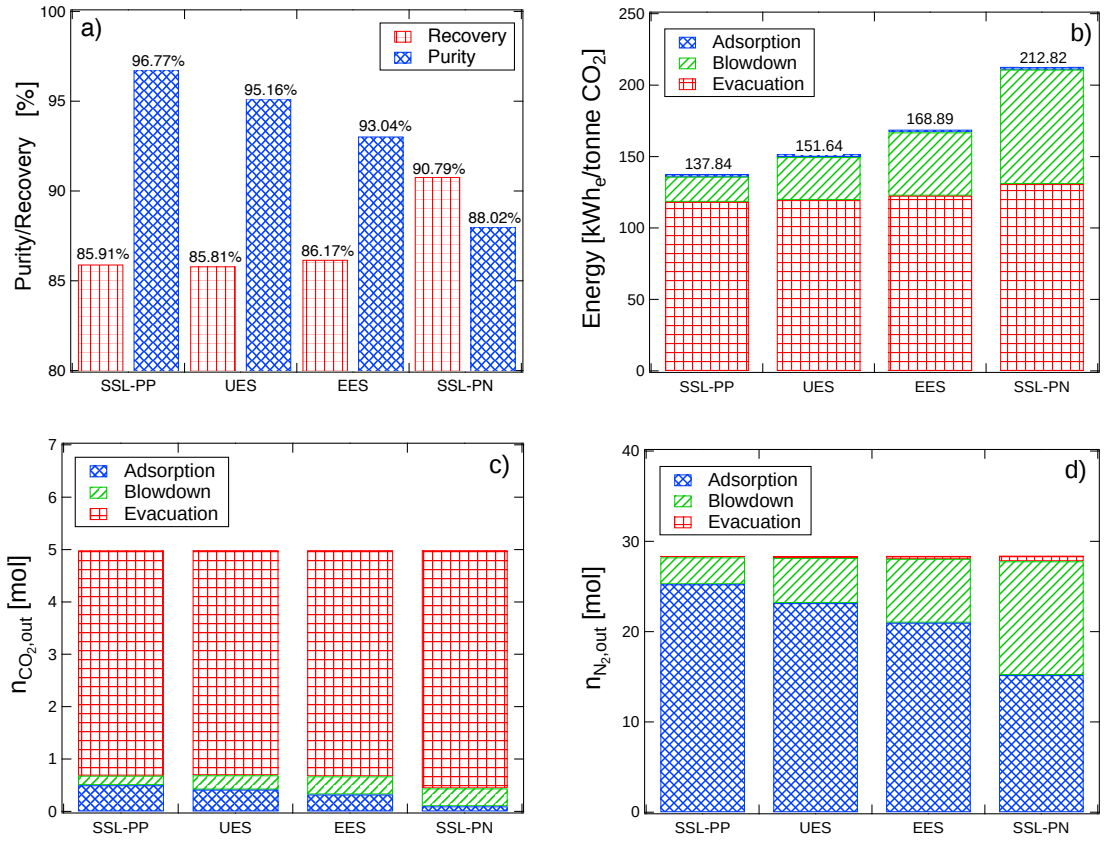

Figure 2.9: Impact of the fitting procedure on the process performance predictions. The bar graphs are ordered from the smallest to largest predicted $q^*_{N_2}$. The (**a**) purities and recoveries, (**b**) the breakdown of the energy consumption of each step and the moles of (**c**) CO_2 and (**d**) N_2 collected per cycle for all the fitting procedures for the 4-step LPP cycle performed at, $t_{ADS} = 90.11$ s, $t_{BLO} = 158.78$ s, $t_{EVAC} = 129.13$ s, $P_I = 0.088$ bar, $P_L = 0.031$ bar and $v = 0.37$ m/s.

tion energy requirement marginally increases with the increase in $q^*_{N_2}$, but practically remains the same. However, the amount of energy required for the blowdown step increases significantly with $q^*_{N_2}$. This is the step in the VSA process where the majority of the N_2 is removed. The SSL-PP and EES fitting procedures require $\approx 43\%$ less and more energy than the UES fitting procedure respectively, while the SSL-PN process requires $\approx 166\%$ more blowdown energy compared to UES.

To understand how the predicted $q^*_{N_2}$ can change the process performance, it helps to look at the amount of moles removed for the adsorption, blowdown and evacuation constituent steps in Figs. 2.9(**c**) and (**d**). The total moles of CO_2, n_{CO_2}, and N_2,

n_{N_2}, removed remains constant, irrespective of the four DSL fitting procedures, since the operating conditions have been kept the same. However, the amount of CO_2 and N_2 removed in each step changes depending on how much N_2 adsorbs. The majority of CO_2 is removed in the evacuation step. This amount becomes slightly larger as the predicted $q^*_{N_2}$ increases. The amount of CO_2 removed in the blowdown also slightly increases with $q^*_{N_2}$. Finally, the amount of CO_2 lost in the desorption step decreases with increasing $q^*_{N_2}$. The overall change for each constituent step is not very large for the SSL-PP, UES and EES fitting procedures, but the change for the SSL-PN fitting procedure is very significant. This increased amount of CO_2 recovered in the evacuation, and decreased amount of CO_2 lost in the adsorption step, improves the recovery of the process as the predicted $q^*_{N_2}$ increases. For N_2, shown in Fig. 2.9(**d**), the change between the fitting procedures is very apparent. As the predicted $q^*_{N_2}$ increases, the amount of N_2 removed increases in the blowdown and evacuation steps, while decreasing in the adsorption step. This shows that as $q^*_{N_2}$ increases, more N_2 is collected with the CO_2 product in the evacuation step, reducing the product purity. Also the separation between CO_2 and N_2 becomes more difficult since, less N_2 is collected in the adsorption step. This helps explain why the predicted energy requirement is greater at a higher predicted $q^*_{N_2}$; more energy must be spent to remove the excess amount of N_2 trapped within the adsorbent in the blowdown and evacuation steps.

2.7 Conclusions

CO_2 and N_2 competition on zeolite 13X was studied. Isotherms for CO_2 and N_2 were measured using volumetry and gravimetry at 0 (only N_2), 25, 50, 75, 100, 125 and 150°C between 1 mbar and 5 bar. Adsorption equilibrium data was fit to a dual-site Langmuir isotherm for both CO_2 and N_2. N_2 was fit to a series of DSL isotherm models that describe CO_2/N_2 competition differently. These fitting procedures all make different assumptions of the N_2 adsorption sites and how CO_2 competes with

those adsorption sites. It was found that while the UES fitting procedure was able to describe the binary equilibrium data most accurately, but it underpredicted the single component loading of N_2. However, if binary data is not collected, the EES fitting procedure provides a decent predictive description of the binary CO_2/N_2 competition. Pure dynamic column breakthrough experiments for CO_2 and N_2 were performed at ≈ 0.98 bar and 22°C. Helium was used as a carrier for all breakthrough experiments. All DCB adsorption experiments were modeled and simulated using the EES isotherm in the adsorption simulator. The DCB experiments and simulations displayed good agreement between both composition and temperature breakthrough profiles. After pure components were simulated, competitive CO_2/N_2 breakthrough experiments were measured at ≈ 0.98 bar and 22°C and simulated with the adsorption simulator. All binary experiments matched the simulated breakthrough predictions for all DSL fitting procedures well. However, it was not possible to determine which fitting procedure was the most accurate using the DCB profiles, since all fitting procedures predicted very similar composition and thermal breakthrough profiles. The competitive N_2 loadings were not able to be quantified with any certainty due to experimental limitations and the inherently low loading of N_2 in competitive CO_2/N_2 mixtures. Therefore, competitive desorption experiments were performed to obtain a clear distinction between the equilibrium models. The competitive desorption experiments were at $\approx$ 22°C, 0.98 and 0.48 bar and with a 50 ccm inlet flow of He. The N_2 loading could be quantified from the competitive desorption experiments with certainty. The binary CO_2/N_2 equilibrium could then be quantified fully; CO_2 was measured using competitive adsorption DCB experiments and N_2 from the competitive desorption experiments. A process study under dry conditions with a fixed set of operating conditions (at 25°C and 1 bar) showed that the purity, recovery and parasitic energy depended on the predicted competitive N_2 loading. The purity and recovery percent deviation from the unequal energy site fitting procedure was between 2 and 8% and 0.1 to 6%, respectively. The parasitic energy deviated up to 40% from the UES fitting

procedure. The main conclusion of this study is that competitive CO_2/N_2 equilibrium data must be collected to accurately understand VSA process performance. Using single component CO_2 and N_2 isotherms for predictive competitive models can only give an approximation of the process performance.

Chapter 3

Measurement of competitive CO_2 and H_2O adsorption on zeolite 13X for post-combustion CO_2 capture

3.1 Introduction

Carbon capture and storage has been proposed as a method to reduce anthropogenic CO_2 emissions that drive climate change [42, 45]. Post-combustion carbon capture is the method where CO_2 is concentrated and removed from the flue gas of a fossil fuel power plant and sent for sequestration or utilization [44, 48]. In a traditional power plant, fuel is combusted in the presence of air to yield primarily H_2O and CO_2. The effluent waste gas would be H_2O, CO_2, unconsumed O_2 and N_2. There are also small amounts of NO_x and SO_x that are formed during the combustion [76]. Often, H_2O is used to scrub the SO_x, saturating the product gas stream. Many adsorptive post-combustion carbon capture papers typically consider a dry gas while neglecting the presence of water [19, 50, 55]. It is usually assumed that the water is removed in an upstream unit.

Zeolite 13X is the benchmark adsorbent for post-combustion carbon capture due its large selectivity of CO_2 over N_2 and low cost. When zeolite 13X is employed in a vacuum swing adsorption process under dry conditions ($y_{CO_2} = 0.15$ and $y_{N_2} =$

This chapter was originally published as: N. S. Wilkins, J. A. Sawada, and A. Rajendran, "Measurement of competitive CO_2 and H_2O adsorption on zeolite 13X for post-combustion CO_2 capture," *Adsorption*, vol. 26, no. 5, pp. 765-779, 2020.

0.85) it can produce a CO_2 purity > 95 mol% with a recovery > 90%, meeting the U.S. Department of Energy (US-DOE) tolerances for carbon capture [55]. Under wet conditions much less is known. Krishnamurthy *et al.* showed through process simulations that a post-combustion process with wet flue gas can achieve US-DOE targets, but at the expense of more energy and a lower productivity than a dry process [41]. These purities and recoveries were achieved with a feed at 25°C and 1 bar total pressure, $y_{CO_2} = 0.15$, $y_{H_2O} = 0.03$ and the balance N_2, in a four-step cycle; the cycle steps were: adsorption, co-current blowdown, counter-current evacuation and counter-current light product pressurization. If a dual stage process with a silica gel pretreatment bed was used before the zeolite 13X bed, the purity-recovery Pareto front became even more favorable.

One of the main challenges of humid post-combustion carbon capture using zeolite 13X is quantifying the competition between N_2, CO_2 and H_2O. Having a good understanding of the competition of these gases on zeolite 13X is important in order to predict pressure/vacuum swing adsorption (P/VSA) process performance. However, even measuring single component H_2O equilibrium on zeolite 13X is challenging [15]. At post-combustion conditions the relative humidity of H_2O is very high, and data under these conditions is scarce. A few papers reported single component H_2O isotherms on zeolite 13X [53, 77–81]. Neither CO_2/H_2O or CO_2/N_2 competitive adsorption follows ideal adsorbed solution theory (IAST) on zeolite 13X [2, 54, 82]. At low H_2O concentrations, IAST over predicts CO_2 adsorption and at higher H_2O concentrations there is an under prediction of CO_2 loading [82]. This is due to the relative magnitudes of the single component equilibrium loadings of CO_2 and H_2O; they are an order of magnitude different on zeolite 13X for normal flue gas mixtures.

Wang and LeVan measured CO_2/H_2O competitive equilibrium data and fit the data to a Virial excess mixing coefficient (VEMC) model [82]. They collected competitive CO_2 loadings at 0, 25 and 50°C for CO_2 partial pressures between 5×10^{-3} and 0.3 bar CO_2 as a function of H_2O loading using volumetry [82]. In these experiments,

water was preloaded onto zeolite 13X and CO_2 was dosed incrementally [82]. They did not notice a change in H_2O loading as a function of CO_2 partial pressure [82]. Joos *et al.* performed molecular simulations of CO_2 and H_2O on zeolite 13X to calculate competitive isotherms and Henry constants [83]. The competitive isotherm predictions from Joos *et al.* matched the experimental measurements by Wang and LeVan [82, 83].

Purdue and Qiao performed grand canonical Monte Carlo simulations to determine the isosteric heat of adsorption of H_2O on zeolite 13X [84]. They prediticted that the isosteric heats of water were fairly homogenous and ranged between 50 and 60 kJ mol^{-1} for the temperatures 25 to 75°C. The predicted values for CO_2 by Purdue and Qiao were similar to those found in our last study [2]. Kim *et al.* calculated the isosteric heats of water on zeolite 13X from isotherm data that ranged from $\approx$ 70 kJ mol^{-1} at low loadings to $\approx$ 45 kJ mol^{-1} at saturation [85]. Hefti and Mazzotti studied binary mixtures of CO_2 and H_2O at 45°C on zeolite 13X at CO_2 partial pressures from 0.12 to 10 bar [15]. These measurements were performed using gravimetry and by preloading the zeolite 13X sample with water before measuring the CO_2 adsorption [15]. Purdue used the data provided by Hefti and Mazzotti (and a previous study by Hefti *et al.*) to predict ternary loadings of CO_2, N_2 and H_2O using grand canonical Monte Carlo simulations [54, 59].

A few studies show experimental single component H_2O dynamic column breakthrough experiments [79, 86, 87]. Ahn and Lee showed a single component H_2O vapor breakthrough experiment and simulation at 23°C and 1.5 mol% H_2O in air [86]. Both of their composition and temperature breakthrough profiles were accurately predicted by their simulation [86]. Ahn and Lee demonstrated single component H_2O breakthrough profiles at 23°C and other concentrations in a mixed silica gel/zeolite 13X bed [86]. Ribiero *et al.* reported a single composition breakthrough of H_2O at 6.3% relative humidity and 30°C on an unspecified zeolite sample which was modeled and simulated [79]. Li *et al.* reports a single CO_2/H_2O competitive breakthrough exper-

iment, without a corresponding simulation, at 8.8 mol% CO_2, 3.4 mol% H_2O and the balance air at 30°C and 1.15 bar total pressure [87]. The competitive CO_2/H_2O breakthrough showed a 99% decrease in CO_2 loading and a 14% decrease in H_2O loading, when compared to similar single component breakthrough experiments [87]. The 14% decrease in H_2O loading in the presence of CO_2 has been quite intriguing; no other experimental or theoretical study has been able to confirm it. To our knowledge, multicomponent CO_2/H_2O breakthrough experiments on zeolite 13X have not been reported. Understanding the competitive equilibrium of CO_2 and H_2O is important to design realistic P/VSA processes for post-combustion CO_2 capture. Further experimental data can also provide vital information for understanding the thermodynamics of competitive adsorption. Considering the importance of this separation, it is in fact surprising that very few studies are available in the literature showing the breakthrough dynamics. The current manuscript is an effort to fill these gaps.

In this paper, single component H_2O isotherms are measured using two techniques: volumetry and gravimetry. The competition between H_2O and CO_2 on zeolite 13X is studied through dynamic column breakthrough (DCB) adsorption and desorption experiments. Single and multi-component dynamic column breakthrough experiments for CO_2 and H_2O were performed. These experiments are described using an empirical, but explicit, competitive isotherm and a detailed dynamic model.

3.2 Materials and Methods

The zeolite 13X (Zeochem Z10-02ND) from our previous study was used in this study in order to obtain a consistent set of equilibrium data [2]. A more detailed description of the material can be found in our previous publication [2]. Most gases in this study (99.999% He, 99.999% Ar and 99.998% CO_2) were supplied by Praxair Canada. Dry instrument air was provided by the University of Alberta and has a dew point of ≤ -40°C. Reagent grade deionized water (ASTM 1) was obtained from Fisher Scientific; it contains less than 60 ppb dissolved solids.

Single component adsorption isotherms for H_2O were measured using volumetry and thermogravimetric analysis. Single component CO_2 adsorption isotherms were reported in our previous study [2]. Single and multi-component adsorption equilibrium and column dynamics were measured with dynamic column breakthrough adsorption and desorption experiments.

3.2.1 Volumetry

Volumetric isotherms for H_2O were measured with a Micromeritics ASAP 2020 (Norcross, GA, USA). The Micromeritics system can measure adsorption equilibrium at very low relative humidities ($\approx 0.05\%$ RH) up to nearly 100% RH at 22°C. Volumetric equilibrium data is measured by expanding a known volume of gas into a chamber filled with an adsorbent. Solving the mass balance from the dose and resulting change in pressure over the length of the experiment yields the amount of gas adsorbed. The sample was regenerated for 12 hours under vacuum at 350°C before each volumetric equilibrium experiment. Approximately 200 mg of zeolite 13X was placed in the sample chamber for these experiments. The Micromeritics system has a loading accuracy of $< 0.15\%$ of the reading and a pressure accuracy of $< 1.3 \times 10^{-7}$ mbar .

3.2.2 Thermogravimetric Analysis

Single component H_2O loadings were measured on a TA Q500 (TA Instruments, New Castle, DE, USA) thermogravimetric analyzer (TGA). The TGA operates at 1 bar total pressure with humid gas fed from a bubbler humidifier. A schematic of the TGA and bubbler humidifier combined system is shown in Fig. 3.1(**a**). To humidify air, a stream of dry gas was split into two streams, one that was injected at the bottom of a tank filled with deionized water. This gas bubbles through the water where it becomes saturated. The relative humidity of this stream is measured. The other stream remained dry and was mixed with the wet stream to attain a desired relative humidity. The humid gas stream flowed over a very small sample (≈ 70 mg)

of zeolite 13X until the mass uptake became constant. The relative humidity of the outlet stream is continuously monitored to ensure that it is consistent with the inlet at the end of an experiment. The change in mass during the experiment, from activation to saturation at a given temperature, was used to calculate the equilibrium loading. Since the TGA operates only at 1 bar pressure, equilibrium data was collected as a function of temperature, starting at the highest equilibrium temperature, 100°C, and making step changes to the lowest desired temperature, 22°C, at a constant relative humidity. Samples in the TGA were activated at 350°C under a flow of dry air for 12 hours before each set of experiments at the same relative humidity.

3.2.3 Dynamic Column Breakthrough Experiments

The DCB apparatus, shown in Fig. 3.1(**b**), is similar to the apparatus used in our previous study, but now it includes a bubbler humidifier to provide humid gas to the column. The concentration of water was measured using either a SensorPush (Brooklynn, NY USA) or Omega HH314A humidity and temperature meter (Omega Engineering, Laval, QC, Canada). The SensorPush has a temperature accuracy of ±0.3°C and a humidity accuracy of ±3% of the signal. The Omega HH314A humidity and temperature meter has a temperature accuracy of ±1°C and a humidity accuracy of ±0.5% relative humidity. A Quantek CO_2/O_2 analyzer was used to measure the CO_2 outlet signal as well as a mass spectrometer. The Quantek has a minimum detection limit of 0.1 mol% and has an accuracy of ±1% of the reading or ±0.2 mol% (whichever is greatest).

The temperature in the lab was maintained at ≈ 22°C. Before every breakthrough experiment, the column was regenerated at 350°C under 350 ccm of dry air or helium for 12 hours. All breakthrough experiments were performed at ≈ 22°C and ≈ 0.98 bar total pressure. In general for an adsorption breakthrough experiment, at time $t < 0$ an inert gas flows through the column. At $t = 0$, the pure or mixed adsorbing gas was sent through the column. The outlet composition, inlet and outlet flows, pressure, pressure

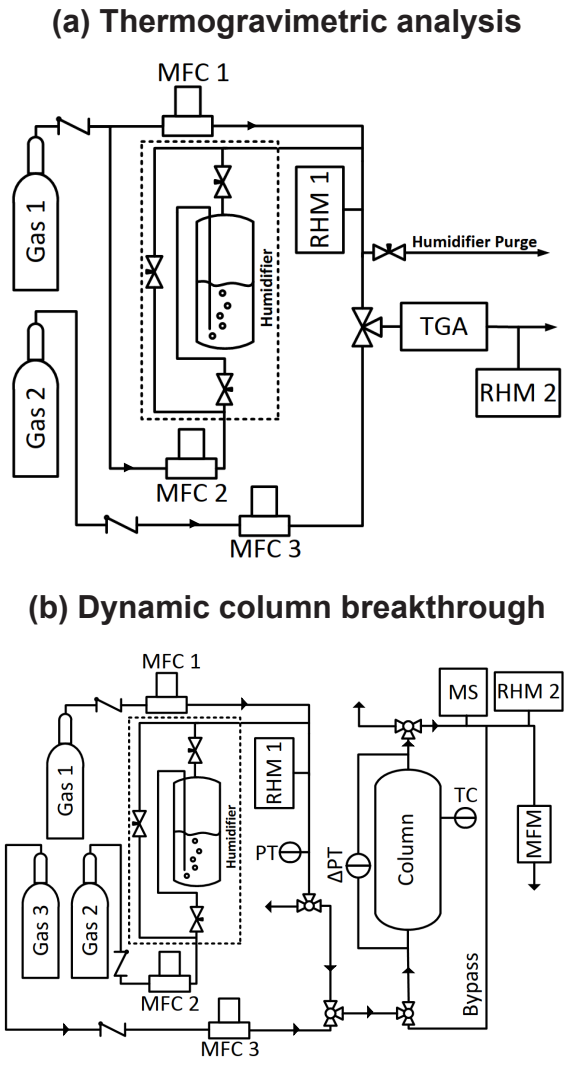

Figure 3.1: Experimental techniques used in this study. (**a**) The thermogravimetric and humidification unit used for the measurement of H_2O equilibrium. (**b**) Schematic of the dynamic column breakthrough apparatus. In these schematics: MFC = mass flow controller, MFM = mass flow meter, MS = mass spectrometer, PT = pressure transducer, ΔPT = differential pressure transducer, RHM = relative humidity meter, TC = thermocouple and TGA = thermogravimetric analyzer.

drop and temperature are recorded in a data acquisition system. The adsorption experiment was completed when the feed concentration and temperature of the gas at the outlet was equal to that of the feed gas. For a desorption experiment, the column was saturated with a known gas concentration at $t < 0$. At $t = 0$, dry helium was introduced. The experiment was stopped when the presence of the adsorbate gas can no longer be detected at the outlet of the column.

3.2.4 Challenges of Humid Breakthrough Experiments

There are many challenges to address while performing humid breakthrough experiments, especially for humid CO_2 experiments. A helpful guide for humid static experiments was provided by Hefti and Mazzotti [15]. For these experiments, the relative humidity was kept far from saturation to ensure no condensation would occur within the system. The relative humidity would be greater at the inlet of the column since the pressure was slightly greater than the outlet. At 22°C this could be 5 to 10% relative humidity greater than the outlet of the column depending on the pressure drop. A significant amount of time is needed for the bubbler humidifier to come to a steady state and produce a constant mole fraction of H_2O. This must be done before the humid stream is sent to the column for a dynamic column breakthrough experiment. Otherwise, the constant boundary condition in most models would not be satisfied.

Another problem can occur when reactivating the column after a humid DCB experiment. Heating the column to 350°C directly from 22°C in the presence of water will destroy the zeolite; this is due to a reaction between H_2O and the zeolite framework that occurs above $\approx$ 150°C [25]. To avoid this, after humid experiments the column was heated to 80°C for 1 hour, then ramped to 130°C for 1 hour and finally ramped to 350°C and held for 10 hours. The column was confirmed to be undamaged by repeating a 100% CO_2 breakthrough experiment and comparing it with results from our last paper after performing many H_2O experiments [2]. This

figure is shown in the supporting information.

One of the main challenges while performing the DCB experiments concerned the measurement of the relative humidity in the presence of CO_2. We observed that CO_2 interfered with the capacitance-based relative humidity sensors and caused the sensors to underpredict the true relative humidity of the gas stream [88]. This was confirmed in the bubbler humidifier by running an experiment where the same flow ratios were used for air as a carrier and CO_2 as a carrier. If the flows for both gases were the same through the bubbler (through the liquid water) and bypassing the bubbler, the same relative humidity should be realized. The measured relative humidity value for humidified CO_2 streams were all consistently lower than the same humidified streams containing only air and water. A calibration is shown in the supporting information that relates the relative humidity obtained from air as compared to CO_2 as the carrier. The calibration curve for the corrected relative humidity at 22°C with a CO_2 carrier is:

$$\mathrm{RH}_{\mathrm{CO_2,corrected}} = 1.3978 \times \mathrm{RH}_{\mathrm{CO_2,measured}} - 1.6881 \tag{3.1}$$

Note that in this paper, for all experiments with CO_2 and H_2O, the H_2O signal was measured in the presence of CO_2. Hence, if experiments were to be performed at other conditions, a suitable calibration is necessary. At higher values of relative humidity, the signal measured in CO_2 was lower than if it were to be in an environment of air. If this effect is not accounted for a lower H_2O competitive loading would be found.

3.3 Modeling Adsorption Dynamics

3.3.1 Dynamic Column Breakthrough Simulation

The dynamic column breakthrough simulator for this study was developed in MATLAB using finite volume techniques [19]. The one-dimensional column was modeled with 30 finite volume nodes and a WENO flux limiter [19]. The simulator assumes the following:

Table 3.1: Equations for modeling adsorption dynamics.

Overall Mass Balance	$\frac{1}{P}\frac{\partial P}{\partial t} - \frac{1}{T}\frac{\partial T}{\partial t} = -\frac{T}{P}\frac{\partial}{\partial z}\left(\frac{P}{T}v\right) - \frac{RT}{P}\frac{1-\epsilon}{\epsilon}\sum_{i=1}^{n_{\text{comp}}}\frac{\partial q_i}{\partial t}$
Component Mass Balance	$\frac{\partial y_i}{\partial t} + \frac{y_i}{P}\frac{\partial P}{\partial t} - \frac{y_i}{T}\frac{\partial T}{\partial t} = D_{\text{L}}\frac{T}{P}\frac{\partial}{\partial z}\left(\frac{P}{T}\frac{\partial y_i}{\partial z}\right) - \frac{T}{P}\frac{\partial}{\partial z}\left(\frac{y_i P}{T}v\right) - \frac{RT}{P}\frac{1-\epsilon}{\epsilon}\frac{\partial q_i}{\partial t}$
Solid Phase Mass Balance	$\frac{\partial q_i}{\partial t} = k_i(q_i^* - q_i)$
Pressure Drop	$-\frac{\partial P}{\partial z} = \frac{150}{4}\frac{\mu v}{r_{\text{p}}^2}\left(\frac{1-\epsilon}{\epsilon}\right)^2$
Column Energy Balance	$\left[\frac{1-\epsilon}{\epsilon}(\rho_{\text{s}}C_{\text{p,s}} + C_{\text{p,a}}\sum_{i=1}^{n_{\text{comp}}} q_i)\right]\frac{\partial T}{\partial t} = \frac{K_z}{\epsilon}\frac{\partial^2 T}{\partial z^2} - \frac{C_{\text{p,g}}}{R}\frac{\partial}{\partial z}(vP) - \frac{C_{\text{p,g}}}{R}\frac{\partial P}{\partial t}$ $-\frac{1-\epsilon}{\epsilon}C_{\text{p,a}}T\sum_{i=1}^{n_{\text{comp}}}\frac{\partial q_i}{\partial t} + \frac{1-\epsilon}{\epsilon}\sum_{i=1}^{n_{\text{comp}}}\left[(-\Delta H_{\text{iso},i})\frac{\partial q_i}{\partial t}\right] - \frac{2h_{\text{in}}}{\epsilon r_{\text{in}}}(T - T_{\text{w}})$
Wall Energy Balance	$\rho_{\text{w}}C_{\text{p,w}}\frac{\partial T_{\text{w}}}{\partial t} = K_{\text{w}}\frac{\partial^2 T_{\text{w}}}{\partial z^2} + \frac{2r_{\text{in}}h_{\text{in}}}{r_{\text{out}}^2 - r_{\text{in}}^2}(T - T_{\text{w}}) - \frac{2r_{\text{out}}h_{\text{out}}}{r_{\text{out}}^2 - r_{\text{in}}^2}(T_{\text{w}} - T_{\text{amb}})$

1. The gas phase is ideal
2. The column is one-dimensional and there are no radial gradients for concentration or temperature
3. An axially dispersed plug flow model adequately describes the flow through the column
4. The ambient temperature is constant
5. Darcy's law adequately describes the pressure drop in the column
6. The solid and gas phases achieve thermal equilibrium instantaneously
7. The adsorbent and bed properties are uniform throughout the column
8. The linear driving force model adequately describes the solid phase mass transfer rate

The simulator is described in detail in Haghpanah *et al.* and our previous study [2, 19]. A summary of the model equations is shown in Table 3.1.

3.3.2 Parameter Estimation

All of the parameters for the experiments and simulations are in Table 3.2. Most of the parameters are the same from our previous study [2]. The specific heat capacities of the gas mixtures, $C_{\mathrm{p,g}}$, were obtained using the NIST REFPROP v9.1 database assuming that they are standard values [75]. The internal and external heat transfer coefficients, h_{in} and h_{out}, and the effective gas thermal conductivity, K_{z}, were determined via an optimization to match the thermal breakthrough profiles of the single component H_2O DCB experiments. Lumped mass transfer coefficients were determined through a similar procedure using the single and multicomponent experiments.

3.3.3 Mass Balance Calculations

A mass balance around the column gives the equilibrium loading after a dynamic column breakthrough experiment. Since there is no reaction within the column, a mole balance can be performed for an adsorption experiment [67]:

$$n_{i,\mathrm{acc}} = n_{i,\mathrm{in}} - n_{i,\mathrm{out}} \tag{3.2}$$

The accumulated moles, $n_{i,\mathrm{acc}}$, is the difference between the moles entering, $n_{i,\mathrm{in}}$, and leaving the column, $n_{i,\mathrm{out}}$. The accumulation is in both the solid and the fluid phases. Assuming that the ideal gas law is valid, the individual terms can be expanded as:

$$m_{\mathrm{ads}} q_i^* + \frac{y_{i,\mathrm{in}} P_{\mathrm{avg}}}{RT_{\mathrm{in}}}\left(V_{\mathrm{b}}\epsilon + V_{\mathrm{d}}\right) = \int_0^{t_{\mathrm{ads}}} \left(\frac{y_{i,\mathrm{in}} P_{\mathrm{in}} Q_{\mathrm{in}}}{RT_{\mathrm{in}}}\right) dt - \int_0^{t_{\mathrm{ads}}} \left(\frac{y_{i,\mathrm{out}} P_{\mathrm{out}} Q_{\mathrm{out}}}{RT_{\mathrm{out}}}\right) dt \tag{3.3}$$

In Eqn. 3.3, y_i is the mole fraction of gas i, P is the total pressure, Q is the gas flowrate, T is the temperature, R is the universal gas constant, ϵ is the column void fraction, V_{b} is the total column volume, V_{d} is the extra-column volume, sometimes called the dead volume, and q_i^* is the bulk equilibrium loading of gas i. Since the pressure drop across the column was small, the average pressure across the column, $P_{\mathrm{ave}} = (P_{\mathrm{in}} + P_{\mathrm{out}})/2$, was used. Solving Eqn. 3.3 for q_i^* yields the equilibrium loading

Table 3.2: Dynamic column breakthrough simulation parameters for zeolite 13X.

Parameter	Value	Source
Column Properties		
adsorbent mass, m [g]	23.02	Measured
column length, L [m]	6.4×10^{-2}	Measured
inner column diameter, d_{in} [m]	2.82×10^{-2}	Manufacturer
outer column diameter, d_{out} [m]	3.18×10^{-2}	Measured
column void fraction, ϵ	0.4	Assumed
particle void fraction, ϵ_{p}	0.35	Assumed
tortuosity, τ	3	Assumed
Properties and Constants		
universal gas constant, R [m^3 Pa mol^{-1} K^{-1}]	8.314	Standard Value
adsorbent particle density, ρ_{p} [kg m^{-3}]	961.7	Assumed
column wall density, ρ_{w} [kg m^{-3}]	7800	Standard Value
specific heat capacity of gas phase, $C_{\text{p,g}}$ [J mol^{-1} K^{-1}]	883.02 (CO_2/H_2O)	NIST database
	1028.2 (H_2O/Air)	
	1215.2 (CO_2/H_2O/He)	
specific heat capacity of adsorbed phase, $C_{\text{p,a}}$ [J mol^{-1} K^{-1}]	$C_{p,g}$	Assumed
specific heat capacity of adsorbent, $C_{\text{p,s}}$ [J mol^{-1} K^{-1}]	856.0	Assumed
specific heat capacity of column wall, $C_{\text{p,w}}$ [J mol^{-1} K^{-1}]	502.0	Standard Value
fluid viscosity, μ [kg m^{-1} s^{-1}]	1.812×10^{-5}	Standard Value
lumped mass transfer coefficient, k_i [s^{-1}]	2.19×10^{-4} (CO_2/H_2O)	Fitted
	8.76×10^{-4} (H_2O/Air)	
effective gas thermal conductivity, K_{z} [W m^{-1} K^{-1}]	4.0×10^{-1}	Fitted
thermal conductivity of column wall, K_{w} [W m^{-1} K^{-1}]	16.0	Standard Value
internal heat transfer coefficient, h_{in} [W m^{-2} K^{-1}]	11.0 (H_2O/Air)	Fitted
external heat transfer coefficient, h_{out} [W m^{-2} K^{-1}]	10.0	Fitted

for the adsorbate for the particular set of conditions [67]. For DCB experiments, only one equilibrium point is found per breakthrough.

For a desorption experiment with an inert feed, the mass balance is:

$$n_{i,\mathrm{acc}} = n_{i,\mathrm{out}} \tag{3.4}$$

At the end of a desorption experiment the individual terms can be written as:

$$m_{\mathrm{ads}} q_i^* + \frac{y_{i,\mathrm{in}} P_{\mathrm{avg}}}{RT_{\mathrm{in}}} \left(V_{\mathrm{b}} \epsilon + V_{\mathrm{d}} \right) = \int_0^{t_{\mathrm{des}}} \left(\frac{y_{i,\mathrm{out}} P_{\mathrm{ave}} Q_{\mathrm{out}}}{RT_{\mathrm{out}}} \right) dt \tag{3.5}$$

where q_i^* is the initial solid phase loading (at $t = 0$). For a desorption experiment, it is important to wait until the column is saturated with the desired feed and at thermal equilibrium before flow is switched to the inert sweep gas. It is important to perform these experiments with a low pressure drop across the column to ensure that q_i^* is uniform across the column. Our previous study emphasized the advantages of using desorption experiments to obtain competitive equilibria, especially for systems that show strong competition [2]. This approach was followed in the current study.

3.4 Results and Discussion

3.4.1 Single Component H_2O Equilibrium

A single H_2O volumetric experiment was performed using the Micromeritics ASAP 2020 (Norcross, GA, USA) at 22°C from 0.05% relative humidity to almost 100% relative humidity. Single component H_2O equilibrium data was also determined using a TA Q500 thermogravimetric analyzer (TA Instruments, New Castle, Delaware, USA) at 22, 30, 40, 50, 75 and 100°C. These samples were activated at 350°C for 12 hours prior to the start of each experiment. The results are shown in Fig. 3.2 and the data is tabulated in the supporting information. The TGA and volumetric equilibrium data at 22°C are in good agreement.

The equilibrium data was fit to a dual-site Langmuir isotherm:

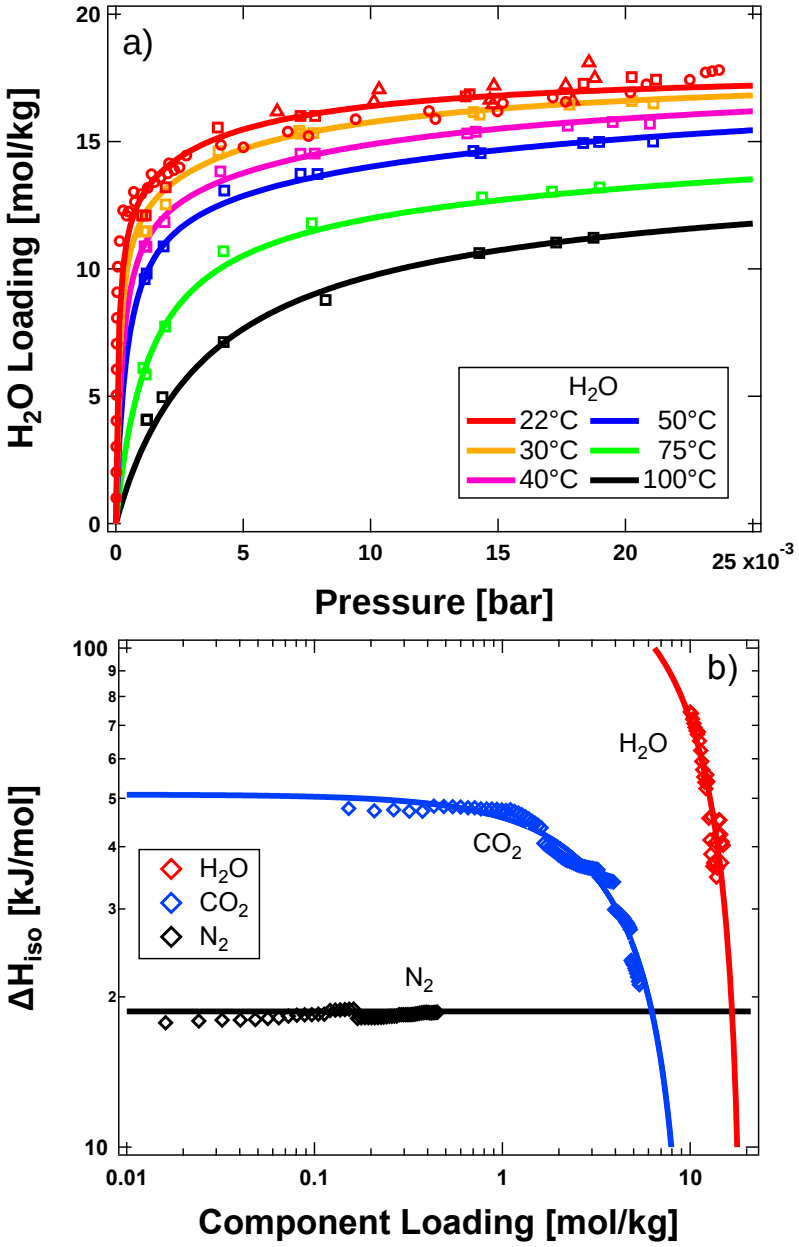

Figure 3.2: (**a**) Single component adsorption equilibrium of H_2O on zeolite 13X. Volumetric data are circles, thermogravimetric data are squares, dynamic column breakthrough experiments are triangles and the dual-site Langmuir fits are lines. (**b**) Isosteric heats of adsorption for N_2, CO_2, and H_2O. The isosteric heats of adsorption for N_2 and CO_2 were taken from our previous study [2]. Symbols show calculated values from the Clausius-Clapeyron equation and the lines are fitted values.

Table 3.3: Dual-site Langmuir isotherm parameters for CO_2 and H_2O on zeolite 13X. The α and β parameters are to model the competitive loading of CO_2 in the presence of H_2O. The other CO_2 dual-site Langmuir isotherm parameters were found in our previous study [2].

Gas	$q_{\mathrm{b}}^{\mathrm{sat}}$	b_0	$-\Delta U_{\mathrm{b}}$	$q_{\mathrm{d}}^{\mathrm{sat}}$	d_0	$-\Delta U_{\mathrm{d}}$	α	β
	[mol/kg]	[m^3/mol]	[kJ/mol]	[mol/kg]	[m^3/mol]	[kJ/mol]	[kg/mol]	[kg/mol]
CO_2	3.257	2.09×10^{-7}	42.67	3.240	1.06×10^{-7}	32.21	0.0574	0.5146
H_2O	5.103	9.56×10^{-8}	44.21	12.820	2.10×10^{-5}	40.16	-	-

$$q_i^*(C_i) = \frac{q_{i,\mathrm{b}}^{\mathrm{sat}} b_i C_i}{1+\sum_{j=1}^{n_{\mathrm{comp}}} b_i C_i} + \frac{q_{i,\mathrm{d}}^{\mathrm{sat}} d_i C_i}{1+\sum_{j=1}^{n_{\mathrm{comp}}} d_i C_i} \tag{3.6}$$

$$b_i(T) = b_{i,0}\exp\left(\frac{-\Delta U_{\mathrm{b}}}{RT}\right) \tag{3.7}$$

$$d_i(T) = d_{i,0}\exp\left(\frac{-\Delta U_{\mathrm{d}}}{RT}\right) \tag{3.8}$$

where b_i and d_i are functions of temperature. The isotherm fitting was performed in the MATLAB Curve Fitting Toolbox for all of the collected TGA data for H_2O. The parameters for each component are in Table 3.3. The isotherm parameters for CO_2 determined in a previous study were retained [2]. The dual-site Langmuir isotherm has been shown to predict non-ideal equilibrium in many cases [2, 21, 57]. The model was chosen since it is easy to implement into a process simulation and since it is an explicit model to predict the loading of both species. Both H_2O and CO_2 strongly adsorb onto zeolite 13X, so both species are modeled assuming that they adsorb into two distinct sites (b and d) on the adsorbent. The fitted isotherms are shown along with the experimental values in Fig. 3.2.

The isosteric heat, ΔH_{iso}, was determined using the Clausius-Clapeyron equation:

$$\left[\frac{\partial \ln(p_i)}{\partial(1/T)}\right]_{q_i} = -\frac{\Delta H_{\mathrm{iso}}}{R} \tag{3.9}$$

The isosteric heat of adsorption, ΔH_{iso}, calculated by numerically differentiating the discrete isotherm points, are shown in Fig. 3.2. All of the collected H_2O equilibrium

data was used to calculate ΔH_{iso}. For H_2O, the isosteric heat decreases as the loading increases. The relative decrease in the isosteric heat of H_2O is similar to that of CO_2 over the loading range investigated. H_2O on zeolite 13X is energetically heterogeneous and this decrease is due to H_2O occupying high energy sites first, before adsorbing into low energy sites at higher loadings [68]. The ΔH_{iso}, in J mol^{-1}, of H_2O was fit to an empirical linear equation as a function of q_{H_2O}, in mol kg^{-1}, for the simulations as shown in Eqn. 3.10.

$$\Delta H_{\text{iso},H_2O} = -7,947 q_{H_2O} + 151,304 \tag{3.10}$$

The calculated ΔH_{iso} of H_2O compares very nicely with the data that Kim *et al.* calculated from their zeolite 13X sample [85]. Kim *et al.* found ΔH_{iso} of H_2O on their zeolite 13X sample was $\approx$ 70 kJ mol^{-1} at low loadings and at the saturation of H_2O the values were $\approx$ 45 kJ mol^{-1}. The trend Kim *et al.* observed was a decreasing exponential which is different than the linear profile we observed [85]. The ΔH_{iso} of H_2O that Purdue and Qiao determined using grand canonical Monte Carlo simulations are similar to ours as the water loading reaches saturation [84]. However, at lower loadings the calculated values of ΔH_{iso} are much greater than the values predicted by Purdue and Qiao. The isosteric heats determined by Purdue and Qiao were essentially energetically homogenous [84].

3.4.2 Single Component Breakthrough Experiments

Single component H_2O breakthrough experiments were performed at $\approx$ 0.97 bar and $\approx$ 22°C. A summary of the breakthrough experiments is shown in Table 3.4. For single component DCB experiments, dry instrument air was used as a carrier. A non-dimensional time, $\bar{t} = tv/L$, was used to describe the results; t is the dimensional time, v is the interstitial feed velocity and L is the length of the column.

All single component H_2O breakthroughs were performed at $0.7 - 1.0$ LPM total flow. Fig. 3.3 shows H_2O concentration and temperature breakthroughs at $\approx$ 36, 54 and 70% relative humidity. All H_2O experiments show classical shock transitions,

Table 3.4: A summary of the single and multicomponent breakthrough experiments on zeolite 13X. For single component H_2O experiments the carrier gas was dry air. Relative humidities are reported at 22°C. Note that for the adsorption experiments y_{CO_2} and y_{H_2O} refer to the feed conditions, while for the desorption experiments they refer to the conditions in which the column was saturated. The single component H_2O desorption experiment likely underpredicted the true H_2O loading since it was only run to the detection limit of the relative humidity meters which is about 0.5% relative humidity.

Experiment	Gas	Q_{in} [ccm]	T [°C]	P [bar]	RH [%]	y_{H_2O} [-]	y_{CO_2} [-]	$q^*_{H_2O}$ [mol kg^{-1}]	$q^*_{CO_2}$ [mol kg^{-1}]
Adsorption	CO_2/He	299	21.6	0.982	-	-	1.0000	-	5.48
	H_2O/Air	935	21.8	0.965	36.1	1.06×10^{-2}	-	16.58	-
	H_2O/Air	936	22.1	0.965	39.6	1.08×10^{-2}	-	17.04	-
	H_2O/Air	818	21.6	1.021	53.2	1.45×10^{-2}	-	16.54	-
	H_2O/Air	911	22.0	0.963	54.0	1.55×10^{-2}	-	17.19	-
	H_2O/Air	940	21.8	0.947	55.1	1.55×10^{-2}	-	16.64	-
	H_2O/Air	805	22.0	0.985	67.6	1.82×10^{-2}	-	16.60	-
	H_2O/Air	798	23.1	0.970	69.9	1.91×10^{-2}	-	17.49	-
	H_2O/Air	722	21.8	0.989	69.9	1.78×10^{-2}	-	17.20	-
	H_2O/Air	798	22.0	0.971	69.9	1.91×10^{-2}	-	18.11	-
	CO_2/H_2O	696	22.2	0.956	37.3	9.74×10^{-3}	0.9903	15.46	-
	CO_2/H_2O	670	23.1	0.952	38.3	9.60×10^{-3}	0.9904	15.47	-
	CO_2/H_2O	731	23.1	1.000	67.1	1.30×10^{-2}	0.9870	18.56	-
	CO_2/H_2O	780	22.9	0.983	70.3	1.89×10^{-2}	0.9811	17.26	-
	CO_2/H_2O	820	22.3	0.966	73.1	1.97×10^{-2}	0.9803	18.09	-
	CO_2/H_2O	696	22.7	0.958	88.1	2.43×10^{-2}	0.9757	18.27	-
	CO_2/H_2O	663	22.0	0.952	88.1	2.43×10^{-2}	0.9757	17.91	-
Desorption	H_2O/Air	1005	21.9	0.999	66.9	1.79×10^{-2}	-	15.42	-
	CO_2/H_2O	200	21.9	0.967	13.3	3.81×10^{-3}	0.9960	-	0.2371
	CO_2/H_2O	200	22.9	0.982	34.2	7.50×10^{-3}	0.9925	-	0.1581
	CO_2/H_2O	50	21.7	0.947	38.3	1.00×10^{-2}	0.9900	-	0.1777
	CO_2/H_2O	50	23.9	0.946	45.8	1.16×10^{-2}	0.9880	-	0.1270
	CO_2/H_2O	200	23.6	0.955	67.1	1.78×10^{-2}	0.9822	-	0.1137
	CO_2/H_2O	200	21.2	0.984	74.4	2.17×10^{-2}	0.9780	-	9.83×10^{-2}

suggesting type 1 isotherm behavior. A similar observation was made by Li *et al.* and Ribeiro *et al.* [79, 87]. The observation that the mean retention time (first moment of the curve) decreases with increasing fluid phase concentration is a further confirmation of the type 1 behavior. At this juncture it is also worth noting the retention times reflect the high capacity for H_2O on zeolite 13X. After the single component H_2O dynamic column breakthrough experiments were completed, saturation loadings at $\approx 22°C$ were found by using Eqn. 3.3. The loadings obtained by such an approach are shown in Fig. 3.2 as triangles alongside the those from volumetry and thermogravimetry. The data from the DCB experiments are in excellent agreement with the other methods. The fact that repeated experiments provided similar loadings indicates that zeolite 13X remained stable after regeneration. A single component desorption experiment, shown in Fig. 3.3(**c**) and (**d**), was performed by initially loading the column with an air stream containing water at 66.9% relative humidity. The extremely slow desorption of H_2O can be seen in Fig. 3.3(**c**), where after desorbing for $\bar{t} > 10^6$, the bed was still not fully regenerated. The slower propagation of the thermal wave at lower values of relative humidity is also clearly seen.

An interesting trend is observed in the temperature profiles, as seen in Fig. 3.3. All temperature profiles for the single component H_2O breakthrough experiments initially increase rapidly ($\approx$ 5 to 10°C increase), but then slow down until a peak is reached at $\approx$ 35 to 45°C ($\approx$ 40000 to 20000 $\bar{t}$, respectively). Then the temperature drops similarly to other temperature profiles noticed in type 1 isotherms, such as CO_2 or N_2 on zeolite 13X, to the inlet temperature [2]. The thermocouple in the breakthrough apparatus was located 80% down the length of the adsorbent bed. The first temperature increase is associated with the convective front as the the composition front lags significantly and would not have reached the location where the thermocouple is located. The second increase is associated with the heat of adsorption.

The adsorption and desorption breakthroughs were simulated using the model described earlier. The results of the simulation are shown as solid lines in Fig. 3.3. An

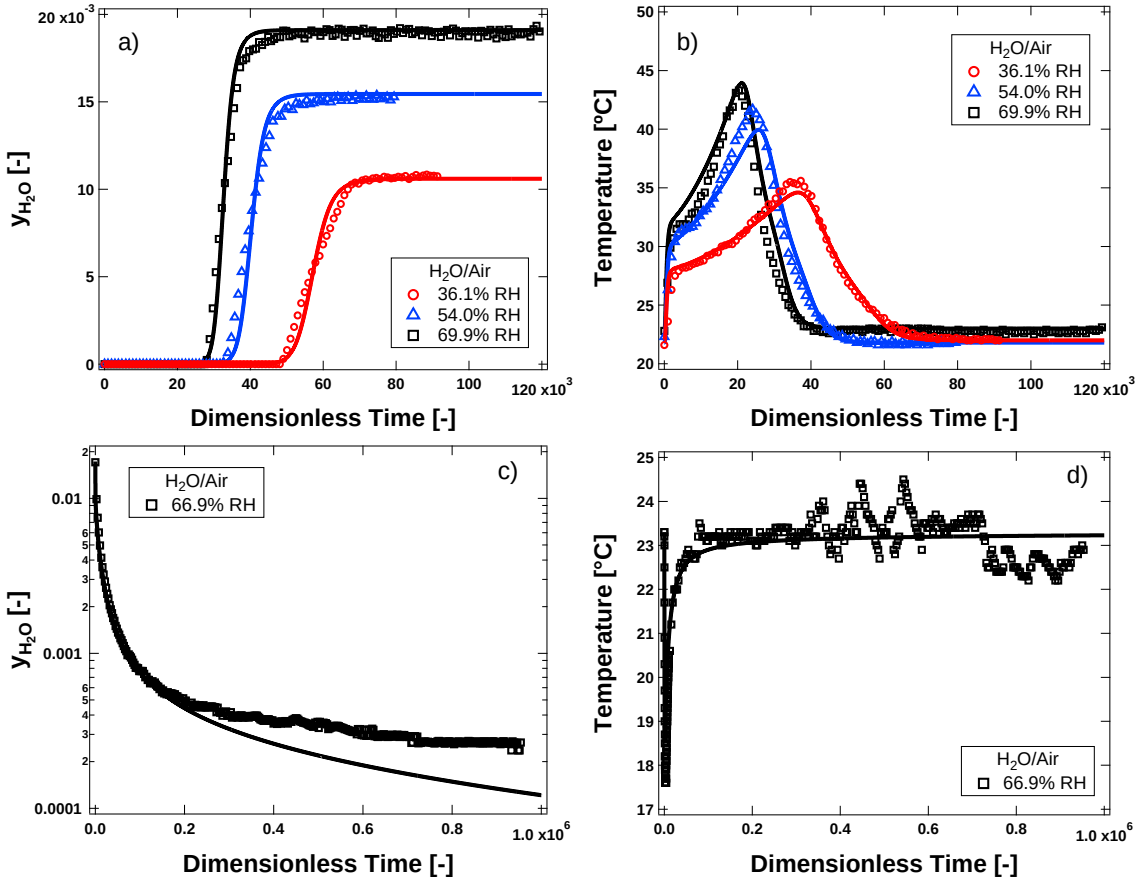

Figure 3.3: Single component DCB experiments of H_2O on zeolite 13X at $\approx 22°C$. (**a**) and (**b**) show the composition breakthrough curves and temperature history for the adsorption experiments, respectively. (**c**) and (**d**) show the corresponding curves for the desorption experiment. Experiments are the markers and simulations are the solid lines. Temperature is measured at $z = 0.8L$.

excellent match for both the composition and temperature histories is observed. Both the position and the spread of the breakthroughs were accurately described.

3.4.3 Binary Breakthrough Experiments

After the single component H_2O breakthroughs were characterized, CO_2/H_2O adsorptive breakthroughs were measured at $\approx 22°C$ and ≈ 0.99 bar by changing the carrier gas from instrument air to CO_2. The CO_2/H_2O adsorption breakthrough experiments are shown in Fig. 3.5. Desorption experiments were also performed to determine the CO_2 loadings after being saturated with a given CO_2/H_2O mixture. It was found in a previous study that for highly selective adsorptive systems, such as H_2O competing with CO_2, it is best to determine the heavy component loading using an adsorption experiment and the loading of the lighter component using a desorption experiment to minimize the error of the measurement [2]. This is due to numerical integration errors that arise in the lighter component mole balance in very long adsorptive DCB experiments. A summary of all the competitive adsorption and desorption breakthrough experiments are shown in Table 3.4 and the corresponding equilibrium points are in Fig. 3.4(**a**).

The composition breakthrough profiles in Fig. 3.5 for CO_2 follow what is expected in a mixed-adsorbing system. Irrespective of the H_2O composition, the CO_2 front breaks through at $\bar{t} \approx 100$ and reaches a value of $y_{CO_2} = 1.0$. In the literature this effect is often interpreted as an indication that CO_2 does not compete with H_2O; which is not the case. The observation is expected since the water front travels at such a low velocity that CO_2 virtually travels through a water free column. However, after a long period of time the water front breaks through the column, the CO_2 "roll-up" ends and its composition returns to the feed conditions. The temperature profiles in the column at $\bar{t} \approx 60$ rise quickly and then decay like expected for a type-1 isotherm. This thermal front corresponds to the adsorption of CO_2 in the column. Before the column temperature returns to the feed temperature, the temperature

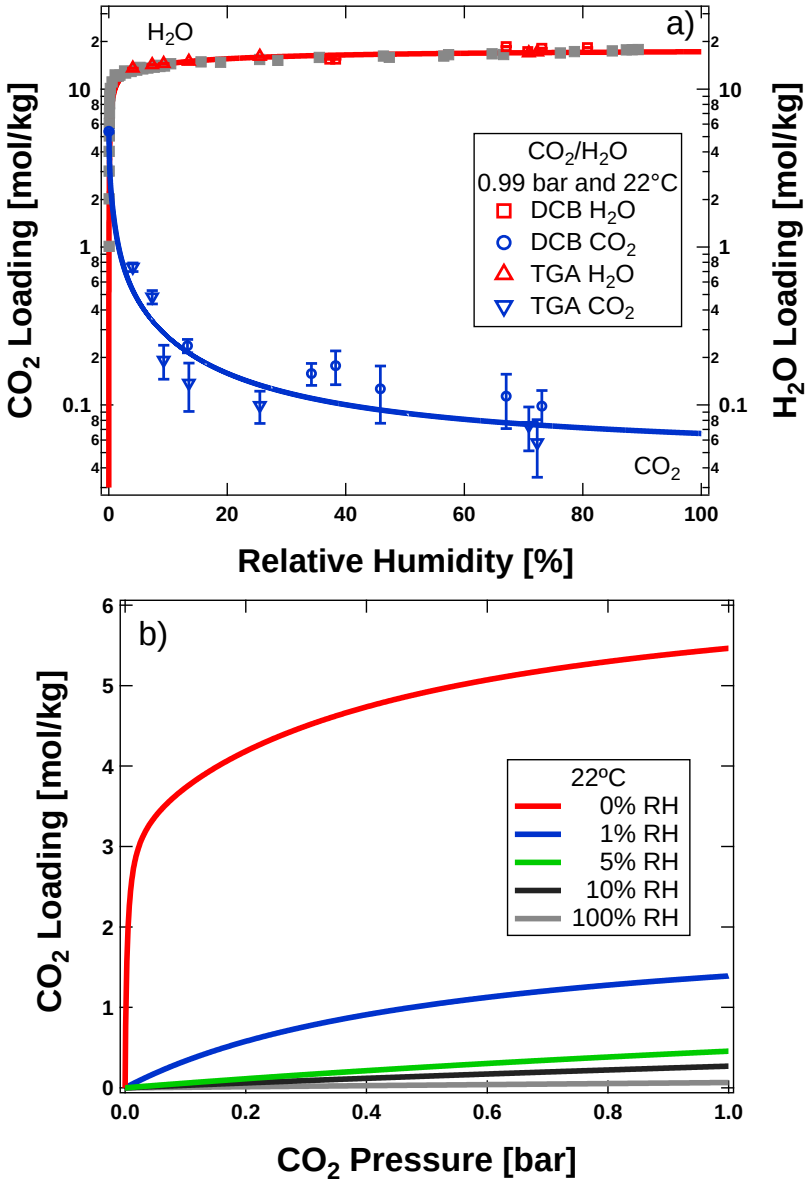

Figure 3.4: (**a**) Competitive CO_2/H_2O equilibrium loadings at 0.99 bar and 22°C. Circles and squares are from dynamic column breakthrough experiments on zeolite 13X while triangles are from thermogravimetrically measured equilibrium experiments. For comparison, the single component water vapor loadings are shown as the gray squares. The modified dual-site Langmuir isotherms are shown as solid lines. (**b**) The effect of H_2O on the CO_2 isotherm modeled by the modified DSL isotherm.

rises again from the adsorption of water. This is dispersed like what was seen for the single component water breakthrough experiments in Fig. 3.3. The competitive H_2O loadings were calculated using Eqn. 3.3 and are shown in Fig. 3.4(**a**). It is worth noting that the H_2O loadings are completely unaffected by CO_2 at the values considered in the experiments.

A comparison of the single component H_2O and binary CO_2/H_2O concentration and thermal breakthrough profiles from the adsorption experiments is shown in Fig. 3.6. The hollow markers are for the single component experiment and the solid markers are for the multicomponent experiment. Both were performed at $\approx$ 70% relative humidity. As seen in Fig. 3.6, at a similar concentration of H_2O the breakthrough profiles remain the same when a different carrier gas is used. In the CO_2/H_2O concentration breakthrough profile, there is slightly more dispersion in the initial breakthrough when compared to the single component H_2O breakthrough. This was observed also by Li *et al.* [87]. When instrument air is saturated with H_2O the concentration and thermal wave velocities are the same as when CO_2 is used instead. This suggests that the loading of H_2O is the same when air or CO_2 is used as a carrier gas. In other words, the loading of H_2O is unaffected by CO_2. This is contrary to what has been observed by Li *et al.* for a breakthrough experiment that was 8.8 mol% CO_2, 95% relative humidity and balance air at 30°C [87]. In the experiment by Li *et al.* a H_2O loading reduction of 14% was observed [87]. We believe that the observation reported by Li *et al.* could be an artifact from the interference of CO_2 in the signal of the RH probe. The only difference between the CO_2 and air experiment is that the heat generated by the H_2O front is slightly less in the CO_2/H_2O breakthrough experiment.

The desorption experiments, shown in Fig. 3.7, were carried out after the column was loaded with a given mixture of CO_2/H_2O at $\approx$ 22°C and $\approx$ 0.99 bar by sweeping the column with a relatively low flowrate (50 to 200 ccm) of Helium. As seen in Fig. 3.7, CO_2 leaves the column almost immediately. By $\bar{t} = 20$ all of the CO_2 has

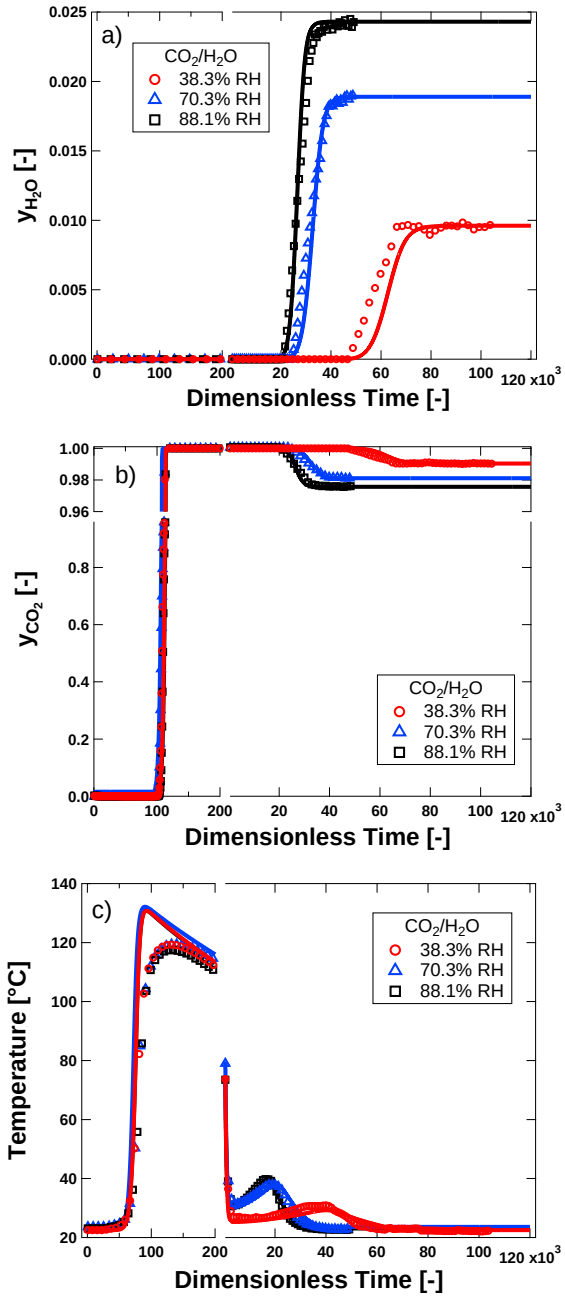

Figure 3.5: Competitive breakthrough profiles on zeolite 13X: (**a**) H_2O breakthrough curve, (**b**) CO_2 breakthrough curve and (**c**) temperature history. Experiments are the markers and simulations are the solid lines. Temperature is measured at $z = 0.8L$.

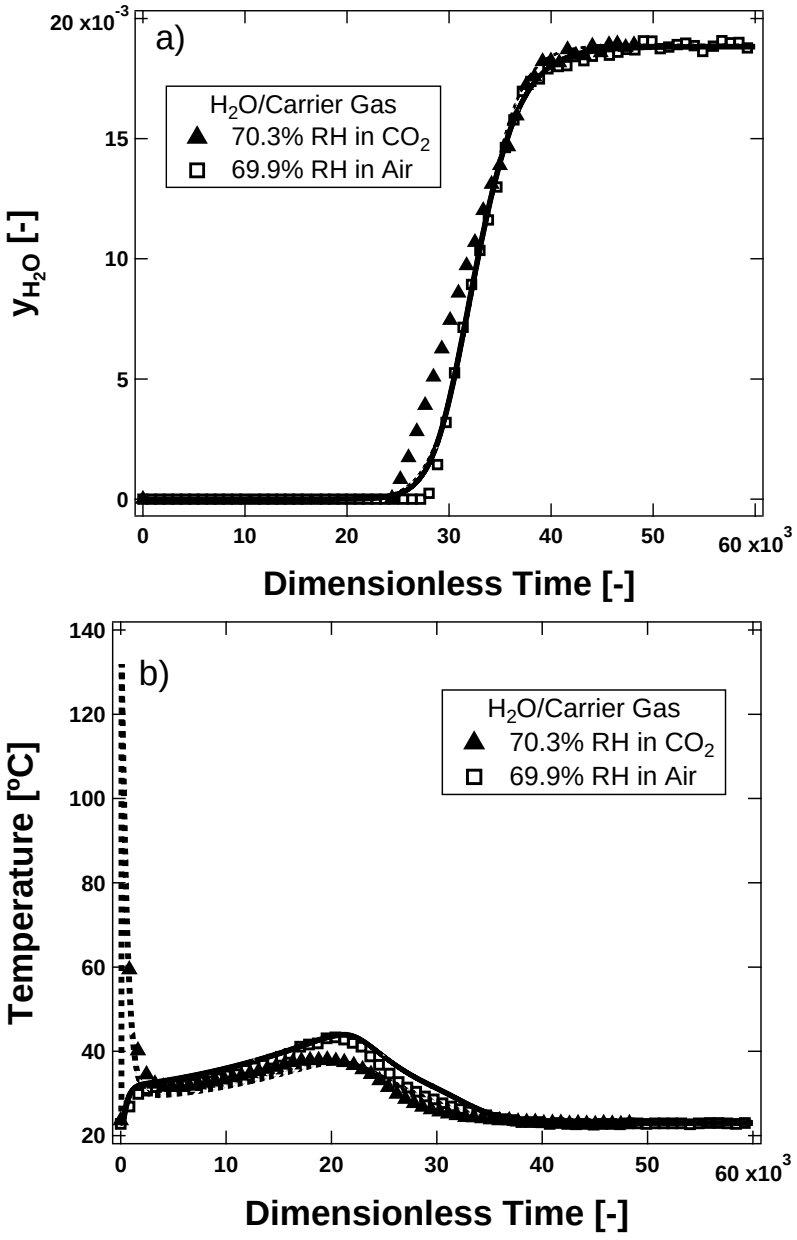

Figure 3.6: Comparison of single and multicomponent H_2O (**a**) concentration and (**b**) temperature breakthrough profiles on zeolite 13X at $\approx 22°C$. The experiments are at $\approx 70\%$ relative humidity. The hollow markers are for H_2O with air as a carrier gas. The solid markers are for H_2O saturated using CO_2 as a carrier gas. The solid lines are the H_2O simulations in air and the dashed lines are the H_2O simulations in CO_2. Temperature is measured at $z = 0.8L$.

desorbed. The humid CO_2 desorptions are significantly faster than a single component CO_2 desorption (also shown in Fig. 3.7). By solving Eqn. 3.5, the CO_2 competitive loadings are found and are shown in Fig. 3.4(**a**). The calculated CO_2 competitive loadings are much lower than than the single component CO_2 loadings. This confirms the observations by Hefti and Mazzotti, Li *et al.* and Wang and LeVan [15, 82, 87]. The calculated loadings show a CO_2 loading reduction between 86.2% and 98.2% (4.05 and 74.4% relative humidity, respectively). Li *et al.* found a 99% loading reduction of CO_2 in the presence of H_2O in their study [87].

The H_2O/CO_2 total loading was confirmed with thermogravimetric experiments. The data is found in the supporting information. A 200 ccm flow of humid CO_2 at 22°C was delivered to the inlet of the TGA. The humidity was successively raised from 3.4% RH to 74.4% RH. At each humidity the total loading in wt% (mass adsorbed/mass adsorbent) was recorded after waiting at least one day after the start of experiments. The total loadings in wt% agree with the total loadings measured in the dynamic column breakthrough experiments. This also confirms that the dynamic loading of CO_2/H_2O yields the same competitive equilibrium as preloading the sample with H_2O before loading CO_2. In fact, it was also possible to measure the CO_2 loading in the presence of water using the TGA. First, the zeolite 13X sample was loaded with H_2O in dry air until it is saturated. After the saturation of H_2O, the carrier gas can be switched to CO_2. Assuming that the H_2O loading remains unchanged in the presence of CO_2, the H_2O mass uptake can be subtracted to yield the competitive CO_2 uptake. These points are also shown in Fig. 3.4(**a**) demonstrating that for pairs of strongly adsorbed components on zeolite 13X, a TGA could be used to obtain data more rapidly than a DCB system. A table of this data can be found in the supporting information. Note that this would not be possible for systems where the selectivity is low.

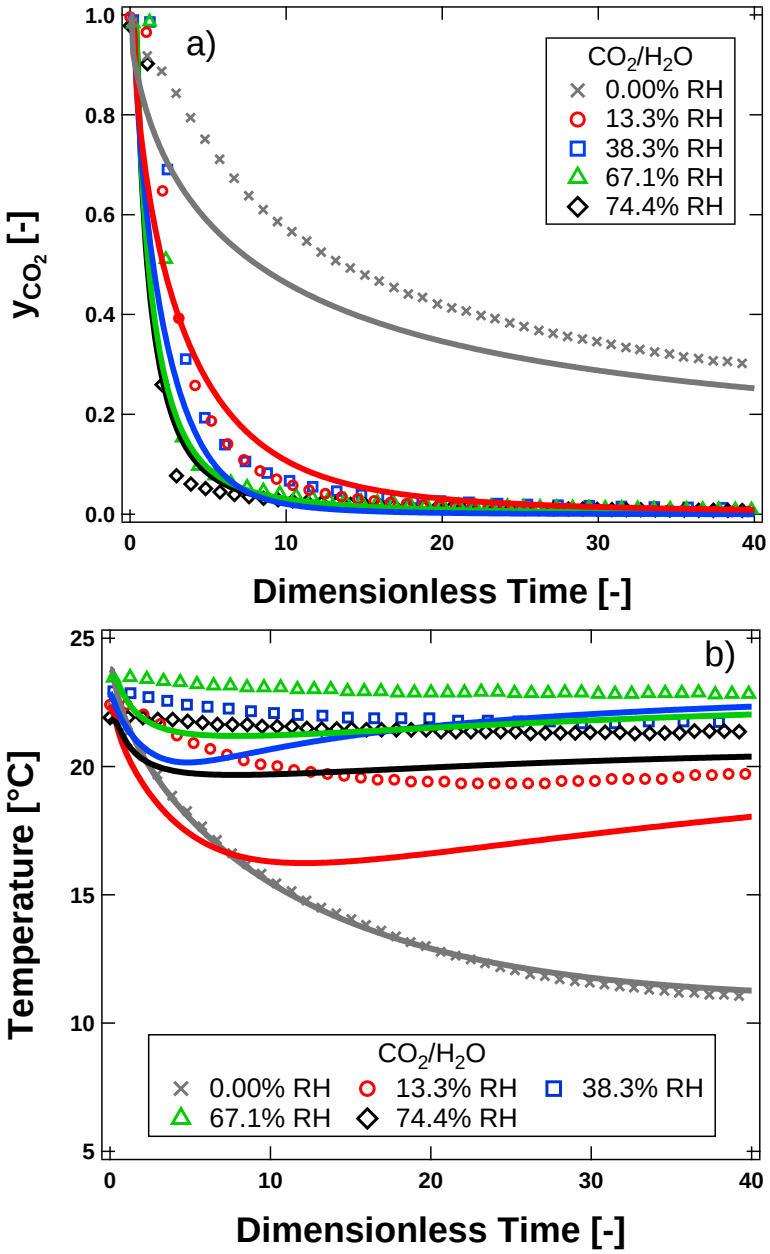

Figure 3.7: Competitive CO_2/H_2O concentration (**a**) and temperature (**b**) desorption profiles on zeolite 13X. The bed was initially saturated at a given relative humidity at $\approx 22°C$. Experiments are the markers and simulations are the solid lines. Temperature is measured at $z = 0.8L$.

3.4.4 Modeling Binary Equilibrium

The competitive equilibrium data for a CO_2/H_2O system at 22°C and 0.99 bar is shown in Fig. 3.4(**a**). When fitting a single component DSL isotherm, the choice of b and d parameters are arbitrary; but, for competitive systems the denominator for the b and d sites change depending on b and d parameters for each species [21, 89]. When both b sites are the high free energy site and both d sites are the low free energy sites this is called the perfect positive (PP) pairing [21]. In other words, both b sites are larger in magnitude than the d sides for each species. When the high free energy site of one component is paired with the low free energy site of the other component, this is called the perfect negative (PN) pairing [21]. Both of the perfect positive and perfect negative pairings for CO_2/H_2O are shown in the supporting information. Neither the PP or PN pairing were able match the collected data well; both exhibit an underprediction of the H_2O loading and an overprediction of the CO_2 loading.

Hefti and Mazzotti proposed an empirical modification to their extended Sipps isotherm model to account for the competition between CO_2 and H_2O on zeolite 13X [15]. The main goal was to obtain a competitive isotherm in an explicit form that can be used in process simulations. Two new parameters (α and β) were added to change the CO_2 saturation loading and nonlinearity constant as a function of H_2O loading [15]. This idea was taken and modified to be used with a dual-site Langmuir isotherm, which we will refer to as the modified DSL:

$$q^*_{\mathrm{CO_2}} = \frac{1}{1+\alpha q^*_{\mathrm{H_2O}}}\left[\frac{q^{\mathrm{sat}}_{\mathrm{CO_2,b}} b_{\mathrm{CO_2}}(T, q^*_{\mathrm{H_2O}}) C_{\mathrm{CO_2}}}{1+b_{\mathrm{CO_2}}(T, q^*_{\mathrm{H_2O}}) C_{\mathrm{CO_2}}} + \frac{q^{\mathrm{sat}}_{\mathrm{CO_2,d}} d_{\mathrm{CO_2}}(T, q^*_{\mathrm{H_2O}}) C_{\mathrm{CO_2}}}{1+d_{\mathrm{CO_2}}(T, q^*_{\mathrm{H_2O}}) C_{\mathrm{CO_2}}}\right] \tag{3.11}$$

$$b_{\mathrm{CO_2}}(T, q^*_{\mathrm{H_2O}}) = b_{\mathrm{CO_2},0}\exp\left(\frac{-\Delta U_{\mathrm{b}}}{RT} - \beta q^*_{\mathrm{H_2O}}\right) = b_{\mathrm{CO_2}}(T) b_{\mathrm{CO_2}}(q^*_{\mathrm{H_2O}}) \tag{3.12}$$

$$d_{\mathrm{CO_2}}(T, q^*_{\mathrm{H_2O}}) = d_{\mathrm{CO_2},0}\exp\left(\frac{-\Delta U_{\mathrm{d}}}{RT} - \beta q^*_{\mathrm{H_2O}}\right) = d_{\mathrm{CO_2}}(T) d_{\mathrm{CO_2}}(q^*_{\mathrm{H_2O}}) \tag{3.13}$$

where the H_2O competitive loading is estimated by the single component DSL isotherm:

$$q^*_{H_2O} = \frac{q^{sat}_{H_2O,b} b_{H_2O} C_{H_2O}}{1 + b_{H_2O} C_{H_2O}} + \frac{q^{sat}_{H_2O,d} d_{H_2O} C_{H_2O}}{1 + d_{H_2O} C_{H_2O}} \tag{3.14}$$

The competitive loading of CO_2 is now made a function of the H_2O loading as predicted by the single component DSL. b_{CO_2} and d_{CO_2} both now have another term, $\exp(-\beta q^*_{H_2O})$, that will make the CO_2 isotherm more linear as the loading of H_2O increases. This term is denoted $b_{CO_2}(q^*_{H_2O})$ or $d_{CO_2}(q^*_{H_2O})$ since it only participates in the competitive model when there is any H_2O loading. The overall saturation capacity is also reduced by a factor of $(1 + \alpha q^*_{H_2O})$ as the loading of H_2O increases. As the loading of H_2O goes to zero, the CO_2 isotherm will reduce to the single component CO_2 isotherm. Another important note is that the terms $b_{H_2O} C_{H_2O}$ and $d_{H_2O} C_{H_2O}$ do not appear in the denominator of the CO_2 isotherm. Both α and β were fitted using the collected competitive CO_2 loadings from the desorption and TGA experiments at 22°C and the CO_2/H_2O data published by Hefti and Mazzotti at 45°C [15]. These comparisons are shown in the supplementary information. α and β are reported with the other DSL isotherm parameters in Table 3.3. It is worth noting that this empirical isotherm describes the competitive loadings both from this work and the ones from Hefti and Mazzotti. There does not seem to be a compromise in the isotherm fit to accurately describe both temperatures and a wide range of pressure. This is indeed interesting as the single component CO_2 DSL isotherm parameters were obtained from experiments that were run up to a maximum of 1 bar, while the data from Hefti and Mazzotti extends to $\approx$ 10 bar. The CO_2 loadings for different values of RH are shown in Fig. 3.4(**b**). Fig. 3.4(**b**) shows that H_2O significantly impacts CO_2. Even at 1% RH, the CO_2 loading is significantly affected.

The CO_2/H_2O adsorptive breakthrough profiles were simulated using the modified DSL and are shown in Fig. 3.5. As seen in Fig. 3.5, the modified DSL predicts the adsorptive H_2O breakthrough profiles well. The temperature profiles are matched decently. The initial magnitude of the temperature peak, which is due to the adsorption

of CO_2, was slightly larger than experimentally observed. The second temperature peak, which is due to the adsorption of H_2O, has a slightly lower magnitude than seen experimentally. The simulated CO_2/H_2O desorption profiles, shown in Fig. 3.7, were matched well. Again the temperature histories are predicted to be much lower than is actually observed experimentally.

3.5 Conclusions

The competitive adsorption of CO_2 and H_2O was studied on zeolite 13X. An explicit model that predicts CO_2 and H_2O competitive adsorption on zeolite 13X was developed. H_2O equilibrium was measured using dynamic column breakthrough and volumetry at 22°C and was also measured using gravimetry at 22, 30, 40, 50, 75 and 100°C. Adsorption equilibrium data was fit to a dual-site Langmuir isotherm for all gases. The dual-site Langmuir isotherm was not able to capture the non-ideality of the CO_2/H_2O system well. A modified dual-site Langmuir isotherm was used to describe CO_2/H_2O competition. This introduced terms that are functions of the water loading in the CO_2 nonlinearity constants and saturation loadings. Carrier gases were humidified using a bubbler humidifier. Single-component dynamic column breakthrough experiments for H_2O in instrument air were performed. All DCB experiments were modeled and simulated using the adsorption simulator. The experiments and simulations displayed good agreement between both concentration and temperature breakthrough profiles. After the single component H_2O DCB experiments were simulated, competitive CO_2/H_2O breakthrough experiments were measured and simulated with the adsorption simulator. For the binary CO_2/H_2O breakthrough experiments, the H_2O loading was obtained during the adsorption experiment and CO_2 was measured during the desorption experiment to minimize the calculated loading error. CO_2 did not affect the competitive loading of H_2O in the DCB or TGA experiments. All binary experiments matched the simulated predictions well. A thermogravimetric analyzer was used to confirm the total loadings measured in the competitive CO_2/H_2O dy-

namic column breakthrough experiments. A CO_2 loading reduction of 86.2 to 98.2% was found from the single component CO_2 loading, depending on the humidity of the system. The data and isotherm parameters obtained in this study could be very helpful in modeling adsorption processes, particularly those that consider realistic situations for CO_2 capture. The explicit nature of the competitive CO_2 isotherm, and its ability to describe equilibrium at multiple temperatures should make them amenable for process optimization studies where thousands of operating conditions would be considered.

This study has implications on process design for CO_2 capture from moist post-combustion flue gas. First it provides an explicit form of the competitive isotherms of CO_2 and H_2O, in a manner that can be easily incorporated into simulation tools. Second, the quantitative data shows that even a moisture content 1% RH can be rather detrimental to the 13X sorbent. This implies that either the upstream drying system should operate with stringent requirements or in the absence of a pre-drying system, a significant part of the 13X bed has to be sacrificed to act as a guard bed [50].

Chapter 4

Quantitative microscale dynamic column breakthrough apparatus for measurement of unary and binary adsorption equilibria on milligram quantities of adsorbent

4.1 Introduction

The design and optimization of separation processes rely on the availability of reliable thermodynamic and kinetic parameters. Several adsorptive separations exploit the differences in equilibrium between the various species in the mixture [18, 58, 90]. At high concentrations, adsorbing species compete (or in some cases co-operate) with each other for the available sites on the adsorbent. In some cases, the extent of this competition can be estimated, based on single component isotherms assuming ideality of the adsorbed phase [20]. However, there are several instances where this assumption does not hold and experimental measurements are imperative [39, 54, 91]. Moreover, the use of incorrect competitive equilibrium can have a impact on the prediction of process performance [2]. Databases of experimental multicompo-

This chapter was originally published as: N. S. Wilkins, J. A. Sawada, and A. Rajendran, "Quantitative microscale dynamic column breakthrough apparatus for measurement of unary and binary adsorption equilibria on milligram quantities of adsorbent," *Ind. Eng. Chem. Res.*, vol. 61, no. 20, pp. 7032-7051, 2022.

nent data do exist, but the data is limited [38, 39]. Also, as new adsorbents such as metal-organic and covalent-organic frameworks are reported in the literature, multicomponent equilibrium data will need to be collected to ensure accurate process simulation on these materials. Note that these measurements can also be valuable for validating and comparing results from molecular simulations.

Several experimental techniques have been described in the literature for the measurement of multi-component adsorption equilibria [92]. A few examples include, dynamic column breakthrough (DCB) [2, 3, 30, 93, 94], volumetry + gas chromatography (GC) [82, 95], volumetry + gravimetry [96], gravimetry + GC [96, 97], concentration pulse chromatography [98, 99], zero-length column (ZLC) [100, 101], and the integral mass balance (IMB) method [102]. Multicomponent volumetry is performed by expanding a known quantity of multicomponent gas into a recirculating chamber with some adsorbent, and sampling the equilibrium gas composition with a GC [82, 95]. A recent multicomponent volumetry study by Shade *et al.* reported using a sample mass of ≈ 5 grams [95]. In the gravimetry + GC method, a mass of adsorbent is placed on a microbalance in a recirculating chamber, and is charged with an initial volume of known multicomponent gas [54, 96]. At equilibrium, the microbalance reading is used to determine the total loading, and the gas composition is measured by a gas chromatograph to solve for each component loading. Multicomponent gravimetry requires $\approx 2-5$ grams of adsorbent that is measured on the microbalance, often with a secondary packed bed of adsorbent (in the circulating volume) containing tens of grams. This secondary packed bed inside the circulating volume is to change the fluid composition enough to determine the equilibrium mass balances reliably [97, 103]. Studies by Ottiger *et al.* used 2.97 g of adsorbent for the microbalance and 37.84 g for the secondary packed bed [97, 103]. The concentration pulse chromatography method introduces a small injection of an adsorbate mixture into a packed bed of interest to measure multicomponent equilibrium. Data is collected dynamically to calculate equilibrium through a transient material balance. A

study by Kennedy and Tezel used approximately 7 grams of adsorbent to measure binary equilibrium [99]. The ZLC technique measures multicomponent equilibrium by initially loading an adsorbate mixture onto a small quantity of adsorbent, and then sweeping that adsorbent with an inert gas [104]. The dynamic response is used to solve a transient material balance to calculate equilibrium [100, 101, 104]. ZLC uses a very small quantity of adsorbent, generally on the order of $5-10$ milligrams [104]. The IMB method combines a DCB experiment with a gravimetric measurement, within the same instrument, to determine the component and total loadings [102]. In the study that introduced the method by Broom *et al.*, a sample size of 3.5 grams was utilized.

Dynamic column breakthrough is a useful technique to obtain adsorption equilibrium and kinetic data, as well as column dynamics for single or multi-component systems [30]. This has also been referred to as an 'open volumetric' experiment in the recent BISON-20 database [39] and a follow-up review by Shade *et al.* [29]. This technique considers a column packed with an adsorbent where a step function of an inert or adsorbing gas is introduced to the column in order to to measure the composition and flow at the column outlet. By performing a mass balance, the adsorbed amount can be calculated. The advantage of the DCB method is that, as long as the the effluent composition and flow can be measured, the same experimental set-up can be used to measure both single, and multi-component equilibria. Quantitative dynamic column breakthrough experiments have classically been performed using fairly large quantities of pelletized or granulated adsorbent ($>$ 10 g of adsorbent). Although, there have been limited examples where quantitative dynamic column breakthrough experiments have been performed on milligram quantities of adsorbent. In the BISON-20 database, there are 13 open volumetric studies that include an effluent flow measurement, of which 12 use sample sizes greater than 10 grams [39]. The last study utilized sub-gram adsorbent sample sizes of 715 and 972 mg [105]. One benefit of a large column breakthrough apparatus is that the blank

response becomes more negligible compared to that of the column. However, large column breakthrough experiments add complexity in terms of the effluent flow measurement, which is a strong function of both gas composition and flow [31]. Further, the DCB method is often seen as a technique that can be used to check the scalability of the adsorbent synthesis. For the characterization of new materials that are typically synthesized in small quantities, usually on the order of hundreds of milligrams to grams, the DCB method is often used only in a qualitative manner to demonstrate the separation capability and rarely as a quantitative tool [29]. Again, for a dynamic column breakthrough experiment to be quantitative, it must include both effluent flow and composition measurements to close the transient mass balance and obtain correct equilibrium data. Omitting the effluent flow measurement can lead to significant loading errors [32, 33], and is only valid for trace adsorbates in an inert carrier. In some situations, it also possible to add an additional carrier gas (often Ar) to normalize the effluent composition signals and approximate the effluent flow [29].

The aim of this study is to build a micro-scale dynamic column breakthrough apparatus (μDCB) that can quantify single and multi-component adsorption equilibrium, and column dynamics, on milligram-scale sized samples. This sample size represents a crystalline, as-synthesized, rare or difficult to scale-up material. The μDCB was also constructed with the aim of keeping the overall costs low in order to facilitate its routine use in synthesis laboratories. We limited ourselves to only use components that are typically available in a material synthesis laboratory, such as a GC, standard lab-scale flow controllers, flow meters and off-the shelf piping. The details of the μDCB system and its operation are described. The system was tested with a series of N_2 and CH_4 single-component adsorption and desorption experiments and multi-component CH_4/N_2 and CO_2/CH_4 experiments on zeolite 13X and activated carbon.

4.2 Materials and Methods

The zeolite 13X (Zeochem Z10-02ND) sample used in this study is identical to the one in our previous studies. This was deliberately chosen in order to obtain consistent sets of equilibrium data [2, 3]. A more detailed description of the zeolite 13X sample can be found in a previous publication [2]. The activated carbon used in this study (Calgon BPL 4x10 CAS#7440-44-00) is a widely studied commercial adsorbent [95, 106–109]. Both the zeolite 13X and activated carbon samples were originally pellitized. For this study, both were crushed and sieved to $16-18$ mesh to pack into the 1/4" Swagelok VCR fittings. All gases in this study (99.99% CH_4, 99.998% CO_2, 99.999% N_2 and 99.999% He) were obtained from Linde Canada.

4.2.1 Volumetric Experiments

Low-pressure volumetric equilibrium data for N_2, CH_4 and CO_2 were measured with a Micromeritics ASAP 2020C (Norcross, GA, USA). The Micromeritics system was used to measure adsorption equilibrium between 1 mbar and 1.2 bar. The system has an accuracy of 0.15% in the loading measurement and a pressure accuracy of 1.3×10^{-7} mbar. A sample mass of 328.3 mg (zeolite 13X) or 477.8 mg (activated carbon) was used for these experiments. Prior to each experiment, the adsorbent was activated for 4 hours under vacuum (5 μbar) at 350°C (zeolite 13X) or 200°C (activated carbon).

4.2.2 Micro Dynamic Column Breakthrough Apparatus

The μDCB system was built into a SRI 8610C gas chromatograph (GC) equipped with a thermal conductivity (TCD) detector. The integration required minor modifications to the GC hardware and the overall system schematic is shown in Fig. 4.1. Photos of the apparatus are shown in the Supporting Information. The internal plumbing of the GC was directed to allow an external mass flow controller (MFC), with a control range of $0.125-25.000$ sccm, to meter the flow through the reference arm of the TCD.

This MFC is used to maintain a constant pressure and flow through the reference arm of the TCD to yield a stable and repeatable signal. Adsorbate and purge gases were delivered to the μDCB bed through a 1/8" Swagelok bulkhead compression fitting that was installed in a hole drilled through the oven wall. The feed end of the bed was connected to the opposite side of the bulkhead connector and the exhaust of the bed was connected to the GC piping that led to the detector array. The outlet of the TCD was connected to a 1/8" Swagelok bulkhead connector that was installed in a hole drilled through the oven wall. The external connection of the bulkhead connector was connected to a length (approx. 2 to 10 meters) of 1/4" OD plastic tubing which delivered the analysis gas to an Alicat mass flow meter, MFM-1, with a $0 - 100.00$ sccm measurement range.

Precise flow measurement and control is of critical importance to the application [31]. The demands of working with small quantities of adsorbent required that the mass flow rates for the purge and analysis gases be known precisely; that the two gas flow rates be as equal as possible; and that the switch between the purge and adsorbate gases be reproducible, relatively instantaneous, and offer a smooth transition from one gas to the other. Of additional importance is the extra-column volume upstream of the bed. The upstream volume from the valve to the bed should be fully swept so as to avoid the complications associated with stranded pockets of gas which can complicate the analysis of the breakthrough curves [110].

To meet these requirements, a Bronkhorst Mini-Cori M12 coriolis mass flow meter (200 ± 0.02 g/hr) was installed upstream of the adsorbate gas mass flow controller, MFC-2. MFC-1 and MFC-2 mass flow controllers (Alicat) were used to control the delivery rate for the various gases but the signal from the coriolis mass flow meter upstream of MFC-2 was used as the true flow value. A flow-matching step was carried out to ensure that the flow rates for both MFC-1 and MFC-2 were equal. This procedure entailed flowing the adsorbate gas (MFC-2) through the system until MFM-1 read a constant value. Once the measured flow rate and composition of the

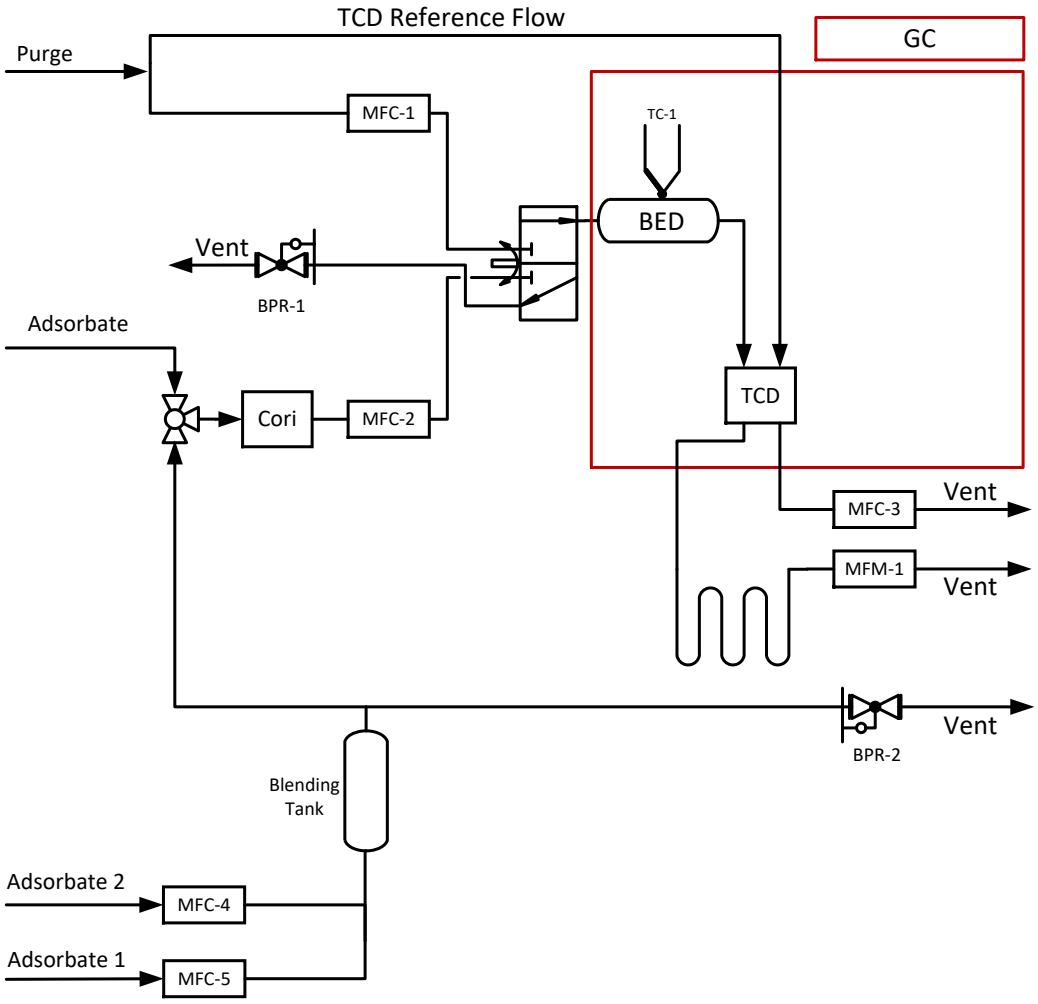

Figure 4.1: General arrangement of components and instrumentation for the μDCB system.

system was constant, the valve was switched. A deviation in the signal for MFM-1, before and after the valve switch, was indicative of a mismatch in flow rate between MFC-1 and MFC-2 and, typically, the set point for MFC-1 was adjusted to match the flow rate delivered by MFC-2. The sequence was repeated until MFM-1 no longer registered a measurable difference between the flow rates from MFC-2 and MFC-1. The tubing placed upstream of MFM-1 facilitated this tuning sequence.

It should be mentioned that the signal output from MFM-1 is a function of both the flow rate and of the composition of the gas stream. The MFM signal is linear if the composition of the fluid is constant. If the flow rate and gas composition are changing simultaneously, then a complicated calibration is required to correct the MFM signal so that the true flow rate can be derived. The calibration can be laborious and lead to serious measurement errors [31]. To avoid this requirement and to maintain a constant gas composition at MFM-1, a $2-10$ meter length of tubing (depending on the adsorbent-adsorbate system) was placed upstream of the flow meter and downstream of the detector. It is worth noting that the flow wave in an adsorption or desorption experiment reaches MFM-1 instantaneously, regardless of the piping length [111]. This tubing created a reservoir of gas sufficient to maintain a constant gas composition at MFM-1 while the secondary gas travelled through the μDCB system. This reservoir of constant-composition gas allows the MFM signal to be normalized, with the normal signal being the inlet gas flowrate. Any deviations from the normal signal are linearly proportional to the inlet gas flowrate. This bypasses a complicated calibration of the MFM signal with respect to gas flow and composition [31] and addresses one of the biggest challenges associated with open-volumetric equilibrium measurements [40]. The miniaturization of the system makes the volume of the tubing manageable. Eventually the secondary gas did displace all of the initial gas in the tubing, and MFM-1 would signal this change in composition, but not before a stable flow trend was achieved. This design feature was instrumental in allowing the desorption flow curves to be collected in the absence of the complicating effects of changing gas

composition.

To minimize the flow surge that inevitably accompanies a flow-switching event, several design features were implemented. Firstly, neither MFC-1 nor MFC-2 were dead-ended or shut-off during the experiment but instead continuously delivered gas at their set points. This feature eliminated the flow surge or flow dip that happens when an MFC has to adjust from zero flow to a set flow. A pneumatically-driven VICI 6-port valve was plumbed so that it had two common outlets. In its de-energized state the flow from MFC-1 was directed to the bed and the flow from MFC-2 was directed to vent. Conversely, when the valve is energized the flow from MFC-2 is directed to the bed and MFC-1 is directed to vent. This configuration required five of the six ports and the sixth, unused port was capped. The internal machining of the valve body ensures that the plenum space in the common ports is purged completely when the valve is switched. Ideally, a 4-port switching valve would be used instead of the 6-port valve.

A manual back-pressure regulator was placed before the vent so that pressure downstream of both MFC-1 and MFC-2 could be matched to within 69.0 Pa,g (0.01 psig). The pressure sensors internal to the Alicat flow instruments facilitated this procedure. Pressure balancing was required to account for the pressure drop across the adsorbent bed. With both mass flow controllers providing the same flow, at the same backpressure, a smooth transition from one gas to another was realized. Pressure balancing was carried out for both adsorption and desorption experiments because the pressure drop across both the bed and the regulator are influenced by the composition of the gas stream.

To ensure repeatable flow switching times and to ensure that the flow switching event was synchronous with the GC data log, a relay internal to the GC was used to trigger the external VICI 6-port valve. The internal GC relay was wired to an external DC-DC solid-state relay which was used to trigger the direct-acting, 3-way solenoid which drove the pneumatic actuator for the VICI 6-port valve. Using a relay

internal to the GC allowed the actuation of the external valve to be programmed into the GC software and actuated automatically at the required times. The solenoid valve was connected to a tank of helium and charged to a pressure of 7.9 bar (100 psig). The lower density of helium compared to compressed air facilitated a faster and more reproducible valve actuation event.

The μDCB bed housing was assembled from Swagelok VCR fittings. The bed consisted of four elements. Two SS-4-VCR-6-200 bodies were connected using a SS-4-VCR-CG coupler with a 20 μm snubber frit installed between the glands of the mating parts. One of the bodies was drilled through to 11/64". Once all four parts were assembled, a quantity of adsorbent ($\approx$ 200 mg) was lightly tap-packed into the drilled-through body. This tap packing was a necessary step to ensure the integrity of the bed because the beds were installed horizontally into the oven. Vertical placement would have been preferred, but geometric constraints in the oven precluded this configuration. The tip of a thermocouple was nested in the leak port of the VCR coupling and wrapped with fiberglass webbing. This modification did not influence the control of the GC, but monitoring the thermocouple temperature was necessary to understand when the bed housing had reached the air temperature reported by the GC. This temperature was monitored during the experiment and remained at a constant set point temperature. The large thermal mass of the bed housing took much longer to heat and to cool compared to the air in the oven.

A second bank of mass flow controllers (Alicat) was used to make binary mixtures. A combined flow of 200 sccm from MFC-4 and MFC-5 were fed into a 50 mL stainless steel blending tank to accomplish the complete mixing of the two gas streams. A typical μDCB experiment used $\approx$ 5 sccm of flow, and so a slipstream was provided to the 3-way valve that fed MFC-2 and the excess flow from MFC-4 and MFC-5 was vented through a back-pressure regulator that was set to 4.46 bar (50 psig).

TCD Calibration: A thermal conductivity detector (TCD) measures the difference between the thermal conductivities of a reference and an unknown (or analysis)

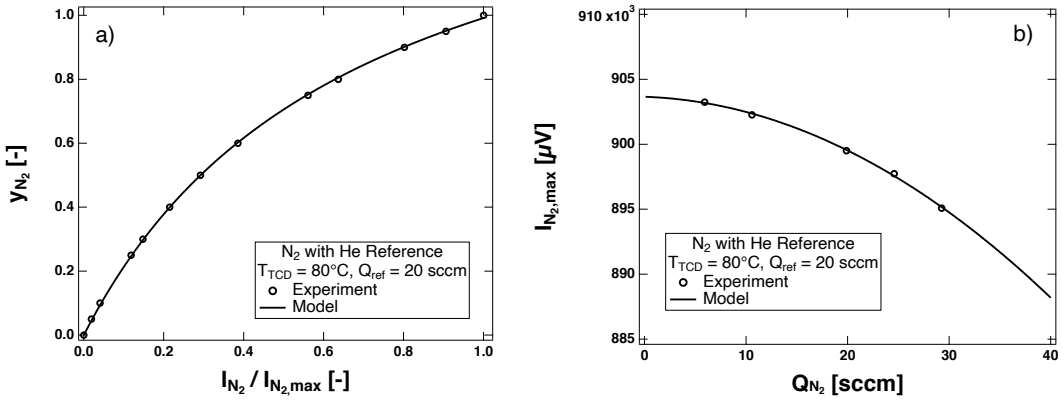

Figure 4.2: N_2/He thermal conductivity detector calibrations at a TCD block temperature of 80°C and a He reference flowrate of 20 sccm. Panel (**a**) shows the mole fraction of N_2 as a function of the normalized TCD signal. Panel (**b**) shows the effect of analyzing gas flow on the 100% N_2 TCD signal; this maximum signal is used to normalize the TCD signal in panel (**a**). The markers denote experimentally collected data and the lines are empirical fits.

gas. The TCD was chosen in this study due to its application in gas chromatography and use in small scale experiments. For small changes in gas composition, the output of the TCD can be assumed to be linear. In the μDCB experiments, the adsorbate concentration in the measurement arm of the TCD traverses very large concentration changes, especially when pure gases are being used. Most importantly though, the thermal conductivity of many common gas mixtures are not linear functions of composition [112–115]. The TCD signal is dependent on the gas mixture and composition, flow rate (in both the reference and analyzing cells), TCD block temperature and filament power [113]. Before a series of experiments began, the TCD signal was calibrated as a function of gas composition at a fixed reference gas flowrate (20 sccm for this study). A gas mixture was prepared using MFC-4 and MFC-5 and the mixture was fed to the TCD until the TCD signal stabilized. The data for a series of thirteen gas mixtures were conditioned in this way, which provided an adequate description of the TCD response over a wide range of mole fractions of adsorbate/purge gas. This calibration curve was used to convert the reported TCD signal in μV values to the mole fraction of the adsorbate. An example TCD calibration is shown in Fig. 4.2 for

N_2/He at a TCD block temperature of 80°C and He reference flow of 20 sccm. The calibration is shown as a normalized signal (see Fig. 4.2(**b**)) to include the effects of flowrate through the analyzing arm of the TCD. Note that the effect of analyzing gas flow on the maximum TCD signal is small. The calibration in Fig. 4.2(**b**) is zoomed in to show this effect. This was also seen in all other analyzing/reference gas pairings shown in Figs. C2 (**c**), (**d**) and C3 (**c**), (**d**) in the Supporting Information. As seen in Fig. 4.2(**a**), the normalized TCD signal increases in a non-linear fashion as a function of y_{N_2}. These trends were fitted to a variety of empirical equations to calculate the corresponding mole fraction from the normalized TCD signal. These figures are similar for the other gas mixtures used in this study and can be found in the Supporting Information along with all the empirical equations used to estimate the mole fractions.

Blank Experiments: The extra-column volume in the μDCB system was substantial compared to the volume of adsorbent present. To account for the accumulation of gas in the extra-column volume, and the fluid or void volume within the column, blank experiments were run at conditions identical to the adsorption experiments. The blank experiments used an equivalent empty VCR bed housing.

Sample Mass: The mass of the activated sample (m_{ads}) needed to be known precisely and so the tare weight of the empty housing, purged with helium, was measured on a 0.1 mg analytical balance. The tare weight of the bed housing included two 1/8" Swagelok plugs that are connected to the inlet and outlet of the housing to prevent air from entering the housing. The empty housing was then filled with a quantity of adsorbent, activated *in situ* in the GC, and cooled under helium to 30°C. The exhaust of the bed was disconnected from the GC piping and plugged with the 1/8" fittings. The feed end of the bed was similarly dismounted and plugged. Using this procedure, air was largely excluded from entering the bed which preserved the sample in its activated state under helium. The entire bed was measured again on the 0.1 mg analytical balance and the difference between the tare and sample

masses was the quantity of adsorbent (on a dry basis) under study. The activated adsorbent masses were measured to be 238.9 mg for zeolite 13X and 180.2 mg for activated carbon. This results in approximate bulk densities of 0.609 and 0.459 g/mL for zeolite 13X and activated carbon, respectively ($V_{\text{col}} \approx 0.392$ mL).

Pycnometric Adjustment: The presence of adsorbent in the bed housing changes the blank volume in the system. As a result, the measured blank response will over-predict the fluid accumulation in the system when adsorbent is present. To correct for the volume occupied by the framework of the solid, the pycnometric (skeletal) density (ρ_{sk}) of the adsorbent was measured. The pycnometric density of the adsorbent was measured using the Micromeritics ASAP 2020C. An empty reference tube was evacuated, filled with helium, and weighed on a 0.1 mg analytical balance to measure its tare weight. This reference tube was mounted to the instrument and the freespace of the tube was measured several times at 30°C to obtain an average value. A known quantity of adsorbent was then added into the same tube, activated *in situ* on the instrument, cooled to 30°C and, again, the freespace was measured several times. The mass of the activated sample and the difference in the measured freespace between the empty reference tube, and the tube including adsorbent, yield the skeletal density of the adsorbent. This density can be used to correct the blank volume of the μDCB because the dry weight of adsorbent in the μDCB column is known. The values are equal to 2.54 and 2.00 g/mL for zeolite 13X and activated carbon, respectively. It is worth noting that using helium to measure the skeletal volumes has its challenges. Assuming helium is non-adsorbing can lead to lead to the estimation of skeletal volume [51, 116]. This can be problematic for high pressure measurements, but is not of concern for low pressures such as the ones studied here.

Blank Response: A blank experiment at 30°C with 100 mol% N_2 (in He) is shown in Fig. 4.3 with a schematic of the blank in Fig. 4.4. The TCD trace in Fig. 4.3(**a**) highlights the need for precise control over all process variables because the transition time from pure helium to pure N_2 is only a matter of seconds, whether transitioning

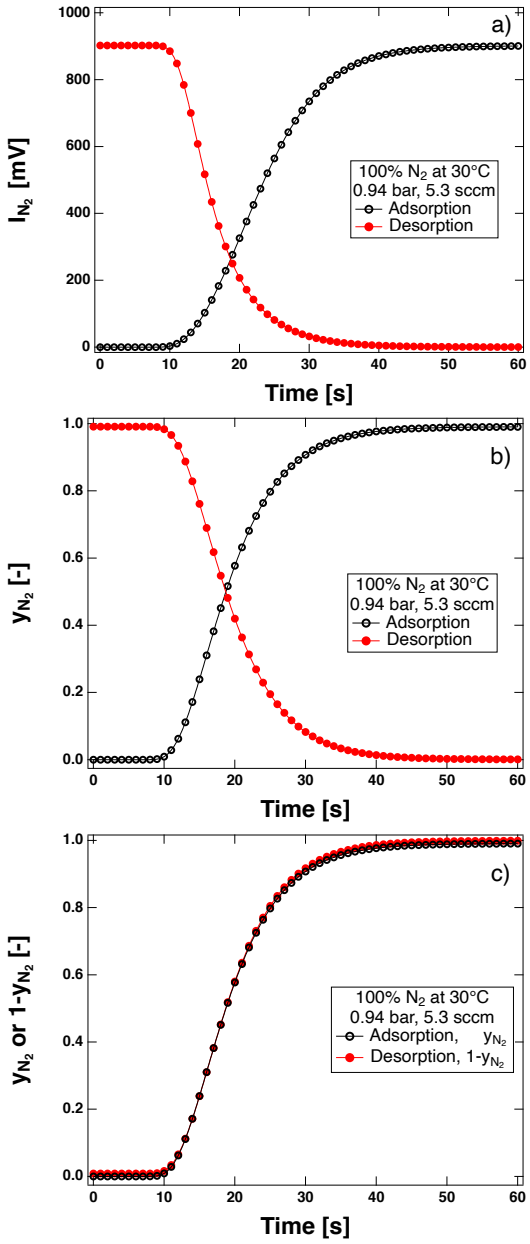

Figure 4.3: Single-component N_2/He adsorption and desorption blank responses at 0.94 bar and 30°C. Panel (**a**) shows the unprocessed TCD signal in mV. Panel (**b**) shows the adsorption and desorption curves as is and (**c**) transforms the desorption curve by $1-y_{N_2}$ to be directly comparable to the adsorption blank. Note that in panel (**c**), the adsorption and desorption experiments overlap. The adsorption curves are shown with hollow symbols and desorption curves are shown with the solid symbols. The reference gas was He for these experiments.

from He to N_2, or from N_2 to He. Note that when the signals are plotted without the calibration curve, they are not symmetric. A blank column should not show any asymmetry between He or N_2 as test gases. This is already an indication that the TCD signal has a non-linear dependency on mole fraction. While not entirely necessary, having a single, continuous mass flow rate somewhat simplifies the mass balance calculations. When the calibration curve is applied to the TCD signal, the adsorption and desorption curves can be plotted together (Fig. 4.3(**b**)) using the valve trigger time as $t = 0$ for each curve. The two curves intersect at their midpoints which indicates that the TCD calibration curve is able to accurately transform a mV response into a molar composition and give confidence for use with a packed bed. Figure 4.3(**c**) plots the mole fraction of N_2 (y_{N_2}) for adsorption and $1 - y_{N_2}$ for desorption to show that both signals overlap. This is further confirmation of the correct calibration and that the instrument is able to capture the correct dynamics of a blank experiment. It is important to emphasize that the goal of the current work is to obtain equilibrium data from DCB experiments. If there is a need either to obtain kinetic data or to compare the experimental results with that of simulations, the dynamics of the blank volume has to be characterized [63, 111].

Typical Experiment: Adsorbents were activated *in situ* and cooled to the analysis temperature under He. Once the analysis temperature (as measured by the thermocouple connected to the μDCB bed) was constant, MFC-2 was pressure balanced using the back pressure regulator (BPR) to match the pressure displayed by MFC-1. Both flow instruments indicate the pressure upstream of the column.

The GC was programmed with a 35 min sequence (for an inlet flow of 5.3 sccm) that involved two valve actuations. An adsorption/desorption sequence collected the He baseline signal for 5 min before the valve was switched to allow the adsorbate gas (N_2) to saturate the bed for a period of 15 min. The valve was then returned to its original position to allow He to displace the N_2 from the bed. The desorption step was 15 min long to ensure that the bed has desorbed all of the N_2 before the

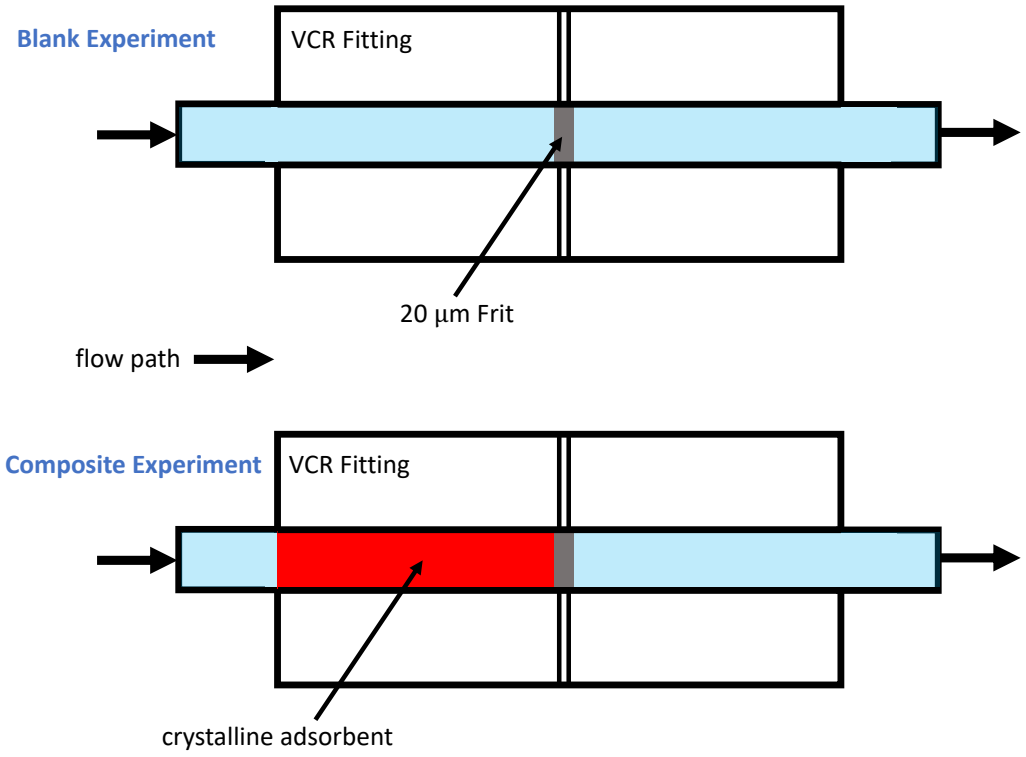

Figure 4.4: Schematic of the blank and composite fluid volumes in the μDCB apparatus. The blank volume, shown as the blue shaded area, contains all upstream, column, and downstream volumes. The composite experiment contains less fluid volume due to the volume occupied by the adsorbent (shown in red).

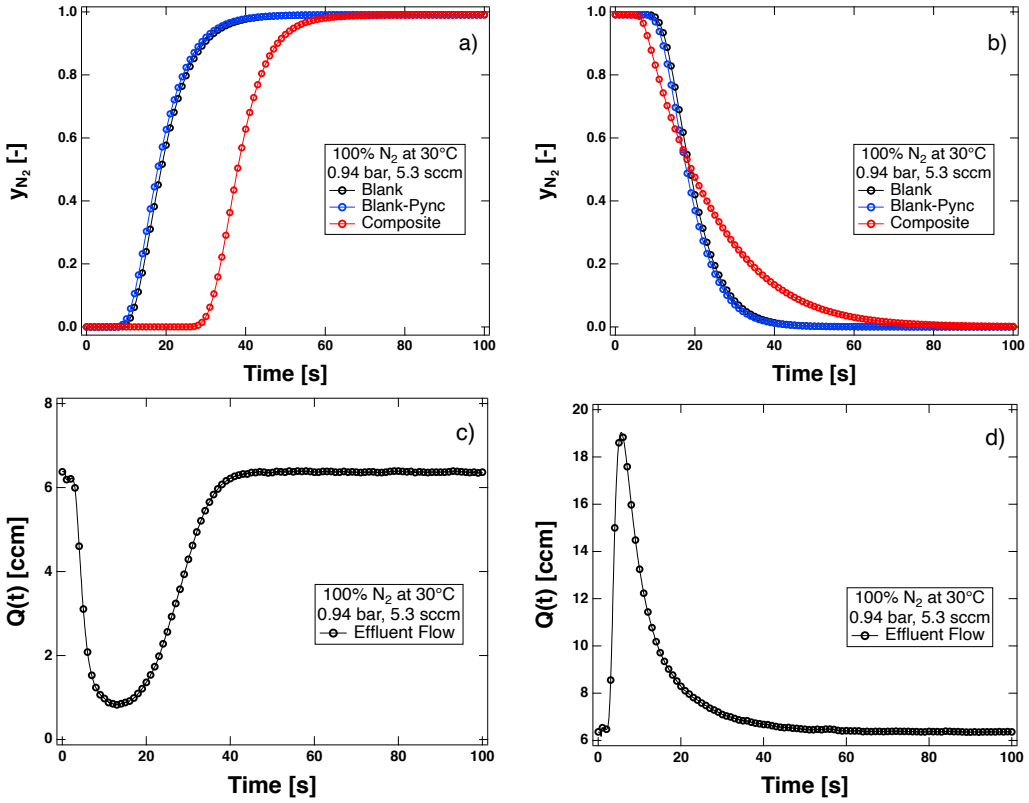

Figure 4.5: Single-component N_2/He adsorption and desorption μDCB experiments for 100 mol% N_2 in He on zeolite 13X at 0.94 bar and 30°C. The top row shows the (**a**) adsorption and (**b**) desorption mole fraction curves. The corresponding effluent flow curves for (**c**) adsorption and (**d**) desorption are shown below the mole fraction responses. The reference gas was He for these experiments.

next experiment was started. Pressure balancing using the BPR-1 was carried out at the 1 min mark and at the 12 to 15 min mark during the experiment. For more strongly adsorbing systems, these timestamps were extended to ensure that complete saturation and regeneration was achieved, along with the gas composition change in the tank before MFM-1.

Figure 4.5 shows the mole-fraction-calibrated TCD trace for a 100 mol% N_2/He experiment on zeolite 13X at 30°C. Data was collected at a rate of 10 Hz giving a time resolution of 100 ms. Again, the composition trace displays a sharp transition for the adsorption experiment, but a more gradual transition in the desorption curve. The MFM-1 data is also shown in Fig. 4.5. The MFM signal shows both the flow

drop associated with the adsorption event (Fig. 4.5(**c**)) and the flow-surge resulting from the desorption of N_2 from the adsorbent (Fig. 4.5(**d**)). Note that the effect of flowrate on the effluent TCD signal calibrations is minor compared to the change in composition. Also, the desorption mole fraction in Fig. 4.5(**b**) leaves the column before the blank. This is due to the elevated flow event associated with the desorption experiment. Sufficient time was allowed for the effluent flowrate (measured by MFM-1) to return to the inlet flowrate (controlled by MFC-1 or MFC-2) and the effluent composition to be identical to that at the inlet allowing the closure of the transient mass balance.

Important Design Considerations: The inlet flowrate, Q_{in}, was an important design parameter in the μDCB experiments. Specifically, if the inlet flow was too large, the breakthrough risks being under kinetic control. This is also a parameter in the design of zero-length column (ZLC) experiments [104]. A nondimensional parameter, L, can be introduced to determine if a ZLC experiment is in equilibrium or kinetic control:

$$L = \frac{1}{3}\frac{Q_{\text{in}}}{H_i V_{\text{ads}}}\frac{R_{\text{p}}^2}{D_{\text{eff},i}} \tag{4.1}$$

where H_i is the dimensionless Henry constant of adsorbate i, V_{ads} is the adsorbent volume, and $\frac{D_{\text{eff},i}}{R_{\text{p}}^2}$ is the effective diffusion time constant. If $L \leq 1$, the system is under equilibrium control. Therefore, the maximum inlet flowrate ($Q_{\text{in,max}}$) should follow the relationship if L is assumed to be 1:

$$Q_{\text{in,max}} \leq 3LH_i V_{\text{ads}}\frac{D_{\text{eff},i}}{R_{\text{p}}^2} \tag{4.2}$$

Note that this requirement, borrowed from the ZLC literature, provides an estimation of the flowrates to be enforced. All flowrates in this study were chosen to be less than $Q_{\text{in,max}}$. At 30°C for the activated carbon bed in this study, $Q_{\text{in,max}}$ is $\approx$ 13.0 sccm for N_2.

The pressure drop across the μDCB system was also very important. Specifically, the pressure drop needed to be as small as possible. This appeared to be a more

significant problem than in larger systems. The best column performance was found in systems with a similar pressure drop to a blank VCR fitting ($\approx$ 0.06 bar). At pressure drops greater than $\approx$ 0.1 bar, the calculated adsorption and desorption equilibrium loadings would no longer be the same value. The pressure drop across the μDCB was reduced by a loose tap-packing of adsorbent into the VCR fitting.

4.3 Mass Balances and Error Analysis

4.3.1 Experimental Mass Balances

To obtain equilibrium data from the μDCB, two separate experiments must be performed: a "blank experiment", which is performed through an empty Swagelok VCR fitting, and a "composite experiment", which is the column/adsorbent response plus the blank response through an equivalent Swagelok VCR fitting.

The blank experiment is performed at a uniform temperature, pressure, inlet flow and composition, without any adsorbent in the VCR fitting. Although these conditions need not strictly be the same as the composite experiment. For the sake of visualization, it is convenient that the conditions for the blank and composite experiments are the same. This approach was taken throughout this study. The mass balance for a blank experiment can be written as:

$$\text{Input} - \text{Output} = \text{Accumulation} \tag{4.3}$$

Assuming isothermal operation and a negligible pressure drop; the following equation can be derived for a blank experiment:

$$\bar{t}_{\text{blank,ads}} = \int_0^{t_\infty} \left(1 - \frac{Q(t)y_i(t)}{Q_{\text{in}}y_{i,\text{in}}}\right)dt = \frac{V_{\text{col}}}{Q_{\text{in}}} \tag{4.4}$$

where Q_{in} and $Q(t)$ are the inlet and outlet volumetric flow rates, $y_{i,\text{in}}$ and $y_i(t)$ are the inlet and outlet adsorbate compositions, V_{col} is the volume of the empty column, and $\bar{t}_{\text{blank,ads}}$ is the blank time, i.e., the average time required for an adsorbent molecule

to travel through the blank volume. This is also referred to as the mean-retention time of the blank experiment. Now let us consider an adsorption experiment where an adsorbent mass of m_{ads} is placed in the same column in which the blank was measured. Under this condition, the mass balance can be derived for the mean-retention time of the composite experiment ($\bar{t}_{\text{comp,ads}}$):

$$\bar{t}_{\text{comp,ads}} = \int_0^{t_\infty} \left(1 - \frac{Q(t)y_i(t)}{Q_{\text{in}}y_{i,\text{in}}}\right)dt = \left(V_{\text{col}} - \frac{m_{\text{ads}}}{\rho_{\text{sk}}}\right)\frac{1}{Q_{\text{in}}} + \frac{RTm_{\text{ads}}q_i^*}{Py_{i,\text{in}}Q_{\text{in}}} \tag{4.5}$$

where where q_i^* is the absolute amount adsorbed in equilibrium at $C_{i,\text{in}} = y_{i,\text{in}}P/(RT)$, and ρ_{sk} is the skeletal density of the adsorbent. Note that the term represented by the integral is measured from the experiment. Equation 4.5 can be written as:

$$\bar{t}_{\text{comp,ads}} = \left[\bar{t}_{\text{blank,ads}} - \bar{t}_{\text{pync}}\right] + \frac{RTm_{\text{ads}}q_i^*}{Py_{i,\text{in}}Q_{\text{in}}} \tag{4.6}$$

where $\bar{t}_{\text{pync}}$ is the pycnometric correction and is defined as:

$$\bar{t}_{\text{pync}} = \frac{m_{\text{ads}}}{\rho_{\text{sk}}}\frac{1}{Q_{\text{in}}} \tag{4.7}$$

These terms can be rearranged to obtain the adsorbate loading from an adsorption experiment:

$$q_{i,\text{ads}}^* = \frac{Py_{i,\text{in}}}{RT}\frac{Q_{\text{in}}}{m_{\text{ads}}}\left[\bar{t}_{\text{comp,ads}} - \bar{t}_{\text{blank,ads}} + \bar{t}_{\text{pync}}\right] \tag{4.8}$$

For a desorption experiment, where the adsorbate is originally in equilibrium at $C_{i,\text{init}} = y_{i,\text{init}}P/(RT)$ in the column, the equilibrium loading can be described as:

$$q_{i,\text{des}}^* = \frac{Py_{i,\text{init}}}{RT}\frac{Q_{\text{init}}}{m_{\text{ads}}}\left[\bar{t}_{\text{comp,des}} - \bar{t}_{\text{blank,des}} + \bar{t}_{\text{pync}}\right] \tag{4.9}$$

where

$$\bar{t}_{\text{comp,des}} = \int_0^{t_\infty} \left(\frac{Q(t)y_i(t)}{Q_{\text{init}}y_{i,\text{init}}}\right)dt = \left(V_{\text{col}} - \frac{m_{\text{ads}}}{\rho_{\text{sk}}}\right)\frac{1}{Q_{\text{init}}} + \frac{RTm_{\text{ads}}q_i^*}{Py_{i,\text{init}}Q_{\text{init}}} \tag{4.10}$$

and

$$\bar{t}_{\text{blank,des}} = \int_0^{t_\infty} \left(\frac{Q(t)y_i(t)}{Q_{\text{init}}y_{i,\text{init}}}\right)dt = \frac{V_{\text{col}}}{Q_{\text{init}}} \tag{4.11}$$

Note that Eqns. 4.8 and 4.9 can be used for either a single-component or multicomponent experiment. When multicomponent experiments are involved, the measured loading corresponds to the competitive/cooperative loading for a given component. The loading measured in the adsorption and desorption experiments should yield identical values. Full derivations of the adsorption and desorption mass balances can be found in the Supporting Information.

4.3.2 Error Analysis

An error analysis was performed to determine the significance of the calculated data. The uncertainty associated with a variable γ in a function f, δf, is given by:

$$\delta f = \left| \left(\frac{\partial f}{\partial \gamma} \right) \delta \gamma \right| \tag{4.12}$$

where $\delta\gamma$ is the uncertainty of γ.

There are eight variables in the μDCB apparatus that add to the uncertainty in the calculation of the equilibrium loading (q^*): m_{ads}, T, P, ρ_{sk}, y_{in}, Q_{in}, $y(t)$ and $Q(t)$. The measurement of both y and Q at the inlet and outlet are split into two separate sets of variables since they are measured with different instruments. The sum of all of these errors yields the total system (plus/minus) error for the equilibrium loading:

$$\delta q^* = \sum_i \left| \left(\frac{\partial q^*}{\partial \gamma_i} \right) \delta \gamma_i \right| \tag{4.13}$$

The uncertainties associated with these terms are shown in Table 4.1. The error propagation equations and derivations are shown in the Supporting Information. The error bars shown in all figures with μDCB equilibrium loading calculations are from these error propagation calculations.

Table 4.1: Measured variables and their associated uncertainties for the calculation of equilibrium loading with the microscale dynamic column breakthrough mass balances.

Measured Variable	Uncertainty
m_{ads}	5×10^{-5} g
P	3.45×10^{-4} bar
T	1 K
ρ_{sk}	0.2 g/mL
y_{in}	1 mV ($\approx$ 0.001 to 0.04, depends on gas mixture)
$y(t)$	1 mV ($\approx$ 0.001 to 0.04, depends on gas mixture)
Q_{in}	0.02 g/h
$Q(t)$	$(0.006)Q_{\text{in}}$ ccm

4.4 Results and Discussion

4.4.1 Volumetric Single-Component Equilibrium

The equilibrium data for N_2, CH_4 and CO_2 on zeolite 13X and for N_2 and CH_4 on activated carbon was measured using the Micromeritics ASAP 2020C (Norcross, GA, USA) and is shown in Fig. 4.6. The N_2 and CH_4 isotherms for zeolite 13X are essentially linear at all temperatures and pressures, which allows them to be reasonably approximated with a linear isotherm:

$$q_i^* = K_i P_i \tag{4.14}$$

with K_i being the temperature dependent Henry constant, and P_i being the partial pressure of gas i. The temperature dependence of K_i is given by the Van't Hoff relationship:

$$K_i = K_{0,i}\exp\left(\frac{-\Delta H_{\mathrm{b},i}}{RT}\right) \tag{4.15}$$

where $K_{0,i}$ is the Henry constant prefactor, and $\Delta H_{\mathrm{b},i}$ is the heat of adsorption of component i. The adsorption of CO_2 on zeolite 13X was described using a dual-site Langmuir (DSL) isotherm. CH_4 equilibrium data on zeolite 13X was also fitted with a DSL isotherm to better estimate competition between CH_4 and CO_2 using an equal-energy sites (EES) approximation [2]. The dual-site Langmuir isotherm is shown below:

$$q_i^* = \frac{q_b^{\mathrm{sat}} b_i P_i}{1+\sum_j^{n_{\mathrm{comp}}} b_j P_j} + \frac{q_d^{\mathrm{sat}} d_i P_i}{1+\sum_j^{n_{\mathrm{comp}}} d_j P_j} \tag{4.16}$$

where q_b^{sat} and q_d^{sat} are the saturation capacities of the b and d sites, respectively and b_i and d_i are the temperature dependent nonlinearity constants. The temperature dependence of b_i and d_i are given by:

$$b_i = b_{0,i}\exp\left(\frac{-\Delta H_{\mathrm{b},i}}{RT}\right) \tag{4.17}$$

$$d_i = d_{0,i}\exp\left(\frac{-\Delta H_{\mathrm{d},i}}{RT}\right) \tag{4.18}$$

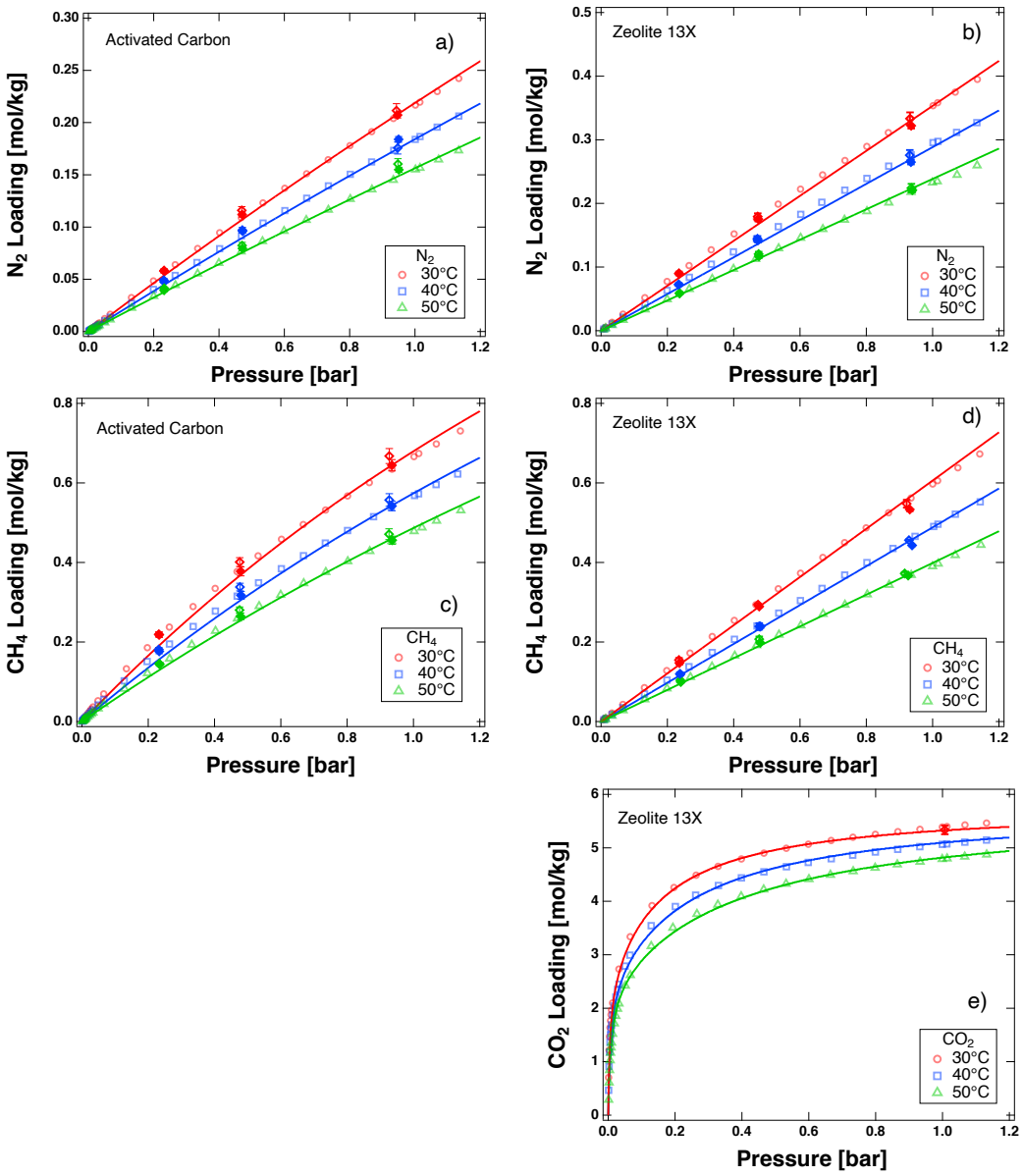

Figure 4.6: Single-component equilibrium data of N_2 (**a**, **b**) and CH_4 (**c**, **d**) on activated carbon and zeolite 13X at 30, 40 and 50°C. Panel (**e**) contains single-component equilibrium data for CO_2 at 30, 40 and 50°C on zeolite 13X. Hollow diamond markers are adsorption breakthrough experiments, and solid diamond markers are desorption experiments. Circle, square and triangle markers are volumetrically collected equilibrium data. Linear, single-site or dual-site Langmuir isotherms are shown with lines.

where $b_{0,i}$ and $d_{0,i}$ are the nonlinearity constant prefactor of component i on sites b and d, and $\Delta H_{\mathrm{d},i}$ is the heat of adsorption of component i in second adsorption site d. The isotherms for N_2 and CH_4 on activated carbon were fitted to single-site Langmuir (SSL) isotherms:

$$q_i^* = \frac{q_b^{\mathrm{sat}} b_i P_i}{1 + \sum_j^{n_{\mathrm{comp}}} b_j P_j} \tag{4.19}$$

The isotherm parameters for all systems are listed in Table 4.2.

Table 4.2: Isotherm parameters for single component N_2, CH_4 and CO_2 equilibrium on activated carbon and zeolite 13X.

Material	Gas	Model	q_b^{sat} [mol kg^{-1}]	q_d^{sat} [mol kg^{-1}]	b_0 [bar^{-1}]	d_0 [bar^{-1}]	K_0 [mol bar^{-1} kg^{-1}]	$-\Delta H_b$ [kJ mol^{-1}]	$-\Delta H_d$ [kJ mol^{-1}]
Zeolite 13X	CO_2	DSL	2.375	3.421	1.675×10^{-2}	2.400×10^{-6}	-	23.80	37.30
Zeolite 13X	CH_4	DSL	2.375	3.421	7.660×10^{-5}	7.660×10^{-5}	-	18.44	18.44
Zeolite 13X	CH_4	Linear	-	-	-	-	7.024×10^{-4}	17.04	-
Zeolite 13X	N_2	Linear	-	-	-	-	6.185×10^{-4}	16.00	-
Activated Carbon	CH_4	SSL	3.016	-	3.657×10^{-4}	-	-	16.83	-
Activated Carbon	N_2	SSL	3.016	-	2.391×10^{-4}	-	-	14.59	-

4.4.2 Single-Component Breakthrough Experiments

Single component breakthrough experiments were performed on zeolite 13X for N_2 and CH_4 at ≈ 0.95 bar and 30, 40 and 50°C. A summary of the breakthrough experiments is shown in Table 4.3. All experiments were performed at 5.3 sccm (standard conditions are: $T_{\text{std}} = 0$°C and $P_{\text{std}} = 1.01325$ bar).

The results of the single-component N_2 adsorption and desorption breakthrough experiments at 30°C on zeolite 13X are shown in Fig. 4.7. The blank measurement is shown in black, the pycnometrically corrected blank is shown in blue and the composite response is shown in red. Helium was used as a sweep gas and diluent for all single component breakthrough experiments. Helium was also the reference gas in the TCD for all single-component experiments. As seen in Fig. 4.7, the composite response always exits later than the pycnometrically corrected blank. The shaded areas in Fig. 4.7(**a**) and (**b**) are proportional to the accumulation in each experiment (between the blue and red curves). Although not essential, a blank experiment was performed for every adsorbate and set of conditions studied. From Fig. 4.7, it is seen that as the composition of N_2 decreases, that the composite adsorption breakthrough curves seem more dispersed, while all sharing the same average retention time at ≈ 40 seconds. This is a common phenomenon observed for adsorbates with a linear isotherm [30, 93].

The adsorption and desorption breakthrough curves are plotted as a normalized molar flow ($y(t)Q(t)/[y_{\text{in}}Q_{\text{in}}]$), a combination of the effluent N_2 mole fraction, $y(t)$, and flow curves, $Q(t)$, divided by the inlet (or initial for desorption) mole fraction (y_{in}) and flow (Q_{in}), to show how N_2 accumulates in the adsorbent. For adsorption, this quantity goes to a value of 1 when breakthrough is finished. During an adsorption experiment the flow at the outlet of the column will decrease to the carrier/inert flowrate (in this case He) as the adsorbate (in this case N_2) adsorbs into the adsorbent. This is seen in Fig. 4.5(**c**). When the adsorbate breaks through the packed bed, the

Table 4.3: Conditions for the single-component adsorption and desorption μDCB experiments performed on zeolite 13X in this study.

Gas	$y_{\text{in/init}}$ [-]	P [bar]	T [°C]	Q_{in} [ccm]	q^*_{ads} [mol kg^{-1}]	q^*_{des} [mol kg^{-1}]
N_2/He	1.000	0.943	30	6.36	0.3346	0.3229
	0.502	0.945	30	6.35	0.1795	0.1755
	0.249	0.944	30	6.36	0.0904	0.0895
	1.000	0.943	40	6.57	0.2759	0.2650
	0.502	0.941	40	6.57	0.1445	0.1419
	0.249	0.942	40	6.57	0.0727	0.0724
	1.000	0.947	50	6.73	0.2242	0.2209
	0.502	0.947	50	6.73	0.1205	0.1171
	0.250	0.948	50	6.72	0.0590	0.0587
CH_4/He	1.000	0.945	30	6.38	0.5478	0.5335
	0.504	0.945	30	6.36	0.2940	0.2893
	0.249	0.947	30	6.34	0.1547	0.1473
	1.000	0.955	40	6.51	0.4561	0.4432
	0.503	0.955	40	6.49	0.2393	0.2391
	0.250	0.958	40	6.48	0.1198	0.1189
	1.000	0.945	50	6.77	0.3726	0.3674
	0.503	0.954	50	6.70	0.2071	0.1980
	0.252	0.954	50	6.69	0.1039	0.0996

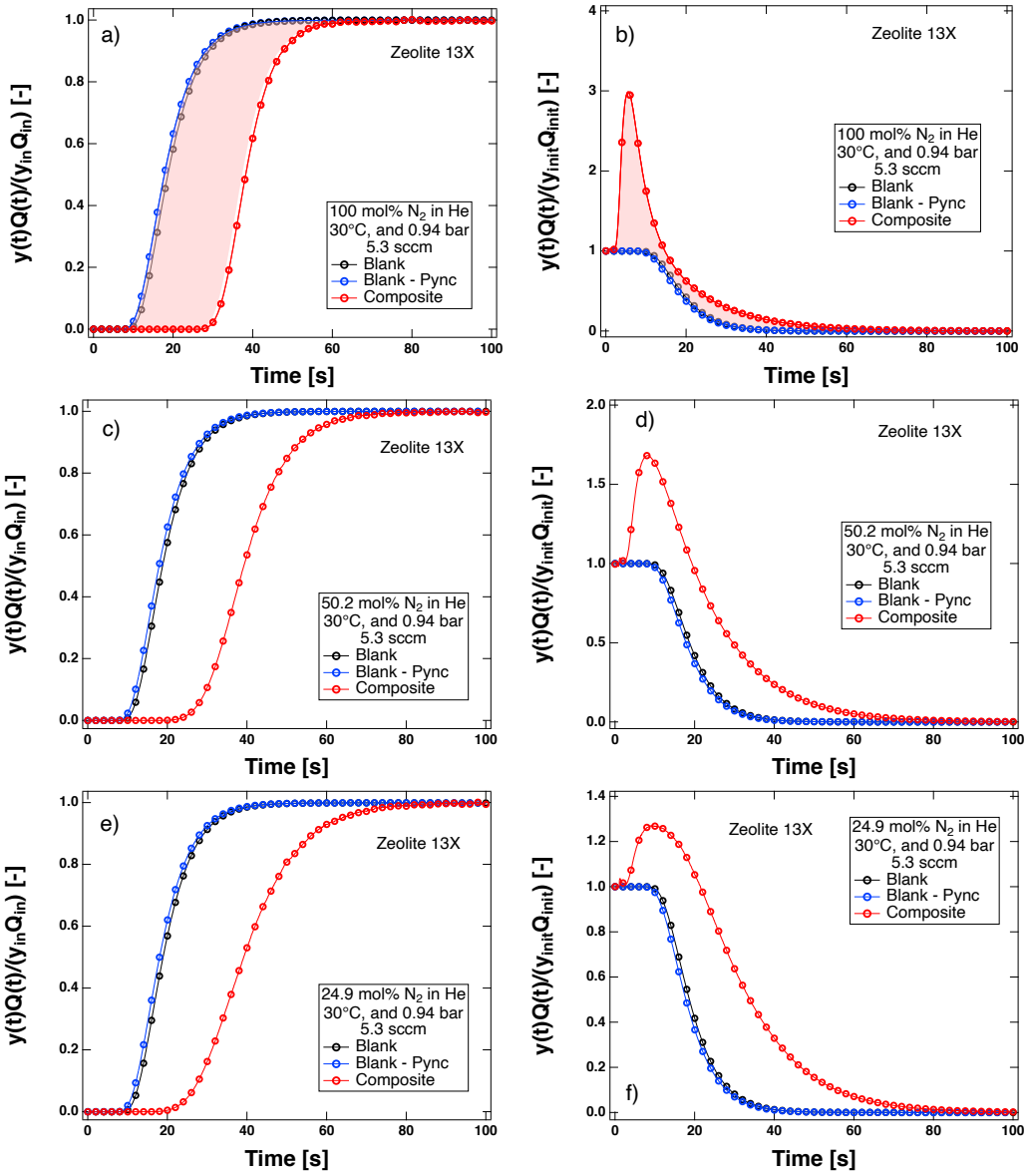

Figure 4.7: Single-component N_2/He adsorption (left) and desorption (right) breakthrough curves at 0.94 bar and 30°C on zeolite 13X. Panels (**a**) and (**b**) are for 100 mol% N_2, (**c**) and (**d**) are for 50.2 mol% N_2/He, and (**e**) and (**f**) are for 24.9 mol% N_2/He. The reference gas was He for these experiments. Every tenth point is shown as a marker.

flow increases to the inlet value with the adsorbate mole fraction. This yields a breakthrough curve (Fig. 4.7(**a**)) that is similar, but not equal to, the mole fraction breakthrough curve (see Fig. 4.5(**a**)) [30]. For desorption, notice that initially the normalized molar flow is above 1; this means that the flow rate of N_2 increases above the inlet flowrate, $Q(t) > Q_{\text{in}}$, during the first few seconds of desorption (until ≈ 16 seconds). This is due to the desorption of N_2, that contributes to an increased flowrate. After the initial flow spike, the flow decreases as N_2 leaves the bed and approaches zero as both $Q(t)$ returns to the inlet flow value, and as $y(t)$ approaches zero. When the desorption normalized molar flow goes to zero, desorption is complete. Single component adsorption and desorption breakthrough experiments were also performed at 40 and 50°C for 25, 50 and 100 mol% N_2 in He, but are shown in the Supporting Information.

Using either Eqn. 4.8 for an adsorption experiment, or Eqn. 4.9 for a desorption experiment, the adsorbate loading can be calculated. These values are shown in Fig. 4.6 together with the volumetrically collected equilibrium data and the linear isotherm fit. Tabulated equilibrium data is given in Table 4.3. As seen in Fig. 4.6, the adsorption data (hollow markers) and desorption data (solid markers) from the μDCB measurements are within 5% of the volumetrically collected data. The error associated with the μDCB calculated loadings is small, generally $4 - 5\%$ of the calculated adsorption/desorption loading.

To demonstrate the repeatability of the μDCB system, a series of 100 mol% N_2/He experiments were performed at 30°C, 0.95 bar and 5.3 sccm. Five repetitions of an adsorption and desorption breakthrough experiment were performed, which resulted in ten estimates for the N_2 equilibrium loading at 30°C and 0.95 bar. These dimensionless molar flow curves are shown in Fig. 4.8. As seen in Fig. 4.8, the five repeated composite adsorption (Fig. 4.8(**a**)) and desorption (Fig. 4.8(**b**)) experiments are virtually indistinguishable from each other. The mass balances were solved, and the calculated equilibrium data is shown with the isotherm and volumetrically collected

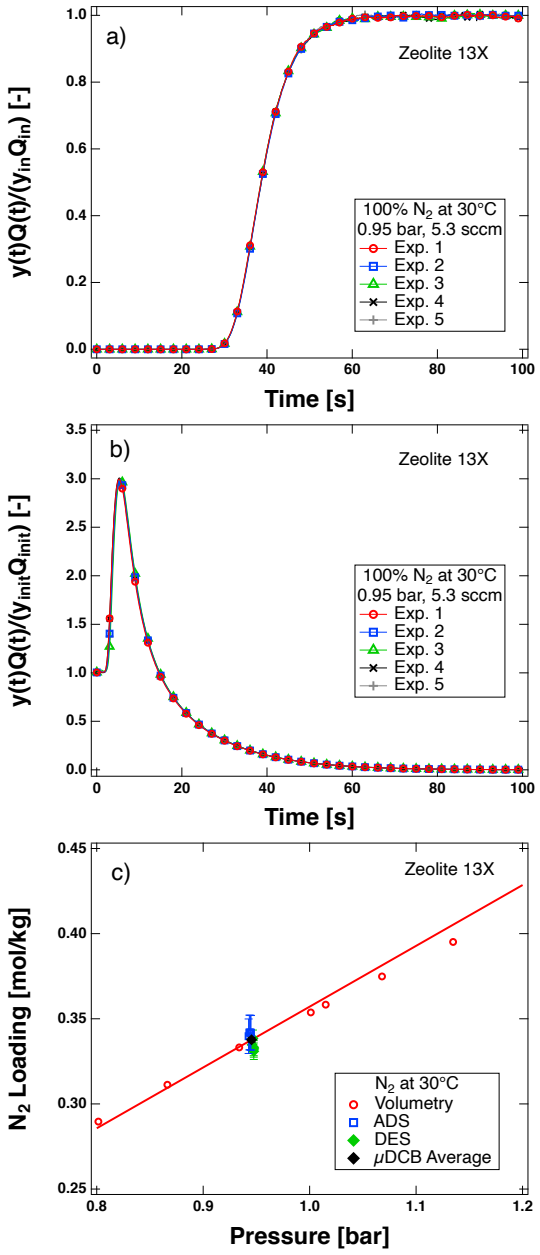

Figure 4.8: A series of single-component N_2/He adsorption and desorption μDCB experiments for 100 mol% N_2 in He on zeolite 13X at $\approx$ 0.95 bar and 30°C. The composite (**a**) adsorption and (**b**) desorption normalized molar flow curves. Every thirtieth point is shown as a marker. (**c**) The corresponding equilibrium loadings of N_2 for the five adsorption and desorption experiments with the isotherm and volumetrically collected data. The reference gas was He for these experiments.

data (at 30°C) in Fig. 4.8(**c**). In Fig. 4.8(**c**), the blue squares are adsorption equilibrium loadings, the green diamonds are desorption equilibrium loadings and the black diamond is the average of all ten adsorption and desorption loadings ($\bar{q}^*_{N_2} = 0.3377$ mol/kg). As seen in Fig. 4.8(**c**), the μDCB is highly repeatable, and agrees very well with the volumetrically collected data. The error bars for the adsorption and desorption equilibrium loadings are estimated with Eqn. 4.13, which represents the largest possible deviation from the measured loading if all measurements are incorrect by their inherent uncertainty. These values range between 4.81×10^{-3} and 1.02×10^{-2} mol/kg. The standard experimental error was calculated to be 1.41×10^{-3} mol/kg, approximately three times less than the lowest estimate from error propagation, showing that experimental variability is less than the estimated error propagation. These results give confidence that the μDCB is able to accurately and precisely calculate the equilibrium loading.

Single-component CH_4 adsorption and desorption experiments were also performed to determine if the μDCB apparatus was able to measure adsorption equilibrium and column dynamics of different species. The CH_4 breakthrough experiments at 30°C for 25, 50 and 100 mol% CH_4 in He are shown in the Supporting Information. Many of the same observations were noticed for CH_4 as were noticed for N_2. As seen in Fig. 4.6, the CH_4 equilibrium data is essentially linear over the pressure and temperature range studied. Therefore, the same adsorption breakthrough time is observed with CH_4 at 30°C on zeolite 13X for all three compositions studied (25, 50 and 100 mol% in He). Since CH_4 is stronger than N_2 on zeolite 13X, CH_4 breaks through later in time than N_2. The CH_4 loadings were calculated using Eqn. 4.8 and Eqn. 4.9 for an adsorption and desorption experiment, respectively. The error of these values are typically between $2 - 4\%$ of the measurement and within 5% of the volumetrically collected CH_4 data. As seen in Fig. 4.6(**d**), the μDCB measurements are in good agreement with the volumetrically collected data. The single-component CH_4 equilibrium data for zeolite 13X is given in Table 4.3.

Single component breakthrough experiments were also performed on an activated carbon (Calgon BPL 4x10 CAS#7440-44-00), for 25, 50 and 100 mol% mixtures of N_2/He and CH_4/He at $\approx$ 0.95 bar and 30, 40 or 50°C. These experiments were performed to determine whether this method would be able to predict consistent and accurate equilibrium data for different types of adsorbent materials. Overall, the same findings were found for activated carbon as were found for zeolite 13X. The adsorption/desorption breakthrough curves are shown in the Supporting Information. The equilibrium data for both N_2 and CH_4 is shown in Fig. 4.6 as hollow and solid diamonds for adsorption and desorption, respectively. Tabulated equilibrium data is given in Table 4.4. As before with zeolite 13X, the μDCB adsorption and desorption measured equilibrium loadings agree well with the volumetrically collected data for both N_2 and CH_4. The error of the activated carbon μDCB measurements is similar to that of zeolite 13X, generally between $2-4\%$ of the measurement and within 5% of the volumetrically collected data.

4.4.3 Non-Competitive Binary Breakthrough Experiments

Due to the small amount of sample used, and the relatively fast experimental times, the μDCB has the potential to be a very rapid method to quantify multicomponent adsorption equilibrium. Mixtures of CH_4 and N_2 on zeolite 13X were chosen to study an ideal case of co-adsorption in the absence of adsorptive competition. This data is provided in Table 4.5. Both N_2 and CH_4 exhibit a linear isotherm on zeolite 13X. Two adsorbates with linear isotherms typically do not show competitive adsorption [20]. Multicomponent μDCB experiments were still run as a binary mixture, but now with the reference helium, and helium carrier, replaced with another adsorbing gas. For example, for a CH_4/N_2 binary experiment, the carrier could either be CH_4 to measure the binary loading of N_2, or N_2 to measure the binary loading of CH_4. This is different than what is usually done in the literature, where a ternary mixture is made with He, or H_2, as an inert sweep gas [2, 105, 117–121]. Although uncommon, this

Table 4.4: Conditions for the single-component adsorption and desorption μDCB experiments performed on activated carbon in this study.

Gas	$y_{\text{in/init}}$ [-]	P [bar]	T [°C]	Q_{in} [ccm]	q^*_{ads} [mol kg^{-1}]	q^*_{des} [mol kg^{-1}]
N_2/He	1.000	0.954	30	6.29	0.2115	0.2073
	0.494	0.953	30	6.29	0.1161	0.1121
	0.243	0.954	30	6.29	0.0579	0.0586
	1.000	0.958	40	6.46	0.1758	0.1840
	0.495	0.954	40	6.49	0.0972	0.0961
	0.243	0.954	40	6.49	0.0491	0.0476
	1.000	0.958	50	6.66	0.1604	0.1549
	0.494	0.954	50	6.68	0.0824	0.0796
	0.243	0.954	50	6.69	0.0395	0.0415
CH_4/He	1.000	0.949	30	6.34	0.6676	0.6446
	0.500	0.958	30	6.27	0.4013	0.3777
	0.242	0.963	30	6.24	0.2194	0.2182
	1.000	0.949	40	6.54	0.5571	0.5421
	0.500	0.958	40	6.47	0.3384	0.3184
	0.242	0.963	40	6.44	0.1813	0.1765
	1.000	0.950	50	6.74	0.4712	0.4561
	0.500	0.957	50	6.68	0.2804	0.2649
	0.243	0.964	50	6.63	0.1453	0.1441

Table 4.5: Conditions for the multicomponent CH_4/N_2 adsorption and desorption μDCB experiments performed on zeolite 13X.

y_{CH_4} [-]	y_{N_2} [-]	P [bar]	T [°C]	Q_{in} [ccm]	$q^*_{N_2,ads}$ [mol kg^{-1}]	$q^*_{N_2,des}$ [mol kg^{-1}]	$q^*_{CH_4,ads}$ [mol kg^{-1}]	$q^*_{CH_4,des}$ [mol kg^{-1}]
0.247	0.753	0.951	30	6.31	-	-	0.1456	0.1426
0.244	0.756	0.945	30	6.34	0.2630	0.2606	-	-
0.513	0.487	0.950	30	6.32	-	-	0.3072	0.2928
0.511	0.489	0.945	30	6.33	0.1720	0.1663	-	-
0.770	0.230	0.950	30	6.32	-	-	0.4441	0.4432
0.769	0.231	0.945	30	6.34	0.0811	0.0784	-	-

method has been used previously to study equilibrium and kinetics of binary mixtures of gases [94]. This limitation arises owing to the decision to use a TCD instead of a multicomponent detector, such as a mass spectrometer. The use of an inert (such as helium) as a reference gas will not be able to distinguish between the two test gases (N_2/CH_4), therefore the idea is to employ one of the test gases as the TCD reference gas. The change of the reference gas does change the TCD calibration (with respect to the analyzed gas), but the change also blinds the TCD to the carrier gas allowing for the analyzed gas to be measured in a competitive experiment. This does require two sets of experiments to complete a binary isotherm at a given temperature and pressure: one for each adsorbate in the mixture. The first set of experiments starts with a bed saturated with N_2 (to measure CH_4) and the second set starts with a bed initially saturated with CH_4 (to measure N_2). Therefore, for an "adsorption" experiment, when the analyzed component adsorbs, the reference component is being desorbed from 100 mol% of the reference component to the feed composition. Likewise for a "desorption" experiment, when the analyzed component desorbs, the reference component is being adsorbed from the feed composition to 100 mol% of the reference component. This at times yields unusual molar flow curves for the light component in the binary mixture. Specifically for a desorption experiment, the effluent flow, $Q(t)$,

can drop below the inlet flow, Q_{in}, which is the different from a single-component experiment. The opposite, where $Q(t)$ increases higher than Q_{in}, is possible as well in an adsorption experiment; however, it is not seen in the normalized molar flow curves since the mole fraction is equal to zero at the coincident times. A sample set of experiments for an approximately 50/50 mol% CH_4/N_2 mixture on zeolite 13X at 30°C and 0.95 bar is shown in Fig. 4.9. Binary mixtures of 25/75 and 75/25 mol% CH_4/N_2 at 30°C and 0.95 bar were also performed, but are not shown in the main body of this paper. All other CH_4/N_2 adsorption and desorption breakthrough curves are shown in the Supporting Information.

For the first set of multicomponent experiments on zeolite 13X, CH_4 was measured while N_2 was used as the TCD reference gas and is blinded. This means that the zeolite 13X bed was initially saturated with 100 mol% N_2 at 0.95 bar and 30°C. In a CH_4/N_2 mixture, CH_4 is the heavy component, exhibiting a larger capacity on zeolite 13X than N_2 at similar conditions (see Fig. 4.6). Since, CH_4 is the heavy component, the adsorption and desorption breakthrough curves will qualitatively look similar to a single-component CH_4 experiment [30, 94]. These curves are shown in Fig. 4.9(**a**) and (**b**), for adsorption and desorption respectively. Due to the increase in flow on desorption, the normalized flow curves initially increase in Fig. 4.9(**b**) to about 20 seconds, where the flow starts to approach the feed flowrate of 5.3 sccm.

The N_2 experiments are shown in Fig. 4.9(**c**) and (**d**). These are separate experiments where the column was initially saturated with CH_4 at 0.95 bar and 30°C with CH_4 used as the TCD reference. Since N_2 is the weaker component in the CH_4/N_2 mixture, the effluent flow curves ($Q(t)$) do not resemble a typical single-component experiment, as explained earlier. Specifically, CH_4 (the heavy component) seems to dictate the behavior of the effluent flow. The effluent flow curves for the 48.7/51.3 mol% N_2/CH_4 experiment are shown in Fig. 4.9(**e**) and (**f**), for adsorption and desorption, respectively. During adsorption, the flow in Fig. 4.9(**e**) initially increases, despite the fact the N_2 is adsorbing into the column. This trend occurs since CH_4

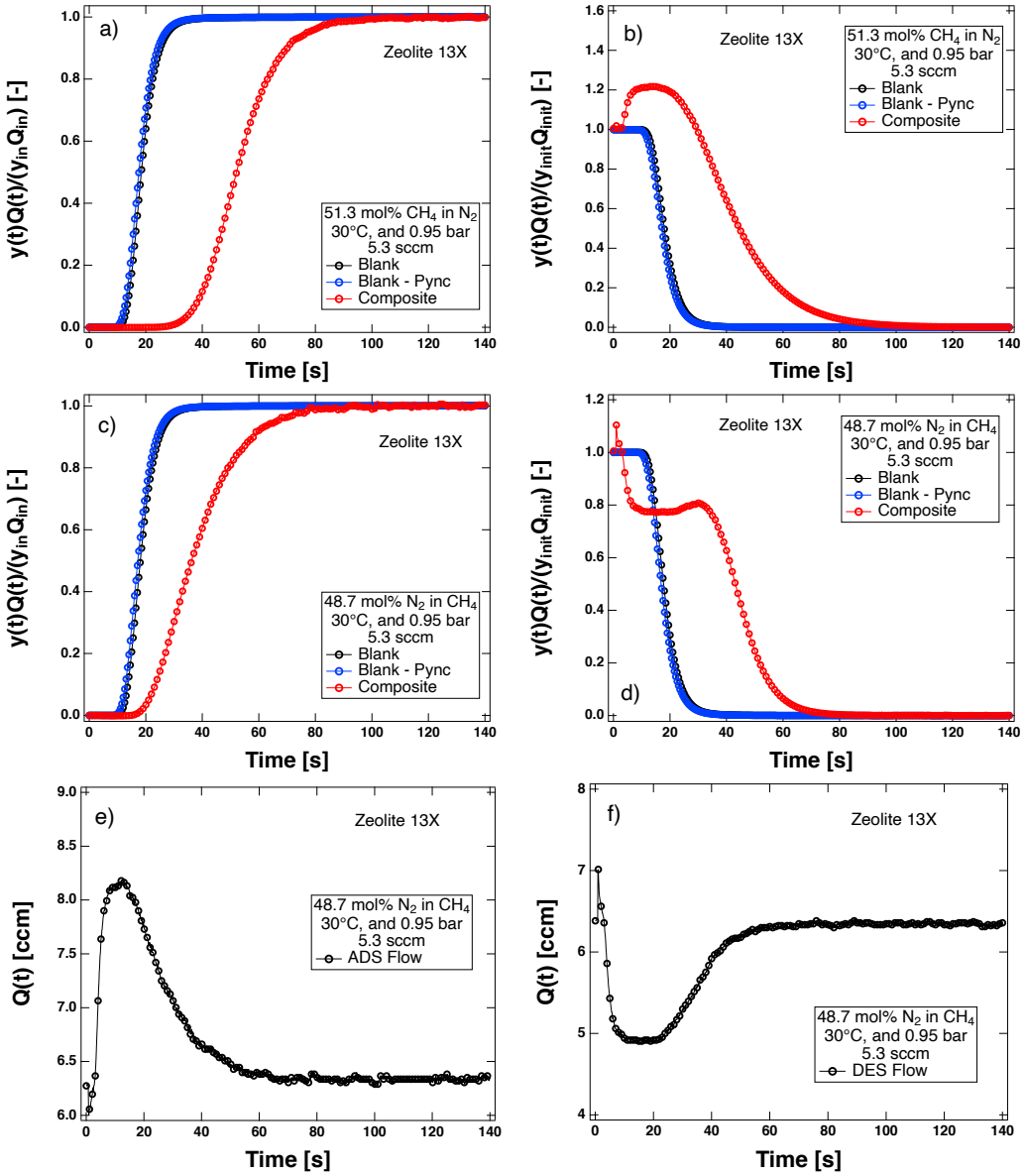

Figure 4.9: Multicomponent adsorption (left) and desorption (right) breakthrough curves on zeolite 13X at 0.95 bar and 30°C for a 51.3/48.7 mol% CH_4/N_2 mixture. Panels (**a**) and (**b**) are adsorption and desorption of CH_4, and panels (**c**) and (**d**) are equivalent experiments for N_2. Panels (**e**) and (**f**) show the corresponding effluent flow curves for the N_2 experiments. Every tenth point is shown as a marker. Note that the CH_4 and N_2 experiments are separate experiments, since the TCD reference changes to detect one gas over the other. The reference gas was N_2 for the CH_4 experiment and CH_4 for the N_2 experiment.

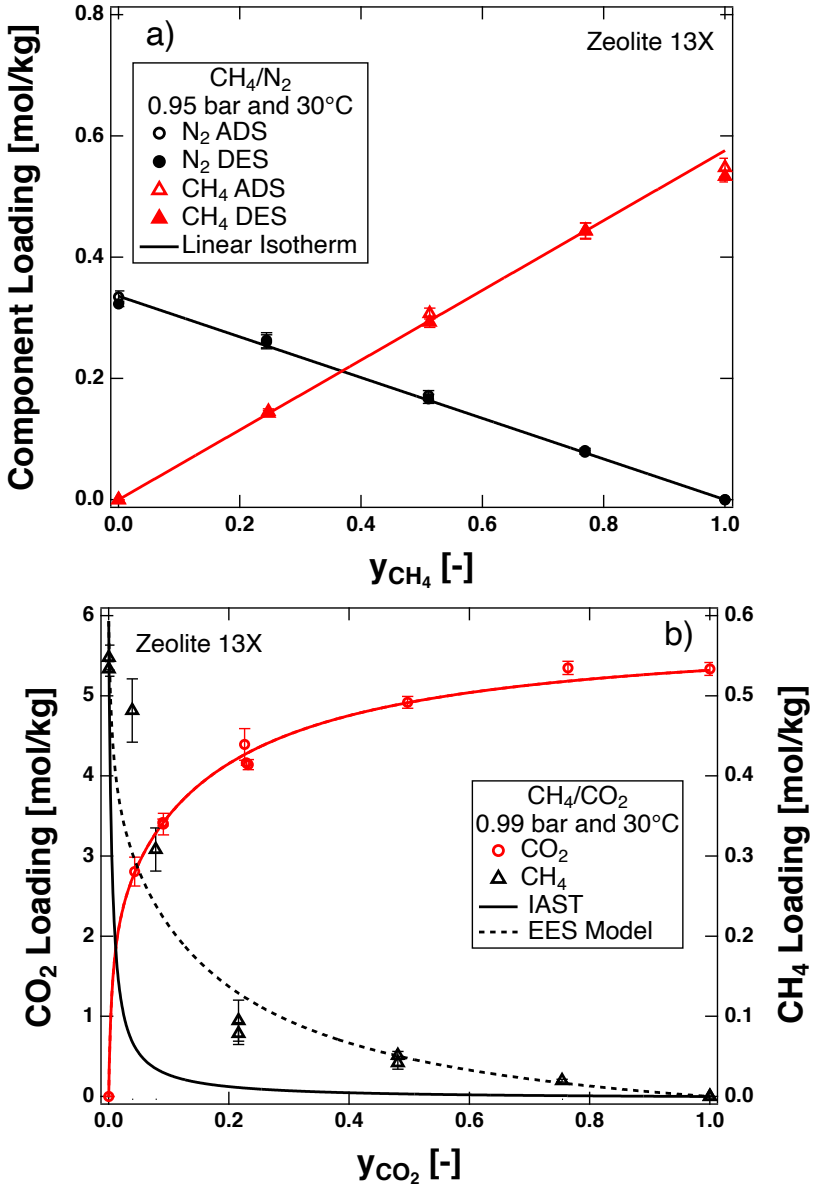

Figure 4.10: Multi-component equilibrium data of (**a**) CH_4/N_2 mixtures and (**b**) CO_2/CH_4 on zeolite 13X at 30°C. Hollow markers are adsorption breakthrough experiments, and solid markers are desorption experiments. Solid lines are ideal adsorbed solution theory predictions and dashed lines are equal-energy sites predictions.

is being simultaneously desorbed and the quantity of CH_4 desorbed is greater than the quantity of N_2 adsorbed. This flow curve yields a N_2 adsorption breakthrough curve that resembles a single-component desorption curve. Likewise for desorption in Fig. 4.9(**d**), N_2 is being desorbed while CH_4 adsorbs. This yields a desorption molar flow curve that has a dip in the initial curve. When the N_2 desorption experiment starts, the flow drops below Q_{in}, since CH_4 is adsorbing (see Fig. 4.9(**f**)). This causes the initial molar flow curve of N_2 to decrease and then increase slightly (never going above one) as CH_4 breaks through the column. At this time, the N_2 molar flow curve begins to decrease again as a typical single component desorption curve. While not shown in the main body of the paper, this becomes more pronounced as the composition of N_2 decreases, or as the quantity of CH_4 increases. In all measured light component breakthroughs (in the Supporting Information), the desorption normalized molar flow curve for the light component was always less than or equal to one. For a single component desorption, this value is initially greater than one, as flow increases during desorption, and then decreases as the mole fraction approaches zero and the flow returns to the feed flow.

Solving the adsorption (hollow markers) and desorption (solid markers) mass balances yields the expected single-component equilibrium values for both N_2 and CH_4. These values are shown in Fig. 4.10(**a**) and are tabulated in Table 4.5. Both the N_2 and CH_4 predictions are virtually indistinguishable from the expected values, assuming single-component linear isotherms, except for the 100 mol% CH_4 (in He) adsorption/desorption experiments, which fall slightly below the single-component isotherm prediction. Again, since both N_2 and CH_4 exhibit linear isotherms on zeolite 13X, the competitive loadings can be predicted with the single-component isotherms. The error associated with these measurements was $\approx 2-5\%$ of the calculated μDCB loading. These experiments confirm that the μDCB is able to measure binary equilibrium data accurately and precisely with the expected noncompetitive, ideal behavior. The four adsorption/desorption measurements for one gas in the binary mixture (Fig. 4.10(**a**)),

and their associated blank measurements, could be measured comfortably in a single work-day ($\approx 5-6$ hours).

4.4.4 Competitive Binary Breakthrough Experiments

A series of CH_4/N_2 experiments were then performed on activated carbon to determine if the μDCB apparatus was able to measure CH_4/N_2 adsorptive competition. Unlike CH_4/N_2 mixtures on zeolite 13X, CH_4 and N_2 can be expected to adsorb competitively on activated carbon due to the nonlinear trend of CH_4 shown in Fig. 4.6. These experiments were performed as 25/75, 50/50 and 75/25 mol% mixtures of CH_4/N_2 initially at 30°C and 0.95 bar. The adsorption and desorption breakthrough curves of all CH_4/N_2 mixtures on activated carbon are shown in the Supporting Information. The calculated adsorption (hollow markers) and desorption (solid markers) equilibrium loadings of N_2 and CH_4 at 30°C are shown in Fig. 4.11(**a**) with IAST predictions as solid lines. Tabulated equilibrium data is given in Table 4.6. As seen in Fig. 4.11(**a**), the N_2 equilibrium loadings appear to follow the predictions from IAST. The calculated N_2 loadings are all slightly less than the IAST predictions, but fall within the error bars. On the other hand, CH_4 appears to compete non-ideally, with all adsorption and desorption equilibrium loadings above the IAST predictions.

The CH_4/N_2 mixture (25/75, 50/50 and 75/25 mol%) experiments were repeated at 40°C and 50°C at 0.95 bar. This was partially initiated to demonstrate the ability of the μDCB to work at different temperatures and to examine if CH_4/N_2 remains a nonideal system on activated carbon at different temperatures. The μDCB adsorption and desorption loadings are shown in Fig. 4.11(**b**) and (**c**) for 40°C and 50°C, respectively. At 40°C and 50°C, N_2 appears to remain ideal. Methane appears to become more ideal as the temperature increases from 30°C to 50°C.

These results are consistent with the literature. Kennedy *et al.* reported slight nonideal competition between CH_4 and N_2 on Xtrusorb A754 activated carbon at 30°C and 1.01 bar [122]. Specifically, Kennedy *et al.* found both CH_4 and N_2 exhibit

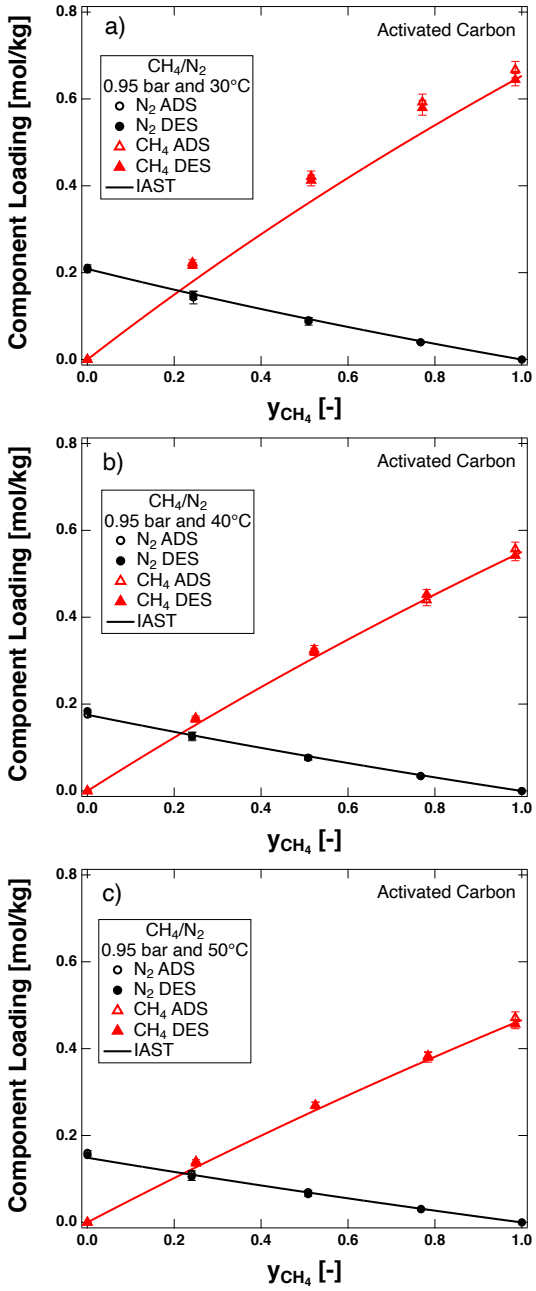

Figure 4.11: Multi-component equilibrium data of CH_4/N_2 mixtures on activated carbon at (**a**) 30°C, (**b**) 40°C and (**c**) 50°C and 0.95 bar. Hollow markers are adsorption breakthrough experiments, and solid markers are desorption experiments. Solid lines are ideal adsorbed solution theory predictions.

Table 4.6: Conditions for the multicomponent CH_4/N_2 adsorption and desorption μDCB experiments performed on activated carbon.

y_{CH_4} [-]	y_{N_2} [-]	P [bar]	T [°C]	Q_{in} [ccm]	$q^*_{N_2,ads}$ [mol kg^{-1}]	$q^*_{N_2,des}$ [mol kg^{-1}]	$q^*_{CH_4,ads}$ [mol kg^{-1}]	$q^*_{CH_4,des}$ [mol kg^{-1}]
0.242	0.758	0.958	30	6.28	-	-	0.2227	0.2167
0.243	0.757	0.944	30	6.36	-	-	0.2214	0.2166
0.244	0.756	0.930	30	6.43	0.1476	0.1428	-	-
0.515	0.485	0.947	30	6.34	-	-	0.4210	0.4126
0.515	0.485	0.944	30	6.36	-	-	0.4239	0.4095
0.509	0.491	0.929	30	6.44	0.0910	0.0879	-	-
0.771	0.229	0.945	30	6.36	-	-	0.5927	0.5798
0.767	0.233	0.926	30	6.48	0.0399	0.0396	-	-
0.249	0.751	0.953	40	6.50	-	-	0.1679	0.1646
0.241	0.759	0.954	40	6.47	0.1272	0.1257	-	-
0.522	0.478	0.952	40	6.51	-	-	0.3255	0.3204
0.508	0.492	0.952	40	6.48	0.0763	0.0766	-	-
0.781	0.219	0.953	40	6.51	-	-	0.4395	0.4523
0.767	0.233	0.953	40	6.49	0.0349	0.0338	-	-
0.250	0.750	0.950	50	6.71	-	-	0.1404	0.1360
0.240	0.760	0.951	50	6.69	0.1123	0.1050	-	-
0.525	0.475	0.954	50	6.69	-	-	0.2694	0.2696
0.508	0.492	0.950	50	6.70	0.0701	0.0649	-	-
0.784	0.216	0.954	50	6.70	-	-	0.3799	0.3836
0.768	0.232	0.950	50	6.71	0.0312	0.0300	-	-

a slightly positive deviation from ideality with CH_4 exhibiting a larger deviation. At higher pressures (4.05 bar), CH_4 could be considered ideal, while N_2 exhibits a larger positive deviation from ideality (than at 1.01 bar). Wu *et al.* found that for pitch-based activated carbon at 30°C and 1.00 bar, both CH_4 and N_2 were ideal [123]. Wu *et al.* also studied mixtures of CH_4 and N_2 up to 5.00 bar at 30°C and 50°C and found a slight negative deviation from ideality in the total loading for N_2 compositions greater than 44.9 mol%. Dreisbach *et al.* found that for Norit A1 Extra activated carbon (at 25°C, pressures from 1.08 to 60.35 bar) CH_4 displays a slight positive deviation from ideality in mixtures with N_2 [96]. The average prediction error from the IAS calculations and the experimental loadings was 3.82% with a 5.20% error in the CH_4 loading in particular. Overall, the data for activated carbons in the literature suggests that a CH_4/N_2 mixture at 30°C and ≈ 1.00 bar is either ideal or weakly nonideal.

To test the ability of the μDCB to predict multicomponent adsorption equilibrium, a more challenging system was chosen. Specifically, mixtures of CO_2 and CH_4 on zeolite 13X. The single-component isotherms of CH_4 and CO_2 are shown in Fig. 4.6(**d**) and (**e**). On zeolite 13X, CH_4 exhibits a linear trend in loading and CO_2 is highly nonlinear. Due to the large capacity of CO_2 on zeolite 13X, the adsorptive competition can be expected to be highly non-ideal [91]. Krishna and van Baten predicted non-ideal adsorption of CH_4 in particular (in mixtures with CO_2) on zeolite 13X at 27°C and 1.00 bar using CBMC simulations [91]. CH_4 adsorption is greater than what is predicted by IAST. Krishna and van Baten also show that the CO_2 loading is virtually unaffected by CH_4 loading. The CH_4/CO_2 phase-diagram found by Krishna and van Baten is shown in the Supporting Information along ideal and real competitive models. This was also found by Avijegon *et al.*, where the experimental selectivity of CO_2 to CH_4 was $\approx 3-40$ times less than what was predicted by IAST at 0, 30 and 50°C at pressures between 1.06 to 9.03 bar [34].

A series of CO_2/CH_4 adsorption experiments were performed on zeolite 13X at 30°C and ≈ 1.01 bar. The mixtures for these experiments were: 5/95, 10/90, 25/75, 50/50

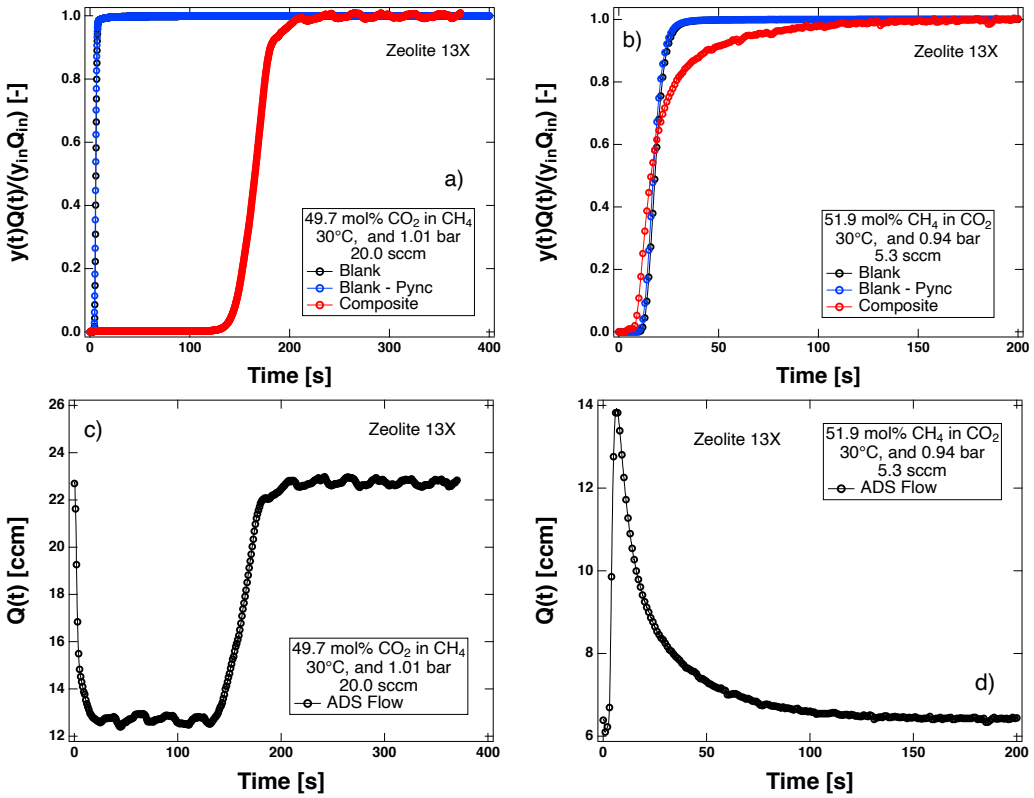

Figure 4.12: Two multicomponent CO_2/CH_4 adsorption breakthrough experiments on zeolite 13X at 30°C. Panel (**a**) shows the adsorption breakthrough of 49.7 mol% CO_2 in CH_4 at 1.01 bar and 20.0 sccm inlet flow. Panel (**b**) shows the adsorption breakthrough of 51.9 mol% CH_4 in CO_2 at 0.94 bar and 5.3 sccm inlet flow. Two separate experiments were required to find both CO_2 and CH_4 loadings. Panels (**c**) and (**d**) show the corresponding effluent flow curves for the multicomponent CO_2/CH_4 experiments. The reference gas was CH_4 for the CO_2 experiment and CO_2 for the CH_4 experiment. Every tenth point is shown as a marker.

Table 4.7: Conditions for the multicomponent CO_2/CH_4 adsorption μDCB experiments performed on zeolite 13X.

y_{CO_2} [-]	y_{CH_4} [-]	P [bar]	T [°C]	Q_{in} [ccm]	$q^*_{CH_4,ads}$ [mol kg^{-1}]	$q^*_{CO_2,ads}$ [mol kg^{-1}]
0.043	0.957	1.01	30	22.88	-	2.8078
0.039	0.961	0.948	30	6.36	0.4816	-
0.090	0.910	1.01	30	22.88	-	3.4193
0.091	0.909	1.01	30	22.88	-	3.3997
0.078	0.922	0.936	30	6.42	0.3082	-
0.226	0.774	0.941	30	6.37	-	4.3939
0.232	0.768	1.01	30	22.72	-	4.1415
0.216	0.784	0.936	30	6.44	0.0785	-
0.497	0.503	1.01	30	22.74	-	4.9188
0.481	0.519	0.938	30	6.41	0.0512	-
0.764	0.236	1.01	30	22.36	-	5.3485
0.754	0.246	0.946	30	6.34	0.0197	-
1.000	0.000	1.01	30	22.36	-	5.3367

and 75/25 mol% CO_2/CH_4 to describe the entire range of competition including a range at low CO_2 composition where the mixture is expected to deviate significantly from ideality. Desorption was not performed for this set of experiments. For a CO_2 measurement, CH_4 was used to saturate the zeolite 13X column at 30°C and 1.01 bar prior to the adsorption experiment. For a CH_4 measurement, the zeolite 13X column was initially saturated with CO_2 at 30°C and 0.94 bar. These results are shown in Fig. 4.10(**b**) with a sample set of adsorption breakthrough curves for an approximately 50/50 mol% CO_2/CH_4 mixture in Fig. 4.12. Many of the same features as the CH_4/N_2 adsorption breakthrough curves are observed in the CO_2/CH_4 adsorption experiments. The breakthrough curve of the heavy component, CO_2, again resembles a single-component adsorption breakthrough curve. The molar flow in Fig. 4.12(**a**) displays a shock transition and the corresponding effluent flow drops (in Fig. 4.12(**c**)), which returns to Q_{in} as CO_2 breaks through. Note that the signal noise in Fig. 4.12(**c**) was due to a defective fan in the GC oven, which since has been repaired. Due to the strong adsorption capacity of CO_2 on zeolite 13X, and the manner in which the collected data was conditioned, this noise did not change the calculated mass balance. The methane adsorption breakthrough curve resembles a desorption wave in Fig. 4.12(**b**) and its corresponding effluent flow (in Fig. 4.12(**d**)) increases initially before dropping to Q_{in} as CO_2 desorbs from the column. The corresponding adsorption equilibrium data (hollow markers) is shown in Fig. 4.10(**b**) with IAST predictions as solid lines and equal energy sites (EES) DSL predictions as the dashed line. The EES DSL model is an extended DSL model, where the single-site Langmuir isotherm parameters for the light component are used in a DSL model where the saturation loadings (q_b^{sat} and q_d^{sat}) are the same as the heavy component [2]. Note that the EES DSL predictions for CO_2 are indistinguishable from the IAST predicitions. Tabulated equilibrium data is given in Table 4.7. As seen in Fig. 4.10(**b**), CO_2 is unaffected by CH_4, as was expected [91]. At almost all CO_2 compositions, the CO_2 equilibrium loadings were predicted by IAST and the EES model. Experiments

at 10/90 and 25/75 mol% CO_2/CH_4 were repeated (when measuring CO_2) to confirm the CO_2 loadings. All the repeated experiments were the same within the propagated error. The measured CH_4 equilibrium loadings are highly nonideal. The only two CH_4 measurements that are predicted by IAST are at the extremes, either 100 mol% CH_4 or 0 mol% CH_4. All other measurements, and their associated errors, do not bisect the CH_4 IAST predictions. The measured CH_4 μDCB data all display a positive deviation from IAST, which again was expected [34, 91]. The EES model is able to predict the measured data better than IAST. This trend was also found for the CH_4/CO_2 CBMC simulations reported by Krishna and van Baten, where the EES model is a very good fit for CH_4 in particular (shown in Supporting Information) [91]. The mixture CO_2/CH_4 adsorption experiments show that the μDCB is able to determine the binary equilibrium loadings of a highly nonideal system. The CO_2 measurements required thermal activation (at 350°C) between measurements, which made data collection slower. The CO_2 measurements plus thermal activation required about 2 hours each (approximately two work-days), while the CH_4 measurements were completed in a single work-day (8 hours).

4.5 Conclusions

A microscale dynamic column breakthrough (μDCB) apparatus was constructed that is able to quantify gas adsorption and desorption equilibrium loadings on a milligram-scale quantity of adsorbent. Small amounts of adsorbent, 238.9 mg of zeolite 13X and 180.2 mg of activated carbon, were used to perform all breakthrough experiments reported in this study. A typical experiment (at 5 sccm) lasted about 35 minutes and yielded two equilibrium measurements. This allowed for five point binary phase diagrams to be measured in a few work-days (a minimum of $10 - 12$ hours). The μDCB was built into an existing GC oven to control temperature and use the onboard thermal conductivity detector for composition measurement. The associated mass balances and description of a blank experiment were provided, and are analogous to

a traditional, large-scale DCB system. Single-component adsorption and desorption breakthrough experiments were performed at ≈ 0.95 bar and 5.3 sccm with N_2 and CH_4 on zeolite 13X, and activated carbon, at 30, 40 and 50°C. These results agree with statically collected equilibrium data at the same conditions. A series of N_2 adsorption and desorption experiments were repeated five times on zeolite 13X and were all found to agree with each other; also, the standard experimental error was less than the propagated error. Methane/nitrogen multicomponent adsorption and desorption experiments were performed on zeolite 13X and activated carbon at ≈ 0.95 bar and 5.3 sccm flow. The μDCB measurements for the CH_4/N_2 mixtures agreed perfectly with the predictions from ideal adsorbed solution theory. Specifically, the values agreed with the linear isotherm predictions, since typically two linear isotherms do not compete. The light-component adsorption and desorption curves were found to have the opposite flow curve than expected. Specifically, the flow curve for a light-component adsorption experiment resembled a desorption experiment and vice versa for desorption. Mixtures of CH_4/N_2 on activated carbon were found to be weakly non-ideal depending on the temperature. The adsorption and desorption equilibrium loadings for N_2 agreed well with IAST, while CH_4 became more ideal as the temperature increased from 30°C to 50°C. The measurements generally agree with the literature, where either CH_4 was found to be ideal, or weakly nonideal. A highly non-ideal system of CO_2/CH_4 was also studied on zeolite 13X at 30°C. The μDCB measured adsorption loadings showed that CO_2 was unaffected by CH_4 adsorption, while CH_4 displayed a positive deviation from IAST. These results agree with what was found in the literature.

The miniaturization of the DCB system also brings in challenges. For instance, using small quantities of adsorbent may not be representative of the large sample that can be deployed in a process. This can be resolved by performing multiple batches. Further, small amounts of leaks can lead to large errors and the presence of strongly adsorbed components, such as water, can have a major impact on the measurements.

Repetition of blank experiments, using reference adsorbents [37], or installing desiccant beds in the gas supply lines [100] can alleviate these challenges. The advantages of the μDCB mainly stem from its ability to be used for very small sample quantities making it ideal for early stage adsorbent development. Although extensive detector calibrations are required, they are not laborious. Thermal conductivity detectors are known to be very stable and reproducible. Once performed, these calibrations hold for a long time. Another key feature of the μDCB is the ability to construct it from relatively inexpensive parts. For instance, no proprietary equipment is needed, and the use of the TCD avoids the need of an expensive detector, such as a mass spectrometer. In summary, μDCB can be a valuable addition to the materials scientist with its ability to generate the fast, accurate, and precise measurements for both single and binary adsorption equilibrium.

Chapter 5

Diffusion of CH_4 and N_2 in barium-exchanged reduced pore zorite (Ba-RPZ) and zeolite 4A

5.1 Introduction

Methane is considered a cleaner form of fossil fuel due to its high energy density and low CO_2 emissions. A significant amount of geologic methane remains stranded in wells which have concentrations of N_2 large enough for the gas to fail pipeline specifications (CH_4 purity > 96 mol%) [124]. Many of the contaminated wells are not of a scale suitable to take advantage of cryogenic distillation but would be able to take advantage of alternate technologies such as pressure swing adsorption (PSA) [106, 124]. Most adsorbents show preferential adsorption of CH_4 over N_2. This means that CH_4 is typically obtained as the low-pressure raffinate product and has to be re-compressed to meet pipeline specifications. To allow methane to be produced as the desired raffinate product, a different type of adsorbent is required; one that can separate CH_4 and N_2 based on their relative molecular sizes. Since CH_4 is the larger of the two in the pair, a PSA incorporating a size-selective molecular sieve is capable of producing methane as the light product [17]. Such adsorbents are typically referred to as "kinetic" adsorbents because they separate gases based on the differences in

This chapter was originally published as: N. S. Wilkins, J. A. Sawada, and A. Rajendran, "Diffusion of CH_4 and N_2 in barium-exchanged reduced pore zorite (Ba-RPZ) and zeolite 4A," *Ind. Eng. Chem. Res.*, vol. 60, no. 29, pp. 10777-10790, 2021.

diffusion rates into the molecular sieve. Many adsorbents have been proposed for the kinetic separation of CH_4 from N_2, such as carbon molecular sieves [106, 125, 126], zeolite 4A [127, 128] and clinoptilolites [129, 130].

Sr-ETS-4, a titanosilicate adsorbent, is used commercially to separate CH_4 and N_2. The pore size of Sr-ETS-4 can be tuned by carefully controlling the temperature to which it is heated [131]. Effective pore size control on the order of 0.1 Å has been shown, and by heating the adsorbent to a temperature of roughly 275°C, the effective pore size of the material contracted to a diameter near the molecular diameter of methane [132]. Ba-ETS-4 and Na-ETS-4 have also been studied for their potential for CH_4/N_2 separations [132, 133]. Marathe *et al.* measured uptake curves and pore diffusional time constants for Sr-ETS-4 and Na-ETS-4 and determined the limiting mass transfer mechanism to be gas diffusion within the micropores [132, 134]. Jayaraman *et al.* simulated a 5-step cycle with Sr-ETS-4 and found process conditions where CH_4 purities greater than 96 mol% were achieved from a feed of 85/15 mol% CH_4/N_2 [129]. Majumdar *et al.* studied Ba-ETS-4 and determined the same limiting mass transfer mechanism as Na- and Sr-ETS-4 [133]. Bhadra *et al.* have performed process studies of Ba-ETS-4 and Sr-ETS-4 using a simple Skarstrom cycle and were able to find operating conditions that could purify CH_4 above 96 mol% from a feed of 90/10 mol% CH_4/N_2 [135].

Another titanosilicate adsorbent that is a potential candidate for the kinetic separation of CH_4/N_2 is Ba-RPZ (barium-exchanged reduced pore zorite) [136, 137]. Reduced pore zorites are structurally analogous to ETS-4 (another synthetic zorite) but are synthesized in a mixture rich in halogen ions other than fluorine. The adsorptive characteristics of the resulting materials indicate that the effective pore size of the material decreases in proportion to the size of the anion present in the synthesis mixture. It has been proposed that the halogen ions can isomorphically substitute the terminal hydroxl group connected to the titania group, which protrudes into the pore channel [138]. In doing so, the substitution of Cl, Br, or I for the smaller hydroxyl

species creates a diffusion barrier within the pore channel that allows the molecular sieve to separate gases based on their relative size [138].

Single component equilibrium data have been reported by in Lin *et al.* for N_2 and CH_4 on Ba-RPZ at an unspecified temperature from 1 mbar to 1 bar pressure [138]. In the Ba-RPZ patent by Sawada *et al.*, single-component isotherms for N_2 and CH_4 at 30°C from vacuum pressures to 50 bar are reported [137]. While the data is conclusive that the adsorbent has a substantial selectivity toward N_2, a more detailed adsorption study is required to compare Ba-RPZ with other molecular sieves and to probe the underlying diffusion mechanism. An accurate mathematical description of the dynamic adsorption behavior of N_2 and CH_4 in Ba-RPZ would provide a key component to the design of a kinetic pressure swing adsorption separation process.

5.2 Materials and Methods

Ba-RPZ crystals were obtained from Extraordinary Adsorbents Inc. (Edmonton, Alberta, Canada). The crystalline Ba-RPZ powder (without binder) is composed of platelets having a crystalline thickness of 94 ± 17 nm and width of 1.079 ± 0.252 μm. The Ba-RPZ sample studied in this paper is most similar to the Ba-RPZ-1 sample that was studied by Lin *et al.* [138]. The zeolite 4A sample is a crystalline powder and was provided by Arkema (NK 10 AP or "Siliporite"). The zeolite 4A sample has cubic crystalline dimensions of 2.81 ± 0.59 μm. The scanning electron microscopy (SEM) images used to estimate the particle sizes of Ba-RPZ and zeolite 4A are shown in the Supporting Information (Fig. D.2). All gases in this study (99.99% CH_4, 99.999% N_2 and 99.999% Ar) were obtained from Praxair Canada. Single component adsorption isotherms and diffusion for N_2 and CH_4 were measured using volumetry.

5.2.1 Equilibrium Measurements

Low-pressure volumetric isotherms for N_2 and CH_4 were measured with a Micromeritics ASAP 2020C (Norcross, GA, USA). The Micromeritics system was used to measure

adsorption equilibrium between 1 mbar to 1.2 bar. The system has a loading accuracy of 0.15% of the reading and pressure accuracy of 1.3×10^{-7} mbar. A sample mass of 339.3 mg (Ba-RPZ) or 212.8 mg (zeolite 4A) was used for these experiments. The saturation loadings of CH_4 and N_2 were determined using a high-pressure volumetry apparatus (HPVA) (VTI Instruments, Hialeah, FL). The HPVA was used to measure equilibrium data between 0.25 and 20 bar and has a pressure accuracy of < 0.1 bar. A sample mass of 625.5 mg (Ba-RPZ) was used for the high-pressure adsorption experiments. The sample chambers for both instruments were thermostated with a 60/40 vol% ethylene glycol/water mixture for the lower temperature (< 20°C) experiments and either a furnace or an oil bath for the higher temperature (> 20°C) experiments. Prior to each experiment, in both the low and high-pressure systems, Ba-RPZ and zeolite 4A were activated for 12 hours under vacuum (5 μbar) at 250°C (Ba-RPZ) or 350°C (zeolite 4A).

5.2.2 Kinetic Measurements

Adsorption uptake experiments were performed using the Rate of Adsorption (ROA) package in the Micromeritics ASAP 2020C (Norcross, GA, USA). The sample chamber was thermostated with an ethylene glycol/water mixture for the lower temperature experiments (< 20°C) and an oil bath at temperatures greater than 20°C. A sample mass of 155.8 mg (large doses) or 169.8 mg (small doses) for Ba-RPZ and 331.1 mg for zeolite 4A was used for these experiments. Uptake data was measured by activating the sample under vacuum at 250°C (Ba-RPZ) or 350°C (zeolite 4A) for 12 hours. After activation, a fixed amount of gas was introduced into the sample chamber, and the pressure was measured as a function of time until the pressure in the system was stable [28, 139]. After equilibrium was reached, the next dosing was applied, and the same sequence followed until a series of uptake experiments were completed for a given temperature. Small pressure steps were introduced to the chamber to ensure that the calculated diffusivities would be along a linear portion of the isotherm and so could

be considered to be constant [139]. The change in pressure between each constant volume experiment was ≈ 15 to 300 mbar. These pressure steps were achieved by dosing a fixed quantity of gas into the sample chamber for each successive dose.

5.3 Modeling

5.3.1 Adsorption Equilibria

The single-site Langmuir (SSL) isotherm was used to fit the collected equilibrium data in this study. The SSL isotherm is shown below:

$$q_i^* = \frac{q_{\mathrm{b},i}^{\mathrm{sat}} b_i p_i}{1 + b_i p_i} \tag{5.1}$$

where p_i is the partial pressure of gas i, and $q_{\mathrm{b}}^{\mathrm{sat}}$ is the saturation capacity of the material. The equilibrium constant b_i is a function of temperature, T:

$$b_i = b_{0,i} \exp\left(\frac{-\Delta H_{\mathrm{ads},i}}{RT}\right) \tag{5.2}$$

where $b_{0,i}$ is the nonlinearity constant, $\Delta H_{\mathrm{ads},i}$ is the heat of adsorption, and R is the universal gas constant. At low pressures, the isotherm reduces to:

$$q_i^* = K_i p_i \tag{5.3}$$

where K_i is the temperature dependent Henry constant:

$$K_i = K_{0,i} \exp\left(\frac{-\Delta H_{\mathrm{ads},i}}{RT}\right) \tag{5.4}$$

The collected equilibrium data was fit to either a linear or SSL isotherm, depending on the sorbate-sorbent pairs, by minimizing the sum of squared errors:

$$J_1 = \sum_{j=1}^{n} \left[q_{\mathrm{exp},j}^* - q_{\mathrm{model},j}^* \right]^2 \tag{5.5}$$

where $q_{\mathrm{exp},j}^*$ and $q_{\mathrm{model},j}^*$ denote the experimentally measured and fitted values, respectively. The isosteric heat of adsorption, ΔH_{iso}, was calculated using the Clausius-Clapeyron equation:

$$\left[\frac{\partial \ln(p_i)}{\partial (1/T)}\right]_{q_i^*} = -\frac{\Delta H_{\mathrm{iso},i}}{R} \tag{5.6}$$

The derivative in Eqn. 5.6 was evaluated numerically using the collected equilibrium data at a fixed value of q_i^*. If a value of q_i^* did not exist for a particular temperature, it was determined through a linear interpolation.

5.3.2 Adsorption Kinetics

The transient mass uptake can be represented as a dimensionless fractional uptake:

$$\frac{m_t}{m_\infty} = \frac{\bar{q}(t) - q(0)}{q(\infty) - q(0)} \tag{5.7}$$

where $\bar{q}(t)$ is the average concentration (or loading) in the solid phase at some time t, $q(0)$ is the initial solid phase concentration and $q(\infty)$ is the solid phase concentration after equilibrium has been achieved [9]. Experimentally, the constant volume apparatus measures the change in pressure during the experiment and then solves for the loadings. If the main mass transfer resistance is not from the macro or mesopores, the mass uptake profiles can be modeled with one of three micropore diffusion models [22, 139, 140].

Micropore Controlled: The first mechanism considers the primary mass transfer resistance to be transport within the micropores. This is due to a very tortuous mean free path that the adsorbed gas molecule must travel inside the micropore. The mass balance inside the micropore of a spherical crystalline particle is:

$$\frac{\partial q}{\partial t} = \frac{1}{r^2}\frac{\partial}{\partial r}\left(r^2 D_\mathrm{c}\frac{\partial q}{\partial r}\right) \tag{5.8}$$

where r is the radius at some point inside the crystal and D_c is the microporous crystalline diffusivity (a function of q_i^* and T) [22]. Assuming that the mass flux at the center of the particle ($r = 0$) is finite and the gas phase concentration outside the particle ($r = r_\mathrm{c}$) is constant, the following boundary conditions are found:

$$\frac{\partial q(0)}{\partial r} = 0 \tag{5.9}$$

$$q(r_\mathrm{c}) = q^*(p_i) \tag{5.10}$$

where $q^*(p_i)$ is a suitable isotherm model (the equilibrium loading of component i at a given pressure). An analytical solution for the transient mass uptake for a micropore limited system can be found [141]:

$$\frac{m_t}{m_\infty} = 1 - \frac{6}{\pi^2}\sum_{n=1}^{\infty}\frac{\exp(-n^2\pi^2\frac{D_c}{r_c^2}t)}{n^2} \tag{5.11}$$

The solution is an infinite series, with the only unknowns being D_c and r_c for a given experiment. These can be combined into a single parameter, D_c/r_c^2, also known as the pore diffusional time constant.

With the chemical potential gradient being the driving force for diffusion, the value of D_c varies as a function of the solid-phase concentration. This typically follows Darken's relationship:

$$\frac{\partial \ln(p)}{\partial \ln(q^*)} = \frac{D_c}{D_{c,0}} \tag{5.12}$$

where $D_{c,0}$, a function of T, is the limiting pore diffusion within the micropore. For the single-site Langmuir isotherm, Eqn. 5.12 can be written as:

$$\frac{D_c}{D_{c,0}} = \frac{1}{1-\theta} \tag{5.13}$$

where θ is the fractional loading ($\theta_i = q_i^*/q_{b,i}^{sat}$). Note that for a linear isotherm the derivative $\partial \ln(p)/\partial \ln(q^*) = 1$, therefore $D_c = D_{c,0}$.

Surface Barrier Controlled: The second mechanism considers that the main mass transfer resistance is at the pore mouth. This is due to a pore mouth that is very small with respect to the micropore and adsorbate. Barrier resistance can arise from either pore blocking, where the surface of a material has few entry points for an adsorbate, or pore narrowing, where the pore mouth is significantly smaller than the micropore interior [142, 143]. In this case, the micropore mass balance takes the form of a linear driving force model:

$$\frac{\partial \bar{q}}{\partial t} = k_b(q^* - \bar{q}(t)) \tag{5.14}$$

where k_b is the barrier constant (a function of q_i^* and T) [22]. Solving the differential equation, the following analytical equation for the mass uptake when surface barrier resistance is dominant is found:

$$\frac{m_t}{m_\infty} = 1 - \exp(-k_b t) \tag{5.15}$$

The only unknown in the equation above is k_b, which can be determined with an experimental uptake curve. This model will be referred to as the surface barrier model.

Like the micropore model, the barrier constant, k_b, is known to be a function of the solid-phase loading. Accordingly, Darken's equation for the barrier constant can be written as:

$$\frac{\partial \ln(p)}{\partial \ln(q^*)} = \frac{k_b}{k_{b,0}} \tag{5.16}$$

where $k_{b,0}$ (a function of T) is the limiting surface barrier resistance at the pore mouth. In the case of a single-site Langmuir isotherm, Darken's equation for the barrier constant is:

$$\frac{k_b}{k_{b,0}} = \frac{1}{1-\theta} \tag{5.17}$$

Dual-resistance Model: The final model assumes that both the surface barrier and micropore contribute to the micropore resistance. This model describes a situation where the pore mouth is occluded and the micropore has a tortuous mean free path. The mass balance is the same as the micropore model (Eqn. 5.8) but the boundary condition at the surface changes to [139]:

$$\frac{3}{r_c} D_c \frac{\partial q(r_c)}{\partial r} = k_b(q^* - \bar{q}(t)) \tag{5.18}$$

Solving the partial differential equation yields an analytical solution for the mass uptake when both the surface barrier and micropore resistances contribute to the

mass transfer resistance:

$$\frac{m_t}{m_\infty} = 1 - \sum_{n=1}^{\infty} \frac{6L^2 \exp(-\beta_n^2 \frac{D_c}{r_c^2} t)}{\beta_n^2(\beta_n^2 + L(L-1))} \tag{5.19}$$

where β_n are the nonzero solutions to:

$$\beta_n \cot \beta_n + L - 1 = 0 \tag{5.20}$$

and

$$L = \frac{k_b r_c^2}{3D_c} \tag{5.21}$$

There are two unknowns: k_b and D_c/r_c^2, that are fitted to experimental data. This model will be referred to as the dual-resistance model [140]. In the limiting case of a very large pore diffusion constant or barrier constant, the dual-resistance model reduces to either a surface barrier model or micropore model [139].

In this work, the diffusion equations were discretized using a finite difference scheme to solve the micropore balance in tandem with concentration dependence equations, such as Darken's equation, for micropore and barrier diffusion (Eqns. 5.8, 5.12 and 5.16, respectively). The boundary conditions for the dual-resistance system (Eqns. 5.9 and 5.18) were used to model both resistances. The r-axis was discretized into 1000 points, and the resulting ordinary differential equations were solved using *ode15s* in MATLAB. This numerical scheme was used to model any dose outside of the linear diffusivity region (when diffusivity is a function of r) and to check Darken's equations against our data. This numerical scheme was validated with the analytical models provided above and data from the literature that are shown in the Supporting Information (Fig. D.3).

The experimental diffusivity was determined using all three analytical models. For these experiments, the diffusivity was determined by the sum of squared error between the experimental and model uptake curves:

$$J_2 = \sum_{j=1}^{n} \left[\left(\frac{m_t}{m_\infty} \right)_{\text{exp},j} - \left(\frac{m_t}{m_\infty} \right)_{\text{model},j} \right]^2 \tag{5.22}$$

The objective function J_2 was minimized in MATLAB using the *fmincon* optimization subroutine.

5.3.3 Kinetic Selectivity

The equilibrium selectivity, α_{E}, of a competitive mixture, A and B, is

$$\alpha_{\mathrm{E(A,B)}} = \frac{q_{\mathrm{A}}^*}{q_{\mathrm{B}}^*}\frac{y_{\mathrm{B}}}{y_{\mathrm{A}}} \tag{5.23}$$

where y is the gas phase mole fraction that is in equilibrium with the solid at a given temperature and total pressure [18]. To account for the differences in diffusivity between two gases, the kinetic selectivity, α_{K}, is defined as [133]:

$$\alpha_{\mathrm{K(A,B)}} = \frac{(m_t/m_\infty)_{\mathrm{A}}}{(m_t/m_\infty)_{\mathrm{B}}}\frac{q_{\mathrm{A}}^*}{q_{\mathrm{B}}^*}\frac{y_{\mathrm{B}}}{y_{\mathrm{A}}} \tag{5.24}$$

The kinetic selectivity approaches the equilibrium selectivity as time goes to infinity [133, 140]. These can be approximated as:

$$\alpha_{\mathrm{K(A,B)}} = \frac{K_{\mathrm{A}}}{K_{\mathrm{B}}}\sqrt{\frac{(D_{\mathrm{c},0})_{\mathrm{A}}}{(D_{\mathrm{c},0})_{\mathrm{B}}}} \tag{5.25}$$

for the pore time diffusional time constant and

$$\alpha_{\mathrm{K(A,B)}} = \frac{K_{\mathrm{A}}}{K_{\mathrm{B}}}\frac{(k_{\mathrm{b},0})_{\mathrm{A}}}{(k_{\mathrm{b},0})_{\mathrm{B}}} \tag{5.26}$$

for the barrier constant where K_{i} is the Henry constant of component i, $D_{\mathrm{c},0}$ is the limiting pore diffusion time constant and $k_{\mathrm{b},0}$ is the limiting barrier coefficient [22]. Limiting constants are for a given temperature as the loading approaches zero. However, Eqns. 5.25 and 5.26 can only be used if there is only a single mass transfer resistance in the system.

5.4 Results and Discussion

5.4.1 Single Component Equilibrium

The equilibrium data for N_2 and CH_4 on both Ba-RPZ and zeolite 4A were measured, and the results are reported in Fig. 5.1. The N_2 and CH_4 isotherms for zeolite 4A

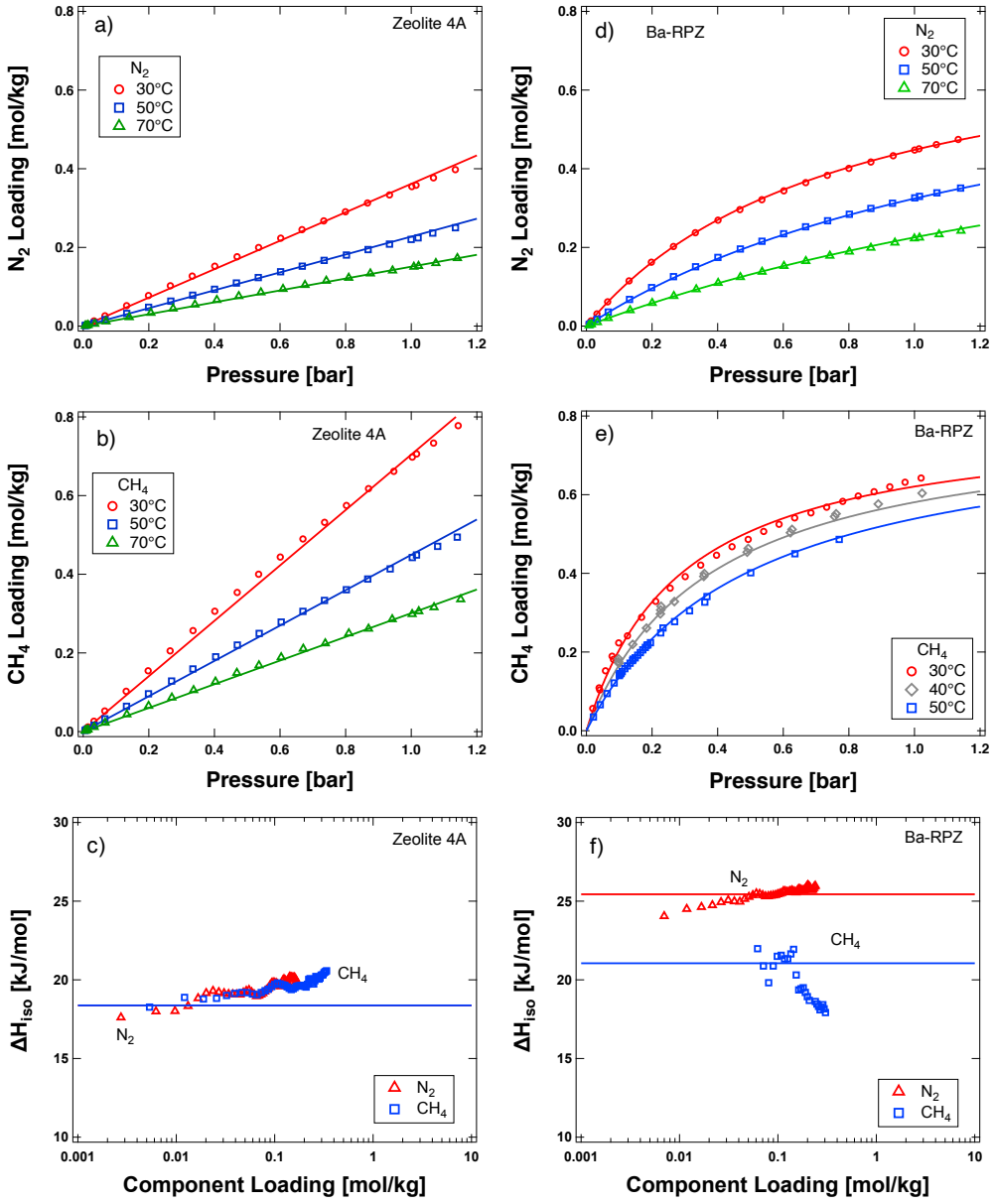

Figure 5.1: Single component adsorption equilibrium on zeolite 4A crystals for (**a**) N_2 and (**b**) CH_4 with linear isotherm fits and Ba-RPZ for (**d**) N_2 and (**e**) CH_4 with single-site Langmuir isotherm fits. Panels (**c**) and (**f**) show the isosteric heats of CH_4 and N_2 on zeolite 4A and Ba-RPZ, respectively. The isosteric heats are shown with the predictions from the isotherm models. Note that for zeolite 4A, the model predicts nearly identical heats of adsorption.

are essentially linear at all temperatures and pressures, which allows them to be reasonably approximated with a linear isotherm and eliminates the need to use the Darken correction in the calculation of diffusivity. Both the N_2 and CH_4 isotherms for Ba-RPZ, however, are distinctly non-linear but could reasonably be described using a single-site Langmuir equation. The isotherm parameters for both adsorbents are listed in Table 5.1. The nonlinearity of the N_2 and CH_4 isotherms on Ba-RPZ required the use of the Darken correction in the calculation of the diffusivity of the two species. Because the Darken correction requires that the saturation capacity for the adsorbents be known, the saturation capacity for N_2 and CH_4 on Ba-RPZ was measured using the HPVA. The saturation capacity for Ba-RPZ was found to be 0.8 mol/kg, and the associated high-pressure isotherms are provided in the Supporting Information (Fig. D.4).

Figure 5.1 also shows the calculated ΔH_{iso} values for the two gases on both adsorbents. These values were calculated from 30 to 70°C and, from vacuum up to 1.2 bar, for both N_2 and CH_4 using numerical derivatives of Eqn. 5.6 at given values of q_i^*. The isosteric heat of N_2 ($\approx$ 25 kJ/mol), and CH_4 ($\approx$ 20 kJ/mol), are fairly constant over the calculated loading ranges. Since there is not a significant change in isosteric heat, both CH_4 and N_2 see the Ba-RPZ surface as essentially energetically homogeneous [68, 69]. For zeolite 4A, the isosteric heats of both N_2 ($\approx$ 18 kJ/mol) and CH_4 ($\approx$ 18 kJ/mol) are essentially constant over the calculated loading ranges. It is interesting to note that the isosteric heats are the same for both gases on zeolite 4A.

5.4.2 Diffusion of N_2 and CH_4 in Zeolite 4A

Uptake curves for N_2 and CH_4 on zeolite 4A are shown in Fig. 5.2. The corresponding pressure curves, measured by the volumetric system, are given in the Supporting Information (Fig. D.5). Uptake curves for CH_4 were measured at 30, 40 and 50°C at $\approx$ 300 mbar pressure steps between limiting vacuum and 1.2 bar. Uptake curves for

Table 5.1: Isotherm parameters for single component N_2 and CH_4 equilibrium on Ba-RPZ and zeolite 4A.

Adsorbent	Gas	Model	q_b^{sat} [mol kg^{-1}]	b_0 [bar^{-1}]	$-\Delta H_{ads}$ [kJ mol^{-1}]	K_0 [mol bar^{-1} kg^{-1}]	$-\Delta H_{ads}$ [kJ mol^{-1}]
Ba-RPZ	CH_4	SSL	0.8000	8.13×10^{-4}	21.06	-	-
	N_2	SSL	0.8000	5.26×10^{-5}	25.44	-	-
Zeolite 4A	CH_4	Linear	-	-	-	4.80×10^{-4}	18.38
	N_2	Linear	-	-	-	2.01×10^{-4}	18.89

N_2 were measured at -20, -10 and 0°C for the same pressure range. The uptake curves are plotted versus square root time to better visualize the shape of the initial uptake [140]. This plot allows for a qualitative determination of the mass transfer resistances: either the initial uptake will be linear (when plotted versus square root time) for a micropore controlled system or sigmoidal for a system that experiences significant barrier resistance (either surface barrier or dual-resistance modelled systems) [139].

Uptake on zeolite 4A was studied as a reference to verify that the selected experimental conditions and equipment were able to reproduce uptake rates reported in the literature. Figure 5.2 shows the uptake of CH_4 as a function of square root time and demonstrates that, as anticipated, the initial CH_4 uptake is linear. This result confirms that the mass transfer resistance resides in the micropores of the adsorbent. This result is consistent with observations found in other studies [26, 139, 144]. Figure 5.2 also shows the measured N_2 uptake on zeolite 4A, which again reveals a micropore controlled system. The measured uptake curves for N_2 equilibrate significantly faster (by $\approx$ 300 s) compared to CH_4 on zeolite 4A. It should be noted that, in Fig. 5.2, for a particular gas at a given temperature, all of the individual uptake curves are virtually indistinguishable from each other. This result is characteristic of adsorption systems having linear isotherms.

The pore diffusion time constants fitted from the uptake curves are plotted in Fig. 5.3 as a function of the adsorbate loading. The data was fit to Darken's equation, and the results of the fit are shown alongside the experimental data. The results

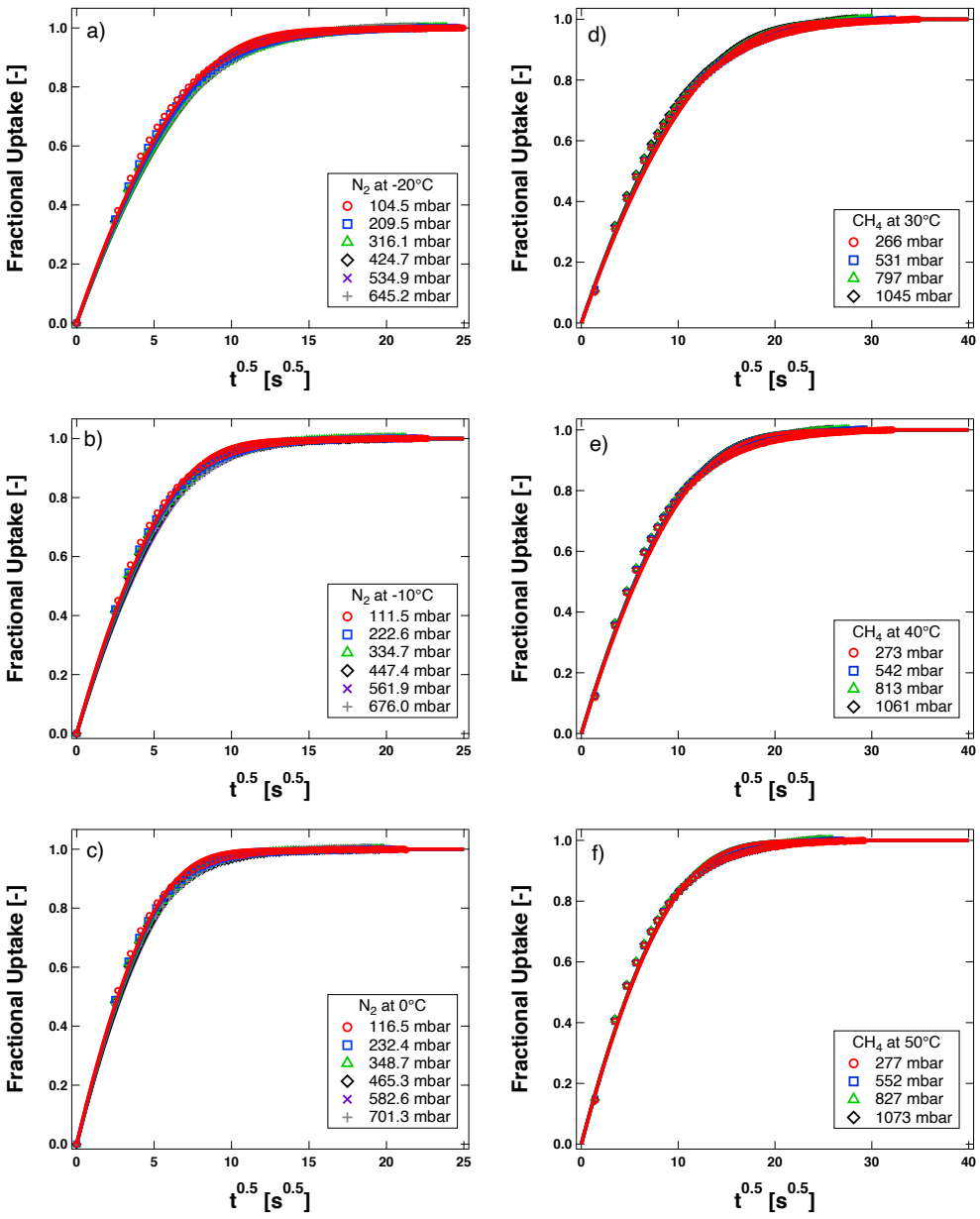

Figure 5.2: Constant diffusivity uptake curves for N_2 at (**a**) -20, (**b**) -10 and (**c**) 0°C and CH_4 at (**d**) 30, (**e**) 40 and (**f**) 50°C on zeolite 4A crystals. The lines show the micropore model fits.

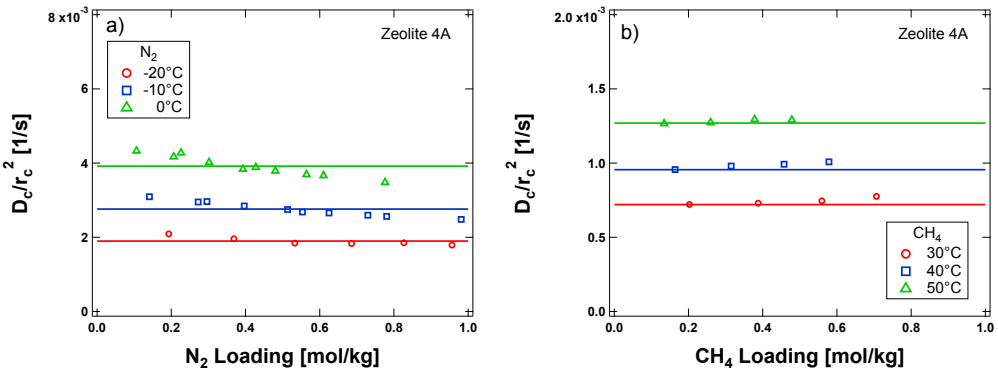

Figure 5.3: Pore diffusion time constants as a function of solid phase concentration for (**a**) N_2 and (**b**) CH_4 on zeolite 4A. The data is overlaid with predictions by Darken's equation (lines).

establish that, for zeolite 4A, the diffusion time constant does not change significantly as the adsorbate loading is increased. The limiting transport parameters are shown in Table 5.2 and were determined by calculating the average of $D_{c,i}$ over the loading range studied. A comparison of the measured limiting diffusivities and values from the literature is shown in Table 5.3. As seen in Table 5.3, our limiting diffusivities are comparable to what has been previously reported. The pore diffusional time constants for N_2 and CH_4 on zeolite 4A were nicely fit with the predictions from Darken's equation. Since a linear isotherm was used, Darken's equation reduces to $D_c = D_{c,0}$. This behavior is consistent with other studies [127, 145].

The temperature dependence of the diffusion parameters on zeolite 4A was determined at 30, 40 and 50°C for CH_4 and -20, -10 and 0°C for N_2 using an Arrhenius relationship in Fig. 5.4. The slope was determined from a plot of $\ln(D_{c,0}/r_c^2)$ versus $1/T$. This yields a straight line where the slope is $-E_{a,d}/R$, where $E_{a,d}$ is the micropore activation energy and R is the universal gas constant. The exponent of the intercept yields the Arrhenius prefactor. This model can be used in tandem with a concentration dependence model to predict gas uptake. Activation energies for N_2 and CH_4 on 4A are shown in Table 5.2. The activation energies are used with the following equation to estimate the limiting transport parameters as a function of

temperature:

$$D_{\mathrm{c},0} = D'_{\mathrm{c},0}\exp\left(\frac{-E_{a,\mathrm{d}}}{RT}\right) \tag{5.27}$$

The calculated activation energy of CH_4 (22.93 kJ/mol) and N_2 (20.86 kJ/mol) on zeolite 4A was determined to be within the range of previously reported values. A few papers have given this information, with $E_{a,\mathrm{d}}$ ranging from 18.66 to 26.78 kJ/mol for CH_4 and 19.00 to 23.43 kJ/mol for N_2 in the range of temperatures measured in this study [26, 127, 144, 145]. This data is also shown in Table 5.3 to compare our measurements to the literature. The agreement between the zeolite 4A data collected during this study and previous studies provides confidence that the instrumentation and techniques being used are capable of providing quantitative diffusivity data.

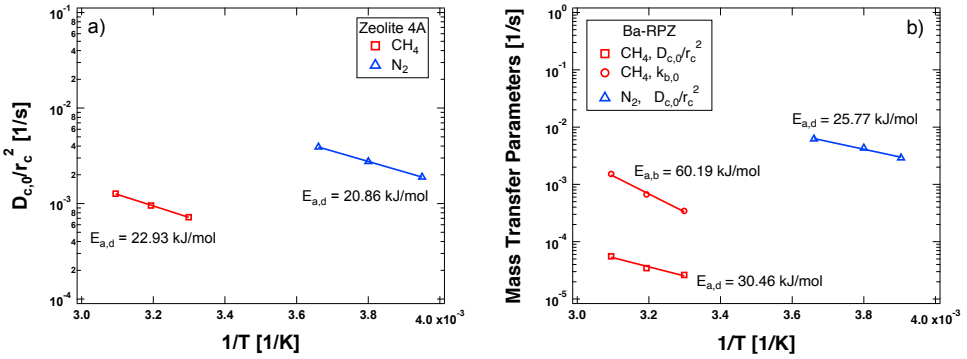

Figure 5.4: Activation energies of N_2 and CH_4 on (**a**) zeolite 4A and (**b**) Ba-RPZ.

Table 5.2: Limiting transport parameters and activation energies for N_2 and CH_4 on Ba-RPZ and zeolite 4A.

Adsorbent	Gas	T [°C]	$D_{c,0}/r_c^2$ [s^{-1}]	$k_{b,0}$ [s^{-1}]	$D'_{c,0}/r_c^2$ [s^{-1}]	$k'_{b,0}$ [s^{-1}]	$E_{a,d}$ [kJ/mol]	$E_{a,b}$ [kJ/mol]	β_b [-]
Zeolite 4A	N_2	-20	1.90×10^{-3}	-	38.15	-	20.86	-	-
		-10	2.76×10^{-3}	-					
		0	3.92×10^{-3}	-					
	CH_4	30	7.21×10^{-4}	-	6.418	-	22.93	-	-
		40	9.56×10^{-4}	-					
		50	1.27×10^{-3}	-					
Ba-RPZ	N_2	-17	2.09×10^{-3}	-	536.6	-	25.77	-	-
		-10	4.30×10^{-3}	-					
		0	6.20×10^{-3}	-					
	CH_4	30	2.63×10^{-5}	3.45×10^{-4}	4.498	7.869×10^{6}	30.46	60.19	5.223
		40	3.46×10^{-5}	6.69×10^{-4}					
		50	5.57×10^{-5}	1.52×10^{-3}					

Table 5.3: Comparison of limiting diffusivities and activation energies of N_2 and CH_4 on zeolite 4A with literature studies.

Gas	Adsorbent	Temperature Range [°C]	$D_{c,0}/r_c^2$ [s^{-1}]	$E_{a,d}$ [kJ/mol]	Citation
CH_4	Synthesized 4A crystals	0 – 50	1.50×10^{-4}	24.69	Yucel and Ruthven [26]
	Linde 4A pellets	50 – 200	6.06×10^{-4} to 5.92×10^{-3}	19.00	Haq and Ruthven [144]
	UOP 4A pellets	-20 – 10	9.99×10^{-5} to 3.80×10^{-4}	26.78	Cao *et al.* [145]
	UOP 4A pellets	0 – 20	8.90×10^{-4} to 1.80×10^{-3}	21.76	Ahn *et al.* [127]
	Arkema NK10AP Siliporite	30 – 50	7.21×10^{-4} to 1.27×10^{-3}	22.93	present study
N_2	Synthesized 4A crystals	-30 – 50	3.00×10^{-3}	23.43	Yucel and Ruthven [26]
	Linde 4A pellets	25 – 90	2.95×10^{-3} to 1.15×10^{-2}	18.66	Haq and Ruthven [144]
	UOP 4A pellets	-20 – 10	1.50×10^{-3} to 4.50×10^{-3}	22.18	Cao *et al.* [145]
	UOP 4A pellets	0 – 20	8.50×10^{-3} to 2.10×10^{-2}	19.25	Ahn *et al.* [127]
	Arkema NK10AP Siliporite	-20 – 0	1.90×10^{-3} to 3.92×10^{-3}	20.86	present study

5.4.3 Diffusion of N_2 and CH_4 in Ba-RPZ

The measurement of N_2 and CH_4 diffusivity in the titanosilicate Ba-RPZ was carried out in a manner similar to the one described for zeolite 4A. Certain adaptations were required to accommodate the differences in adsorptive characteristics between zeolite 4A and the novel titanosilicate. Similar experimental temperatures were used for the two adsorbates, but the non-linear isotherms for N_2 and CH_4 on Ba-RPZ required a specific dosing protocol. The dose quantity for either N_2 or CH_4 was selected to ensure that the change in adsorbate loading on the solid was maintained within a linear portion of the related isotherm. Selecting small dose quantities helps to ensure that the diffusivity rate for the adsorbate will be effectively constant throughout the course of the uptake experiment. The adsorbate doses selected to maintain a constant diffusivity are, herein, termed "small" doses. The curvature of the N_2 and CH_4 isotherms for Ba-RPZ also provides an opportunity to measure how the diffusivity changes across a non-linear portion of the isotherm. The dose quantities of adsorbate required to move across a broader section of the isotherm were correspondingly larger and are termed "large" doses. Uptake curves for CH_4 were measured at 30, 40 and 50°C at $\approx$ 15 to 300 mbar pressure steps between limiting vacuum and 1.2 bar. Uptake curves for N_2 were measured at -17, -10 and 0°C for the same pressure range.

Figure 5.5 provides the measured uptake profiles for N_2 and CH_4 on Ba-RPZ. The corresponding pressure curves are given in the Supporting Information (Fig. D.6). The diffusional resistance that N_2 experienced on Ba-RPZ was found to be comparable to that of zeolite 4A. As a result, it was necessary to measure the N_2 uptake curves at sub-ambient temperatures. It can be seen that even at -17°C the initial uptake for N_2 is linear, which indicates that the diffusional resistance is primarily microporous in nature. This result suggests that N_2 is able to access and diffuse through the Ba-RPZ structure without any special restriction to its movement.

In contrast to the N_2 uptake curves, the initial uptake curves for CH_4 adsorption

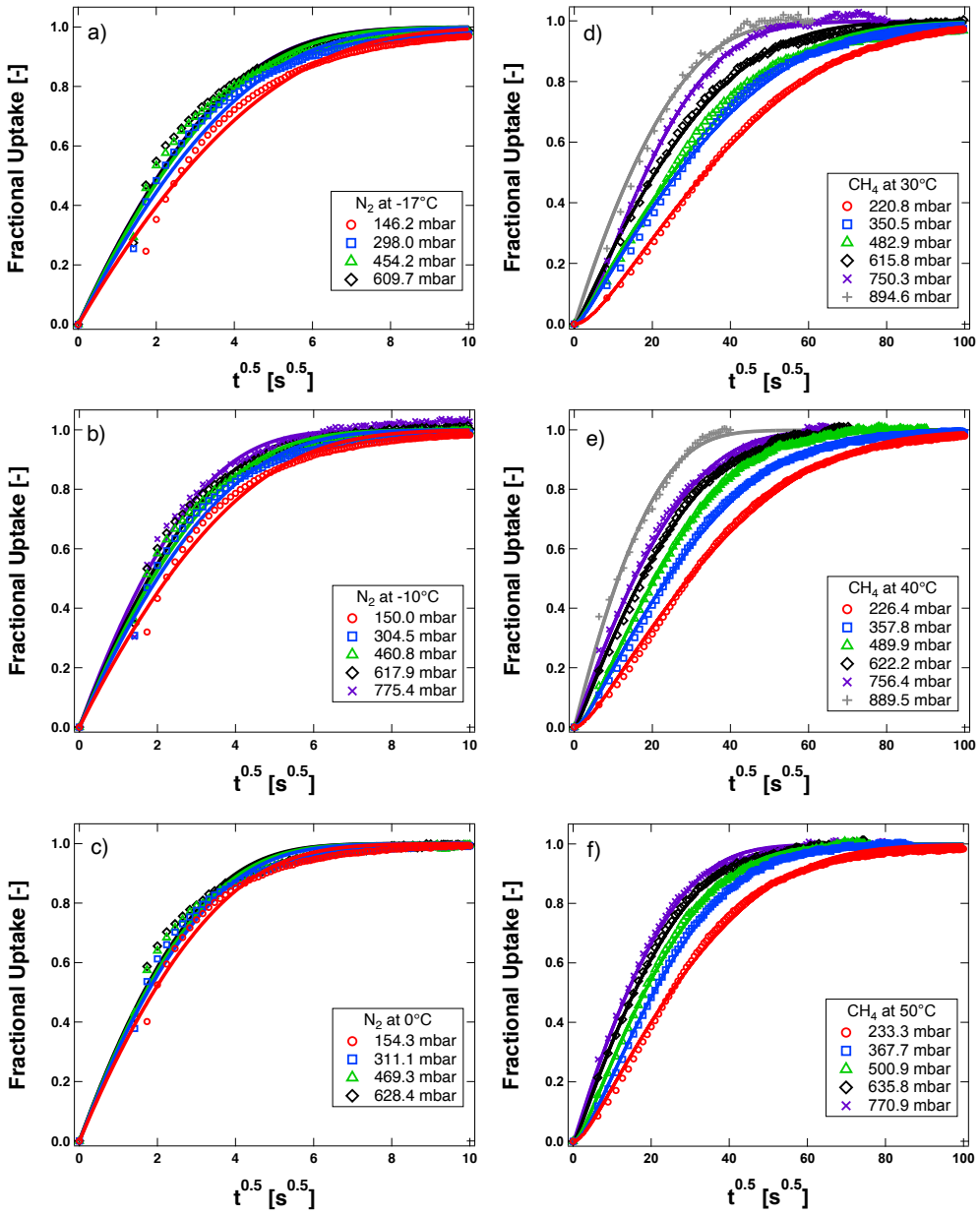

Figure 5.5: Small dose (constant diffusivity) uptake curves for N_2 at (**a**) -17, (**b**) -10 and (**c**) 0°C and CH_4 at (**d**) 30, (**e**) 40 and (**f**) 50°C on Ba-RPZ crystals. The lines show either the micropore or dual-resistance model fits for N_2 and CH_4, respectively.

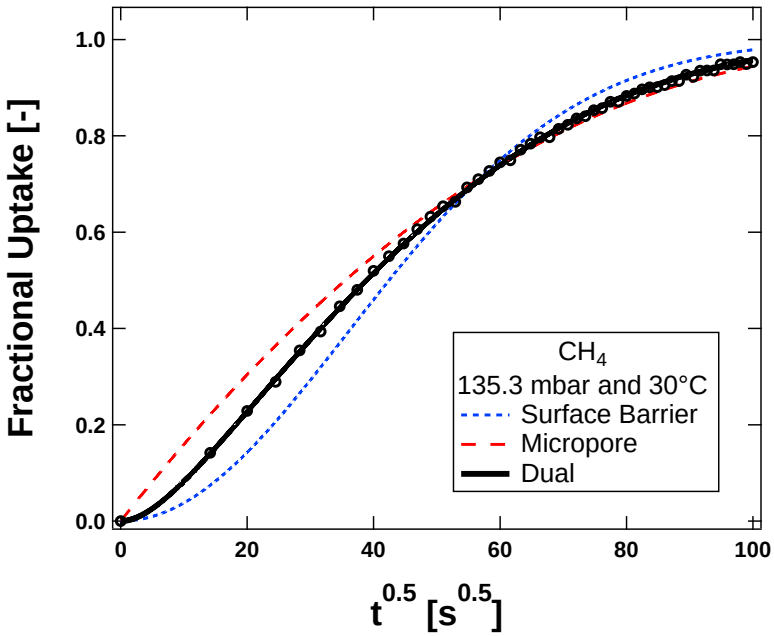

Figure 5.6: A small dose (constant diffusivity) uptake curve for CH_4 on Ba-RPZ crystals at 135.3 mbar and 30°C. The symbols denote the experimental data while the lines denote fits by various analytical uptake models.

display a sigmoidal shape, which indicates the presence of a barrier resistance. The presence of a barrier resistance indicates that the adsorbent features a constriction which is on the order of the molecular diameter of methane and serves to significantly impede the rate of diffusivity. The barrier resistance is most pronounced at the lowest temperature studied (30°C) and became less pronounced as the temperature increases.

The surface barrier model (Eqn. 5.14) alone was not able to accurately match the entire experimental uptake curves. While the initial sigmoidal shape could be accurately described using the surface barrier model, the model predicts CH_4 equilibrium sooner than what is experimentally observed. This result suggests that there is also a non-negligible transport resistance within the micropores. A hybrid model was constructed that incorporated both barrier and microporous elements, and it was found that this dual-resistance model was able to acceptably describe the experimental uptake profiles. A comparison of the three mathematical models (micropore,

barrier, and barrier plus micropore) with a typical experimental CH_4 uptake curve on Ba-RPZ is shown in Fig. 5.6. The dual-resistance model was used to describe each uptake curve of CH_4 (k_b and D_c/r_c^2 values were fitted) while the micropore model was used to describe each uptake curve of N_2 (D_c/r_c^2 values were fitted).

Figure 5.7 shows the concentration dependence (in fractional loading $\theta_i = q_i^*/q_{b,i}^{sat}$) of CH_4 and N_2 diffusion on Ba-RPZ. It is worth noting that this figure contains all of the diffusivity data collected, including repeated experiments. The micropore diffusion time constants for both N_2 and CH_4 on Ba-RPZ were in good agreement with the predictions from Darken's equation. The barrier constant was modelled using an empirical equation:

$$\frac{k_b}{k_{b,0}} = \exp(\beta_b \theta) \tag{5.28}$$

where $\beta_b = 5.223$ was fitted to the experimental data. Figure 5.7(**c**) shows both Darken's prediction and the empirical fit for the barrier constant. While the Darken equation could be forced to follow the barrier constant at low fractional loadings, no parameters were found that would allow the Darken equation to describe the barrier constant trend across the full range of fractional loadings. The trend in the barrier constant as a function of CH_4 fractional loading indicates that the rate of diffusion of methane in the barrier increases faster than the rate of change in the chemical potential at the sieve surface. As the fractional loading increases, the rate of diffusivity across the barrier increases and, at a certain point, the barrier diffusivity rate is so high that a sigmoidal shape is no longer evident in the uptake curves. The absence of the sigmoidal shape signals that the contribution of the barrier resistance has become negligible and, beyond this point, the diffusion becomes dominated by micropore resistance. As a result, the barrier constant calculations are only included up to $\theta_{CH_4} = 0.5$. A sensitivity analysis is given in the Supporting Information (Fig. D.7) to show that at $\theta_{CH_4} > 0.5$, the calculation of the barrier constant fitting becomes unreliable because any suitably large k_b can be used to fit the uptake curve.

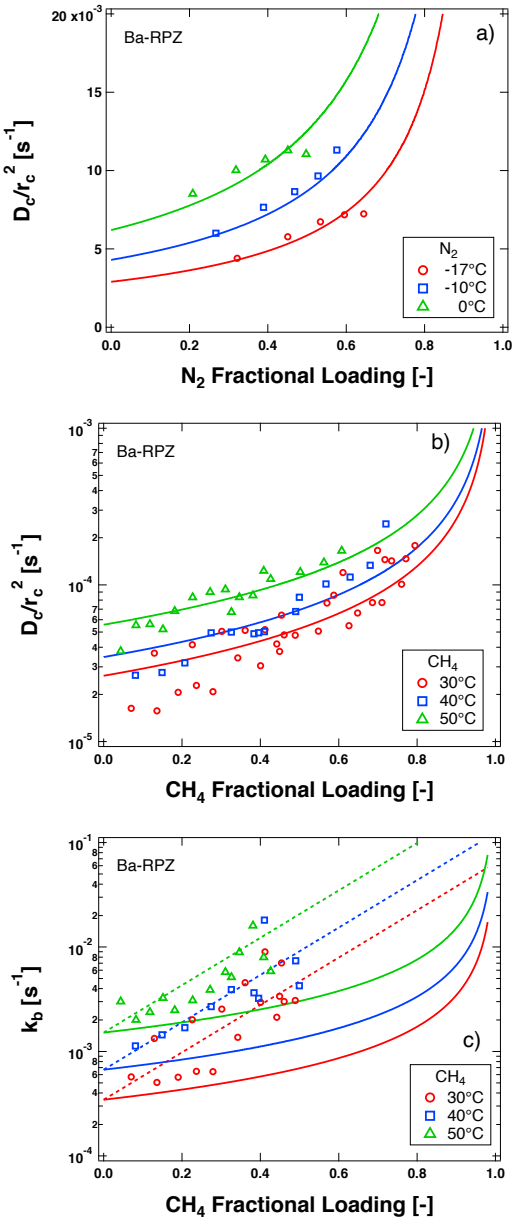

Figure 5.7: Diffusional constants as a function of solid phase concentration for (**a**) N_2 and (**b**, **c**) CH_4 on Ba-RPZ. The solid lines are Darken predictions and the dashed line is the empirical barrier model prediction.

The calculated limiting transport parameters are shown in Table 5.2 and were determined at a given temperature by minimizing the squared error between all collected data with an assumed concentration dependence model, such as Darken's equation. The following objective functions were used for the micropore and surface-barrier constants, respectively:

$$J_3 = \sum_{j=1}^{n} \left[\left(\log_{10}\left(\frac{D_c}{r_c^2} \right) \right)_{\text{exp},j} - \left(\log_{10}\left(\frac{D_c}{r_c^2} \right) \right)_{\text{model},j} \right]^2 \tag{5.29}$$

$$J_4 = \sum_{j=1}^{n} \left[\left(\log_{10}(k_b) \right)_{\text{exp},j} - \left(\log_{10}(k_b) \right)_{\text{model},j} \right]^2 \tag{5.30}$$

A logarithm was used to yield a better estimate of the limiting diffusivities at low values of θ. The limiting diffusivities for CH_4 were used to determine the ratio $k_{b,0}/(D_{c,0}/r_c^2)$ as a function of temperature. This relation is expected to be constant if the surface barrier resistance is due to pore blocking (limited access to the crystal but facile diffusion within it), while it will not be constant if the surface barrier resistance is due to narrowing at the pore mouth (pore entrances approach the molecular diameter of the adsorbate) [142]. The ratio of the barrier resistance to the micropore diffusivity (shown in the Supporting Information in Fig. D.8) increases with temperature, indicating that surface barrier resistance in Ba-RPZ is consistent with a narrowing of the pore mouth relative to the micropore interior. It should be noted that neither the data nor the model can determine whether the barrier resistance exists at the surface of the crystals or within the structure of the molecular sieve (an internal barrier) [146].

The temperature dependence of the CH_4 and N_2 diffusivities on Ba-RPZ was calculated in the same way as was described for zeolite 4A and are likewise presented in Fig. 5.4. For Ba-RPZ, the Arrhenius relationship for both the micropore and barrier resistances were plotted to determine the activation energies from either $\ln(k_{b,0})$ or $\ln(D_{c,0}/r_c^2)$ versus $1/T$. The calculated activation energies are shown in Table 5.2. The activation energies are used with Eqn. 5.27 and the following analogue for the

barrier resistance to estimate the limiting diffusivities as a function of temperature:

$$k_{\mathrm{b},0} = k'_{\mathrm{b},0}\exp\left(\frac{-E_{a,\mathrm{b}}}{RT}\right) \tag{5.31}$$

The micropore activation energies for CH_4 on Ba-RPZ was calculated to be $E_{a,\mathrm{d}} = 30.46$ kJ/mol and the barrier resistance activation energy was calculated to be $E_{a,\mathrm{b}} = 60.19$ kJ/mol. For N_2, a micropore diffusion activation energy was calculated to be $E_{a,\mathrm{d}} = 25.77$ kJ/mol. The activation energies for both N_2 and CH_4 on Ba-RPZ are significantly larger than those found for zeolite 4A, which will make the diffusion of N_2 and CH_4 in Ba-RPZ a strong function of temperature. The difference in activation energy between the barrier and micropore ($E_{a,\mathrm{b}} - E_{a,\mathrm{d}}$) is ≈ 30 kJ/mol and is consistent with the observation of an internal barrier for n-butane in silicalite [146].

5.4.4 Model Validation

The sigmoidal shape presented by the methane uptake experiments on Ba-RPZ signifies the presence of a restriction in the molecular sieve that has a significant influence on the diffusion of CH_4. The uptake data were described using a dual-resistance model, which assumed that two independent resistances (barrier and micropore) are present in the molecular sieve. The proposed adsorption mechanism for Ba-RPZ, however, describes a crystalline system having a highly uniform channel system incorporating a series of halogen obstructions [138]. While the mathematical construct of the dual-resistance model used in this work may not perfectly reflect the adsorption mechanism proposed for Ba-RPZ, such incongruity does not infer that the model cannot accurately predict the adsorptive behavior of the sieve. Being able to accurately describe the diffusion behavior of a molecular sieve mathematically is a critical step in being able to predict the performance of that adsorbent in selected adsorptive separations.

A series of large dose experiments were performed at 30, 40 and 50°C to understand whether the dual-resistance model could accurately predict complex diffusion

behavior. As was previously mentioned, diffusivity is a function of solid loading, and so a large dose creates a non-linear change in loading to deliberately generate a constantly changing diffusivity. The associated uptake data can thus be used to validate whether the diffusion model (which was constructed from the small dose, constant-diffusivity experiments) can successfully predict complex diffusion behavior. The full numerical solution to Eqn. 5.8 is required along with an appropriate concentration dependence model to describe the large-dose experiment. The resulting concentration-dependent dual-resistance model is expected to be able to predict the changing diffusivity behavior evident in the large dose experiments.

The results from the large dose experiments are shown in Fig. 5.8. The central curve in black in Fig. 5.8(**a**) represents an experiment carried out at 30°C where a single dose of CH_4 was used to move the equilibration pressure from limiting vacuum to 211.1 mbar. The small dose (constant diffusivity) experiments that bound this large dose experiment are also presented in Fig. 5.8(**a**). The lower pressure small dose from 0 to 19.2 mbar (which resides in the limiting diffusivity region) is shown in red and the higher pressure small dose, from 176.6 to 218.3 mbar, is shown in blue. The large dose curve initially follows the red, limiting diffusion curve until ≈ 30 $s^{0.5}$ where the curve inflects, signifying that diffusion is becoming more rapid. As time proceeds, the profile of the large dose curve mirrors that of the blue, higher pressure small dose. The concentration-dependent dual-resistance model was used to describe all three curves, and the results are shown as solid lines in the corresponding color. The concentration-dependent dual-resistance model generally fits the large dose data in Fig. 5.8(**a**) well, although it does predict a more rapid uptake and trend to equilibrium compared to the experimental data. The independent, small dose curves were also described using the concentration-dependent dual-resistance model, and the results show that the model can accurately describe the uptake curve for the constant diffusivity experiments as well. The same experiments and calculations were carried out for CH_4 on Ba-RPZ at 40 and 50°C and the results are provided

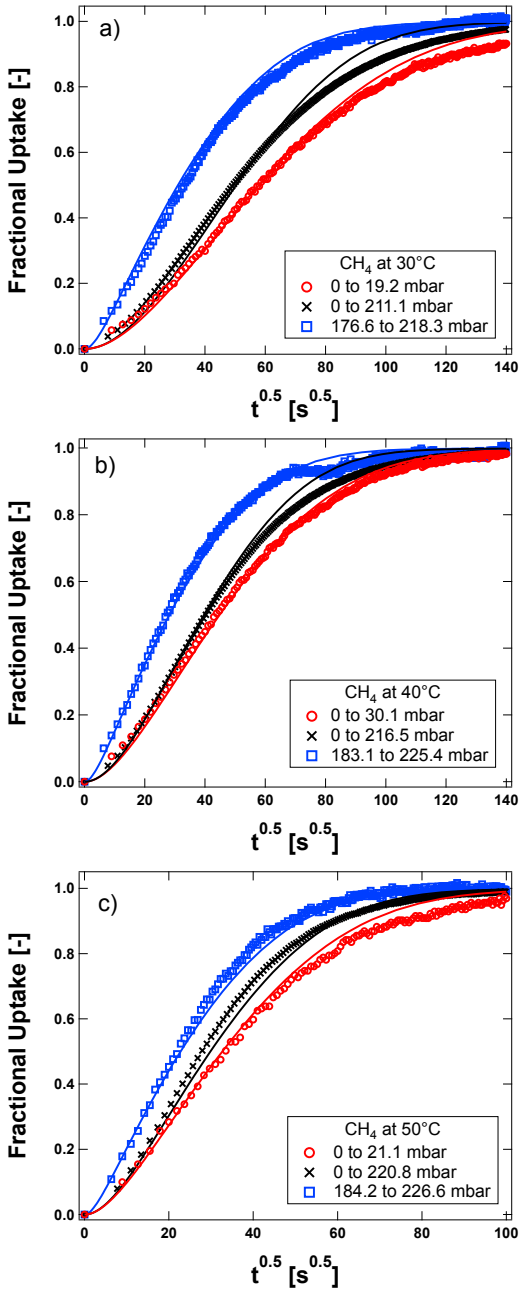

Figure 5.8: Large dose (non-constant diffusivity) uptake curves for CH_4 on Ba-RPZ crystals at (**a**) 30, (**b**) 40 and (**c**) 50°C. The symbols denote the experimental data while the lines denote the model prediction. Constant diffusivity uptake experiments are shown in red and blue, while large dose experiments are shown in black.

in Fig. 5.8(**b**) and 5.8(**c**), respectively. As was observed for the experiment at 30°C, the large dose curve follows the limiting diffusion curve at short times and the higher pressure constant diffusivity curve closer to equilibrium. As was seen with the 30°C data, the concentration-dependent dual-resistance model provided a good description of the experimental large dose experiments, although some discrepancy is noted. Likewise, the concentration-dependent dual-resistance model was able to accurately describe the independent constant diffusivity experiments that bounded each large-dose experiment at sequentially higher temperatures. The concentration-dependent dual-resistance model can thus be used to accurately predict complex diffusion behavior across both temperature and pressure for Ba-RPZ.

5.4.5 Kinetic Selectivity

Having established the diffusion mechanisms and the equilibrium, the kinetic selectivity for a N_2/CH_4 gas mixture can be calculated. The kinetic selectivities for zeolite 4A, Sr-ETS-4 and Ba-RPZ were determined at 10°C for an 80/20 mol% mixture of CH_4/N_2 from zero loading to 1 bar. This temperature was selected because comparable data for Sr-ETS-4 was available at this temperature, and because 10°C represents only a mild extrapolation for measured data for N_2 and CH_4. The full solution for each individual adsorbate uptake was solved, as per Eqn. 5.24, to determine the kinetic selectivity as a function of time for all adsorbents. The full numerical solution of the micropore and dual-resistance models assumed that the diffusivities followed a concentration-dependence model (found and validated in the previous sections) and that there is no equilibrium competition between CH_4 and N_2. For CH_4 on Ba-RPZ, both the barrier and micropore resistances were accounted for when determining the kinetic selectivity. Figure 5.9(**a**) demonstrates that, at low contact times, the kinetic selectivity on Ba-RPZ is greater than 1000. This selectivity is generated almost exclusively by the barrier resistance that Ba-RPZ imposes on CH_4 because N_2, by contrast, is effectively equilibrium controlled at 10°C. As the contact time proceeds,

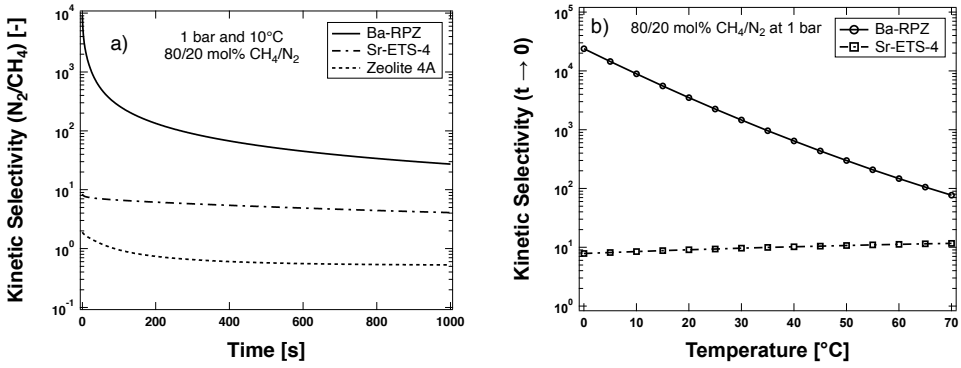

Figure 5.9: The (**a**) kinetic selectivity for an 80/20 mol% mixture of CH_4/N_2 at 10°C on zeolite 4A, Ba-RPZ and Sr-ETS-4. The (**b**) limiting kinetic selectivity of both Ba-RPZ and Sr-ETS-4 as a function of temperature. Sr-ETS-4 data was calculated from Marathe *et al.* [134].

the N_2/CH_4 selectivity decreases as the kinetic selectivity collapses toward the equilibrium selectivity. It should be noted that even after a contact time of 1000s Ba-RPZ has not reached equilibrium.

The calculated kinetic selectivities for zeolite 4A and Sr-ETS-4 are also shown in Fig. 5.9(**a**). The rapid decrease in selectivity noted at short times for zeolite 4A is not due to a barrier resistance because the diffusion behavior in this molecular sieve is micropore-controlled for both N_2 and CH_4. The results reflect that zeolite 4A loses its kinetic selectivity as it rapidly approaches equilibrium at around 300 s. The Sr-ETS-4 equilibrium and kinetic data used in the calculation of the kinetic selectivity were calculated from Marathe *et al.* [134]. The diffusion of N_2 and CH_4 in Sr-ETS-4 has been demonstrated to be solely micropore controlled. The kinetic selectivity for Sr-ETS-4 does not display the barrier resistance influence seen with Ba-RPZ, nor does it reach equilibrium as quickly as zeolite 4A. These results imply that the effective pore size of Sr-ETS-4 likely falls somewhere between 4A and Ba-RPZ. While the calculated micropore diffusion time constants for the two titanosilicates are comparable [133] the presence of the barrier resistance to CH_4 in Ba-RPZ distinguishes this adsorbent and gives rise to its exceptional kinetic selectivity.

Figure 5.9(**b**) shows the limiting kinetic selectivity calculated for Ba-RPZ and Sr-

ETS-4 using an 80/20 mol% mixture of CH_4/N_2 at 1 bar at temperatures between 0 and 70°C. The limiting kinetic selectivity is defined here as the kinetic selectivity value at $t \rightarrow 0$ s. The trend displayed for Ba-RPZ shows that the limiting kinetic selectivity progressively decreases as temperature increases. This trend is governed by methane diffusion in the sieve because the activation energy for diffusion in Ba-RPZ is much greater for CH_4 than it is for N_2. Sr-ETS-4, by contrast, demonstrates a limiting kinetic selectivity that increases slightly with temperature.

The diffusivity behavior that Ba-RPZ displays toward N_2 and CH_4 is unique. The presence of a barrier resistance for methane and the relatively free diffusion of N_2 suggests that the mode of transport for these two gases within the pores and channels of Ba-RPZ is unlike similar small-pored molecular sieves. The complex diffusivity behavior can be accurately described using existing diffusion models, and the remarkable kinetic selectivity displayed by the molecular sieve seems to make it an ideal candidate for addressing nitrogen contamination in natural gas wells.

5.5 Conclusions

A detailed study of the adsorption of N_2 and CH_4 on Ba-RPZ was completed. The thermodynamics of adsorption were determined, and the diffusivity rates for the two adsorbates were measured. It was found that, under the conditions explored, N_2 diffusion is microporous in nature and encounters little resistance to entering and diffusing through the Ba-RPZ framework. This was not the case for methane, where it was found that the Ba-RPZ framework exerts a strong barrier resistance toward CH_4 which significantly impedes the diffusion into or through the adsorbent crystals. The complex diffusion behavior of CH_4 could be described using a concentration-dependent dual-resistance diffusion model which incorporated both barrier and microporous diffusion elements. The model was challenged, experimentally, using large dose methane uptake experiments, and it was found that the model was able to successfully describe the complex transition from barrier-limited diffusion to micropore-

limited diffusion across a range of temperatures. The exact nature of the origin of the barrier resistance, i.e., external or internal barrier, could not be firmly established. Nevertheless, it was found Ba-RPZ can offer kinetic selectivities that can be orders of magnitude greater than current benchmark material for CH_4 upgrading, namely, Sr-ETS-4. The barrier resistance contributes significantly to this selectivity improvement. The results here suggest that Ba-RPZ could be a potential candidate for CH_4 upgrading.

Chapter 6

Qualitative kinetic dynamic column breakthrough on milligram quantities of barium-exchanged reduced pore zorite (Ba-RPZ) and zeolite 4A

6.1 Introduction

Dynamic column breakthrough (DCB) is a technique that is able to measure single and multicomponent adsorbate-adsorbent equilibrium and kinetics. Specifically, the retention time of the breakthrough curve contains information about adsorbent equilibrium, and the spread of the breakthrough curve contains kinetic information [30]. Well designed breakthrough experiments can shed light on possible mass transport mechanisms and yield quantitative diffusivities [94]. These experiments follow many of the same restrictions that a constant volume uptake experiment must follow [142]. The main restrictions being that the system must remain isothermal, and the change in concentration must be along a linear chord of the isotherm. These are to ensure that the diffusivity remains constant throughout the breakthrough experiment. Due to these design considerations, most studies involving kinetic DCB experiments are performed in the limiting region [27]. Operating in the limiting region also ensures that the packed bed will remain as isothermal as possible.

Performing qualitative, and quantitative, dynamic breakthrough experiments for gas-phase diffusion are challenging due to the amount of heat that is released during adsorption. Even for weakly adsorbing species, such as N_2 on zeolite 13X, a measurable amount of heat will be released in a traditional-scale packed column (10s to 100s of grams) [2]. This change in temperature will influence the measured diffusivity. The two most common methods to obtain a diffusivity from a packed bed response, either the method proposed by Haynes and Sarma [147] or by fitting the spread of the curve with a breakthrough simulator [30], both require the system to be isothermal. This is usually achieved by running dilute experiments [27]. However, this heat is proportional to the mass of the adsorbent. If the mass of adsorbent is reduced, the quantity of heat released is also reduced. This is true for zero-length column (ZLC) experiments, where typically $5-10$ mg of adsorbent is utilized to measure gas diffusion [104]. Brandani and Mangano explain that minimizing the mass of adsorbent is particularly advantageous for a strongly adsorbing system, where a large amount of heat would be otherwise released [104]. This suggests that the microscale dynamic column breakthrough (μDCB) apparatus, detailed in Chapter 4, may be a useful technique to measure gas diffusion in small-pore adsorbents.

The aim of this study is to measure the multicomponent CH_4/N_2 diffusivities on zeolite 4A and Ba-RPZ using a microscale dynamic column breakthrough (μDCB) apparatus. This technique is being used in part since very little heat will be generated from the milligram-sized samples. A series of unary and binary CH_4/N_2 adsorption and desorption breakthrough experiments are performed for a range of compositions and temperature. These experiments should highlight differences in diffusivity through the shape of the breakthrough curve. Unary equilibrium data is also collected for N_2 with the μDCB apparatus to ensure the integrity of zeolite 4A and Ba-RPZ samples. These qualitative breakthrough trends will be compared with the quantitative data measured in a previous Chapter 5 (and publication [5]).

6.2 Materials and Methods

The Ba-RPZ and zeolite 4A samples are the same as a previous study [5]. A more detailed description of these materials can be found in our previous publication. Ba-RPZ crystals were obtained from Extraordinary Adsorbents Inc. (Edmonton, Alberta, Canada). The crystalline Ba-RPZ powder contains no binder. The zeolite 4A sample is also a crystalline powder and was provided by Arkema (NK 10 AP or "Siliporite"). All gases in this study (99.97% CH_4, 99.999% N_2 and 99.999% He) were obtained from Linde Canada. Single component adsorption isotherms for N_2 were measured using volumetry and microscale dynamic column breakthrough.

6.2.1 Volumetry

Volumetric isotherms for N_2 were measured with a Micromeritics ASAP 2020C (Norcross, GA, USA). The Micromeritics system was used to measure static adsorption equilibrium between 1 mbar to 1.2 bar. The system has a loading accuracy of 0.15% of the reading and a pressure accuracy of 1.3×10^{-7} mbar. A sample mass of 252.8 mg (Ba-RPZ) or 332.0 mg (zeolite 4A) was used for these experiments. Prior to each experiment, in both the low and high-pressure systems, Ba-RPZ and zeolite 4A were activated for 12 hours under vacuum (5 μbar) at 250°C (Ba-RPZ) or 350°C (zeolite 4A).

6.2.2 Microscale Dynamic Column Breakthrough

The microscale dynamic column breakthrough (μDCB) apparatus in this study is the same apparatus as described in Chapter 4. A more detailed description of the instrument is found in Chapter 4, along with a schematic of the apparatus in Fig. 4.1. For this study, two VCR columns were packed, one with crystalline Ba-RPZ (131.6 mg) and another with crystalline zeolite 4A (152.9 mg). These sample sizes are smaller (by approx. $50 - 100$ mg) than in the previous equilibrium-based study. These smaller sample sizes were used to minimize heat-effects and the temperature

increase due to adsorption. The adsorbent was very lightly packed into the VCR fittings to ensure a small pressure-drop across the bed (< 0.70 kPa). One minor modification was made to the apparatus to measure the very long transients inherent to kinetic experiments. Specifically, a longer length of 1/4" tubing was used for unary and binary CH_4 experiments. This tubing was approximately 10 meters in length. The original 2 meter length was used for unary N_2 experiments.

A thermal activation was performed after each μDCB experiment involving CH_4 (either CH_4/He or CH_4/N_2) to ensure a clean bed for the next experiment. This was due to the increased mass transfer resistance for CH_4 in both materials, which would require a long desorption with an inert gas. For unary N_2 experiments, a thermal activation was performed once, before the experimental campaign.

The same nomenclature will be used as in Chapter 4. A "blank" experiment is a breakthrough experiment performed in an empty VCR fitting. A "composite" experiment is a breakthrough experiment in a VCR fitting packed with an adsorbent of interest. The pycnometrically corrected blank ("Blank − Pync") is the extra-solid blank response; this response removes the volume occupied by the solid adsorbent in the blank experiment.

6.3 Mass Balances and Error Analysis

6.3.1 Experimental Mass Balances

The equilibrium loading can be calculated from a dynamic column breakthrough experiment with an integral mass balance. For an adsorption breakthrough experiment, the following integral balance is found:

$$n_{i,\text{acc}} = n_{i,\text{in}} - n_{i,\text{out}} \tag{6.1}$$

The accumulated moles, $n_{i,\text{acc}}$, is the difference between the moles entering, $n_{i,\text{in}}$, and leaving, $n_{i,\text{out}}$, the column. Accumulation is found in both the solid (adsorbed) and the fluid phases. Assuming that the ideal gas law is valid, the individual terms can

be expanded and rearranged as:

$$m_{\text{ads}}q_i^* + \frac{y_{i,\text{in}}P}{RT}\left(V_{\text{blank}} - m_{\text{ads}}\rho_{\text{sk}}\right) = \frac{y_{i,\text{in}}PQ_{\text{in}}}{RT}\int_0^{t_{\text{ads}}}\left(1 - \frac{y_i(t)Q(t)}{y_{i,\text{in}}Q_{\text{in}}}\right)dt \qquad (6.2)$$

In Eqn. 6.2, y_i is the mole fraction of gas i, P is the total pressure, Q is the gas flowrate, T is the temperature, R is the universal gas constant, ρ_{sk} is the pycnometric (or skeletal) density of the adsorbent, and q_i^* is the bulk equilibrium loading of gas i. V_{blank} is the blank volume, which includes the extra-column volume plus the fluid and adsorbent volume inside the column. Solving Eqn. 6.2 for q_i^* after the experiment reaches equilibrium (t_{ads}) yields the equilibrium loading for the adsorbate for the particular set of experimental conditions ($y_{i,\text{in}}$, T and P) [67]. Using this mass balance, one equilibrium point is found per breakthrough.

For a desorption experiment with an inert feed, the mass balance is:

$$n_{i,\text{acc}} = n_{i,\text{out}} \qquad (6.3)$$

At the end of a desorption experiment the individual terms can be written as:

$$m_{\text{ads}}q_i^* + \frac{y_{i,\text{init}}P}{RT}\left(V_{\text{blank}} - m_{\text{ads}}\rho_{\text{sk}}\right) = \frac{y_{i,\text{init}}PQ_{\text{init}}}{RT}\int_0^{t_{\text{des}}}\left(\frac{y_i(t)Q(t)}{y_{i,\text{init}}Q_{\text{init}}}\right)dt \qquad (6.4)$$

where q_i^* is the initial solid phase loading (at $t = 0$). For a desorption experiment, it is important to wait until the column is in equilibrium with the desired feed before flow is switched to the inert sweep gas. This means that the inlet composition and flow are observed at the outlet, before the inlet gas is switched to an inert sweep gas. Note that in a desorption experiment, the calculated equilibrium is the initial ("init") condition of the bed, not the final condition as in an adsorption experiment. Again, only one equilibrium point is found per desorption breakthrough.

6.3.2 Error Analysis

Error analysis was performed to determine the significance of the calculated equilibrium data. The uncertainty associated with a variable γ in a function f, δf, is given by:

$$\delta f = \left| \left(\frac{\partial f}{\partial \gamma} \right) \delta \gamma \right| \tag{6.5}$$

where $\delta\gamma$ is the uncertainty of γ.

There are eight variables in the μDCB apparatus that add to the uncertainty in the calculation of the equilibrium loading (q^*): m_{ads}, T, P, ρ_{sk}, y_{in}, Q_{in}, $y(t)$ and $Q(t)$. The measurement of both y and Q at the inlet and outlet are split into two separate sets of variables since they are measured with different instruments. The sum of all of these errors yields the total system (plus/minus) error for the equilibrium loading:

$$\delta q^* = \sum_i \left| \left(\frac{\partial q^*}{\partial \gamma_i} \right) \delta \gamma_i \right| \tag{6.6}$$

The uncertainties associated with these terms were reported in a previous chapter (Table 4.1). The error bars shown in all figures with μDCB equilibrium loading calculations are from these error propagation calculations.

6.4 Results and Discussion

6.4.1 Single Component N_2 Breakthrough Experiments

Single component adsorption and desorption breakthrough experiments were performed first with mixtures of N_2/He on both zeolite 4A and Ba-RPZ, since N_2 has a relatively fast diffusivity on both of these materials. These experiments were also performed to check consistency with independently collected equilibrium data. These breakthrough experiments were performed at approximately 0.96 bar at 30, 40 and 50°C. All experiments were performed at 3.5 sccm (standard conditions are: $T_{\text{std}} = 0$°C and $P_{\text{std}} = 1.01325$ bar).

The results for N_2/He adsorption and desorption breakthrough experiments on zeolite 4A are shown in Fig. 6.1. Similar to Chapter 4, the blank measurement is shown in black, the pycnometrically corrected blank is shown in blue and the composite response is shown in red. Helium was used as a sweep gas and diluent for

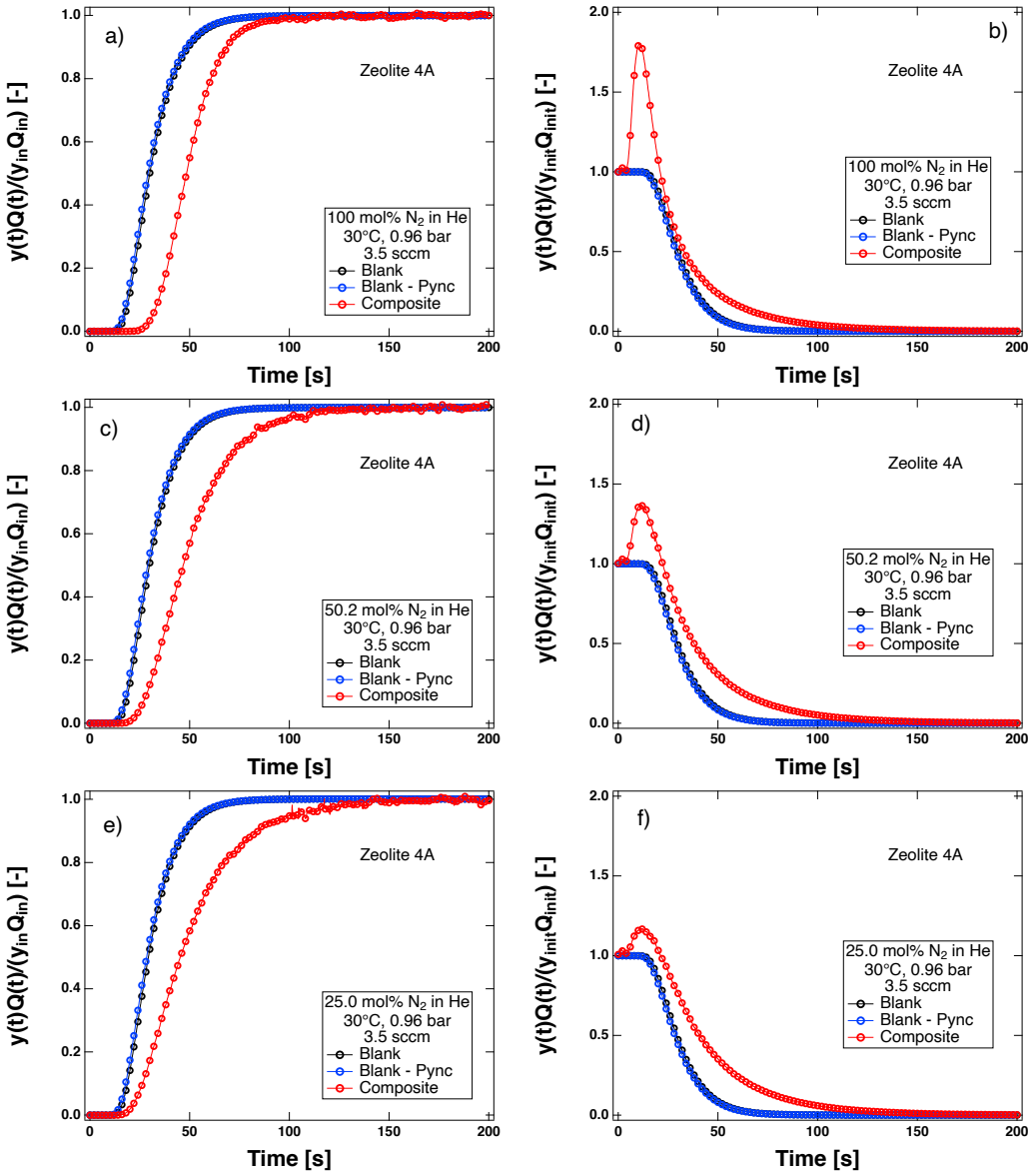

Figure 6.1: Single-component N_2/He adsorption (left) and desorption (right) breakthrough curves at 0.96 bar and 30°C on zeolite 4A. Panels (**a**) and (**b**) are for 100 mol% N_2, (**c**) and (**d**) are for 50.2 mol% N_2/He, and (**e**) and (**f**) are for 24.9 mol% N_2/He. The reference gas was He for these experiments. Every twentieth point is shown as a marker.

all single component breakthrough experiments. As seen in Fig. 6.1, the composite response always exits later than the pycnometrically corrected blank; this signifies that there is some adsorption of N_2 into zeolite 4A. The area between the composite (red) and pycnometrically corrected blank (blue) is proportional to the equilibrium loading of N_2 at a particular set of conditions.

As in Chapter 4, the adsorption and desorption breakthrough curves are plotted as a normalized molar flow ($y(t)Q(t)/[y_{\text{in}}Q_{\text{in}}]$), which is a combination of the effluent N_2 mole fraction, $y(t)$, and flow curves, $Q(t)$, divided by the inlet (or initial for desorption) mole fraction (y_{in}) and flow (Q_{in}). This term is also found in the mass balance in either Eqn. 6.2 or 6.4. For adsorption, this quantity goes to a value of 1 when breakthrough has reached equilibrium. For all compositions, N_2 breaks through at essentially the same time (≈ 50 seconds) and is completely adsorbed at 125 seconds. This is a feature of an adsorbate with linear isotherm. As seen in Fig. 6.3, zeolite 4A is linear for N_2 in this range. Note that the approach to equilibrium becomes rounder, as the composition decreases from 100 mol% to 25.0 mol% N_2. As the N_2 composition decreases, the breakthrough curve will become more axially dispersed and will also have additional dispersion due to the greater diffusional resistance to N_2 uptake in the micropores [5]. For desorption, notice that normalized molar flow is initially above 1 due to the desorption of N_2, that contributes to an increased effluent flowrate. After the initial flow spike, the flow decreases as N_2 leaves the bed and approaches zero as both $Q(t)$ returns to the inlet flow value, and as $y(t)$ approaches zero. Once the desorption normalized molar flow equals zero, desorption is complete, which occurs at ≈ 125 seconds. Unary adsorption and desorption breakthrough experiments were also performed at 40 and 50°C for 25, 50 and 100 mol% N_2 in He, but the breakthrough curves are not shown due to brevity.

The results for N_2/He adsorption and desorption breakthrough experiments on Ba-RPZ are shown in Fig. 6.2. A few differences are observed when compared to zeolite 4A. The main difference is that the adsorption experiments no longer breakthrough

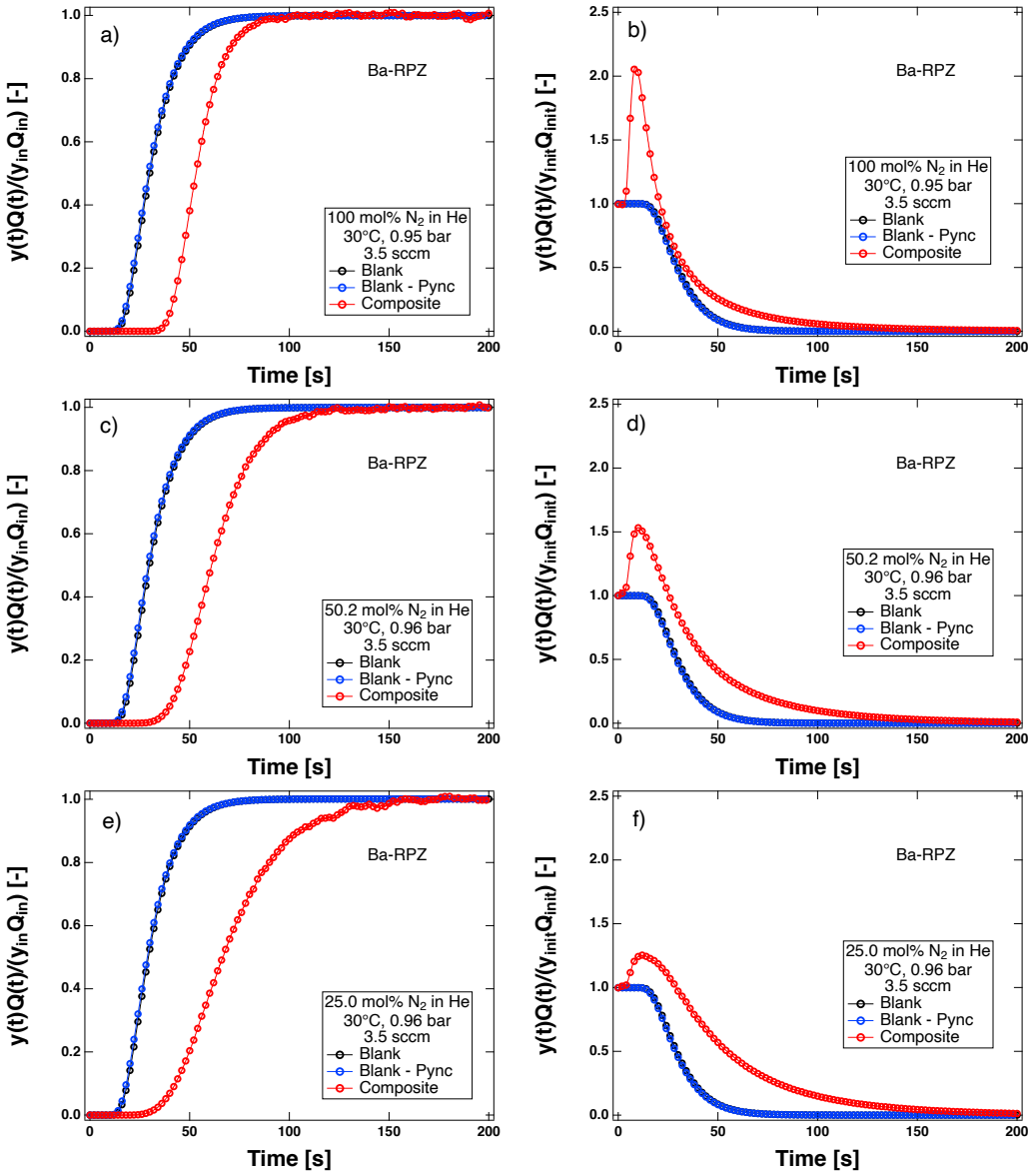

Figure 6.2: Single-component N_2/He adsorption (left) and desorption (right) breakthrough curves at 0.96 bar and 30°C on Ba-RPZ. Panels (**a**) and (**b**) are for 100 mol% N_2, (**c**) and (**d**) are for 50.2 mol% N_2/He, and (**e**) and (**f**) are for 24.9 mol% N_2/He. The reference gas was He for these experiments. Every twentieth point is shown as a marker.

Table 6.1: Conditions for the unary N_2 adsorption and desorption μDCB experiments performed on zeolite 4A and Ba-RPZ.

Adsorbent	$y_{in/init}$ [-]	P [bar]	T [°C]	Q_{in} [ccm]	q^*_{ads} [mol kg^{-1}]	q^*_{des} [mol kg^{-1}]
Zeolite 4A	1.000	0.963	30	4.05	0.3140	0.3010
	0.502	0.960	30	4.06	0.1621	0.1643
	0.250	0.969	30	4.06	0.0864	0.0860
	1.000	0.959	40	4.19	0.2515	0.2529
	0.503	0.971	40	4.14	0.1324	0.1360
	0.251	0.961	40	4.18	0.0661	0.0659
	1.000	0.962	50	4.31	0.2160	0.2001
	0.503	0.972	50	4.27	0.1157	0.1118
	0.251	0.963	50	4.31	0.0487	0.0527
Ba-RPZ	1.000	0.953	30	4.092	0.4476	0.4331
	0.502	0.957	30	4.08	0.3139	0.3094
	0.250	0.954	30	4.09	0.1957	0.1932
	1.000	0.949	40	4.25	0.3684	0.3514
	0.502	0.951	40	4.24	0.2482	0.2470
	0.250	0.954	40	4.21	0.1455	0.1466
	1.000	0.957	50	4.35	0.3202	0.3215
	0.503	0.949	50	4.37	0.1938	0.1931
	0.250	0.953	50	4.36	0.1166	0.1135

at the same time. As the composition decreases from 100 to 25.0 mol% N_2, the breakthrough time increases from 53 seconds to 67 seconds. This is due to the fact that N_2 exhibits a non-linear trend in equilibrium on Ba-RPZ (see Fig. 6.3). The time to reach equilibrium is also more exaggerated as the N_2 compositions decreases. This is shown explicitly by the sharp adsorption breakthrough profile in the 100 mol% N_2 experiment, and the longer tail to equilibrium in the 25.0 mol% N_2 experiment.

After an adsorption or desorption breakthrough experiment is complete, the equilibrium loading can be calculated by solving either Eqn. 6.2 or 6.4. This data is

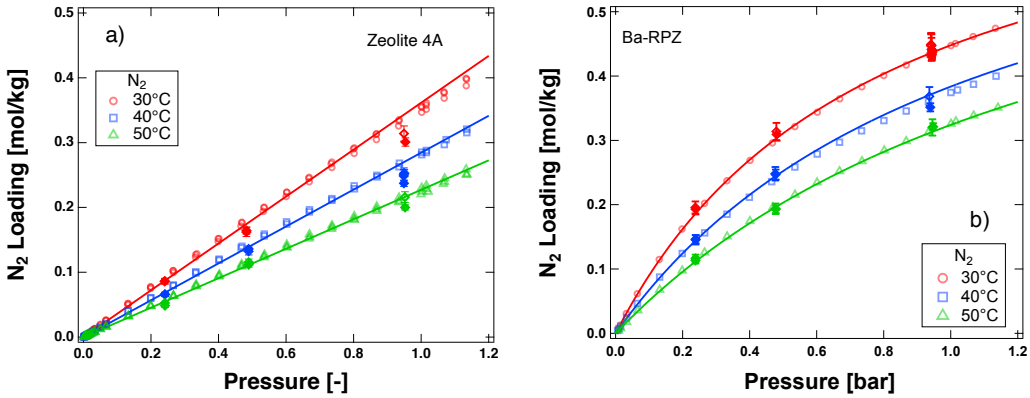

Figure 6.3: Single-component equilibrium data of N_2 on zeolite 4A (**a**) and Ba-RPZ (**b**) at 30, 40 and 50°C. Hollow diamond markers are adsorption breakthrough experiments, and solid diamond markers are desorption experiments. Circle, square and triangle markers are volumetrically collected equilibrium data. Linear and single-site Langmuir isotherms are shown with lines. The isotherm parameters are found in Chapter 5.

shown in Fig. 6.3 and is overlaid with independently collected data from a volumetric apparatus and fitted isotherms. Tabulated data is given in Table 6.1. The corresponding isotherm parameters for both materials can be found in a previous study [5]. The adsorption and desorption loadings are shown as hollow and solid diamond markers, respectively. As seen in Fig. 6.3, there is overall good agreement with all calculated loadings for N_2 on zeolite 4A and Ba-RPZ. The μDCB loadings typically agree with the volumetrically collected data within $1-2\%$, but can deviate as high as 5% in loading. These results show that the zeolite 4A and Ba-RPZ beds can provide equilibrium data that is consistent with independently collected data.

6.4.2 Single Component CH_4 Breakthrough Experiments

Single component CH_4 adsorption experiments were then performed at approximately 0.96 bar and 30, 50 and 70°C. All experiments were performed at 5.3 sccm. Methane will experience a large amount of diffusional resistance adsorbing into zeolite 4A and Ba-RPZ. This is much less pronounced in zeolite 4A than it is for Ba-RPZ [5].

This uptake resistance is seen in the CH_4 adsorption breakthrough curves in Fig. 6.4 for zeolite 4A. As seen in the 100 mol% CH_4 experiment in Fig. 6.4(**a**), CH_4 breaks

through initially resembling a shock after the blank curve. Soon after the initial breakthrough, the curve begins to tail and takes hundreds of seconds to reach equilibrium. Interestingly, this part of the breakthrough curve is dominated by $Q(t)$, the effluent mole fraction is essentially a square-wave with a long tail from about 99% of the full signal. The long tail in molar flow is directly due to the resistance to CH_4 diffusion through the micropores of zeolite 4A. This is also true for the 50.4 and 25.4 mol% CH_4 in He breakthrough experiments. Methane displays a linear isotherm on zeolite 4A at the conditions studied. This long tail is characteristic of a diffusion-controlled system [148].

Figure 6.5(**a**) shows the breakthrough curves of all three CH_4/He mixtures overlaid on one another. As seen, the profiles lie almost on top of one another. This is especially true in the range above $y(t)Q(t)/[y_{\text{in}}Q_{\text{in}}] = 0.9$. The only difference is the small change in axial dispersion which is seen in the initial shock at low concentrations ($y(t)Q(t)/[y_{\text{in}}Q_{\text{in}}] < 0.5$). A small deviation above $y(t)Q(t)/[y_{\text{in}}Q_{\text{in}}] = 0.8$ is also seen for 100 mol% CH_4, which may be due to the greater amount of heat released during adsorption when compared to the 50.4 and 24.4 mol% experiments. This behavior follows the expected trend, where the most concentrated breakthrough (100 mol% CH_4) is the least dispersed curve, and the least concentrated breakthrough (25.4 mol% CH_4) is the most dispersed curve. At the conditions considered for these breakthrough curves, CH_4 exhibits a linear isotherm on zeolite 4A [5]. Therefore, it is expected that the diffusivity of all three CH_4/He experiments should be the same, as long as the temperature of the experiment is held constant. The same experiments were repeated at 50 and 70°C, to confirm the trends observed at 30°C. Figure 6.5(**c**) and (**e**) shows equivalent experiments at 50 and 70°C, respectively. As expected, all three CH_4/He mixtures do lay on top of each other. Again, a small difference is seen in the axial dispersion of the three curves. This confirms that at elevated temperatures, the curves show a comparable diffusivity. Figure 6.6 shows the CH_4 breakthrough curves at the same composition ($\approx$ 25 mol% CH_4) as a function

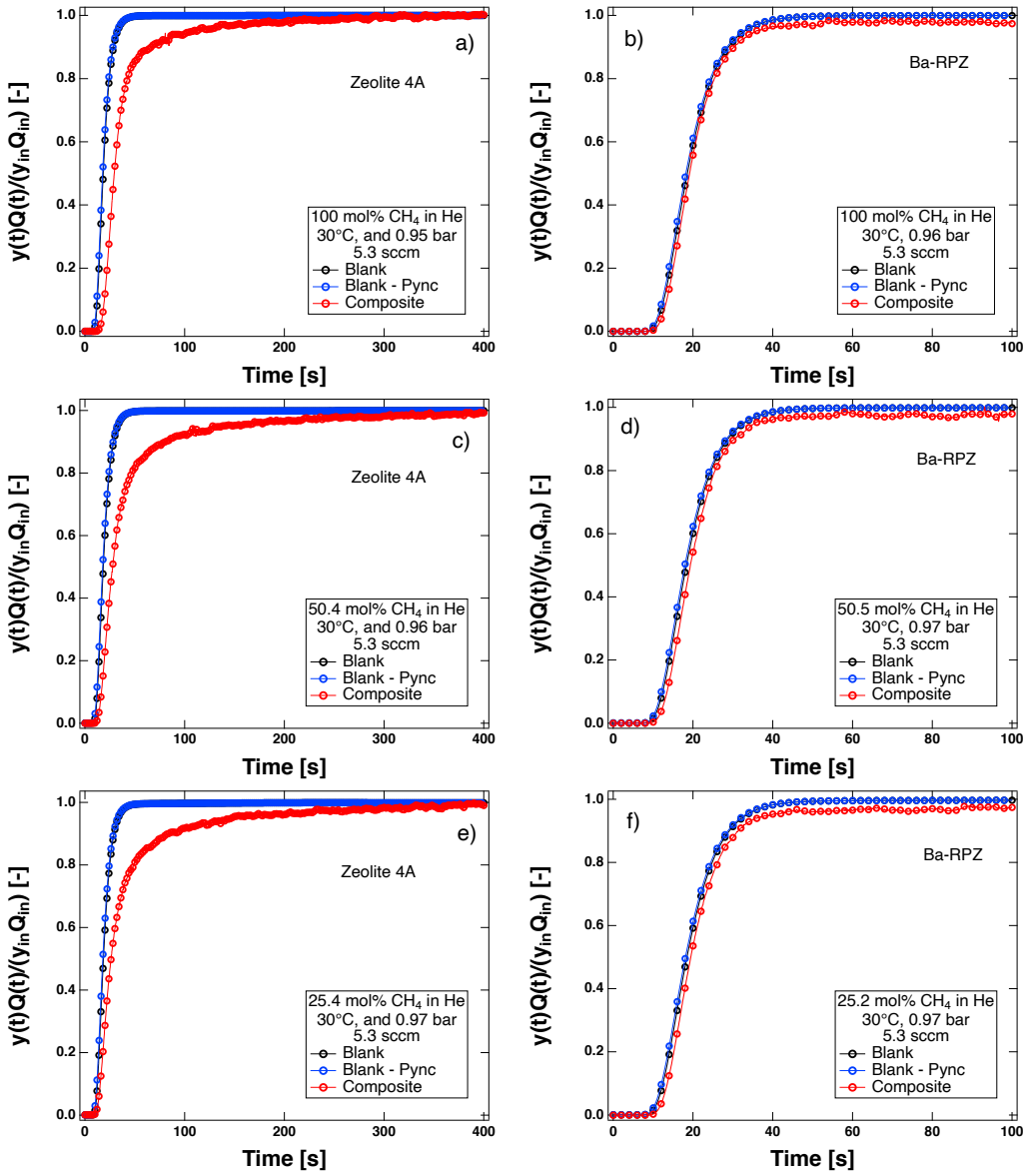

Figure 6.4: Single-component CH_4/He adsorption breakthrough curves at 0.96 bar and 30°C on zeolite 4A (left) and Ba-RPZ (right). Panels (**a**) and (**b**) are for 100 mol% CH_4, (**c**) and (**d**) are for 50 mol% N_2/He, and (**c**) and (**f**) are for 25 mol% CH_4/He. The reference gas was He for these experiments. Every twentieth point is shown as a marker.

of temperature. As the temperature increases from 30 to 70°C, the breakthrough curves become less dispersed and the tail in the molar flow profile reaches equilibrium faster. This is more easily seen in the Fig. 6.6(**b**). This result is intuitive, as the temperature of the experiment increases, the diffusivity also increases. This confirms two of the observations found in a previous study; CH_4 on zeolite 4A exhibits a constant diffusivity at a fixed temperature and that the CH_4 diffusivity increases with increasing temperature.

Similar CH_4/He adsorption breakthrough experiments were also performed the for Ba-RPZ and are shown in Fig. 6.4. As seen in the 100 mol% CH_4 experiment in Fig. 6.4(**b**), CH_4 breaks through coincidentally with the pycnometrically corrected blank response and goes above $y(t)Q(t)/[y_{\text{in}}Q_{\text{in}}] = 0.95$. The approach to equilibrium, $y(t)Q(t)/[y_{\text{in}}Q_{\text{in}}] = 1$, takes many more hours to finish. This is seen in Fig. 6.4(**b**), where the composite experiment signal does not reach a value of 1 (the inlet conditions). This is also seen for the other methane compositions in Fig. 6.4. Eventually, $y(t)Q(t)/[y_{\text{in}}Q_{\text{in}}]$ should approach a value of 1, when equilibrium is reached. As previously mentioned, there is a massive resistance to CH_4 uptake into Ba-RPZ. This is due to both micropore transport and surface-barrier resistances [5].

This trend in normalized molar flow is very noisy as the signal approaches unity. This is unfortunately a limitation of our current instrumentation; specifically, the mass flow meter signal. The thermal conductivity detector (TCD) signal is much less noisy; therefore, a plot of the normalized mole fraction ($y(t)/y_{\text{in}}$) versus time is used instead to assess the diffusional resistance of CH_4 into Ba-RPZ. This is an assumption, since the effluent flow will change slightly over the course of the experiment. This variation in flow is expected to have a minor effect. The maximum change in effluent flow during the 100 mol% CH_4 experiment is a 2.7% drop in the inlet flow just before the initial CH_4 breakthrough. The effluent flow returns to roughly 1.0% of the inlet value after 600 seconds. Figure 6.5(**b**) shows the three CH_4/He mixtures 30°C in the approach to equilibrium. In normalized mole fraction, it is easy to see

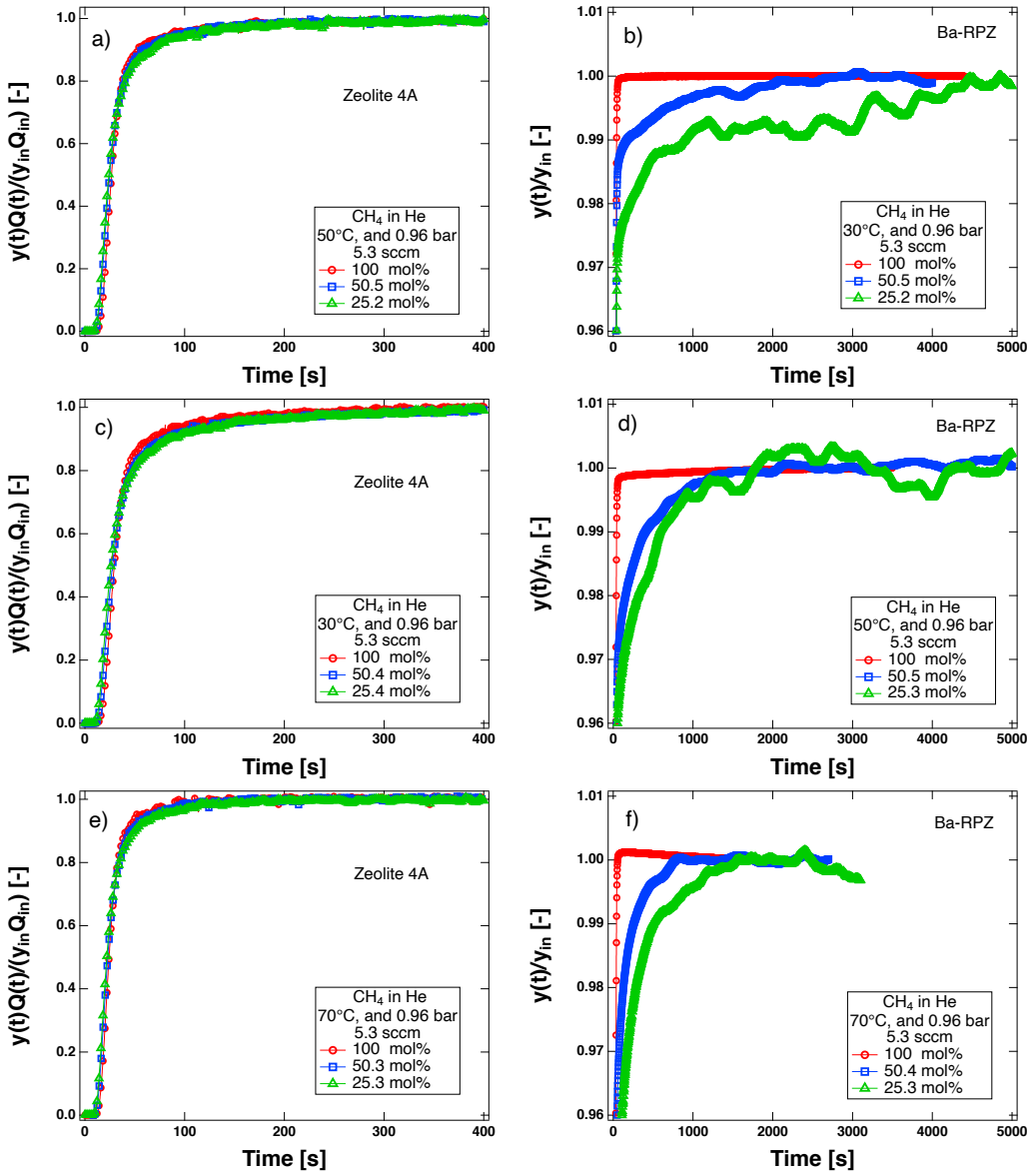

Figure 6.5: Single-component CH_4/He adsorption breakthrough curves at 30°C (**a**, **b**), 50°C (**c**, **d**) and 70°C (**e**, **f**) at 0.96 bar on zeolite 4A (left) and Ba-RPZ (right). Three composite experiments are shown in each graph at approximately 100, 50 and 25 mol% CH_4 in helium. The reference gas was He for these experiments. Every twentieth point is shown as a marker.

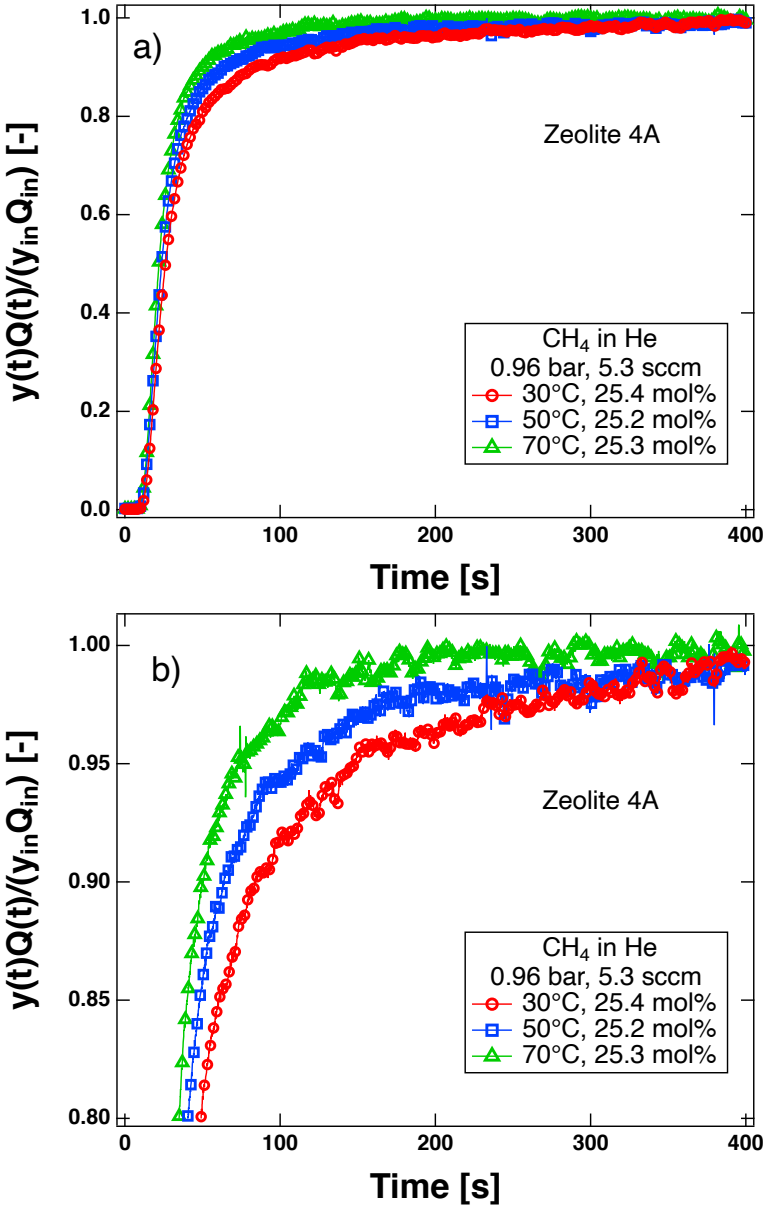

Figure 6.6: 25 mol% CH_4/He adsorption breakthrough curves at 30, 50 and 70°C (**a**) at 0.96 bar on zeolite 4A. Panel (**b**) shows the same curves as (**a**) but, is zoomed in on the y-axis to better show the differences between the curves. The reference gas was He for these experiments. Every twentieth point is shown as a marker.

the trend of the three inlet compositions above $y(t)/y_{\text{in}} = 0.96$. Specifically, the 100 mol% CH_4 experiment goes to equilibrium faster than 50.5 mol%, which is faster than 25.2 mol%. This trend was observed in our previous study. Specifically, as the concentration increases, the CH_4 both the micropore and surface-barrier diffusivities into the adsorbent increases. This is a thermodynamic phenomenon, as the adsorbed concentration increases there is less resistance to mass transport in the micropores [22]. These trends were also observed at 50°C and 70°C, as shown in Fig. 6.5 (**d**) and (**f**).

However, the instrumentation was not sensitive enough to definitively measure the difference of CH_4 diffusivity as a function of temperature. This difference was measurable in a constant volume apparatus (see Chapter 5). However, the variations in the approach to equilibrium were too small to quantify. As seen in Fig. 6.7(**b**), the curves at 50 and 70°C essentially overlap. Although, the curve at 30°C clearly takes more time to reach equilibrium than 50 and 70°C. This effect was small in the zeolite 4A experiments, but noticeable. In the Ba-RPZ breakthrough experiments, the signal noise was too large to conclude anything as a function of temperature. Again, this is likely due to the much greater mass transfer resistance for CH_4 into Ba-RPZ than zeolite 4A.

In theory, the experimental CH_4 equilibrium loadings for zeolite 4A and Ba-RPZ could be calculated using Eqn. 6.2. The long tail in CH_4 composition and effluent flow represents the very slow uptake of CH_4 into the adsorbent. Over time, the integrated mass balance should yield equilibrium loadings. In practice, this seemed to yield inconsistent results that did not agree with the volumetrically collected equilibrium data. This was likely due to the noisy mass flow meter (MFM) signal coupled with the long experimental times [31]. It is also likely that none of the Ba-RPZ experiments ever reached equilibrium, as this took hours with similar volumetric experiments. In DCB experiments, error accumulates over time with the integral solution. Since the equilibrium loadings were inconsistent, they will not be reported in this study.

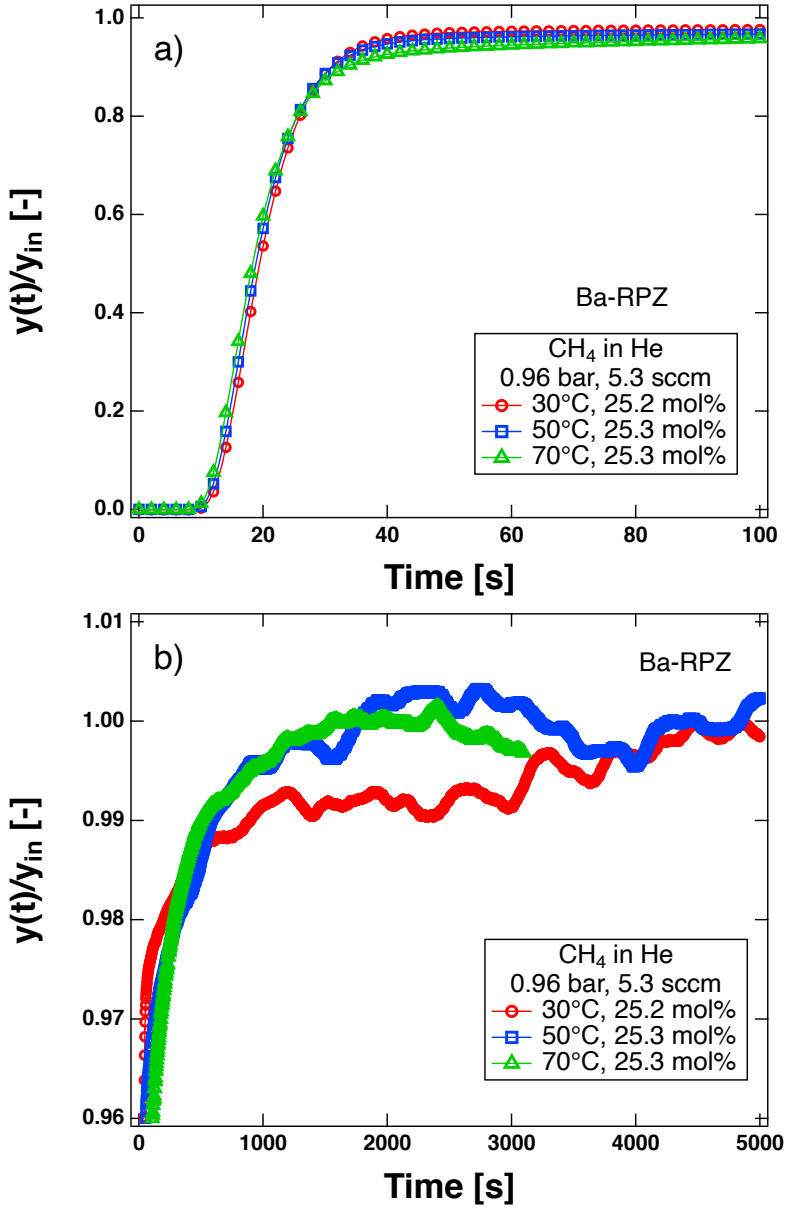

Figure 6.7: 25 mol% CH_4/He adsorption breakthrough curves at 30, 50 and 70°C (**a**) at 0.96 bar on Ba-RPZ. Panel (**b**) shows the same curves as (**a**) but, is zoomed in on the y-axis to better show the differences between the curves. The reference gas was He for these experiments. Every twentieth point is shown as a marker.

6.4.3 Binary Adsorption of CH_4 and N_2

The main aim of this study is to determine the binary CH_4/N_2 diffusivities into zeolite 4A and Ba-RPZ. These were measured using binary CH_4/N_2 adsorption experiments and were performed in a similar manner as the multicomponent equilibrium experiments in Chapter 4. The packed bed was equilibrated with 100 mol% N_2 and then fed a mixture of CH_4/N_2 at the same temperature and pressure. For these experiments, only the CH_4 composition was recorded with the TCD. All of these experiments were performed at 5.3 sccm of inlet flow.

Adsorption breakthrough experiments were performed at 50.6 and 24.9 mol% CH_4 in N_2 at 30°C on zeolite 4A. These conditions were chosen to directly compare with equivalent CH_4/He adsorption experiments (at 50.4 and 25.4 mol% CH_4 in He). These comparisons are given in Fig. 6.8(**a**). As seen in Fig. 6.8(**a**), the CH_4 breakthrough time and shape is qualitatively the same when either N_2 or He is used as a carrier gas. This suggests that there is no change in CH_4 diffusivity when another adsorbing gas, in this case N_2, is present. This was also confirmed at 50°C. The results at higher temperatures are shown in Fig. 6.8(**b**). This is likely due to the shape of the CH_4 and N_2 isotherms on zeolite 4A. Both CH_4 and N_2 are linear (with pressure) on zeolite 4A at these conditions [5]. In a previous study [5], both were found to follow Darken's equation, also know as the thermodynamic correction factor [149]:

$$\frac{D_{c,i}}{D_{c0,i}} = \frac{q_i^*}{p_i}\frac{\partial p_i}{\partial q_i^*} = \frac{\partial \ln(p_i)}{\partial \ln(q_i^*)} \tag{6.7}$$

where $D_{c,i}$ is the crystalline diffusivity, $D_{c0,i}$ is the limiting crystalline diffusivity, also known as the self-diffusivity, and p_i is the partial pressure of gas i. Darken's equation relates the diffusion of a gas through a porous material with the equilibrium isotherm. Both CH_4 and N_2 can be fitted reasonably with a linear isotherm:

$$q_i^* = H_i p_i \tag{6.8}$$

where H_i is the Henry constant. Therefore, the diffusivity of both species in either

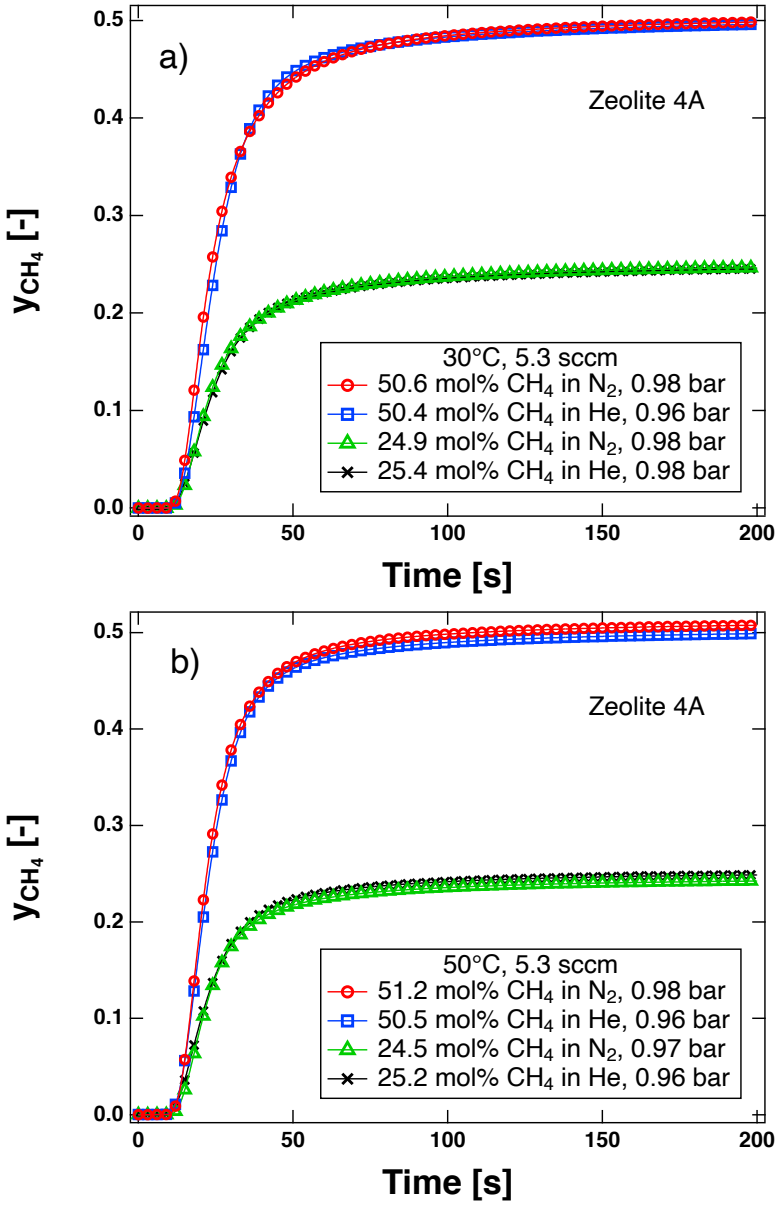

Figure 6.8: A comparison of CH_4/He and CH_4/N_2 adsorption mole fraction breakthrough curves at ≈ 0.97 bar and 30°C (**a**) and 50°C (**b**) on zeolite 4A. The reference gas was either N_2 or He for these experiments.

a unary or binary experiment should remain constant, and not be influenced by the other. Darken's equation reduces to $D_{c,i} = D_{c0,i}$ for a linear isotherm. This is also true thermodynamically, as linear isotherms usually do not competitively adsorb into the adsorbent sites [20]. This further corroborates the observed trend.

In the literature, a few studies have measured binary CH_4/N_2 diffusivities on zeolite 4A [150–152]. Habgood found that CH_4 was essentially unaffected in binary CH_4/N_2 mixtures [150]. Habgood performed these experiments in a constant volume apparatus at 0 and -79°C for 10/90, 50/50 and 90/10 mol% mixtures of CH_4/N_2. There was enhancement in the N_2 diffusivity, but relatively no change for CH_4. Ruthven and Kumar studied binary CH_4/N_2 mixtures on zeolite 4A at 32°C using chromatographic techniques [151]. Ruthven and Kumar found that for a binary CH_4/N_2 mixture, CH_4 and N_2 diffused independently of each other. However, they caution that this conclusion could be due to the low gas concentrations used in their experiments. Mohr *et al.* found that the binary CH_4 and N_2 diffusivities were essentially the same as their unary self-diffusivities at similar conditions [152]. This was done with the isotope-exchange technique (IET) at -20, 0 and 10°C for binary CH_4/N_2 mixtures between 20 and 50 mol% CH_4, at total pressures between 0.5 and 3.7 bar. Mohr *et al.* found that the binary diffusivities usually deviated about $5-15\%$ from the unary diffusivities. These studies appear to corroborate the results found in binary CH_4/N_2 breakthrough experiments.

Similar CH_4/N_2 adsorption breakthrough experiments were also performed on Ba-RPZ, and are shown in Fig. 6.9. These again are shown with their corresponding CH_4/He experiments. As seen in Fig. 6.9, it is difficult to distinguish any difference between the two carrier gases. Although, this could be due to the signal-noise, as was observed in the unary CH_4 experiments as a function of temperature. Both CH_4 and N_2 exhibit a non-linear isotherm on Ba-RPZ and both can be reasonably fitted to a single-site Langmuir isotherm [5]. At equilibrium, a single-site Langmuir isotherm extension predicts ideal competition [18, 20]. There are multiple mathemat-

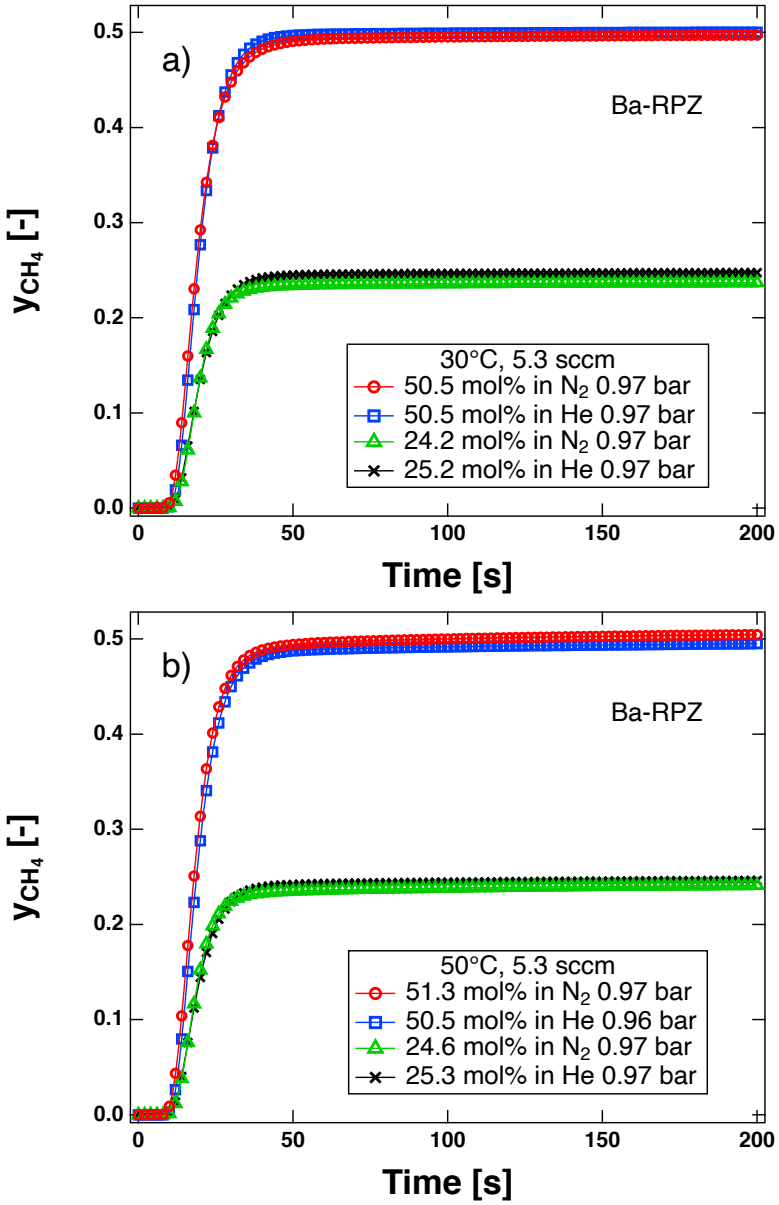

Figure 6.9: A comparison of CH_4/He and CH_4/N_2 adsorption mole fraction breakthrough curves at ≈ 0.97 bar and 30°C (**a**) and 50°C (**b**) on Ba-RPZ. The reference gas was either N_2 or He for these experiments.

ical formulations to describe multicomponent diffusion in porous materials of varying complexity [22]. Using the Maxwell-Stefan formulation, an ideal competition, single-site Langmuir isotherm should display competitive diffusion [149]. This suggests that the species should compete diffusively on Ba-RPZ during the time it takes to establish an equilibrium. It is likely that the binary CH_4 diffusivities are different from the unary diffusivities on Ba-RPZ, but with the limitations of the current experimental hardware, no firm conclusions can be made.

6.5 Conclusions

This study explored the feasibility of the microscale dynamic column breakthrough apparatus to determine multicomponent diffusivities. Dynamic column breakthrough experiments can be used to measure qualitative and quantitative diffusivities, but generally suffer from the large amount of heat released during adsorption. The microscale dynamic column breakthrough apparatus utilizes about $100 - 150$ mg of adsorbent, which should reduce the quantity of heat released during these experiments. This was tested with unary and binary CH_4 and N_2 experiments on zeolite 4A and Ba-RPZ. First N_2 was studied, since it diffuses faster into both materials. For unary N_2 experiments on both zeolite 4A and Ba-RPZ, the transient mass balance provided equilibrium data that agreed with independently collected volumetric data. This was not possible for CH_4, likely due to the accumulation of error over the long experiment. Unary CH_4 diffusivities on zeolite 4A were qualitatively the same, in both composition and temperature, as found in a previous study. Binary CH_4/N_2 diffusivities appeared to be qualitatively the same as the unary CH_4 diffusivities into zeolite 4A. This finding is in agreement with studies in the literature. However, both unary CH_4 and binary CH_4/N_2 qualitative diffusion in Ba-RPZ was inconclusive. This is likely due to the instrumentation used in this study; the effluent composition and flow signals were not stable, or strong, enough to determine a firm set of conclusions. The signals could be improved by working in a region where the effluent flow

is negligible (< 10 mol% adsorbate) [32] and with a stronger concentration detector such as a flame ionization detector.

Chapter 7

Optimization of pressure-vacuum swing adsorption processes for nitrogen rejection from natural gas streams using a nitrogen selective metal organic framework

7.1 Introduction

Methane is an important fuel in the transition to a cleaner energy grid [42, 45]. Compared to other fossil fuels, it has the lowest CO_2 intensity per unit amount of energy produced, and results in a cleaner combustion. This makes methane an ideal candidate to replace higher polluting fuels such as coal. It is also the most calorific fuel on a per mass basis (in kJ/kg CH_4), although at standard temperatures and pressures it is a gas and therefore it must be compressed to a liquid before burned. There are also issues with methane leakage from pipelines, that may diminish the benefits of methane over other fossil fuels [153]. Methane is the principle component of natural gas, which is also comprised of other alkanes, such as ethane and propane. Methane is usually extracted from drilled wells, and landfills, where it is present with primarily nitrogen and other minor components. Methane is also a far more potent

This chapter was originally published as: N. S. Wilkins, K. N. Pai, and A. Rajendran, "Optimization of pressure-vacuum swing adsorption processes for nitrogen rejection from natural gas streams using a nitrogen selective metal organic framework," *Can. J. Chem. Eng.*, 2022.

greenhouse gas when compared to CO_2, and hence, the capture and concentration of methane not only provides a value addition, but also can be an effective tool to reduce man-made climate change.

Pressure swing adsorption (PSA) is utilized in commercial processes to separate CH_4 and N_2 [17, 52, 154, 155]. Two types of PSA processes are employed for this separation: kinetic, and equilibrium-based. The kinetic PSA process employs a sorbent in which N_2 diffuses faster as compared to CH_4 due to the relative molecular size of CH_4 (3.80 Å) and N_2 (3.64 Å) [18, 22]. In a kinetic PSA process, CH_4 is collected as the light (raffinate) product and N_2 as the heavy product. Examples of sorbents used for kinetic separations include several variants of Engelhard titanosilicates (ETS) [5, 156]. Variants of these sorbents that show better performance have recently been presented in the literature [135]. For equilibrium separations, activated carbons are typically used [106, 157, 158]. In these sorbents, CH_4 adsorbs stronger compared to N_2 and is therefore recovered as the low-pressure extract product. This means that the product must be repressurized for pipeline transportation and that the process requires a higher energy consumption [106]. However, equilibrium separations result in better recoveries which may be able to offset the higher energy consumption in the raffinate process. The choice of selecting the process depends on the specific situation and hence, both equilibrium and kinetic processes can be seen in practice.

For landfill gas, the composition of CH_4 varies between $30 - 92$ mol% with the balance being mostly N_2, some CO_2 and other impurities like NO_x, SO_x and H_2O [106, 125]. Landfill gas studies generally consider a feed at $20 - 40°C$ and $1 - 45$ bar total pressure [12, 16, 17, 106]. However, landfill gas is generally available at atmospheric pressure, therefore, it is compressed from the outlet of the landfill (usually to $4 - 5$ bar [16]) to yield better separations using kinetic PSA cycles [17].

Many PSA cycle optimization studies are found in the literature and most aim to achieve the "pipeline transport specification" of 96 mol% CH_4. This purity is a recommended value that includes less than 4 mol% combined CO_2 and N_2 in the up-

graded CH_4 product to increase its heating value [159]. This is not a fixed value for all pipelines, but has a high enough methane composition to minimize pipe fouling and hydrate formation. Commercial PSA processes for CH_4 purification often use carbon molecular sieves (CMS) or activated carbons. Fatehi *et al.* performed experimental studies using a 60/40 and 92/8 mol% CH_4/N_2 feed in a two column set-up packed with an unspecified CMS [154]. Kinetic PSA (KPSA) cycles were run experimentally in a parametric study to optimize CH_4 purity. They performed these experiments using the Skarstrom cycle with the constituent steps: adsorption, counter-current evacuation, counter-current light reflux and co-current feed pressurization [154]. With this cycle, methane purities up to 75.84 and 96.25 mol% were achieved for feed compositions of 60/40 and 92/8 mol% CH_4/N_2, respectively. Yang *et al.* also performed KPSA process optimizations from a 30/70 mol% CH_4/N_2 feed [160]. They considered an activated carbon characterized by Sheikh *et al.* [161]. The process was a 7-step cycle with the following constituent steps: adsorption, pressure equalization donor, co-current light reflux, counter-current blowdown, counter-current evacuation, pressure equalization receiver and co-current feed pressurization [160]. Yang *et al.* found a CH_4 purity of 80 mol% and 97% recovery under optimal conditions [160]. Effendy *et al.* optimized purity, recovery, energy consumption and productivity of a 6-step and 9-step KPSA cycle using a Takeda CMS characterized by Qinglin *et al.* [17, 139]. A 6-step cycle consisting of: adsorption, pressure equalization donor, counter-current blowdown, counter-current evacuation, pressure equalization receiver and co-current feed pressurization was considered [17]. A 9-step cycle, that built on the 6-step cycle by using part of the blowdown and evacuation product to pressurize the column instead of a feed pressurization, was also considered. Effendy *et al.* were able to achieve CH_4 recoveries over 90% (up to $\approx 94\%$) while meeting the 96 mol% CH_4 purity constraint from a feed gas containing at least 80 mol% CH_4 [17]. Their cycles operated at 25°C and adsorption pressures between $3 - 45$ bar. Erden *et al.* considered many heavy-reflux cycles that used a BPL activated carbon to purify a

stream of 88/12 mol% CH_4/N_2 [106]. These cycles were able to achieve a CH_4 purity of 99.4 mol% at a recovery of 99.2% [106]. Xiao *et al.* used a CMS (MSC-3K 172) and a dual-reflux cycle to purify CH_4 from a 75/25 mol% CH_4/N_2 mixture [162]. They were able to purify CH_4 up to 90 mol% at a 90% recovery [162].

Titanosilicate adsorbents have also been considered for the kinetic separation of CH_4 from N_2. In particular Sr-, Na- and Ba-ETS-4 and have been considered for this separation. Sr-ETS-4 has been commercialized for nitrogen rejection separations due to its tuneable 3 to 4 Å pore size [131]. Jayaraman *et al.* simulated a 5-step cycle with Sr-ETS-4 and found process conditions where CH_4 purities greater than 96 mol% were achieved from a feed of 85/15 mol% CH_4/N_2 [129]. Bhadra *et al.* performed parametric studies using the Skarstrom cycle to evaulate Ba- and Sr-ETS-4 process performance [135]. Bhadra *et al.* found operating conditions that could purify CH_4 above 96 mol% from a feed of 90/10 mol% CH_4/N_2 [135].

Recently, Jaramillo *et al.* reported a vanadium metal-organic framework (MOF), $V_2Cl_{2.8}$(btdd), that has a stronger affinity for N_2 than CH_4 [163]. For the sake of simplicity, we will refer to this adsorbent as V-MOF in this paper. Generally, CH_4 will exhibit the same adsorption affinity or a greater affinity than N_2 for a given adsorbent owing to the higher polarizability of CH_4 compared to N_2. The electronic structure of the vanadium metal-site allows π-complexation bonds with suitable species like N_2. This π-complex lends the unique adsorption selectivity to N_2. These interactions greatly increase the N_2 affinity compared to CH_4. Adsorption equilibrium data for CH_4 and N_2 on V-MOF from vacuum to 1 bar total pressure at 25, 35 and 45°C was measured and the isosteric heats of CH_4 ($\approx$ 35 kJ/mol) and N_2 ($\approx$ 55 kJ/mol) were reported. The material was also shown to maintain adsorption capacity after multiple cycles of N_2 adsorption and desorption, suggesting that the adsorption of N_2 is reversible and that the material is durable.

The V-MOF provides the opportunity to separate CH_4 as a high-pressure raffinate product, that can be advantageous compared to obtaining CH_4 as a low pressure

heavy product. In this paper, the V-MOF will be evaluated at a range of operating conditions to determine possible CH_4/N_2 PSA process performance. Adsorption equilibrium data was taken from Jaramillo *et al.* to determine whether a PSA process can purify methane to 96 mol% using the basic 3-step cycle and Skarstrom cycle [163]. These two cycles are chosen due to their simplicity and industrial significance [9]. The effect of feed temperature, feed CH_4 composition (in N_2), adsorption pressure and evacuation pressure are studied to determine the best overall operating conditions with machine learning aided optimization. These are then compared with other adsorbents used to purify methane. To improve the computational efficiency of the optimizations, we deploy surrogate models based on artificial neural networks. Hence, an additional objective is to explore the efficacy of machine learning models for rapid optimization of PSA processes.

7.2 Materials and Methods

7.2.1 $V_2Cl_{2.8}$(btdd) Metal-Organic Framework

The V-MOF, or $V_2Cl_{2.8}$(btdd), is a vanadium(II/III) MOF with H_2btdd (bis(1*H*-1,2,3-triazolo[4,5-*b*],[4',5'-*i*])dibenzo[1,4]dioxin) organic ligands. This combination exposes the V(II/III) metal site and allows π backbonding of π-acidic gases, such as N_2 [163]. The framework is comprised of 1-dimensional, hexagonal channels, where the vertices are the vanadium metal sites and the linker being the H_2btdd ligands. The structure has an effective pore size of approximately $16.5 - 18.4$ Å. No kinetic data was reported in the paper by Jaramillo *et al.*, but since the effective pore size is much larger than either CH_4 (3.80 Å) or N_2 (3.64 Å), it is safe to assume that this material is not kinetically limited.

Adsorption equilibrium data for CH_4 and N_2 from vacuum to 1 bar at 25, 35 and 45°C on V-MOF was taken from Jaramillo *et al.* and is shown in Fig. 7.1 (**a**) and (**b**) [163]. Both CH_4 and N_2 show classical type-I adsorption isotherms [164]. In order

for the crystalline form to be deployed in a process, we assume that an inert binder of 25 wt% is added to pelletize the MOF. The reported crystalline loadings (on a per gram adsorbent basis) are therefore derated by 25% [163]. This data was fitted to a dual-site Langmuir isotherm:

$$q_i^* = \frac{q_{\mathrm{b}}^{\mathrm{sat}} b_i C_i}{1 + \sum_{j=1}^{m_{\mathrm{comp}}} b_j C_j} + \frac{q_{\mathrm{d}}^{\mathrm{sat}} d_i C_i}{1 + \sum_{j=1}^{m_{\mathrm{comp}}} d_j C_j} \tag{7.1}$$

where the temperature dependence of b and d are described with a Van't Hoff type relationship:

$$b_i = b_{i,0} \exp\left(\frac{-\Delta U_{\mathrm{b,i}}}{RT}\right) \tag{7.2}$$

$$d_i = d_{i,0} \exp\left(\frac{-\Delta U_{\mathrm{d,i}}}{RT}\right) \tag{7.3}$$

In Eqn. 7.1, q_i^* represents the solid phase loading of component i that is in equilibrium with a fluid phase concentration C_i. $q_{\mathrm{b}}^{\mathrm{sat}}$ and $q_{\mathrm{d}}^{\mathrm{sat}}$ represent the saturation capacities of the b and d sites respectively, with b_i and d_i representing the corresponding equilibrium constants. The internal energies of adsorption on these sites are given by $\Delta U_{\mathrm{b,i}}$ and $\Delta U_{\mathrm{d,i}}$. The dual-site parameters where regressed to the loadings reported by Jaramillo *et al.* and are given in Table 7.1 [163]. The isosteric heats of adsorption for both CH_4 and N_2 are very similar to the range that was reported in Jaramillo *et al.* [163]. CH_4 can be fit to a single-site Langmuir isotherm with reasonable accuracy, however, a dual-site Langmuir isotherm was used instead to better estimate the competitive adsorption of the CH_4/N_2 mixture [2]. The isotherm fits are shown to 5 bar pressure in the Supporting Information.

Since little is known about the crystalline parameters of V-MOF, some material properties were assumed. These material properties include the particle density (961.7 kg/m^3) and the adsorbent heat capacity (960.0 J mol^{-1} K^{-1}). These are material properties for a zeolite 13X sample used in a previous study [2]. The pellets are assumed to be spherical and uniformly packed to give a bed void fraction (ϵ) of 0.35. The particle voidage (ϵ_{p}) was assumed to be 0.33 [19]. All material properties are listed in Table 7.3.

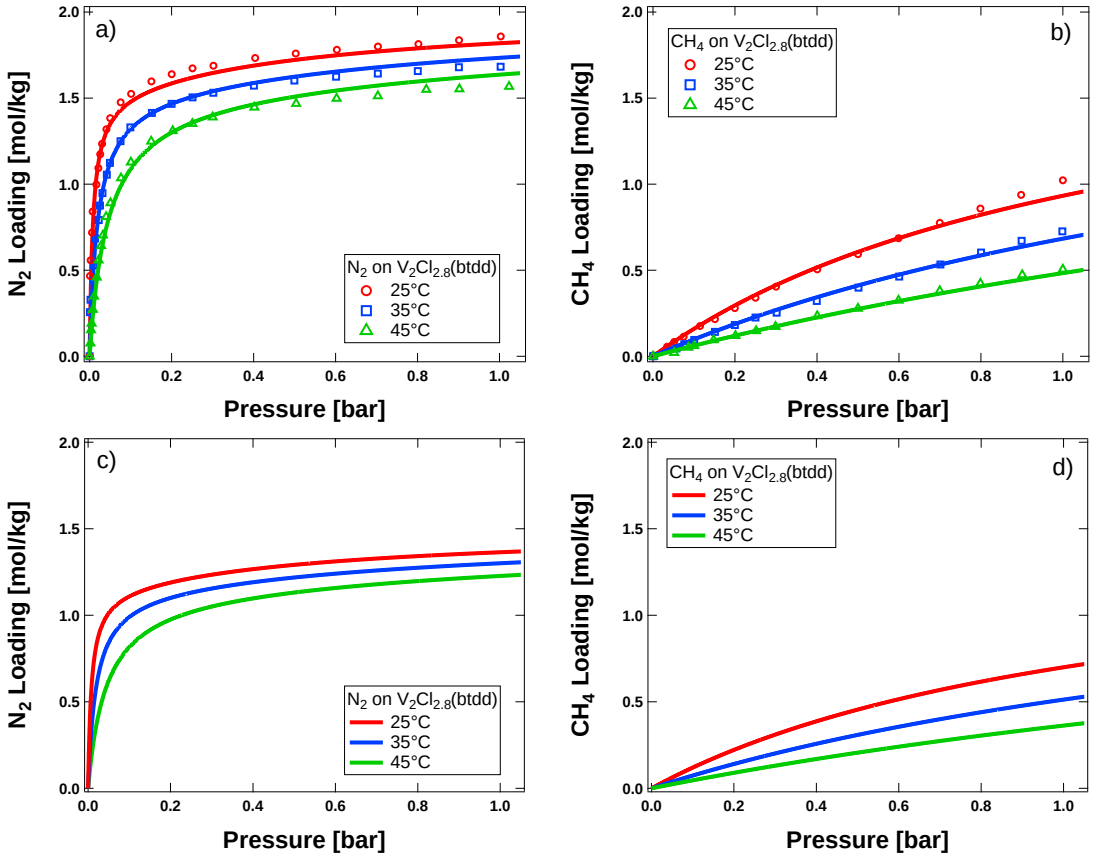

Figure 7.1: Adsorption equilibrium data (markers) for N_2 (**a**) and CH_4 (**b**) on V-MOF, $V_2Cl_{2.8}$(btdd), at 25, 35 and 45°C from vacuum to 1 bar pressure [163]. Lines are the dual-site Langmuir fits to the data measured by Jaramillo *et al.* Panels (**c**) and (**d**) show the isotherms used in this study, with a 25% reduction from the crystalline loading.

Table 7.1: Dual-site Langmuir isotherm parameters for single component N_2 and CH_4 on crystalline $V_2Cl_{2.8}$(btdd). A 25% reduction of q_b^{sat} and q_d^{sat} was used in the detailed model to account for $V_2Cl_{2.8}$(btdd) pelletization.

Gas	q_b^{sat}	b_0	$-\Delta U_b$	q_d^{sat}	d_0	$-\Delta U_d$
	[mol/kg]	[m^3/mol]	[kJ/mol]	[mol/kg]	[m^3/mol]	[kJ/mol]
CH_4	1.52	7.00×10^{-9}	37.00	0.50	7.00×10^{-9}	37.00
N_2	1.52	1.90×10^{-11}	64.00	0.50	4.00×10^{-9}	40.00

Table 7.2: Equations for modeling adsorption dynamics.

Overall Mass Balance	$\frac{1}{P}\frac{\partial P}{\partial t} - \frac{1}{T}\frac{\partial T}{\partial t} = -\frac{T}{P}\frac{\partial}{\partial z}\left(\frac{P}{T}v\right) - \frac{RT}{P}\frac{1-\epsilon}{\epsilon}\sum_{i=1}^{m_{\text{comp}}}\frac{\partial q_i}{\partial t}$
Component Mass Balance	$\frac{\partial y_i}{\partial t} + \frac{y_i}{P}\frac{\partial P}{\partial t} - \frac{y_i}{T}\frac{\partial T}{\partial t} = D_{\text{L}}\frac{T}{P}\frac{\partial}{\partial z}\left(\frac{P}{T}\frac{\partial y_i}{\partial z}\right) - \frac{T}{P}\frac{\partial}{\partial z}\left(\frac{y_i P}{T}v\right) - \frac{RT}{P}\frac{1-\epsilon}{\epsilon}\frac{\partial q_i}{\partial t}$
Solid Phase Mass Balance	$\frac{\partial q_i}{\partial t} = k_i(q_i^* - q_i)$
Pressure Drop	$-\frac{\partial P}{\partial z} = \frac{150}{4}\frac{\mu v}{r_{\text{p}}^2}\left(\frac{1-\epsilon}{\epsilon}\right)^2$
Column Energy Balance	$\left[\frac{1-\epsilon}{\epsilon}(\rho_{\text{s}}C_{\text{p,s}} + C_{\text{p,a}}\sum_{i=1}^{m_{\text{comp}}} q_i)\right]\frac{\partial T}{\partial t} = \frac{K_z}{\epsilon}\frac{\partial^2 T}{\partial z^2} - \frac{C_{\text{p,g}}}{R}\frac{\partial}{\partial z}(vP) - \frac{C_{\text{p,g}}}{R}\frac{\partial P}{\partial t}$ $-\frac{1-\epsilon}{\epsilon}C_{\text{p,a}}T\sum_{i=1}^{m_{\text{comp}}}\frac{\partial q_i}{\partial t} + \frac{1-\epsilon}{\epsilon}\sum_{i=1}^{m_{\text{comp}}}\left[(-\Delta H_{\text{iso},i})\frac{\partial q_i}{\partial t}\right] - \frac{2h_{\text{in}}}{\epsilon r_{\text{in}}}(T - T_{\text{w}})$
Wall Energy Balance	$\rho_{\text{w}}C_{\text{p,w}}\frac{\partial T_{\text{w}}}{\partial t} = K_{\text{w}}\frac{\partial^2 T_{\text{w}}}{\partial z^2} + \frac{2r_{\text{in}}h_{\text{in}}}{r_{\text{out}}^2 - r_{\text{in}}^2}(T - T_{\text{w}}) - \frac{2r_{\text{out}}h_{\text{out}}}{r_{\text{out}}^2 - r_{\text{in}}^2}(T_{\text{w}} - T_{\text{amb}})$

7.2.2 Process Simulations

The pressure swing adsorption (PSA) process simulator was developed in MATLAB using finite-volume techniques [19]. The simulator solves coupled partial differential equations that describe the mass and energy balances for 30 volumes within the one-dimensional column using the van Leer flux limiter [19]. The model equations are shown in Table 7.2 and the bed properties are in Table 7.3. The process simulator assumes that:

1. the gas phase is ideal. Since the maximum pressure for all simulations was 500 kPa, the ideal gas assumption is justified.

2. the column is one-dimensional with no radial gradients in temperature or concentration.

3. an axially dispersed plug flow describes flow in the column.

4. Darcy's law adequately models the column pressure drop. For this study, the flow will either be in the laminar or transition regime, and never in the turbulent regime ($\text{Re}_{\text{p}} < 350$).

5. the solid and gas phases achieve thermal equilibrium instantaneously.

6. the column and adsorbent properties are uniform in the packed bed.

7. the linear driving force (LDF) model describes mass transfer in the bed. This assumption is justified since the effective pore size ($\approx 16.5 - 18.4$ Å) of the V-MOF is large compared to CH_4 (3.80 Å) and N_2 (3.64 Å).

This process simulator is explained in much more detail by Haghpanah *et al.* [19] and has been experimentally validated at pilot and lab-scale [41, 165].

The PSA process simulator is run cyclically, where a single constituent step of the process (such as adsorption) is run at a time. After a constituent step is solved, the next cycle step is solved until a cyclic steady state (CSS) is achieved. Cyclic steady state was defined after at least 20 process cycles were completed, and when there was a mass balance error of less than 1% for 5 continuous cycles. The mass balance error is defined as:

$$\left| \frac{n_{\text{in}} - n_{\text{out}}}{n_{\text{in}}} \right| \times 100\% \leq 1\% \tag{7.4}$$

In Eqn. 7.4, n is the total number of moles of CH_4 and N_2 either entering or leaving the process over the course of one cycle iteration.

Two processes were considered in this study: the 3-step cycle and the Skarstrom cycle. Both are detailed in the following sections.

7.2.3 3-Step Cycle

For V-MOF, CH_4 is the light product and N_2 is the heavy product. Due to this, the 3-step cycle can be used to separate CH_4 as the high-pressure raffinate product from N_2. The 3-step cycle is the simplest light-product cycle and will be studied to determine which operating conditions, if any, can purify CH_4 to 96 mol%. A schematic of the 3-step cycle is shown in Fig. 7.2 and the constituent cycle steps are:

Table 7.3: Detailed cycle simulation parameters for $V_2Cl_{2.8}$(btdd).

Parameter	Value	Source
Column Properties		
column length, L [m]	1.4	assumed
inner column radius, r_{in} [m]	0.10	assumed
outer column radius, r_{out} [m]	0.12	assumed
column void fraction, ϵ	0.35	assumed
particle void fraction, ϵ_{p}	0.33	assumed
tortuosity, τ	3	assumed
Properties and Constants		
universal gas constant, R [m^3 Pa mol^{-1} K^{-1}]	8.314	standard value
adsorbent particle density, ρ_{p} [kg m^{-3}]	961.7	assumed
column wall density, ρ_{w} [kg m^{-3}]	7800	standard value
specific heat capacity of the gas, $C_{\text{p,g}}$ [J mol^{-1} K^{-1}]	1877.8 (N_2/CH_4)	NIST database
specific heat capacity of the adsorbed phase, $C_{\text{p,a}}$ [J mol^{-1} K^{-1}]	$C_{\text{p,g}}$	assumed
specific heat capacity of the adsorbent, $C_{\text{p,s}}$ [J mol^{-1} K^{-1}]	960	[24]
specific heat capacity of the column wall, $C_{\text{p,w}}$ [J mol^{-1} K^{-1}]	502	standard value
fluid viscosity, μ [kg m^{-1} s^{-1}]	1.234×10^{-5}	standard value
molecular diffusion, D_{m} [m s^{-2}]	1.6×10^{-5}	Chapman-Enskog
effective gas thermal conductivity, K_z [W m^{-1} K^{-1}]	9.03×10^{-2}	[19]
thermal conductivity of column wall, K_{w} [W m^{-1} K^{-1}]	16.0	standard value
internal heat transfer coefficient, h_{in} [W m^{-2} K^{-1}]	8.6	[19]
external heat transfer coefficient, h_{out} [W m^{-2} K^{-1}]	2.5	[19]

1. **Adsorption (ADS):** During this step, the feed is introduced to the column at $z = 0$ at the adsorption pressure, P_{H}, and the feed temperature, T_{feed}, at the interstitial velocity, v_{feed}, for t_{ADS} seconds. High purity CH_4 is collected at the end of the column ($z = L$).

2. **Counter-current Evacuation (EVAC):** During the evacuation, the column effluent ($z = L$) is closed and the pressure is reduced from P_{H} to P_{L} through the feed end ($z = 0$). This reduction in pressure removes most adsorbed N_2 and CH_4 in the column as well as CH_4 and N_2 trapped in the fluid void space for t_{EVAC} seconds.

3. **Co-current Feed Pressurization (FP):** During the feed pressurization, the feed gas (of a given CH_4/N_2 composition) is sent to the inlet of the column ($z = 0$), while the column effluent ($z = L$) is closed to raise the pressure from P_{L} to P_{H} for 20 seconds.

These constituent steps are shown in Fig. 7.2 with their corresponding pressure profiles. A 3-step cycle simulation requires seven input variables: the adsorption time (t_{ADS}), evacuation time (t_{EVAC}), adsorption pressure (P_{H}), evacuation pressure (P_{L}), interstitial velocity (v_{feed}), the feed methane composition (y_{CH_4}), and the feed temperature (T_{feed}). The feed pressurization time was fixed at 20 seconds to ensure the adsorption step always restarted at the adsorption pressure. The range of input variables for the 3-step cycle optimizations are given in Table 7.4.

7.2.4 Skarstrom Cycle

The Skarstrom cycle is a frequently used light product cycle that can achieve relatively high product purities [135]. A schematic of the Skarstrom cycle is shown in Fig. 7.2. The Skarstrom cycle is comprised of 4 steps, three from the 3-step cycle and one additional step:

1. **Adsorption (ADS):** This step is analogous to the 3-step cycle.

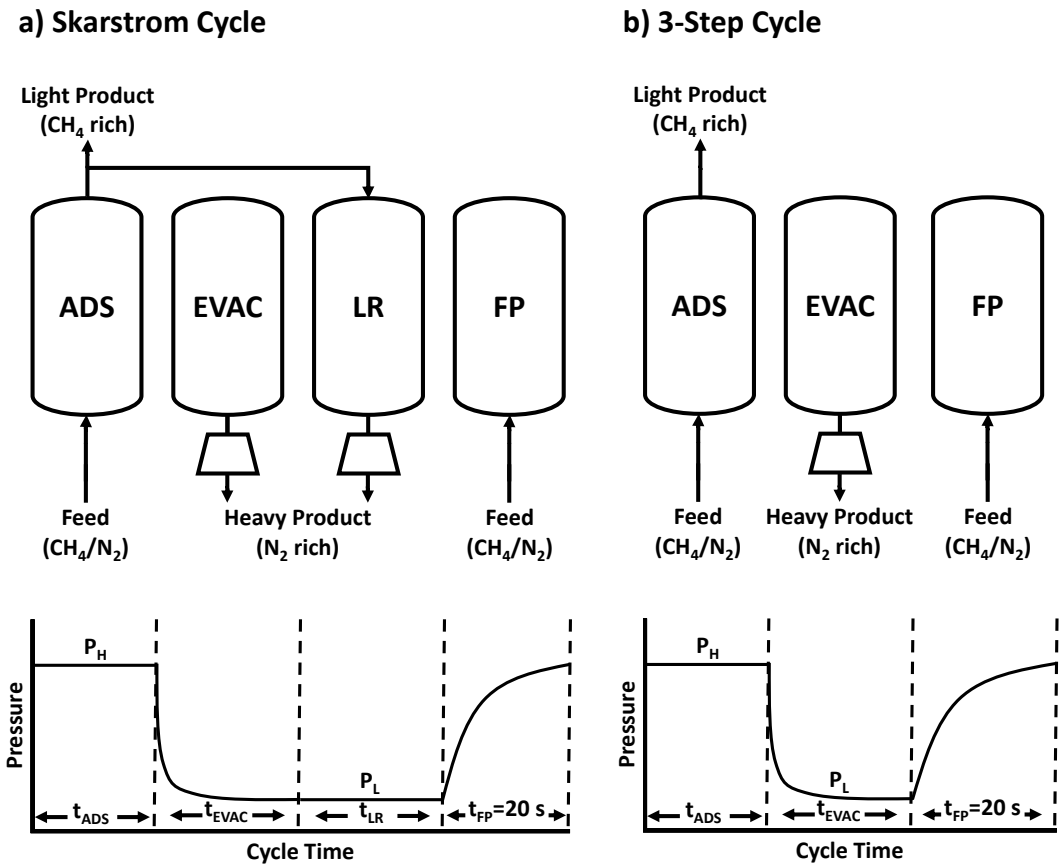

Figure 7.2: A schematic of the (**a**) Skarstrom and (**b**) 3-step cycles used in this study with the associated qualitative pressure profiles.

Table 7.4: Range of decision variables for the Skarstrom and 3-step cycle process optimizations.

Cycle	t_{ADS} [s]	t_{EVAC} [s]	t_{LR} [s]	P_{L} [kPa]	P_{H} [kPa]	v_{feed} [m/s]
3-Step	2 – 200	2 – 200	-	3 – 60	95 – 500	0.01 – 2.0
Skarstrom	2 – 200	2 – 200	2 – 198	3 – 60	95 – 500	0.01 – 2.0

2. **Counter-current Evacuation (EVAC):** This step is analogous to the 3-step cycle.

3. **Light Reflux (LR):** During this step, part of the CH_4 product from the adsorption step is sent to the ($z = L$) end of the column, while the column inlet ($z = 0$) is open. This step operates at P_{L} for t_{LR} seconds and helps purge adsorbed N_2 from the column, replacing it with high purity CH_4.

4. **Co-current Feed Pressurization (FP):** This step is analogous to the 3-step cycle.

These constituent steps are shown in Fig. 7.2 with their corresponding pressure profiles. A Skarstrom cycle simulation requires eight input variables, with the first seven being those of the 3-step cycle and the remaining input being the light-reflux time (t_{LR}). The light reflux time was forced to be less than the adsorption time with the following constraint (in seconds):

$$t_{\mathrm{ADS}} - t_{\mathrm{LR}} \geq 0.1 \text{ [s]} \tag{7.5}$$

Again, the feed pressurization time was fixed at 20 seconds to ensure the adsorption step always restarted at the adsorption pressure. The range of input variables for the Skarstrom cycle are also given in Table 7.4.

7.2.5 Process Performance Metrics

After a PSA process reaches cyclic steady state, its process performance can be evaluated using key process performance indicators such as the purity (Pu), recovery (Rec) and productivity (Pr). The CH_4 purity is defined below:

$$\text{Pu} = \frac{n_{\text{CH}_4}^{\text{ADS,out}}}{n_{\text{CH}_4}^{\text{ADS,out}} + n_{\text{N}_2}^{\text{ADS,out}}} \tag{7.6}$$

In both the 3-step and Skarstrom cycles, the high-pressure raffinate product is collected at the column effluent during the adsorption step. This gas is a mixture of both CH_4 and N_2, therefore both the molar quantities of CH_4 ($n_{\text{CH}_4}^{\text{ADS,out}}$) and N_2 ($n_{\text{N}_2}^{\text{ADS,out}}$) leaving the column are required to determine the purity. Purity will be the key process performance metric, due to the pipeline transport specification of ≥ 96 mol% CH_4.

The CH_4 recovery is calculated with the following equation:

$$\text{Rec} = \frac{n_{\text{CH}_4}^{\text{ADS,out}}}{n_{\text{CH}_4}^{\text{ADS,in}} + n_{\text{CH}_4}^{\text{FP}}} \tag{7.7}$$

Methane only enters the process in the adsorption and feed pressurization steps. The corresponding molar quantities are ($n_{\text{CH}_4}^{\text{ADS,in}}$) and ($n_{\text{CH}_4}^{\text{FP}}$) in the adsorption and feed pressurization steps, respectively. There is no recovery specification, but a high recovery is preferred to minimize losses. In an actual process, recovery has a cost associated with it.

The process productivity is defined as:

$$\text{Pr} = \frac{m_{\text{CH}_4}^{\text{ADS,out}}}{(\text{total adsorbent volume}) \times t_{\text{cycle}}} \tag{7.8}$$

The volume of adsorbent was fixed for all of the simulations performed. The cycle time, t_{cycle}, which is equal to the sum of all constituent step times in a given PSA process, did change for each simulation. This value is calculated with the following equation: $t_{\text{cycle}} = t_{\text{ADS}} + t_{\text{EVAC}} + t_{\text{LR}} + t_{\text{FP}}$.

7.2.6 Machine Learning Optimization Framework

A primary goal of the current work is to calculate the trade-offs between key performance indicators. This can be done by coupling a global search method, such as the nondominated sorting genetic algorithm II (NSGA-II), with the detailed PSA process simulator [19]. This methodology starts with an initial population of samples (combinations of input variables or operating conditions). Each sample is fed to the PSA process simulator that solves the detailed model to calculate the purity, recovery and productivity. After the key performance indicators for the initial population are computed, combinations of the best performing samples are made and a second generation is fed to the process simulator. This process continues until a predefined number of generations has been completed. In this work, we refer to this approach as the traditional framework. This framework has been applied in many studies for different adsorbent-adsorbate combinations and has been experimentally validated [17, 19].

While the traditional framework is able to determine the optimal operating conditions of a given PSA process, it is quite computationally expensive as the detailed model must be calculated until cyclic steady state. For a CO_2 capture vacuum swing adsorption (VSA) process, using zeolite 13X, the traditional optimization framework takes about 550 core-hours to finish a single optimization [166]. One possible alternative, that has been successfully used, is to replace the detailed PSA process simulator with a surrogate model [166]. A surrogate model is a function of the form $\bar{y} = \hat{f}(X_i)$, where X_i is a vector containing the input variables (one sample) and $\bar{y}$ is an estimate of a process performance indicator (either purity, recovery or productivity). The function $\hat{f}(X_i)$ can be estimated using training data that is either from a detailed model or experiments. Since PSA experiments can be time consuming and expensive, numerical simulations are used in this study.

A machine learning surrogate model must be trained with samples in order to

regress the input variables, X_i, to the output variables (process performance indicators), $\bar{y}$. The goodness of fit depends on how well the sample space is represented in the trained samples. To ensure a representative sampling, Latin hypercube sampling (LHC) was used to generate 10000 samples for both cycles in this study. These samples, a vector of the PSA process operating conditions, were then run in the detailed process simulator to determine the purity, recovery and productivity. For this study we used 6325 samples for the 3-step cycle and 4096 for the Skarstrom cycle to train the machine learning surrogate models. A sensitivity analysis in the Supporting Information shows that 3000 samples is sufficient ($R^2_{\text{adj}} > 0.99$) in the ANN training for a 1-output, 8-input model. 15% of the remaining samples were used as a test set of samples to validate that the regression models are not over-fitted. Approximately 3500 core-hours were needed to generate the samples and train the surrogate models in this study. This is the time required for about six iterations of the traditional optimization framework [166].

Previous studies have compared the performance of various machine learning surrogates, and artificial neural networks (ANN) have been found to perform well in PSA systems [36]. Accordingly, ANNs were used as the machine learning surrogate model in this study. ANN uses multiple layers of "neurons" to construct a nonlinear set of equations between the input and output variables. Additional "hidden" layers may be added to develop more complicated relationships between the input and output variables. The best combination found for the 3-step and Skarstrom cycles were 3 hidden layers, each containing 8 neurons (shown in the Supporting Information). This is similar to what was found in a previous study [36]. Bayesian regularization with back propogation was used to train the neural network architecture.

Parity plots of the PSA process simulator (detailed model) outputs and the ANN surrogate model outputs can be found in Fig. 7.3 for both the 3-step and Skarstrom cycles. For both cycles, the ANN surrogate model agrees very well with the samples from the detailed simulations, with some deviations for the recovery and especially

Table 7.5: The sampling space for the Skarstrom and 3-step cycles used to train the ANN machine learning models. Note that $t_{LR} = 0$ for the 3-step cycle.

Bound	t_{ADS} [s]	t_{EVAC} [s]	t_{LR} [s]	P_L [kPa]	P_H [kPa]	v_{feed} [m/s]	y_{feed} [CH_4 mol%]	T_{feed} [°C]
High	200	200	199	90	700	2.0	96	70
Low	2	2	1	1	95	0.001	40	10

purity. The R^2_{adj} was greater than 0.99 in all cases. For both the 3-step and Skarstrom cycles, the ANN model productivity predictions are almost exactly the same as the detailed process simulation. This is likely due to the fact the process step times (t_{ADS}, t_{EVAC}, t_{LR}), which are involved in the calculation of productivity, are inputs to the surrogate model and that the volume of the adsorbent is fixed. This allows the ANN model to easily map the input space to the productivity. The recovery ANN model predictions are also described very well. While the ANN model deviates mildly from the detailed simulation predictions, the overall predictions rarely deviate more than ±3%, which is shown as the blue highlighted region in Fig. 7.3. There are more outliers present for the Skarstrom cycle, but this is mostly in a range where the optimizations do not need to be extremely accurate (less than about 50% recovery). Purity, in both processes, contained the most outliers and is a less optimal fit that than other performance metrics; this unfortunately also occurs within the range of interest (> 90 mol% purity). However, the quantity of outliers is still a small percentage of the overall number of points in the training set (at least 4096 samples).

An optimization framework using the trained ANN surrogate models could then be developed. The sequence steps are detailed below:

1. Determine the optimal operating conditions using the ANN surrogate models for either purity-recovery or recovery-productivity (with a constraint of Pu ≥ 96 mol% CH_4) using the NSGA-II genetic algorithm. This step was repeated at least 4 times to ensure a global optimum and to reduce the effect of outliers.

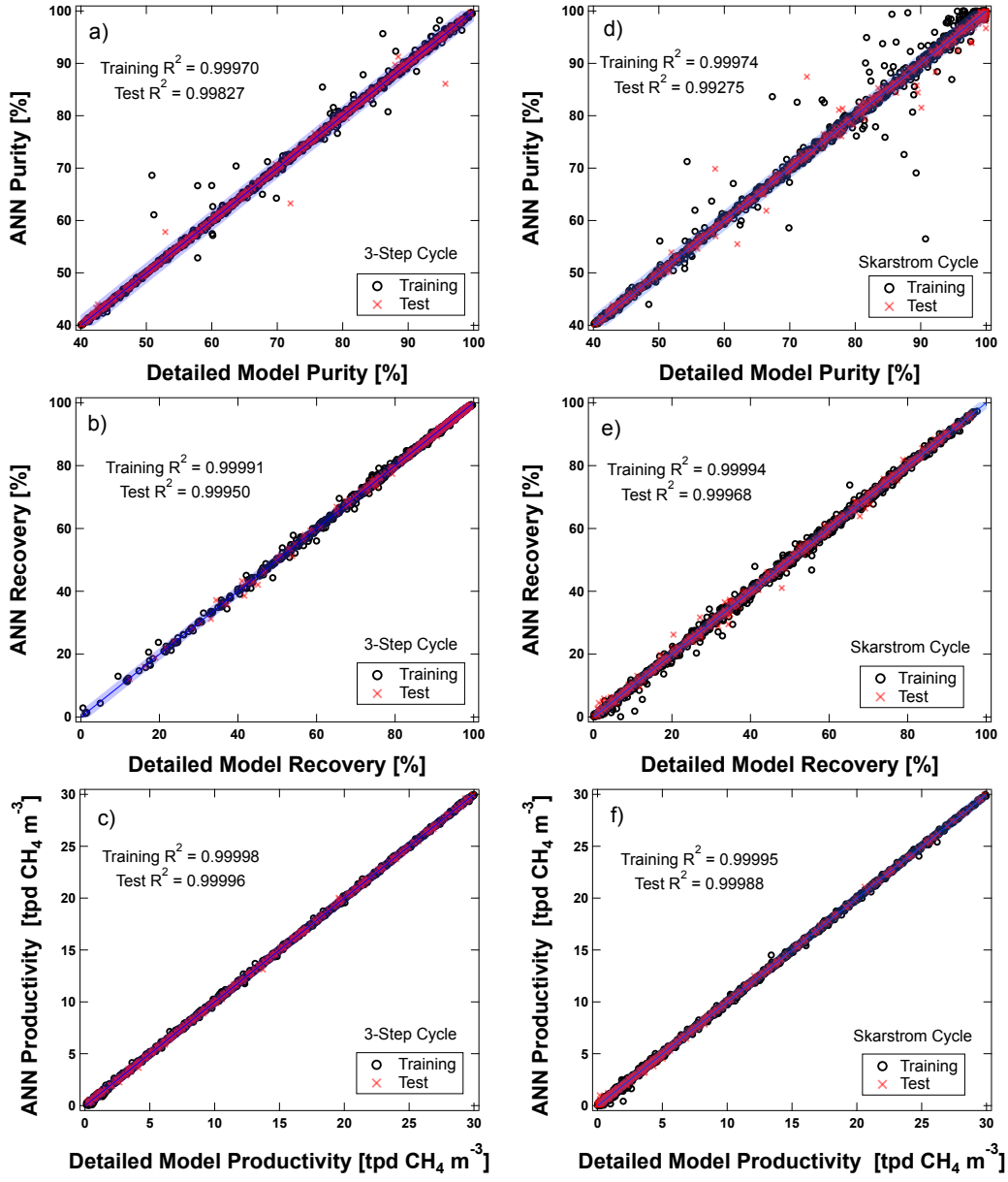

Figure 7.3: Parity plots of purity, recovery and productivity against the predicted values from the trained artificial neural network models for the 3-step cycle (panels **a**, **b**, **c**) and Skarstrom cycle (panels **d**, **e**, **f**). 15% of each training set (shown as red 'x' markers) was used as a test set.

The number of generations was limited to 50.

2. The trade-off curve was extracted from each of the previous optimizations and combined.

3. These operating conditions were then fed to the detailed PSA process simulator to calculate the detailed model process performance indicators. These are the reported values in the trade-off curves that are presented in this study.

The first two steps of this framework are analogous to the traditional framework explained earlier, but using a surrogate model instead of the detailed process simulator.

In this work two sets of multi-objective optimizations were performed. The first one dealt with the simultaneous maximization of CH_4 purity and recovery for a Pu $\geq$ 96 mol%. The second dealt with the maximization of recovery and productivity. The following objective functions were used to determine the purity-recovery and recovery-productivity trade-off curves:

$$J_{\mathrm{Pu}} = \frac{1}{\mathrm{Pu}} \tag{7.9}$$

$$J_{\mathrm{Rec}} = \frac{1}{\mathrm{Rec}} \tag{7.10}$$

$$J_{\mathrm{Pr}} = \frac{1}{\mathrm{Pr}} + 5000 \times \max\left[0, (0.96 - \mathrm{Pu})\right]^2 \tag{7.11}$$

The objective function for Pr includes a penalty function for the CH_4 purity tolerance of 96 mol%.

The final step ensures accuracy and removes possible outliers generated from the ANN surrogate models. All of the Pareto curves shown in this study follow this framework. The trade-off curve depicts the best trade off between purity-recovery or recovery-productivity in a given PSA process; points at values greater than the trade-off curve are infeasible, and points with lower values than the trade-off curve are sub-optimal.

7.3 Optimization of the 3-Step Cycle

Using the trained ANN surrogate models, a series of parametric process optimizations were performed at different operating conditions. The separation of natural gas, or landfill gas, is not well defined and therefore, the feed composition ($y_{CH_4,feed}$ and $y_{N_2,feed}$), feed temperature (T_{feed}) and adsorption pressure (P_H) can vary as the methane source changes. In the literature, these conditions are: a molar feed composition between $y_{CH_4,feed} = 0.30$ and 0.92, a feed temperature between $T_{feed} = 20$ and 40°C and adsorption pressures from ambient up to 45 bar [12, 16, 17, 106]. Due to this wide range of possible operating conditions, three feed compositions ($y_{CH_4,feed} = 0.55$, 0.80 and 0.92), three feed temperatures (T_{feed} = 30, 40 and 50°C) and a range of adsorption pressures ($P_H = 100$ to 500 kPa) were selected to generate purity-recovery trade-off curves. A small bound was added to each temperature (±1°C) and pressure (±5 kPa) range studied to ensure numerical stability; for example a parametric optimization at 30°C would be allowed to vary between $29 - 31$°C and a parametric optimization at 100 kPa would be allowed to vary between $95 - 105$ kPa. This range was not added for any of the methane mole fractions listed above.

The next sections describe the effects of different parametric optimizations on the 3-step cycle process performance. In this study, a parametric optimization is an optimization performed at either a CH_4 molar feed composition of 0.55, 0.80 or 0.92, with the feed temperature and adsorption pressure fixed, a feed temperature of 30, 40 or 50°C with the methane feed composition and adsorption pressure fixed, or finally an adsorption pressure of 100 kPa or varied between 100 and 500 kPa with the methane feed composition and feed temperature fixed. The other input variables were allowed to vary within the ranges given in Table 7.4.

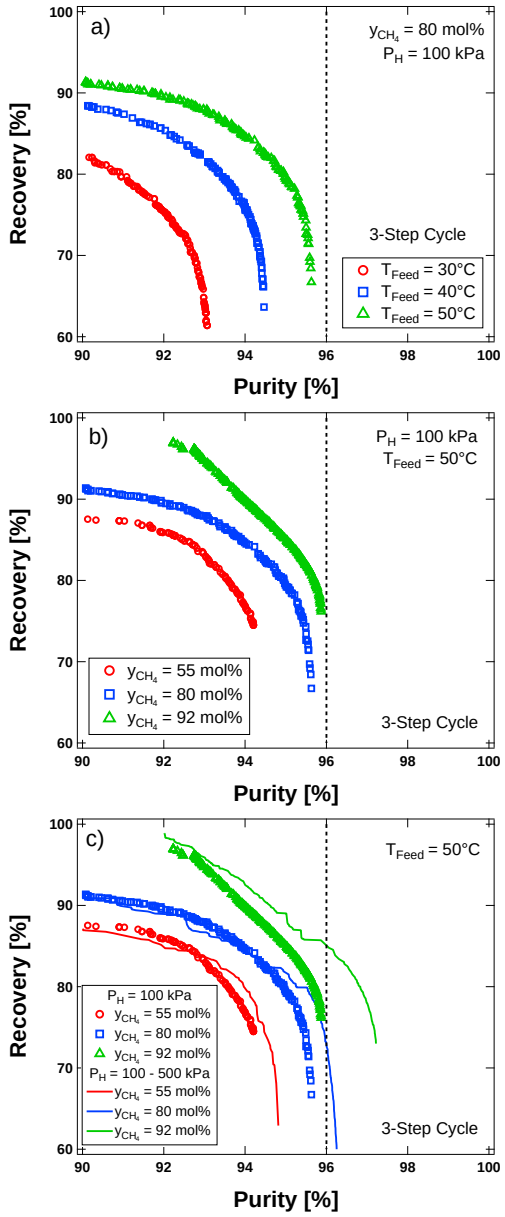

Figure 7.4: 3-step cycle optimization results for the simultaneous maximization of purity and recovery of CH_4. (**a**) The effect of feed temperature (T_{feed} = 30, 40 or 50°C) at a fixed feed composition ($y_{CH_4,\text{feed}}$ = 0.80) and high pressure (P_H = 100 kPa). (**b**) The effect of CH_4/N_2 feed composition ($y_{CH_4,\text{feed}}$ = 0.55, 0.80 or 0.92) at a fixed feed temperature (T_{feed} = 50°C) and high pressure (P_H = 100 kPa). (**c**) The effect of feed pressure (P_H = 100 or 100 − 500 kPa) at a variable feed composition ($y_{CH_4,\text{feed}}$ = 0.55, 0.80 or 0.92) and a fixed feed temperature (T_{feed} = 50°C). In panel (**c**), the lines have a variable high pressure from from 100 to 500 kPa, while hollow markers have a fixed high pressure at 100 kPa.

7.3.1 Effect of Feed Temperature

The 3-step cycle was first studied at a fixed adsorption pressure ($P_{\mathrm{H}} = 100$ kPa) and methane composition ($y_{\mathrm{CH_4,feed}} = 0.80$) with a variable feed temperature ($T_{\mathrm{feed}} = 30$, 40 and 50°C). A Pareto curve was generated for each temperature at these operating conditions and are shown in Fig. 7.4(**a**). It is clear from Fig. 7.4(**a**) that at an adsorption pressure of 100 kPa and methane feed composition of 80 mol% CH_4, a higher feed temperature yields a better recovery at a desired purity. It also appears that as the process temperature increases, from 30 to 50°C, some methane purities that were previously infeasible are now possible. The maximum purities at a process temperature of 30, 40 and 50°C are 93.1, 94.5 and 95.6 mol%, respectively. Note that none of these conditions are able to meet the 96 mol% purity requirement, although 50°C is just below the pipeline specification.

This observation is likely due to the high isosteric heats of adsorption for N_2 (40 to 67 kJ/mol) on V-MOF. This was explored through axial-bed profiles at optimal operating conditions at 30, 40 and 50°C, to see how recovery is affected at a fixed calculated purity. Since the 3-step cycle was not able to achieve 96 mol% CH_4 purity under these conditions, a lower value of 93 mol% was chosen to study. These trends are shown in Fig. 7.5(**a**). Six axial profiles are shown, the top three being those for the adsorption step at a given temperature, and the bottom three for the corresponding evacuation step at cyclic steady-state. In Fig. 7.5, $z/L = 0$ is the feed end of the column and $z/L = 1$ is the product end. As seen in Fig. 7.5(**a**), as the temperature lowers from 50 to 30°C, more CH_4 is able to be loaded into the column. At 50°C, the V-MOF bed is almost entirely loaded at 0.1 mol/kg CH_4 or lower ($0.10 < z/L < 0.86$), while half of the bed ($z/L \geq 0.51$) at 30°C is at 0.2 mol/kg CH_4 loading or greater. For all three temperatures, essentially all the adsorbed CH_4 is removed in the following evacuation step. The evacuation steps do follow the same pattern as the adsorption profiles, where at lower temperatures more CH_4 remains loaded. However, these

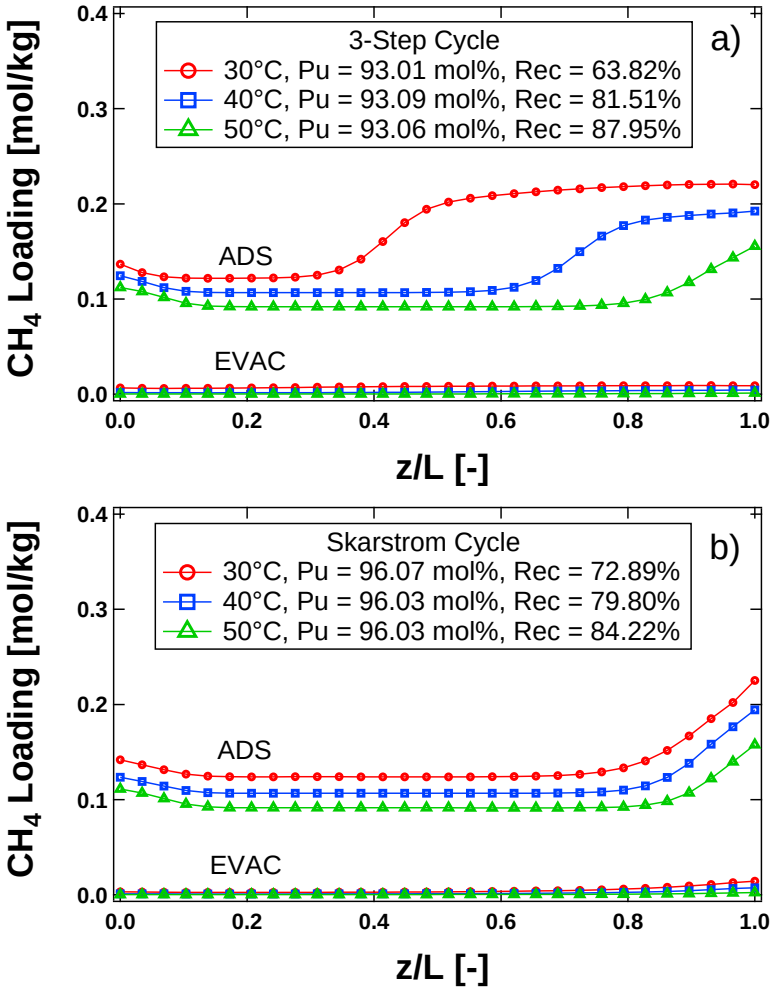

Figure 7.5: Adsorption and evacuation step axial profiles on $V_2Cl_{2.8}$(btdd) at 30, 40 and 50°C feed temperatures for the (**a**) 3-step and (**b**) Skarstrom cycle optimal operating conditions for 93 mol% or 96 mol% CH_4 purity, respectively.

values are all very small $\approx 1 \times 10^{-3}$ to 9×10^{-3} mol/kg compared to the quantity loaded during adsorption. These axial bed profiles show that between the adsorption and evacuation steps, a large quantity of CH_4 is lost per unit cycle, and this quantity increases as the temperature decreases (at optimal operating conditions). This is shown by the area between an ADS and EVAC axial profile at any given temperature. This quantity of lost CH_4 is directly responsible for the reduction in recovery at a fixed optimal CH_4 purity.

7.3.2 Effect of Feed Composition

A similar study was conducted at a fixed adsorption pressure (P_{H} = 100 kPa) and feed temperature (T_{feed} = 50°C) with a variable feed composition ($y_{\mathrm{CH_4,feed}}$ = 0.55, 0.80 and 0.92). This was done to determine which feed compositions, if any, were able to meet the pipeline purity specification of 96 mol% CH_4. 55 mol% CH_4 was also considered to include a large range of CH_4 compositions found in the literature; even though it is unlikely to make the 96 mol% purity requirement, since 80 mol% CH_4 was insufficient in the previous optimizations. A feed temperature of 50°C was chosen since it outperformed both 30 and 40°C in the previous parametric optimization. These results are shown in Fig. 7.4(**b**).

As the methane feed composition increases, the separation performance increases. In other words, at a feed temperature of 50°C and adsorption pressure of 100 kPa, a methane feed composition of 92 mol% outperforms 80 mol%, which outperforms 55 mol%. This is seen as the trade-off curve travels into the top-right corner of the figure. This is expected for a raffinate cycle. As the feed composition of the light-product increases, the separation should be facilitated. This is also seen in the three curves for a given CH_4 purity. For example, at 94 mol% CH_4 purity, the optimal recovery increases as the feed composition increases. At 94 mol% CH_4 purity, a feed of 55, 80 and 92 mol% CH_4 can optimally recover 77.1, 84.5 and 90.0% of the fed methane, respectively. However, still none of the feed compositions are able to meet the 96 mol% purity requirement. The closest is a methane feed composition of $y_{\mathrm{CH_4,feed}} = 0.92$, which barely misses the pipeline specification at 95.9 mol% CH_4 and 76.1% recovery. Methane feed compositions of $y_{\mathrm{CH_4,feed}} = 0.55$ and 0.80 are able to purify methane above 90 mol%, but are limited to 94.2 and 95.6 mol%, respectively.

7.3.3 Effect of Feed Pressure

The previous parametric optimizations at a feed temperature of 50°C and feed compositions of 55, 80 and 92 mol% CH_4 were optimized again allowing the adsorption

pressure to vary from 100 to 500 kPa. It should be noted that 500 kPa is a significant extrapolation of the equilibrium data given for V-MOF by Jaramillo *et al.* [163]. The experimentally measured equilibrium data for both CH_4 and N_2 on V-MOF goes only up to $\approx$ 100 kPa.

These parametric optimizations were performed to determine if a pressure-vacuum swing adsorption (PVSA) process would improve the process performance of the 3-step cycle. Also, collecting methane at a high pressure is preferred since less energy is required to liquefy the raffinate gas for pipeline transport. However, on the one hand, the N_2 isotherm exhibited by V-MOF is very rectangular, signifying that an increase in pressure likely will not drastically improve the process performance. On the other hand, a mild purity improvement in the trade-off curves in Fig. 7.4(**b**) could be enough to obtain a 96 mol% CH_4 purity. For a methane feed composition of 80 or 92 mol%, this required improvement is less than 1 mol% purity. For 55 mol%, an improvement of 2 mol% purity is required to obtain the pipeline transport specification.

The PVSA results are shown in Fig. 7.4(**c**). As seen in Fig. 7.4(**c**), a mild improvement in methane purity for all compositions was found. This improvement was enough to achieve the 96 mol% purity requirement for both $y_{CH_4,feed} = 0.80$ and 0.92. The recoveries for $y_{CH_4,feed} = 0.80$ and 0.92 were at 79.6% and 85.7% at 96 mol% CH_4 purity, respectively. However, the increase in purity was not enough to reach pipeline specifications for a feed CH_4 composition of 55 mol%. The maximum CH_4 purity for a methane feed composition of 55 mol% was 94.8 mol% at a 62.9% recovery. An interesting observation is seen in Fig. 7.4(**c**) where the higher adsorption pressures only seem to help at relatively high methane purities. This occurs just before 94 mol% purity for a methane feed composition of 55 mol% and about 95 mol% for both 80 and 92 mol% methane in the feed.

The optimal adsorption pressures that could obtain 96 mol% purities were found between 200 and 400 kPa, as seen in Fig. E.6. Specifically for a methane feed composition of 80 mol%, the optimal adsorption pressures were found between 316 and

355 kPa. For 92 mol%, these values lowered to adsorption pressures between 254 and 274 kPa. It should be noted that the corresponding evacuation pressures were all between $3-4$ kPa, suggesting that optimal conditions are found at the deepest allowable evacuation pressures. This result is consistent with previous studies [19], where the optimizer tends toward the lower vacuum bound to remove the most adsorbed material possible. While 55 mol% CH_4 in the feed does not meet the 96 mol% purity specification, its purity-recovery trade-off curve does improve at higher pressures. These adsorption pressures are lower than both 80 and 92 mol%, at approximately 184 kPa for purities above 92 mol%.

7.4 Optimization of the Skarstrom Cycle

Similar to the previous section, a series of parametric optimizations were performed for the Skarstrom cycle. Again, combinations of feed compositions ($y_{CH_4,feed} = 0.55$, 0.80 or 0.92), feed temperatures ($T_{feed} = 30$, 40 or 50°C) and adsorption pressures ($P_H = 100 - 500$ kPa) were explored to determine at which operating conditions the Skarstrom cycle is able to produce 96 mol% methane and at which recoveries. The other input variables were allowed to vary within the ranges given in Table 7.4.

7.4.1 Effect of Feed Composition and Temperature

The parametric optimizations for feed composition and temperature were repeated for the Skarstrom cycle. These include a parametric optimization at a fixed adsorption pressure ($P_H = 100$ kPa) and methane composition ($y_{CH_4,feed} = 0.80$) with a variable feed temperature ($T_{feed} = 30$, 40 and 50°C) or a fixed feed temperature ($T_{feed} = 50$°C) and adsorption pressure ($P_H = 100$ kPa) with a variable feed composition ($y_{CH_4,feed} =$ 0.55, 0.80 and 0.92).

Figure 7.6(**a**) shows the parametric optimizations for a variable feed temperature ($T_{feed} = 30$, 40 or 50°C) with the methane feed composition and adsorption pressure fixed at 80 mol% CH_4 and 100 kPa. As with the 3-step cycle, the process performance

increases with an increasing feed temperature. The main observation is the Skarstrom cycle is able to purify CH_4 above 96 mol% at all temperatures. The first point to cross the 96 mol% purity threshold for $T_{\text{feed}} = 30$, 40 and 50°C are at 72.9%, 79.8% and 84.2% recovery, respectively. All of these feed temperatures also are able to achieve much greater methane purities; this was as high as 99.5 mol% at 50°C. The axial bed profiles were also studied to determine how temperature effects recovery at an optimal purity. In this case, the Pareto point that could achieve 96 mol% CH_4 in the Skarstrom cycle was studied to see the effect of methane loading as a function of temperature. The axial bed profiles for these conditions are shown in Fig. 7.5(**b**). Similarly to the 3-step cycle, as the temperature decreases, the quantity of CH_4 loaded into the column during the ADS step increases. These values plateau in the mid-section of the V-MOF bed ($0.10 < z/L < 0.86$), and are approximately 0.091, 0.107 and 0.124 mol/kg CH_4 at 50, 40 and 30°C, respectively. This also is found in the EVAC profiles, but to a much lesser extent. These methane evacuation loadings range from $\approx 3 \times 10^{-4}$ mol/kg (50°C) to 3×10^{-3} mol/kg (30°C) at their lowest values. Essentially all the adsorbed methane is removed in the EVAC step. The area between a given temperature's ADS and EVAC profile shows the amount of CH_4 lost in a given cycle. This increases as the feed temperature decreases from 50 to 30°C, demonstrating the same behavior as in the 3-step cycle.

Figure 7.6(**b**) shows the parametric optimizations for a variable feed composition ($y_{\text{CH}_4,\text{feed}} = 0.55$, 0.80 or 0.92) at a fixed feed temperature (50°C) and adsorption pressure (100 kPa). Again, 50°C was chosen as a feed temperature since it outperformed the other temperatures in the previous parametric optimization. The same observation is made as for the 3-step cycle. As the composition of methane increases in the feed, the separation performance increases. All three feed compositions are able to achieve 96 mol% methane purity. The first point that achieves the pipeline specification for $y_{\text{CH}_4,\text{feed}} = 0.55$, 0.80 or 0.92 are: 80.3%, 84.2% and 88.3% recovery, respectively. Unlike the feed temperature parametric optimizations, the three

trade-off curves are less stratified and seem to converge around 99 mol% CH_4. For both the temperature and composition parametric optimizations, the 96 mol% purity requirement was met.

7.4.2 Effect of Feed Pressure

The methane feed composition parametric optimizations were re-run allowing the adsorption pressure to vary between 100 to 500 kPa. These were performed to determine if a PVSA process would improve the process performance of the Skarstrom cycle, like what was observed for the 3-step cycle. These optimizations were conducted at 50°C with a variable feed composition of methane at either $y_{CH_4,feed} = 0.55$, 0.80 or 0.92. The results are shown in Fig. 7.6(**c**).

As seen in Fig. 7.6(**c**), a marginal improvement in methane recovery for $y_{CH_4,feed} = 0.55$ and 0.80, at a given purity, was found in some purity regions. For $y_{CH_4,feed} = 0.55$, this region with an improved recovery is approximately between 94 and 98 mol% purity and for $y_{CH_4,feed} = 0.80$ a wider region is found up to almost 99 mol% purity. This improvement in recovery is limited to about 2%, with most improvements, at a given purity, being less than 1%. For a feed composition of $y_{CH_4,feed} = 0.92$, no improvement in purity is found, except past 99 mol% purity, where the optimizer was now able to find additional trade-off points. These results suggest that there is a minimal improvement with high pressure operation. The range of optimal adsorption pressures, corresponding to these parametric optimizations, are found in Fig. E.7. As seen in Fig. E.7, for all feed compositions meeting the 96 mol% purity specification, the optimal adsorption pressures are between 95 and 200 kPa before a purity of 99 mol%. These pressure bounds are between $97-133$, $100-123$ and $102-158$ kPa for $y_{CH_4,feed} = 0.55$, 0.80 and 0.92 methane feed compositions, respectively. After a purity of 99 mol% CH_4, the three feed compositions find optimal adsorption pressures well above 150 kPa, being as high as 327 kPa when $y_{CH_4,feed} = 0.55$ with a corresponding purity of 99.9 mol% CH_4 and recovery of 9.8%. Although, the region above 99 mol% purity

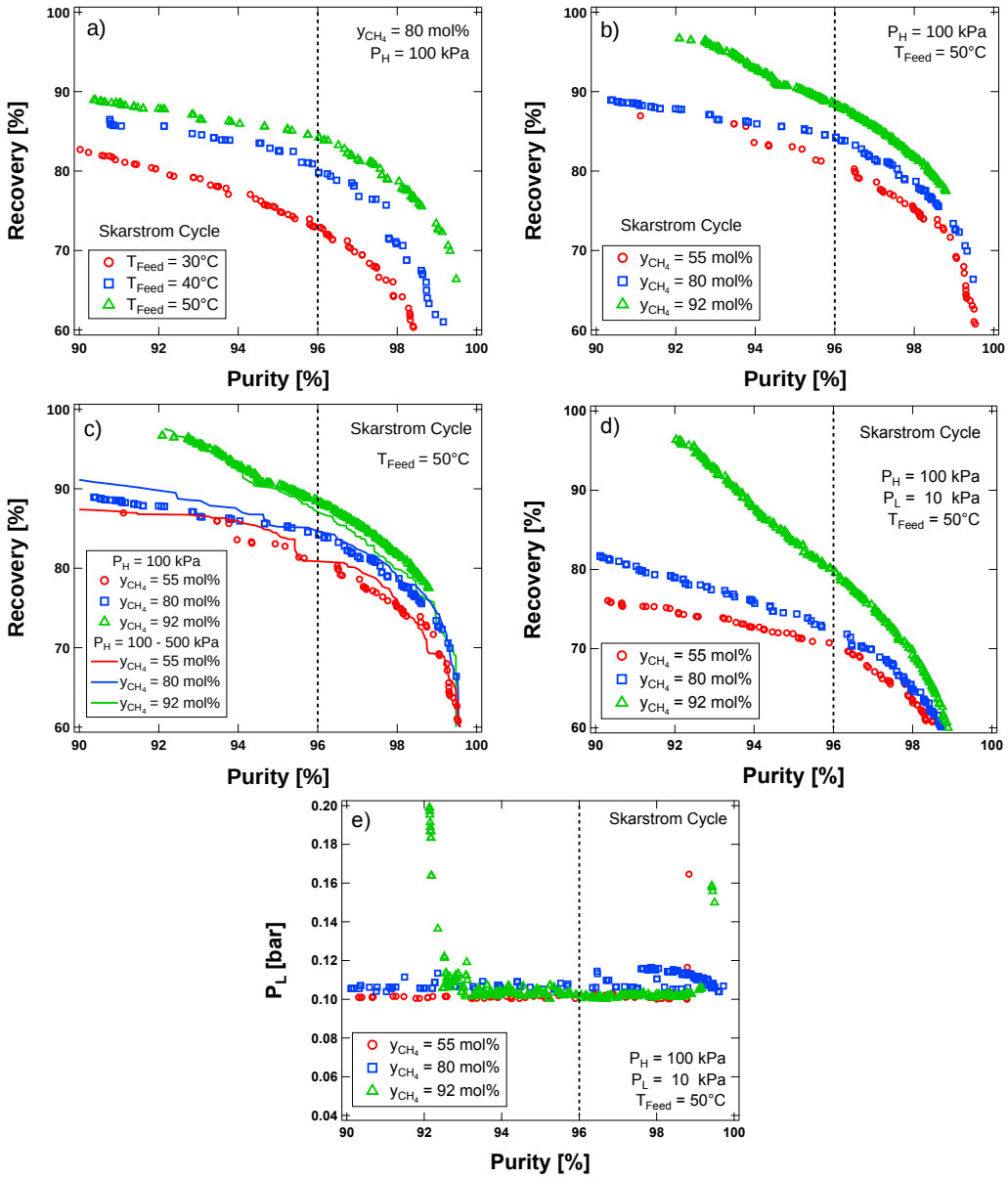

Figure 7.6: Skarstrom cycle optimization results for the simultaneous maximization of purity and recovery of CH_4. (**a**) The effect of feed temperature ($T_{\text{feed}} = 30$, 40 or 50°C) at a fixed feed composition ($y_{CH_4,\text{feed}} = 0.80$) and high pressure ($P_{\text{H}} = 100$ kPa). (**b**) The effect of CH_4/N_2 feed composition ($y_{CH_4,\text{feed}} = 0.55$, 0.80 or 0.92) at a fixed feed temperature ($T_{\text{feed}} = 50$°C) and high pressure ($P_{\text{H}} = 100$ kPa). (**c**) The effect of feed pressure ($P_{\text{H}} = 100$ or $100-500$ kPa) at a variable feed composition ($y_{CH_4,\text{feed}} = 0.55$, 0.80 or 0.92) and a fixed feed temperature ($T_{\text{feed}} = 50$°C). In panel (**c**), the lines have a variable high pressure from from 100 to 500 kPa, while hollow markers have a fixed high pressure at 100 kPa. (**d**) The effect of an elevated evacuation pressure ($P_{\text{L}} = 10-60$ kPa) at a fixed feed composition ($y_{CH_4,\text{feed}} = 0.80$), temperature ($T_{\text{feed}} = 50$°C) and pressure ($P_{\text{H}} = 100$ kPa). Panel (**e**) contains the evacuation pressures corresponding to the trade-off curves in panel (**d**).

yields fairly poor recoveries for all feed compositions, the maximum of any being 72.3% (99.0% purity, $y_{CH_4,feed} = 0.92$). However, the points that barely achieve the pipeline transport specification are all just above ambient pressure. The adsorption pressures at the first available point to achieve the pipeline transport specification for the three feed compositions are: 118, 100 and 128 kPa for $y_{CH_4,feed} = 0.55$, 0.80 and 0.92 methane feed compositions, respectively. While some improvements in recovery are possible for the Skarstrom cycle at slightly superambient pressures, it is likely not worth pressurizing landfill gas above ambient pressure to achieve 96 mol% purity CH_4.

7.4.3 Effect of Evacuation Pressure

The evacuation pressure bounds for the the previous parametric optimizations have been 3 to 60 kPa for both the 3-step and Skarstrom cycles. Since both N_2 and CH_4 are type-I isotherms on V-MOF, the optimizer generally finds optimal points very close to the lower bound (about $3-5$ kPa); suggesting that the cycle performs optimally at the deepest allowed evacuation pressures. These results are consistent with what is expected for type-I isotherms, the optimal operation is when the column is completely regenerated, or tends towards complete regeneration [19]. While it is common in PSA process optimization studies to consider an evacuation pressure of $P_L = 3$ kPa, many commercial vacuum pumps become less efficient as the vacuum pressure decreases [167]. As the adsorbent bed size increases, the loss in efficiency increases the time, and energy, necessary to achieve a desired vacuum level [167]. Therefore, the last parametric optimization performed was to determine the effect of evacuation pressure on the process purities and recoveries. From the previous parametric optimizations, which again all allowed the possibility for evacuation pressures between $3 - 60$ kPa, it is expected that the process performance will suffer; but, the question is whether the pipeline transport specification is still achieved and at which recoveries.

These optimizations were performed at 50°C with a variable feed composition of

methane at either $y_{CH_4,feed} = 0.55$, 0.80 or 0.92 with P_H fixed at 100 kPa. The evacuation pressure (P_L) bound was changed from $3 - 60$ kPa to $10 - 60$ kPa to consider values greater than 10 kPa. The results are shown Fig. 7.6(**d**). As expected, the higher evacuation pressure bounds performed less optimally. All three methane feed compositions were still able to achieve 96 mol% purity, however at reduced recoveries. In other words the purity-recovery trade-off curve shifted towards the bottom-left corner of the figure. For at least 96 mol% purity, the three methane feed compositions, $y_{CH_4,feed} = 0.55$, 0.80 and 0.92, were able to achieve recoveries of 69.7%, 71.8% and 79.8%, respectively. These recoveries are significantly smaller than their equivalents with a $3 - 60$ kPa evacuation pressure bound; these recovery values are: 80.3%, 84.2% and 88.3%, respectively, a decrease of $8.5 - 12.4\%$ recovery. As seen in Fig. 7.6(**e**), the optimized evacuation pressures all tended toward 10 kPa. This is especially apparent in the purity region greater than 96 mol%. The evacuation pressure does increase slightly to approximately 12 kPa as purity increases above 98 mol%, but this region is also where the methane recovery drops to less than 65%. From these optimizations is it clear that the Skarstrom cycle can operate at an elevated evacuation pressure and achieve 96 mol% purity methane for the entire range of feed compositions studied ($55 - 92$ mol%). This comes at the cost of an $\approx 10\%$ lower methane recovery at a given purity.

7.4.4 Comparison with the 3-Step Cycle

From the previous parametric optimizations, it is clear that the Skarstrom cycle outperforms the 3-step cycle. Every set of parametric optimizations for the Skarstrom cycle was able to achieve 96 mol% CH_4, while only a handful were able for the 3-step cycle. One sample of the Skarstrom cycle was taken to highlight the differences between the cycles. The operating conditions for this point were $y_{CH_4,feed} = 80$ mol%, $T_{feed} = 50°C$, $t_{ADS} = 153.83$ s, $t_{EVAC} = 81.86$ s, $t_{LR} = 18.19$ s, $P_H = 100$ kPa, $P_L = 5.72$ kPa and $v_{feed} = 0.462$ m/s. This point was able to achieve 96.0 mol%

purity and 80.0% recovery. If this same point is run in the 3-step cycle ($t_{LR} = 0$), the purity drops to 86.7 mol%, but the recovery increases to 88.4%.

The solid-phase cyclic steady state (CSS) bed profiles for this sample are shown in Fig. 7.7, where $z/L = 0$ is the feed end and $z/L = 1$ is the product end of the column. The y-axis contains either the N_2 or CH_4 loading at that particular point within the column. Each constituent step is shown with a unique marker and color to aid comparisons between the two cycles. As seen in Fig. 7.7, during the ADS step, the Skarstrom cycle contains much more CH_4 (0.158 mol/kg) and much less N_2 (0.440 mol/kg) at the product end of the column ($z/L = 1$) than the 3-step cycle (0.105 and 0.650 mol/kg respectively). This allows for a relatively higher purity of CH_4 in the Skarstrom cycle compared to the 3-step cycle (for these particular conditions). The higher CH_4 recovery in the 3-step cycle likely is due to extra CH_4 removed in the Skarstrom cycle through the feed end of the column ($z/L = 0$) in the LR step. As seen for the Skarstrom cycle, the EVAC step CH_4 loading goes to the same level as the 3-step cycle, but afterwards a LR is performed and a small amount of CH_4 is lost. The CH_4 loading at the feed end of the column ($z/L = 0$) for LR is 0.015 mol/kg. The LR step does not exist in the 3-step cycle. While this is not a large amount of CH_4 at $z/L = 0$, it is enough to potentially lower the process recovery. However, The LR step is able to remove a significant amount of N_2 from the bed in the Skarstrom cycle. Between the EVAC and LR steps in the Skarstrom cycle, the N_2 loading reduces from 0.413 mol/kg to 0.173 mol/kg at the column effluent, where the raffinate CH_4 product is collected. This quantity of N_2 is not removed in the 3-step cycle, reducing the CH_4 purity. At the feed end of the column ($z/L = 0$), the profiles of both species are similar in the FP, ADS and EVAC steps of both cycles. With the addition of the LR step, the Skarstrom cycle is able to increase the CH_4 purity to the 96 mol% requirement, at the cost of a lower CH_4 recovery.

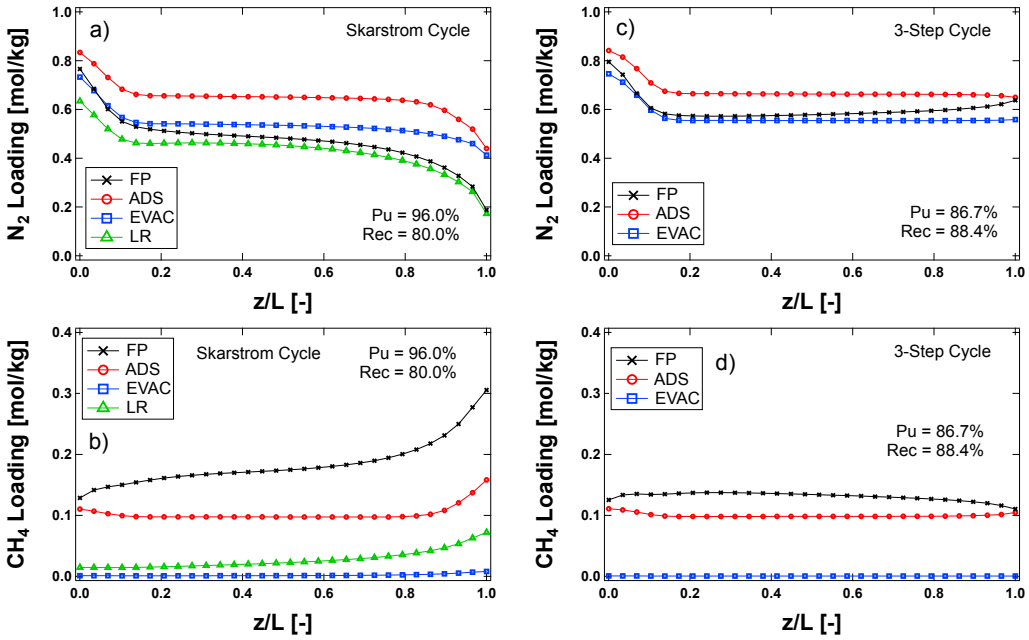

Figure 7.7: Skarstrom (**a**, **b**) and 3-step (**c**, **d**) cyclic steady state axial loading profiles from the detailed simulation. The operating conditions for this figure were $y_{CH_4,feed} = 80$ mol%, $T_{feed} = 50°C$, $t_{ADS} = 153.83$ s, $t_{EVAC} = 81.86$ s, $t_{LR} = 18.19$ s, $P_H = 100$ kPa, $P_L = 5.72$ kPa and $v_{feed} = 0.462$ m/s.

7.4.5 Recovery-Productivity Optimizations

Several combinations of operating conditions were able to achieve the pipeline purity specification for the Skarstrom cycle. Many of these conditions were able to produce methane at purities much greater than 96 mol%. Therefore, we can explore the recovery-productivity trade-off curve. The productivity is a measure of the quantity of methane captured (per volume adsorbent per time) in the PSA process and will be represented in units of tonne CH_4 m^{-3} day^{-1} (tpd m^{-3}). The productivity also provides insight into how the process would scale. These curves include points where a purity of at least 96 mol% CH_4 is achieved and are based on a single column of V-MOF. The previous parametric optimizations suggest that a VSA process ($P_H = 100$ kPa) operated at 50°C outperforms other studied conditions. These inputs variables were fixed and the feed composition of methane was varied to either $y_{CH_4,feed} = 55$, 80 or 92 mol%. The other input variables were allowed to vary within the ranges given in

Table 7.4. The results are shown in Fig. 7.8(**a**). As seen in Fig. 7.8(**a**), a higher feed composition is able to yield a higher recovery and productivity pairing at 96 mol% purity. Specifically at $y_{CH_4,feed} = 92$ mol%, the recoveries range from 85.1% to 89.4% with the productivities ranging from 21.18 to 10.96 tpd m^{-3}, respectively. This range for $y_{CH_4,feed} = 80$ mol% lowers to 73.0% to 84.0% with the productivities from 9.37 to 5.53 tpd m^{-3}. Finally, for $y_{CH_4,feed} = 55$ mol%, the recoveries are between 68.5% and 76.4% with the productivities ranging from 2.86 to 1.40 tpd m^{-3}. The results are intuitive, a process that starts with a greater quantity of methane is able to capture a greater quantity of methane. However, what is more interesting is the variability of allowable productivities. For $y_{CH_4,feed} = 92$ mol%, a small change in the recovery can change the productivity greatly. For example, the highest productivity of 21.18 tpd m^{-3} occurs at 85.1% recovery. This productivity drops to 10.92 tpd m^{-3} at 89.4% recovery. A 4% change in recovery nearly halves the allowable productivity. Similar behavior is seen for both for $y_{CH_4,feed} = 80$ and 55 mol%, but over wider ranges of recovery. These results show that high values of recovery are possible, at relatively lower productivities.

A study by Effendy *et al.* also looked at the trade-off between recovery and productivity for a kinetic PSA process using a CMS [17]. In particular, Effendy *et al.* studied a 6-step cycle that included the following constituent steps: adsorption, pressure equalization donor, counter-current blowdown, counter-current evacuation, pressure equalization receiver and co-current feed pressurization [17]. They provided recovery-productivity trade-off curves for this cycle at 25°C, an adsorption pressure of 800 kPa, and three feed compositions ($y_{CH_4,feed} = 80$, 85 and 90 mol%). A single recovery-productivity value (91.5%, 0.88 tpd m^{-3}) of the Molecular Gate SPEC PLANT, labeled Sr-ETS-4, was also included. These trade-off curves are shown in Fig. 7.8(**b**). The CMS is able to achieve productivities from 3.92 tpd m^{-3} at 51.6% recovery to 3.68 tpd m^{-3} at 53.1% recovery when the feed composition is 80 mol% methane. These values increase to 12.12 tpd m^{-3} at 77.2% recovery to 6.36 tpd m^{-3}

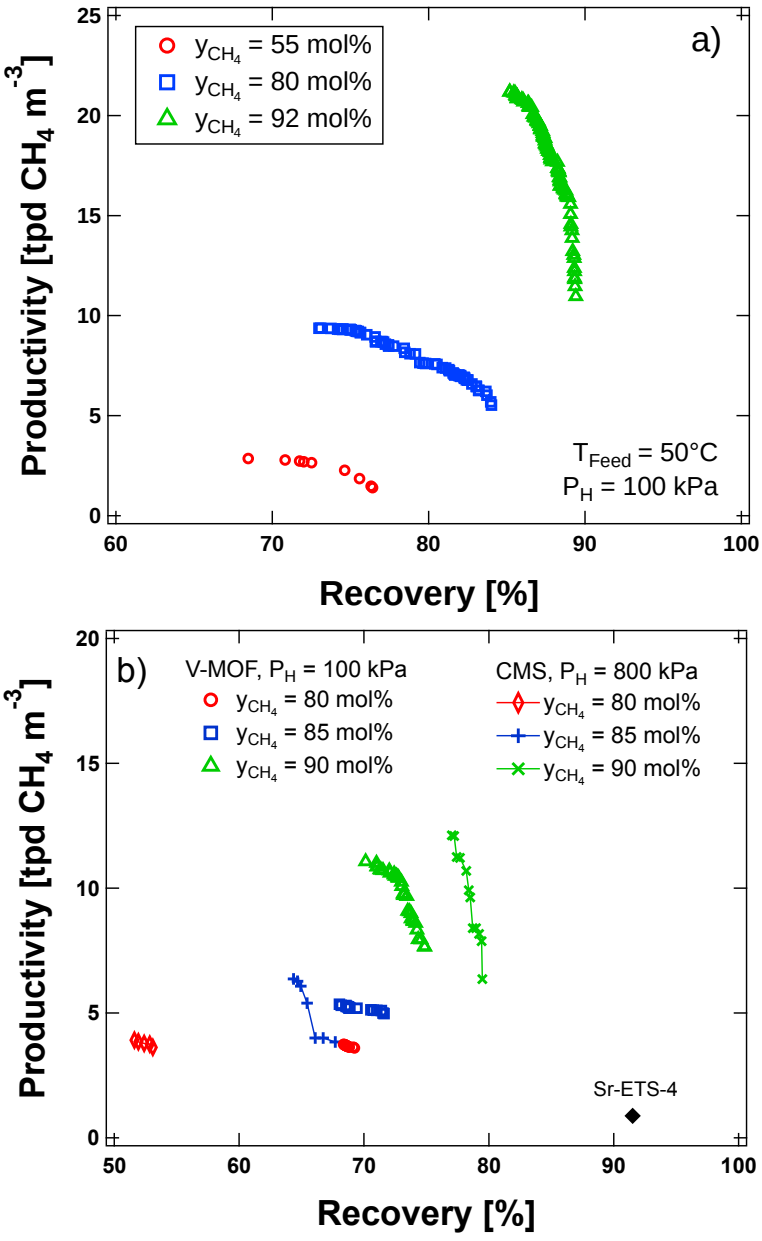

Figure 7.8: Recovery-productivity optimizations for the Skarstrom cycle for (**a**) a varied feed composition of CH_4/N_2 at 50°C and an adsorption pressure of 100 kPa. All of these points achieved the 96 mol% methane purity constraint. Panel (**b**) shows a comparison with a carbon molecular sieve and Sr-ETS-4 at 25°C obtained from the literature [17].

at 79.5% recovery when the feed composition is 90 mol% methane. These recovery-productivity curves were replicated using the V-MOF at 25°C, 100 kPa and the three methane feed compositions from Effendy *et al.* and are overlaid in Fig. 7.8(**b**). As seen, V-MOF is able to outperform the CMS in a simpler cycle if the methane composition is between 80 to 85 mol% CH_4; at 90 mol% CH_4, CMS outperforms the V-MOF. For a methane feed composition between $80-85$ mol%, V-MOF is able to achieve much greater recoveries at similar productivity values (≈ 4 tpd m^{-3}). The range of achievable productivities are very similar to those found for CMS, these values ranging from $\approx 4-12$ tpd m^{-3}. However, it appears that the range of achieveable recoveries is much more limited in V-MOF, reaching a maximum recovery of 74.9% at 7.65 tpd m^{-3}. It is worth noting that V-MOF exceeds CMS when comparing the previously discussed data at 50°C. For $y_{CH_4,feed} = 80$ mol% and 50°C, the achievable recoveries were approximately 20% greater and there is almost a doubling in productivity when compared to the CMS. However, neither adsorbent/process pair (for the presented cycles) is able to break 90% recovery, which Sr-ETS-4 is able to achieve, albeit at a low productivity.

7.5 Conclusions

The adsorptive equilibrium separation of CH_4 and N_2 was evaluated with two cycles: the 3-step and Skarstrom cycles using a vanadium MOF, $V_2Cl_{2.8}$(btdd). V-MOF is able to separate CH_4 from N_2 with CH_4 as the light product. To determine if the V-MOF is able purify methane to the 96 mol% pipeline specification, a series of simulated process studies were performed. The Skarstrom cycle was studied with a wide range of operating conditions, using different inlet compositions (55/45, 80/20 and 92/8 mol% CH_4/N_2), process temperatures (30, 40 and 50°C) and a range of high pressures (from 100 to 500 kPa). These conditions were chosen to span the range of possible natural gas or landfill gas inlet conditions. The inlet conditions were used to generate at least 4000 samples to train an ANN surrogate model to perform a

machine learning aided optimization for purity-recovery and recovery-productivity trade-off curves. The 3-step cycle was unable to reach the pipeline specification in most of the parametric optimizations. When the feed temperature was fixed at 50°C and the adsorption pressure was allowed to vary between $100 - 500$ kPa, a methane feed composition of 0.80 or 0.92 was able to achieve 96 mol% methane purity at 79.6% and 85.7% recovery, respectively. The Skarstrom cycle was able to achieve 96 mol% methane in all parametric optimizations performed. The optimal conditions were at a feed temperature of 50°C, an adsorption pressure at 100 kPa and a methane feed composition of 92 mol%. These conditions could yield a recovery of 88.3% at 96 mol% purity. Interestingly, the best performing conditions were all at an elevated temperature. 50°C was consistently able to outperform 30 and 40°C. This appears to be a due to the adsorption of CH_4, which decreases at higher temperatures, allowing less CH_4 to be lost per unit cycle. The Skarstrom cycle results were then compared with another study using a CMS by Effendy *et al.* [17]. For comparable conditions, such as 80 mol% methane in the feed, the V-MOF was able to outperform the CMS. Under optimal conditions, the achievable recoveries were approximately 20% greater in recovery with almost a doubling in productivity.

Chapter 8

Conclusions, Recommendations and Future Work

8.1 Conclusions

This thesis studied various aspects of single and multicomponent adsorption equilibrium and kinetics, most commonly with dynamic column breakthrough experiments. The experiments were performed both to produce useful data and models, and to provide recommendations to obtain repeatable, precise and accurate data. A summary of the conclusions of the main chapters are given below.

In Chapter 2, the multicomponent adsorption equilibrium of CO_2 and N_2 mixtures were measured on the benchmark post-combustion carbon capture adsorbent, zeolite 13X. The mixtures were first considered under dry conditions, since H_2O would also be present in coal-fired flue gas. These CO_2/N_2 mixtures were found to adsorb nonideally under conditions where a possible vacuum-swing adsorption process would operate. Specifically, the competitive CO_2 equilibrium loadings were largely unaffected in the range studied when compared to its single-component equilibrium. On the other hand, the competitive N_2 equilibrium was affected due to CO_2 adsorption, but was not described by ideal adsorbed solution theory. The measured competitive N_2 loadings were greater than what ideal adsorbed solution theory predicted. An equal-energy site extension to the dual-site Langmuir isotherm was proposed to predict multicomponent CO_2/N_2 mixtures. Different competitive isotherm models were used in a basic 4-step

vacuum-swing adsorption cycle simulator to show their effect on process performance. It was found that an incorrect competitive isotherm can massively effect process performance. This was due to the quantity of N_2 that was assumed to adsorb in each competitive isotherm model. This equilibrium data was measured using dynamic column breakthrough experiments. Recommendations were also made to measure the light-component loading in highly selective adsorbate-adsorbent systems. Specifically, that the heavy component (CO_2) should be measured in an adsorption experiment and the light component (N_2) should be measured in a desorption experiment to minimize the error associated with the effluent flow measurement.

Chapter 3 was a follow-up study to Chapter 2. In Chapter 3, the multicomponent adsorption equilibrium of CO_2 and H_2O mixtures were measured on zeolite 13X, to consider a more realistic post-combustion flue gas. The same recommendation for the measurement of the heavy (H_2O) and light (CO_2) component competitive loadings was tested with a much more selective system. Water was found to be completely unaffected by CO_2 under the conditions studied. However, the CO_2 equilibrium loadings were massively reduced, this was approximately 98% less than the single-component CO_2 loading at equivalent conditions. Similar to CO_2/N_2 mixtures, CO_2/H_2O mixtures were not able to be described using ideal adsorbed solution theory. An empirical competitive isotherm was proposed for process simulations. This model was able to accurately describe a wide range of unary and binary CO_2/H_2O dynamic column breakthrough experiments.

In Chapter 4, a quantitative microscale dynamic column breakthrough apparatus was built and described to measure unary and binary adsorption equilibrium data on milligram-sized samples. This sample size was considered to be similar to the quantities that adsorbent synthesis chemists and materials scientists would prepare. Measuring quantitative data on milligram quantities of adsorbent makes these experiments fairly challenging, but also provides many benefits. The system was first tested with unary N_2 and CH_4 adsorption and desorption breakthrough experiments. The

measured loadings were in excellent agreement with independently collected volumetric data. The system was then tested with a series of ideal and nonideal binary gas pairings. Due to the size of the microscale dynamic column breakthrough apparatus, it was able to collect this data relatively quickly when compared to a traditional, tens of grams scale, dynamic column breakthrough apparatus. This was fast enough to build a phase-diagram in as little as 10 to 12 hours (including blank measurements). Also due to its small size, a relatively complicated effluent flow calibration was avoided completely by using a large tank of constant composition fluid.

Chapter 5 studied the microporous diffusion of N_2 and CH_4 into two small pore adsorbents: zeolite 4A and Ba-RPZ. The separation of CH_4 and N_2, commonly known as nitrogen-rejection or methane upgrading, can be performed kinetically in a pressure-swing adsorption apparatus. This is done by exploiting the relatively fast diffusion of N_2 compared to the relatively slow diffusion of CH_4. The diffusivities and diffusion mechanisms of both CH_4 and N_2 were found using constant volume uptake experiments. For zeolite 4A, the mechanism for both species was found to be transport through the micropores, which is in agreement with the literature. For Ba-RPZ, N_2 was found to be limited by transport through the micropores. However, CH_4 displayed a dual-resistance, where both surface-barrier and micropore-transport resistances were observed. All N_2 and CH_4 diffusivities were described with concentration and temperature dependence models to be used in kinetic pressure-swing adsorption process simulations. These models were tested and validated for non-constant CH_4 diffusivity experiments on Ba-RPZ at multiple temperatures.

In Chapter 6, dynamic column breakthrough experiments were performed for CH_4 and N_2 on both zeolite 4A and Ba-RPZ with the microscale dynamic column breakthrough apparatus from Chapter 4. These were done in part to study the impact of diffusion on the dynamic uptake of methane and nitrogen into these materials. For zeolite 4A, the qualitative CH_4 diffusion was the same as in the static constant volume experiments in Chapter 5 in both concentration and temperature. For the conditions

studied, the single-component diffusion of CH_4 in Ba-RPZ followed the same trends in concentration at a given temperature. The breakthrough experiments were not sensitive enough to see the thermal effects observed in constant volume experiments. These breakthrough experiments were also performed to study the binary diffusion of CH_4 and N_2 into these materials. For CH_4/N_2 mixtures on zeolite 4A, the multicomponent diffusivities appear to be the same as the single component experiment at all compositions and temperatures studied. On Ba-RPZ, the binary CH_4/N_2 diffusivities are inconclusive. They appear to be similar to the unary CH_4 diffusivities, but it may just be a limitation of our current hardware.

In Chapter 7, machine-learning aided optimization was used to study nitrogen-rejection on a novel vanadium-based metal-organic framework for pressure swing adsorption processes. This novel vanadium-based metal-organic framework displays a unique equilibrium selectivity towards N_2 instead of CH_4. This allowed light-product, or raffinate, pressure-swing adsorption cycles to be optimized for the high pressure separation of CH_4. The aim was to purify CH_4 from N_2 to the pipeline purity specification of 96 mol% CH_4. Two cycles in particular were studied: the basic 3-step cycle and the Skarstrom cycle. The basic 3-step cycle was unable to reach the 96 mol% CH_4 purity requirement in almost all cases studied. If the feed gas was pressurized, it was able to achieve the methane purity requirement. However, the Skarstrom cycle was able to reach 96 mol% CH_4 in all conditions studied. The vanadium-based metal-organic framework was also compared with other nitrogen-rejection materials. It was able to be similarly productive as a carbon molecular sieve at similar levels of recovered methane.

8.2 Future Work

Multicomponent equilibrium and kinetic data is scarce in the literature. Pressure and temperature swing adsorption process simulations require well-described equilibrium and kinetic data to accurately predict process performance. This data is also helpful

to validate molecular dynamics simulations. As more metal-organic, and covalent-organic frameworks are synthesized, some will be considered for pressure/temperature swing adsorption, and will require multicomponent equilibrium and diffusion data. The development of the microscale dynamic column breakthrough apparatus, and the associated techniques to minimize calculated loading error, opens the door to rapid multicomponent adsorption equilibrium data collection on as-synthesized adsorbents. This analysis could be applied much earlier in process development, to help screen potential adsorbents for their usefulness in a proposed adsorptive process. While this thesis only considered binary mixtures in the microscale dynamic column breakthrough apparatus, the method can be extended to ternary (or higher) mixtures with the use of a mass spectrometer. This could be extended to more realistic systems, such as humid post-combustion flue gas (CO_2, N_2 and H_2O), any methane-upgrading application (mixtures of CH_4, CO_2, N_2 and H_2O), or any other application of interest. Especially with the rise in popularity of adsorption-based carbon capture technologies, this technique could be a useful, and quick, method to screen multicomponent adsorption equilibrium.

It may also be possible to quantify multicomponent diffusion with the microscale dynamic column breakthrough apparatus. Experimentally, this data is rare in the literature since it is difficult to measure; although, this is also partially due to the narrow set of adsorbate-adsorbent pairings that would be of industrial and academic interest. For kinetically-controlled separations, such as some adsorbents with CH_4/N_2 or alkane/alkene/alkyne mixtures, this method could potentially be very useful. This is especially true since the small adsorbent sample sizes allow the breakthrough experiments to be practically isothermal. I unfortunately did not have enough time to fully explore multicomponent diffusion during this thesis.

Microscale dynamic column breakthrough experiments may also facilitate process design and optimization of niche or specialty separations due to its small size. Expensive gases, such as neon, krypton, radon or xenon could be studied with breakthrough

experiments to assess competitive adsorption and diffusion in a more cost-effective way. This could be enabling, since less gas would be required to obtain reliable data when compared to a traditional breakthrough apparatus. It may also be a safer way to run dynamic column breakthrough experiments using hazardous materials, such as CO or H_2S, again since less gas would be required to obtain reliable data.

Bibliography

[1] N. S. Wilkins, "Characterizing adsorbents for pre- and post-combustion carbon capture," M.S. thesis, University of Alberta, 2017.

[2] N. S. Wilkins and A. Rajendran, "Measurement of competitive CO_2 and N_2 adsorption on zeolite 13X for post-combustion CO_2 capture," *Adsorption*, vol. 25, no. 2, pp. 115–133, 2019.

[3] N. S. Wilkins, J. A. Sawada, and A. Rajendran, "Measurement of competitive CO_2 and H_2O adsorption on zeolite 13X for post-combustion CO_2 capture," *Adsorption*, vol. 26, no. 5, pp. 765–779, 2020.

[4] N. S. Wilkins, J. A. Sawada, and A. Rajendran, "Quantitive microscale dynamic column breakthrough apparatus for measurement of unary and binary adsorption equilibria on milligram quantities of adsorbent," *Ind. Eng. Chem. Res.*, vol. 61, no. 20, pp. 7032–7051, 2022.

[5] N. S. Wilkins, J. A. Sawada, and A. Rajendran, "Diffusion of CH_4 and N_2 in barium-exchanged reduced pore zorite (Ba-RPZ) and zeolite 4A," *Ind. Eng. Chem. Res.*, vol. 60, no. 29, pp. 10 777–10 790, 2021.

[6] N. S. Wilkins, K. N. Pai, and A. Rajendran, "Optimization of pressure-vacuum swing adsorption processes for nitrogen rejection from natural gas streams using a nitrogen selective metal organic framework," *Can. J. Chem. Eng.*, 2022.

[7] D. S. Sholl and R. P. Lively, "Seven chemical separations to change the world," *Nature*, vol. 532, no. 7600, pp. 435–437, 2016.

[8] P. C. Wankat, *Separation Process Engineering*. Prentice Hall, 2007.

[9] D. M. Ruthven, S. Farooq, and K. S. Knaebel, *Pressure Swing Adsorption*. 1994, vol. 1.

[10] M. W. Ackley, "Medical oxygen concentrators: A review of progress in air separation technology," *Adsorption*, vol. 25, no. 8, pp. 1437–1474, 2019.

[11] S. U. Rege, R. T. Yang, and M. A. Buzanowski, "Sorbents for air prepurification in air separation," *Chem. Eng. Sci.*, vol. 55, no. 21, pp. 4827–4838, 2000.

[12] C. A. Grande, "Biogas upgrading by pressure swing adsorption," *Biofuel Eng. Process Tech.*, pp. 65–84, 2011.

[13] R. Haghpanah, R. Nilam, A. Rajendran, S. Farooq, and I. A. Karimi, "Cycle synthesis and optimization of a VSA process for postcombustion CO_2 capture," *AIChE J.*, vol. 59, no. 12, pp. 4735–4748, 2013.

[14] N. Casas, J. Schell, L. Joss, and M. Mazzotti, "A parametric study of a PSA process for pre-combustion CO_2 capture," *Sep. Sci. Technol.*, vol. 104, pp. 183–192, 2013.

[15] M. Hefti and M. Mazzotti, "Postcombustion CO_2 capture from wet flue gas by temperature swing adsorption," *Ind. Eng. Chem. Res.*, vol. 57, no. 45, pp. 15 542–15 555, 2018.

[16] K. S. Knaebel and H. E. Reinhold, "Landfill gas: From rubbish to resource," *Adsorption*, vol. 9, no. 1, pp. 87–94, 2003.

[17] S. Effendy, C. Xu, and S. Farooq, "Optimization of a pressure swing adsorption process for nitrogen rejection from natural gas," *Ind. Eng. Chem. Res.*, vol. 56, no. 18, pp. 5417–5431, 2017.

[18] D. M. Ruthven, *Principles of Adsorption and Adsorption Processes*. John Wiley & Sons, 1984.

[19] R. Haghpanah, A. Majumder, R. Nilam, A. Rajendran, S. Farooq, I. A. Karimi, and M. Amanullah, "Multiobjective optimization of a four-step adsorption process for postcombustion CO_2 capture via finite volume simulation," *Ind. Eng. Chem. Res.*, vol. 52, no. 11, pp. 4249–4265, 2013.

[20] A. L. Myers and J. M. Prausnitz, "Thermodynamics of mixed-gas adsorption," *AIChE J.*, vol. 11, no. 1, pp. 121–127, 1965.

[21] J. A. Ritter, S. J. Bhadra, and A. D. Ebner, "On the use of the dual-process Langmuir model for correlating unary equilibria and predicting mixed-gas adsorption equilibria," *Langmuir*, vol. 27, no. 8, pp. 4700–4712, 2011.

[22] J. Kärger, D. M. Ruthven, and D. N. Theodorou, *Diffusion in nanoporous materials*. John Wiley & Sons, 2012.

[23] R. R. Vemula and S. Sircar, "Comments on the reliability of model simulation of a rapid pressure swing adsorption process for high-purity product," *Ind. Eng. Chem. Res.*, vol. 56, no. 31, pp. 8991–8994, 2017.

[24] S. A. Hosseinzadeh Hejazi, L. Estupiñan Perez, A. Rajendran, and S. M. Kuznicki, "Cycle development and process optimization of high-purity oxygen production using silver-exchanged titanosilicates," *Ind. Eng. Chem. Res.*, vol. 56, no. 19, pp. 5679–5691, 2017.

[25] D. W. Breck, *Zeolite Molecular Sieves*. Wiley New York, 1974, vol. 4.

[26] H. Yucel and D. M. Ruthven, "Diffusion in 4A zeolite. Study of the effect of crystal size," *J. Chem. Soc. Faraday Trans.*, vol. 76, pp. 60–70, 1980.

[27] S. Farooq, H. Qinglin, and I. A. Karimi, "Identification of transport mechanism in adsorbent micropores from column dynamics," *Ind. Eng. Chem. Res.*, vol. 41, no. 5, pp. 1098–1106, 2002.

[28] J. Wang, E. Mangano, S. Brandani, and D. M. Ruthven, "A review of common practices in gravimetric and volumetric adsorption kinetic experiments," *Adsorption*, pp. 1–24, 2020.

[29] D. Shade, B. W. S. Bout, D. S. Sholl, and K. S. Walton, "Opening the toolbox: 18 experimental techniques for measurement of mixed gas adsorption," *Ind. Eng. Chem. Res.*, 2022.

[30] N. S. Wilkins, A. Rajendran, and S. Farooq, "Dynamic column breakthrough experiments for measurement of adsorption equilibrium and kinetics," *Adsorption*, vol. 27, no. 3, pp. 397–422, 2020.

[31] O. Talu, J. Li, R. Kumar, P. M. Mathias, J. D. Moyer Jr., and J. M. Schork, "Measurement and analysis of oxygen/nitrogen/5A-zeolite adsorption equilibria for air separation," *Gas Sep. Pur.*, vol. 10, no. 3, pp. 149–159, 1996.

[32] A. Malek, S. Farooq, M. N. Rathor, and K. Hidajat, "Effect of velocity variation due to adsorption-desorption on equilibrium data from breakthrough experiments," *Chem. Eng. Sci.*, vol. 50, no. 4, pp. 737–740, 1995.

[33] S. Brandani, "On the chromatographic measurement of equilibrium isotherms using large concentration steps," *Adsorption*, vol. 11, no. 1, pp. 231–235, 2005.

[34] G. Avijegon, G. Xiao, G. Li, and E. F. May, "Binary and ternary adsorption equilibria for $CO_2/CH_4/N_2$ mixtures on zeolite 13X beads from 273 to 333 K and pressures to 900 kPa," *Adsorption*, vol. 24, no. 4, pp. 381–392, 2018.

[35] T. D. Burns, K. N. Pai, S. G. Subraveti, S. P. Collins, M. Krykunov, A. Rajendran, and T. K. Woo, "Prediction of mof performance in vacuum swing adsorption systems for postcombustion CO_2 capture based on integrated molecular simulations, process optimizations, and machine learning models," *Env. Sci. Technol.*, vol. 54, no. 7, pp. 4536–4544, 2020.

[36] K. N. Pai, V. Prasad, and A. Rajendran, "Generalized, adsorbent-agnostic, artificial neural network framework for rapid simulation, optimization, and adsorbent screening of adsorption processes," *Ind. Eng. Chem. Res.*, vol. 59, no. 38, pp. 16 730–16 740, 2020.

[37] H. G. T. Nguyen, L. Espinal, R. D. van Zee, M. Thommes, B. Toman, M. S. L. Hudson, E. Mangano, S. Brandani, D. P. Broom, M. J. Benham, *et al.*, "A reference high-pressure CO_2 adsorption isotherm for ammonium zsm-5 zeolite: Results of an interlaboratory study," *Adsorption*, vol. 24, no. 6, pp. 531–539, 2018.

[38] D. W. Siderius, V. K. Shen, R. D. Johnson III, and R. D. van Zee, "NIST/ARPA-E database of novel and emerging adsorbent materials," *National Institute of Standards and Technology, Gaithersburg*, vol. 3, 2018.

[39] X. Cai, F. Gharagheizi, L. W. Bingel, D. Shade, K. S. Walton, and D. S. Sholl, "A collection of more than 900 gas mixture adsorption experiments in porous materials from literature meta-analysis," *Ind. Eng. Chem. Res.*, vol. 60, no. 1, pp. 639–651, 2020.

[40] D. P. Broom and K. M. Thomas, "Gas adsorption by nanoporous materials: Future applications and experimental challenges," *MRS Bull.*, vol. 38, no. 5, pp. 412–421, 2013.

[41] S. Krishnamurthy, R. Haghpanah, A. Rajendran, and S. Farooq, "Simulation and optimization of a dual-adsorbent, two-bed vacuum swing adsorption process for CO_2 capture from wet flue gas," *Ind. Eng. Chem. Res.*, vol. 53, no. 37, pp. 14 462–14 473, 2014.

[42] N. Stern, "The economics of climate change," *Am. Econ. Rev.*, vol. 98, no. 2, pp. 1–37, 2008.

[43] A. Samanta, A. Zhao, G. K. H. Shimizu, P. Sarkar, and R. Gupta, "Post-combustion CO_2 capture using solid sorbents: A review," *Ind. Eng. Chem. Res.*, vol. 51, no. 4, pp. 1438–1463, 2011.

[44] M. Bui, C. S. Adjiman, A. Bardow, E. J. Anthony, A. Boston, S. Brown, P. S. Fennell, S. Fuss, A. Galindo, L. A. Hackett, *et al.*, "Carbon capture and storage (CCS): The way forward," *Energy Environm. Sci.*, vol. 11, no. 5, pp. 1062–1176, 2018.

[45] IPCC, "Special report on carbon capture and storage," Intergovernmental Panel on Climate Change (IPCC), Tech. Rep., 2005.

[46] S. E. Zanco, L. Joss, M. Hefti, M. Gazzani, and M. Mazzotti, "Addressing the criticalities for the deployment of adsorption-based CO_2 capture processes," *Enrgy. Proced.*, vol. 114, pp. 2497–2505, 2017.

[47] B. Smit, J. A. Reimer, C. M. Oldenburg, and I. C. Bourg, *Introduction to Carbon Capture and Sequestration*. World Scientific, 2014.

[48] M. E. Boot-Handford, J. C. Abanades, E. J. Anthony, M. J. Blunt, S. Brandani, N. Mac Dowell, J. R. Fernández, M. Ferrari, R. Gross, J. P. Hallett, *et al.*, "Carbon capture and storage update," *Energy Environm. Sci.*, vol. 7, no. 1, pp. 130–189, 2014.

[49] W Lu, Y Ying, W Shen, P Li, and J Yu, "CO_2 capture from flue gas in an existing coal power plant," in *6th Pacific Basin Conference on Adsorption Science and Technology, Taipei, Taiwan, May*, 2012, pp. 20–23.

[50] P. Xiao, J. Zhang, P. Webley, G. Li, R. Singh, and R. Todd, "Capture of CO_2 from flue gas streams with zeolite 13X by vacuum-pressure swing adsorption," *Adsorption*, vol. 14, no. 4-5, pp. 575–582, 2008.

[51] T. Hocker, A. Rajendran, and M. Mazzotti, "Measuring and modeling supercritical adsorption in porous solids. carbon dioxide on 13X zeolite and on silica gel," *Langmuir*, vol. 19, no. 4, pp. 1254–1267, 2003.

[52] S. Cavenati, C. A. Grande, and A. E. Rodrigues, "Separation of $CH_4/CO_2/N_2$ mixtures by layered pressure swing adsorption for upgrade of natural gas," *Chem. Eng. Sci.*, vol. 61, no. 12, pp. 3893–3906, 2006.

[53] Y. Wang and M. D. LeVan, "Adsorption equilibrium of carbon dioxide and water vapor on zeolites 5A and 13X and silica gel: Pure components," *J. Chem. Eng. Data*, vol. 54, no. 10, pp. 2839–2844, 2009.

[54] M. Hefti, D. Marx, L. Joss, and M. Mazzotti, "Adsorption equilibrium of binary mixtures of carbon dioxide and nitrogen on zeolites ZSM-5 and 13X," *Micropor. Mesopor. Mat.*, vol. 215, pp. 215–228, 2015.

[55] A. K. Rajagopalan, A. M. Avila, and A. Rajendran, "Do adsorbent screening metrics predict process performance? A process optimisation based study for post-combustion capture of CO_2," *Int. J. Greenh. Gas Con.*, vol. 46, pp. 76–85, 2016.

[56] A. K. Rajagopalan and A. Rajendran, "The effect of nitrogen adsorption on vacuum swing adsorption based post-combustion CO_2 capture," *Int. J. Greenh. Gas Con.*, vol. 78, pp. 437–447, 2018.

[57] A. H. Farmahini, S. Krishnamurthy, D. Friedrich, S. Brandani, and L. Sarkisov, "From crystal to adsorption column: Challenges in multiscale computational screening of materials for adsorption separation processes," *Ind. Eng. Chem. Res.*, 2018.

[58] S. Sircar, "Basic research needs for design of adsorptive gas separation processes," *Ind. Eng. Chem. Res.*, vol. 45, no. 16, pp. 5435–5448, 2006.

[59] M. J. Purdue, "Explicit flue gas adsorption isotherm model for zeolite 13X incorporating enhancement of nitrogen loading by adsorbed carbon dioxide and multi-site affinity shielding of co-adsorbate dependent upon water vapor content," *J. Phys. Chem. C*, 2018.

[60] S. Krishnamurthy, V. R. Rao, S. Guntuka, P. Sharratt, R. Haghpanah, A. Rajendran, M. Amanullah, I. A. Karimi, and S. Farooq, "CO_2 capture from dry flue gas by vacuum swing adsorption: A pilot plant study," *AIChE J.*, vol. 60, no. 5, pp. 1830–1842, 2014.

[61] S. Sircar, "Gibbsian surface excess for gas adsorption revisited," *Ind, Eng. Chem. Res.*, vol. 38, no. 10, pp. 3670–3682, 1999.

[62] A. Rajendran, T. Hocker, O. Di Giovanni, and M. Mazzotti, "Experimental observation of critical depletion: Nitrous oxide adsorption on silica gel," *Langmuir*, vol. 18, no. 25, pp. 9726–9734, 2002.

[63] A. Rajendran, V. Kariwala, and S. Farooq, "Correction procedures for extra-column effects in dynamic column breakthrough experiments," *Chem. Eng. Sci.*, vol. 63, no. 10, pp. 2696–2706, 2008.

[64] X. Hu, E. Mangano, D. Friedrich, H. Ahn, and S. Brandani, "Diffusion mechanism of CO_2 in 13X zeolite beads," *Adsorpt.*, vol. 20, no. 1, pp. 121–135, 2014.

[65] E. Gleuckauf and J. I. Coates, "The influence of incomplete equilibrium on the front boundary of chromatograms and the effectiveness of separation," *J. Chem. Soc.*, vol. 1315, 1947.

[66] S. A. Hosseinzadeh Hejazi, A. Rajendran, J. A. Sawada, and S. M. Kuznicki, "Dynamic column breakthrough and process studies of high-purity oxygen production using silver-exchanged titanosilicates," *Ind. Eng. Chem. Res.*, vol. 55, no. 20, pp. 5993–6005, 2016.

[67] S. Guntuka, S. Farooq, and A. Rajendran, "A-and B-site substituted lanthanum cobaltite perovskite as high temperature oxygen sorbent. 2. column dynamics study," *Ind. Eng. Chem. Res.*, vol. 47, no. 1, pp. 163–170, 2008.

[68] S. Sircar and D. V. Cao, "Heat of adsorption," *Chem. Eng. Tech.*, vol. 25, no. 10, pp. 945–948, 2002.

[69] S. Sircar, "Comments on practical use of Langmuir gas adsorption isotherm model," *Adsorption*, vol. 23, no. 1, pp. 121–130, 2017.

[70] Q. H. Dirar and K. F. Loughlin, "Intrinsic adsorption properties of CO_2 on 5A and 13X Zeolite," *Adsorption*, vol. 19, no. 6, pp. 1149–1163, 2013.

[71] M. Mazzotti and A. Rajendran, "Equilibrium theory-based analysis of nonlinear waves in separation processes," *Annu. Rev. Chem. Biomol. Eng.*, vol. 4, pp. 119–141, 2013.

[72] A. L. Myers, "Activity coefficients of mixtures adsorbed on heterogeneous surfaces," *AIChE J.*, vol. 29, no. 4, pp. 691–693, 1983.

[73] G. N. Nikolaidis, E. S. Kikkinides, and M. C Georgiadis, "A model-based approach for the evaluation of new zeolite 13X-based adsorbents for the efficient post-combustion CO_2 capture using P/VSA processes," *Chem. Eng. Res. Des.*, vol. 131, pp. 362–374, 2018.

[74] A. De Klerk, "Voidage variation in packed beds at small column to particle diameter ratio," *AIChE J.*, vol. 49, no. 8, pp. 2022–2029, 2003.

[75] E. W. Lemmon, M. L. Huber, and M. O. McLinden, "NIST standard reference database 23: Reference fluid thermodynamic and transport properties-REFPROP, version 9.1," *NIST Pubs*, 2013.

[76] F. Rezaei, A. A. Rownaghi, S. Monjezi, R. P. Lively, and C. W. Jones, "SO_x/NO_x removal from flue gas streams by solid adsorbents: A review of current challenges and future directions," *Energy Fuels*, vol. 29, no. 9, pp. 5467–5486, 2015.

[77] Y. K. Ryu, S. J. Lee, J. W. Kim, and C. Leef, "Adsorption equilibrium and kinetics of H_2O on zeolite 13X," *Korean J. Chem. Eng.*, vol. 18, no. 4, pp. 525–530, 2001.

[78] J. Kim, C. Lee, W. Kim, J. Lee, J. Kim, J. Suh, and J. Lee, "Adsorption equilibria of water vapor on alumina, zeolite 13X, and a zeolite X/activated carbon composite," *J. Chem. Eng. Data*, vol. 48, no. 1, pp. 137–141, 2003.

[79] A. M. Ribeiro, T. P. Sauer, C. A. Grande, R. F. P. M. Moreira, J. M. Loureiro, and A. E. Rodrigues, "Adsorption equilibrium and kinetics of water vapor on different adsorbents," *Ind. Eng. Chem. Res.*, vol. 47, no. 18, pp. 7019–7026, 2008.

[80] D. Ferreira, R. Magalhães, P. Taveira, and A. Mendes, "Effective adsorption equilibrium isotherms and breakthroughs of water vapor and carbon dioxide on different adsorbents," *Ind. Eng. Chem. Res.*, vol. 50, no. 17, pp. 10 201–10 210, 2011.

[81] H. Kim, H. J. Cho, S. Narayanan, S. Yang, H. Furukawa, S. Schiffres, X. Li, Y. Zhang, J. Jiang, and O. M. Yaghi, "Characterization of adsorption enthalpy of novel water-stable zeolites and metal-organic frameworks," *Sci. Rep.*, vol. 6, p. 19 097, 2016.

[82] Y. Wang and M. D. LeVan, "Adsorption equilibrium of binary mixtures of carbon dioxide and water vapor on zeolites 5A and 13X," *J. Chem. Eng. Data*, vol. 55, no. 9, pp. 3189–3195, 2010.

[83] L. Joos, J. A. Swisher, and B. Smit, "Molecular simulation study of the competitive adsorption of H_2O and CO_2 in zeolite 13X," *Langmuir*, vol. 29, no. 51, pp. 15 936–15 942, 2013.

[84] M. J. Purdue and Z. Qiao, "Molecular simulation study of wet flue gas adsorption on zeolite 13X," *Micropor. Mesopor. Mat.*, vol. 261, pp. 181–197, 2018.

[85] K. Kim, H. Oh, S. Lim, K. Ho, Y. Park, and C. Lee, "Adsorption equilibria of water vapor on zeolite 3A, zeolite 13X, and dealuminated Y zeolite," *J. Chem. Eng. Data*, vol. 61, no. 4, pp. 1547–1554, 2016.

[86] H. Ahn and C. Lee, "Adsorption dynamics of water in layered bed for air-drying TSA process," *AIChE J.*, vol. 49, no. 6, pp. 1601–1609, 2003.

[87] G. Li, P. Xiao, P. Webley, J. Zhang, R. Singh, and M. Marshall, "Capture of CO_2 from high humidity flue gas by vacuum swing adsorption with zeolite 13X," *Adsorption*, vol. 14, no. 2-3, pp. 415–422, 2008.

[88] A. Lorek and J. Majewski, "Humidity measurement in carbon dioxide with capacitive humidity sensors at low temperature and pressure," *Sensors*, vol. 18, no. 8, p. 2615, 2018.

[89] J. A. Ritter, K. C. Bumiller, K. J. Tynan, and A. D. Ebner, "On the use of the dual process Langmuir model for binary gas mixture components that exhibit single process or linear isotherms," *Adsorption*, 2019.

[90] R. T. Yang, *Gas Separation by Adsorption Processes*. Imperial College Press, Jun. 19, 1997, 364 Seiten.

[91] R. Krishna and J. M. van Baten, "Using molecular simulations for elucidation of thermodynamic nonidealities in adsorption of CO_2-containing mixtures in NaX zeolite," *ACS Omega*, vol. 5, no. 32, pp. 20 535–20 542, 2020.

[92] S. Sircar, "Recent developments in macroscopic measurement of multicomponent gas adsorption equilibria, kinetics, and heats," *Ind. Eng. Chem. Res.*, vol. 46, no. 10, pp. 2917–2927, 2007.

[93] S. N. Nobar and S. Farooq, "Experimental and modeling study of adsorption and diffusion of gases in Cu-BTC," *Chem. Eng. Sci.*, vol. 84, pp. 801–813, 2012.

[94] P. Goyal, M. J. Purdue, and S. Farooq, "Adsorption and diffusion of N_2 and CO_2 and their mixture on silica gel," *Ind. Eng. Chem. Res.*, vol. 58, no. 42, pp. 19 611–19 622, 2019.

[95] D. Shade, W. P. Mounfield III, Y. Huang, B. Marszalek, and K. S. Walton, "An automated multi-component gas adsorption system (MC GAS)," *Rev. Sci. Instrum.*, vol. 92, no. 5, p. 054 102, 2021.

[96] F. Dreisbach, R. Staudt, and J. U. Keller, "High pressure adsorption data of methane, nitrogen, carbon dioxide and their binary and ternary mixtures on activated carbon," *Adsorption*, vol. 5, no. 3, pp. 215–227, 1999.

[97] S. Ottiger, R. Pini, G. Storti, and M. Mazzotti, "Competitive adsorption equilibria of CO_2 and CH_4 on a dry coal," *Adsorption*, vol. 14, no. 4-5, pp. 539–556, 2008.

[98] P. J. E. Harlick and F. H. Tezel, "Use of concentration pulse chromatography for determining binary isotherms: Comparison with statically determined binary isotherms," *Adsorption*, vol. 9, no. 3, pp. 275–286, 2003.

[99] D. Kennedy and F. H. Tezel, "Improved method for determining binary adsorption isotherms by using concentration pulse chromatography: Adsorption of CO_2 and N_2 by silicalite at different pressures," *Adsorption*, vol. 20, no. 1, pp. 189–199, 2014.

[100] F. Brandani and D. Ruthven, "Measurement of adsorption equilibria by the zero length column (ZLC) technique part 2: Binary systems," *Ind. Eng. Chem. Res.*, vol. 42, no. 7, pp. 1462–1469, 2003.

[101] F. Brandani and D. M. Ruthven, "The effect of water on the adsorption of CO_2 and C_3H_8 on type X zeolites," *Ind. Eng. Chem. Res.*, vol. 43, no. 26, pp. 8339–8344, 2004.

[102] D. P. Broom, O. Talu, and M. J. Benham, "Integral mass balance (IMB) method for measuring multicomponent gas adsorption equilibria in nanoporous materials," *Ind. Eng. Chem. Res.*, vol. 59, no. 46, pp. 20 478–20 491, 2020.

[103] S. Ottiger, R. Pini, G. Storti, and M. Mazzotti, "Measuring and modeling the competitive adsorption of CO_2, CH_4, and N_2 on a dry coal," *Langmuir*, vol. 24, no. 17, pp. 9531–9540, 2008.

[104] S. Brandani and E. Mangano, "The zero length column technique to measure adsorption equilibrium and kinetics: Lessons learnt from 30 years of experience," *Adsorption*, vol. 27, no. 3, pp. 319–351, 2021.

[105] S. A. Peter, G. V. Baron, J. Gascon, F. Kapteijn, and J. F. M. Denayer, "Dynamic desorption of CO_2 and CH_4 from amino-MIL-53 (Al) adsorbent," *Adsorption*, vol. 19, no. 6, pp. 1235–1244, 2013.

[106] L. Erden, A. D. Ebner, and J. A. Ritter, "Separation of landfill gas CH_4 from N_2 using pressure vacuum swing adsorption cycles with heavy reflux," *Energy Fuels*, vol. 32, no. 3, pp. 3488–3498, 2018.

[107] Y. He, J. H. Yun, and N. A. Seaton, "Adsorption equilibrium of binary methane/ethane mixtures in BPL activated carbon: Isotherms and calorimetric heats of adsorption," *Langmuir*, vol. 20, no. 16, pp. 6668–6678, 2004.

[108] P. Brea, J. A. Delgado, V. I. Águeda, and M. A. Uguina, "Modeling of breakthrough curves of N_2, CH_4, CO, CO_2 and a SMR type off-gas mixture on a fixed bed of BPL activated carbon," *Sep. Pur. Tech.*, vol. 179, pp. 61–71, 2017.

[109] B. P. Russell and M. D. Levan, "Pore size distribution of BPL activated carbon determined by different methods," *Carbon*, vol. 32, no. 5, pp. 845–855, 1994.

[110] M. Verbraeken, A. Centineo, L. Canobbio, and S. Brandani, "Accurate blank corrections for zero length column experiments," *Adsorption*, vol. 27, no. 1, pp. 129–145, 2021.

[111] L. Joss and M. Mazzotti, "Modeling the extra-column volume in a small column setup for bulk gas adsorption," *Adsorption*, vol. 18, no. 5-6, pp. 381–393, 2012.

[112] J. M. Miller and A. E. Lawson, "Gas chromatographic detector response using carrier gases of low thermal conductivity.," *Anal. Chem.*, vol. 37, no. 11, pp. 1348–1351, 1965.

[113] A. J. Rothman and L. A. Bromley, "High temperature thermal conductivity of gases," *Ind. Eng. Chem.*, vol. 47, no. 5, pp. 899–906, 1955.

[114] A. L. Lindsay and L. A. Bromley, "Thermal conductivity of gas mixtures," *Ind. Eng. Chem.*, vol. 42, no. 8, pp. 1508–1511, 1950.

[115] L. J. Schmauch and R. A. Dinerstein, "Response of thermal-conductivity cells in gas chromatography," *Anal. Chem.*, vol. 32, no. 3, pp. 343–352, 1960.

[116] A. L. Myers and P. A. Monson, "Physical adsorption of gases: The case for absolute adsorption as the basis for thermodynamic analysis," *Adsorption*, vol. 20, no. 4, pp. 591–622, 2014.

[117] N. Casas, J. Schell, R. Pini, and M. Mazzotti, "Fixed bed adsorption of CO_2/H_2 mixtures on activated carbon: Experiments and modeling," *Adsorption*, vol. 18, no. 2, pp. 143–161, 2012.

[118] N. Casas, J. Schell, R. Blom, and M. Mazzotti, "MOF and UiO-67/MCM-41 adsorbents for pre-combustion CO_2 capture by PSA: Breakthrough experiments and process design," *Sep. Pur. Tech.*, vol. 112, pp. 34–48, 2013.

[119] T. L. H. Saleman, G. C. Y. Watson, T. E. Rufford, P. S. Hofman, K. I. Chan, and E. F. May, "Capacity and kinetic measurements of methane and nitrogen adsorption on H^+-mordenite at 243–303 K and pressures to 900 kPa using a dynamic column breakthrough apparatus," *Adsorption*, vol. 19, no. 6, pp. 1165–1180, 2013.

[120] Y. Park, D. K. Moon, D. Park, M. Mofarahi, and C. H. Lee, "Adsorption equilibria and kinetics of CO_2, CO, and N_2 on carbon molecular sieve," *Sep. Pur. Tech.*, vol. 212, pp. 952–964, 2019.

[121] J. B. Lin, T. T. T. Nguyen, R. Vaidhyanathan, J. Burner, J. M. Taylor, H. Durekova, F. Akhtar, R. K. Mah, O. Ghaffari-Nik, S. Marx, N. Fylstra, S. S. Iremonger, K. W. Dawson, P. Sarkar, P. Hovington, A. Rajendran, T. K. Woo, and G. K. H. Shimizu, "A scalable metal-organic framework as a durable physisorbent for carbon dioxide capture," *Science*, vol. 374, no. 6574, pp. 1464–1469, 2021.

[122] D. A. Kennedy, M. Mujcin, E. Trudeau, and F. H. Tezel, "Pure and binary adsorption equilibria of methane and nitrogen on activated carbons, desiccants, and zeolites at different pressures," *J. Chem. Eng. Data*, vol. 61, no. 9, pp. 3163–3176, 2016.

[123] Y. J. Wu, Y. Yang, X. M. Kong, P. Li, J. G. Yu, A. M. Ribeiro, and A. E. Rodrigues, "Adsorption of pure and binary CO_2, CH_4, and N_2 gas components on activated carbon beads," *J. Chem. Eng. Data*, vol. 60, no. 9, pp. 2684–2693, 2015.

[124] T. E. Rufford, S. Smart, G. C. Y. Watson, B. F. Graham, J. Boxall, J. C. Diniz da Costa, and E. F. May, "The removal of CO_2 and N_2 from natural gas: A review of conventional and emerging process technologies," *J. Petrol. Sci. Eng.*, vol. 94, pp. 123–154, 2012.

[125] S. Cavenati, C. A. Grande, and A. E. Rodrigues, "Separation of methane and nitrogen by adsorption on carbon molecular sieve," *Sep. Sci. Tech.*, vol. 40, no. 13, pp. 2721–2743, 2005.

[126] S. U. Nandanwar, D. R. Corbin, and M. B. Shiflett, "A review of porous adsorbents for the separation of nitrogen from natural gas," *Ind. Eng. Chem. Res.*, vol. 59, no. 30, pp. 13 355–13 369, 2020.

[127] H. Ahn, H. Yoo, Y. Shul, S. Hyun, and C. Lee, "Diffusion mechanism of N_2 and CH_4 in pelletized zeolite 4A, 5A and CaX," *J. Chem. Eng. Jpn*, vol. 35, no. 4, pp. 334–345, 2002.

[128] R. Seabra, A. M. Ribeiro, K. Gleichmann, A. F. P. Ferreira, and A. E. Rodrigues, "Adsorption equilibrium and kinetics of carbon dioxide, methane and nitrogen on binderless zeolite 4A adsorbents," *Microporous and Mesoporous Mater.*, vol. 277, pp. 105–114, 2019.

[129] A. Jayaraman, A. J. Hernandez-Maldonado, R. T. Yang, D. Chinn, C. L. Munson, and D. H. Mohr, "Clinoptilolites for nitrogen/methane separation," *Chem. Eng. Sci.*, vol. 59, no. 12, pp. 2407–2417, 2004.

[130] D. Kennedy and F. Tezel, "Cation exchange modification of clinoptilolite–screening analysis for potential equilibrium and kinetic adsorption separations involving methane, nitrogen, and carbon dioxide," *Microporous and Mesoporous Mater.*, vol. 262, pp. 235–250, 2018.

[131] S. M. Kuznicki, V. A. Bell, I. Petrovic, and B. T. Desai, *Small-pored crystalline titanium molecular sieve zeolites and their use in gas separation processes*, US Patent 6,068,682, 2000.

[132] R. P. Marathe, K. Mantri, M. P. Srinivasan, and S. Farooq, "Effect of ion exchange and dehydration temperature on the adsorption and diffusion of gases in ETS-4," *Ind. Eng. Chem. Res.*, vol. 43, no. 17, pp. 5281–5290, 2004.

[133] B. Majumdar, S. J. Bhadra, R. P. Marathe, and S. Farooq, "Adsorption and diffusion of methane and nitrogen in barium exchanged ETS-4," *Ind. Eng. Chem. Res.*, vol. 50, no. 5, pp. 3021–3034, 2011.

[134] R. P. Marathe, S. Farooq, and M. P. Srinivasan, "Modeling gas adsorption and transport in small-pore titanium silicates," *Langmuir*, vol. 21, no. 10, pp. 4532–4546, 2005.

[135] S. J. Bhadra and S. Farooq, "Separation of methane–nitrogen mixture by pressure swing adsorption for natural gas upgrading," *Ind. Eng. Chem. Res.*, vol. 50, no. 24, pp. 14 030–14 045, 2011.

[136] A. Ansón, S. M. Kuznicki, T. Kuznicki, B. C. Dunn, E. M. Eyring, and D. B. Hunter, "Separation of argon and oxygen by adsorption on a titanosilicate molecular sieve," *Sep. Sci. Technol.*, vol. 44, no. 7, pp. 1604–1620, 2009.

[137] J. A. Sawada, E. J. Rode, S. M. Kuznicki, and C. C. I. Lin, *Silicate materials, method for their manufacture, and method for using such silicate materials for adsorptive fluid separations*, US Patent 8,545,608, 2013.

[138] C. C. H. Lin, J. A. Sawada, L. Wu, T. Haastrup, and S. M. Kuznicki, "Anion-controlled pore size of titanium silicate molecular sieves," *J. Am. Chem. Soc.*, vol. 131, no. 2, pp. 609–614, 2008.

[139] H. Qinglin, S. M. Sundaram, and S. Farooq, "Revisiting transport of gases in the micropores of carbon molecular sieves," *Langmuir*, vol. 19, no. 2, pp. 393–405, 2003.

[140] X. Jin, A. Malek, and S. Farooq, "Production of argon from an oxygen-argon mixture by pressure swing adsorption," *Ind. Eng. Chem. Res.*, vol. 45, no. 16, pp. 5775–5787, 2006.

[141] J. Crank, *Mathematics of Diffusion*. Oxford University Press, 1956.

[142] D. M. Ruthven, J. Kärger, S. Brandani, and E. Mangano, "Sorption kinetics: Measurement of surface resistance," *Adsorption*, pp. 1–13, 2020.

[143] G. Sastre, J. Kärger, and D. M. Ruthven, "Surface barriers and symmetry of adsorption and desorption processes," *Adsorption*, pp. 1–9, 2020.

[144] N. Haq and D. M. Ruthven, "Chromatographic study of sorption and diffusion in 4A zeolite," *J. Colloid and Interf. Sci.*, vol. 112, no. 1, pp. 154–163, 1986.

[145] D. V. Cao, R. J. Mohr, M. B. Rao, and S. Sircar, "Self-diffusivities of N_2, CH_4, and Kr on 4A zeolite pellets by isotope exchange technique," *J. Phys. Chem. B*, vol. 104, no. 45, pp. 10 498–10 501, 2000.

[146] S. Vasenkov and J. Kärger, "Evidence for the existence of intracrystalline transport barriers in MFI-type zeolites: A model consistency check using MC simulations," *Microporous Mesoporous Mater.*, vol. 55, no. 2, pp. 139–145, 2002.

[147] H. W. Haynes and P. N. Sarma, "A model for the application of gas chromatography to measurements of diffusion in bidisperse structured catalysts," *AIChE J.*, vol. 19, no. 5, pp. 1043–1046, 1973.

[148] H. W. Haynes, "The experimental evaluation of catalyst effective diffusivity," *Catal. Rev. Sci. Eng.*, vol. 30, no. 4, pp. 563–627, 1988.

[149] R. Krishna, "Multicomponent surface diffusion of adsorbed species: A description based on the generalized Maxwell-Stefan equations," *Chem. Eng. Sci.*, vol. 45, no. 7, pp. 1779–1791, 1990.

[150] H. W. Habgood, "The kinetics of molecular sieve action. sorption of nitrogen–methane mixtures by linde molecular sieve 4a," *Can. J. Chem.*, vol. 36, no. 10, pp. 1384–1397, 1958.

[151] D. M. Ruthven and R. Kumar, "A chromatographic study of the diffusion of N2, CH4 and binary CH4-N2 mixtures in 4A molecular sieve," *Can. J. Chem. Eng.*, vol. 57, no. 3, pp. 342–348, 1979.

[152] R. J. Mohr, D. Vorkapic, M. B. Rao, and S. Sircar, "Pure and binary gas adsorption equilibria and kinetics of methane and nitrogen on 4A zeolite by isotope exchange technique," *Adsorption*, vol. 5, no. 2, pp. 145–158, 1999.

[153] Z. D. Weller, S. P. Hamburg, and J. C. von Fischer, "A national estimate of methane leakage from pipeline mains in natural gas local distribution systems," *Environ. Sci. Tech.*, vol. 54, no. 14, pp. 8958–8967, 2020.

[154] A. I. Fatehi, K. F. Loughlin, and M. M. Hassan, "Separation of methane–nitrogen mixtures by pressure swing adsorption using a carbon molecular sieve," *Gas Sep. Purif.*, vol. 9, no. 3, pp. 199–204, 1995.

[155] M. Kim, Y. Bae, D. Choi, and C. Lee, "Kinetic separation of landfill gas by a two-bed pressure swing adsorption process packed with carbon molecular sieve: Nonisothermal operation," *Ind. Eng. Chem. Res.*, vol. 45, no. 14, pp. 5050–5058, 2006.

[156] S. M. Kuznicki, V. A. Bell, S. Nair, H. W. Hillhouse, R. M. Jacubinas, C. M. Braunbarth, B. H. Toby, and M. Tsapatsis, "A titanosilicate molecular sieve with adjustable pores for size-selective adsorption of molecules," *Nature*, vol. 412, no. 6848, p. 720, 2001.

[157] T. L. Saleman, G. K. Li, T. E. Rufford, P. L. Stanwix, K. I. Chan, S. H. Huang, and E. F. May, "Capture of low grade methane from nitrogen gas using dual-reflux pressure swing adsorption," *Chem. Eng. J*, vol. 281, pp. 739–748, 2015.

[158] R. Weh, G. Xiao, M. A. Islam, and E. F. May, "Nitrogen rejection from natural gas by dual reflux-pressure swing adsorption using activated carbon and ionic liquidic zeolite," *Sep. Pur. Tech.*, vol. 235, p. 116 215, 2020.

[159] J. H. Hackworth, R. W. Koch, and A. J. Rezaiyan, "Economic evaluation and market analysis for natural gas utilization. topical report," U.S. Department of Energy, Tech. Rep., 1995.

[160] H. Yang, C. Yin, B. Jiang, and D. Zhang, "Optimization and analysis of a VPSA process for N_2/CH_4 separation," *Sep. Pur. Tech.*, vol. 134, pp. 232–240, 2014.

[161] M. A. Sheikh, M. M. Hassan, and K. F. Loughlin, "Adsorption equilibria and rate parameters for nitrogen and methane on maxsorb activated carbon," *Gas Sep. Pur.*, vol. 10, no. 3, pp. 161–168, 1996.

[162] G. Xiao, T. L. Saleman, Y. Zou, G. Li, and E. F. May, "Nitrogen rejection from methane using dual-reflux pressure swing adsorption with a kinetically-selective adsorbent," *Chem. Eng. J.*, vol. 372, pp. 1038–1046, 2019.

[163] D. E. Jaramillo, D. A. Reed, H. Z. H. Jiang, J. Oktawiec, M. W. Mara, A. C. Forse, D. J. Lussier, R. A. Murphy, M. Cunningham, V. Colombo, *et al.*, "Selective nitrogen adsorption via backbonding in a metal–organic framework with exposed vanadium sites," *Nat. Mater.*, pp. 1–5, 2020.

[164] M. Thommes, K. Kaneko, A. V. Neimark, J. P. Olivier, F. Rodriguez-Reinoso, J. Rouquerol, and K. S. W. Sing, "Physisorption of gases, with special reference to the evaluation of surface area and pore size distribution (IUPAC technical report)," *Pure Appl. Chem*, vol. 87, no. 9-10, pp. 1051–1069, 2015.

[165] L. E. Perez, P. Sarkar, and A. Rajendran, "Experimental validation of multi-objective optimization techniques for design of vacuum swing adsorption processes," *Sep. Pur. Tech.*, vol. 224, pp. 553–563, 2019.

[166] K. N. Pai, V. Prasad, and A. Rajendran, "Experimentally validated machine learning frameworks for accelerated prediction of cyclic steady state and optimization of pressure swing adsorption processes," *Sep. Pur. Tech.*, p. 116 651, 2020.

[167] H. Jiang, A. D. Ebner, and J. A. Ritter, "Importance of incorporating a vacuum pump performance curve in dynamic adsorption process simulation," *Ind. Eng. Chem. Res.*, vol. 59, no. 2, pp. 856–873, 2019.

[168] C. Shen, C. A. Grande, P. Li, J. Yu, and A. E. Rodrigues, "Adsorption equilibria and kinetics of CO2 and N2 on activated carbon beads," *Chem. Eng. J.*, vol. 160, no. 2, pp. 398–407, 2010.

[169] J. A. Delgado, V. I. Águeda, M. A. Uguina, J. L. Sotelo, P. Brea, and C. A. Grande, "Adsorption and diffusion of H2, CO, CH4, and CO2 in BPL activated carbon and 13X zeolite: Evaluation of performance in pressure swing adsorption hydrogen purification by simulation," *Ind. Eng. Chem. Res.*, vol. 53, no. 40, pp. 15 414–15 426, 2014.

[170] M. I. Hossain, C. E. Holland, A. D. Ebner, and J. A. Ritter, "Mass transfer mechanisms and rates of CO2 and N2 in 13X zeolite from volumetric frequency response," *Ind. Eng. Chem. Res.*, vol. 58, no. 47, pp. 21 679–21 690, 2019.

[171] A. Ansón, S. M. Kuznicki, T. Kuznicki, T. Haastrup, Y. Wang, C. C. H. Lin, J. A. Sawada, E. M. Eyring, and D. Hunter, "Adsorption of argon, oxygen, and nitrogen on silver exchanged ETS-10 molecular sieve," *Microporous Mesoporous Mater.*, vol. 109, no. 1-3, pp. 577–580, 2008.

Appendix A: Supporting Information for "Measurement of competitive CO_2 and N_2 adsorption on zeolite 13X for post-combustion CO_2 capture"

A.1 Single Component Equilibrium Data

Table A.1: Unary CO_2 static equilibrium data on zeolite 13X.

25°C		50°C		75°C		100°C		125°C		150°C	
p_{CO_2} [bar]	$q^*_{CO_2}$ [mol/kg]	p_{CO_2} [bar]	$q^*_{CO_2}$ [mol/kg]	p_{CO_2} [bar]	$q^*_{CO_2}$ [mol/kg]	p_{CO_2} [bar]	$q^*_{CO_2}$ [mol/kg]	p_{CO_2} [bar]	$q^*_{CO_2}$ [mol/kg]	p_{CO_2} [bar]	$q^*_{CO_2}$ [mol/kg]
0.000	0.000	0.000	0.000	0.000	0.000	0.000	0.000	0.000	0.000	0.000	0
0.001	1.064	0.001	0.386	0.001	0.122	0.001	0.043	0.180	1.233	0.180	0.74373
0.002	1.256	0.002	0.527	0.002	0.174	0.002	0.065	0.390	1.694	0.390	1.14499
0.003	1.384	0.003	0.648	0.003	0.229	0.003	0.085	0.590	2.023	0.590	1.42958
0.004	1.540	0.004	0.820	0.004	0.308	0.004	0.115	0.790	2.272	0.790	1.64837
0.005	1.659	0.005	0.945	0.005	0.376	0.005	0.146	0.990	2.463	0.990	1.83813
0.006	1.756	0.006	1.053	0.007	0.496	0.006	0.196	1.190	2.627	1.190	2.00028
0.007	1.852	0.007	1.150	0.009	0.606	0.009	0.258	1.400	2.769	1.390	2.13749
0.009	2.001	0.009	1.284	0.011	0.700	0.011	0.301	1.600	2.891	1.590	2.2598
0.011	2.127	0.011	1.408	0.012	0.755	0.012	0.333	1.790	3.001	1.800	2.37077
0.012	2.187	0.012	1.459	0.014	0.819	0.014	0.378	2.000	3.102	2.000	2.47027
0.013	2.251	0.013	1.537	0.015	0.878	0.015	0.402	2.500	3.311	2.500	2.68134
0.018	2.468	0.017	1.670	0.018	0.972	0.018	0.467	3.000	3.485	3.000	2.85861
0.021	2.597	0.022	1.832	0.020	1.020	0.020	0.504	3.510	3.631	3.500	3.01067
0.028	2.794	0.028	1.976	0.022	1.098	0.022	0.549	4.000	3.756	4.000	3.14481
0.036	2.990	0.036	2.136	0.025	1.168	0.025	0.604	4.490	3.866	4.500	3.26018
0.044	3.137	0.045	2.290	0.028	1.228	0.028	0.653	5.010	3.966	5.000	3.36056
0.057	3.347	0.056	2.462	0.032	1.313	0.032	0.714				
0.072	3.514	0.072	2.647	0.035	1.370	0.035	0.764				
0.090	3.682	0.090	2.820	0.044	1.506	0.043	0.867				
0.114	3.866	0.115	3.013	0.057	1.678	0.056	1.021				
0.145	4.047	0.144	3.197	0.072	1.820	0.072	1.175				
0.180	4.533	0.180	3.350	0.088	1.967	0.090	1.318				
0.184	4.214	0.184	3.387	0.117	2.162	0.115	1.478				
0.230	4.371	0.230	3.580	0.144	2.309	0.145	1.636				
0.292	4.534	0.297	3.778	0.180	2.509	0.180	1.692				
0.372	4.686	0.373	3.956	0.181	2.480	0.183	1.799				
0.390	4.957	0.390	3.885	0.234	2.679	0.230	1.965				
0.471	4.834	0.470	4.131	0.293	2.847	0.293	2.150				
0.590	5.193	0.590	4.203	0.370	3.032	0.371	2.328				
0.596	4.972	0.594	4.307	0.390	3.025	0.390	2.191				
0.749	5.102	0.753	4.477	0.473	3.218	0.470	2.512				
0.790	5.352	0.790	4.427	0.590	3.378	0.590	2.530				
0.852	5.175	0.850	4.567	0.591	3.397	0.594	2.698				
0.950	5.236	0.951	4.640	0.754	3.581	0.750	2.888				
1.000	5.475	0.990	4.598	0.790	3.637	0.790	2.785				
1.013	5.274	1.013	4.684	0.846	3.672	0.847	2.988				
1.077	5.308	1.077	4.727	0.952	3.758	0.948	3.081				
1.190	5.572	1.190	4.729	0.990	3.843	0.990	3.001				
1.201	5.368	1.203	4.806	1.012	3.805	1.013	3.134				
1.390	5.653	1.390	4.834	1.076	3.852	1.076	3.181				
1.590	5.721	1.600	4.924	1.190	3.992	1.190	3.172				
1.790	5.781	1.790	5.004	1.202	3.932	1.201	3.273				
1.990	5.833	2.000	5.072	1.390	4.121	1.390	3.325				
2.500	5.941	2.500	5.213	1.590	4.225	1.590	3.452				
3.000	6.027	3.000	5.325	1.790	4.326	1.800	3.560				
3.490	6.098	3.500	5.417	2.000	4.411	2.000	3.660				
4.000	6.158	4.000	5.496	2.500	4.589	2.500	3.864				
4.510	6.210	4.500	5.565	3.000	4.722	3.000	4.034				
5.000	6.256	4.990	5.625	3.500	4.838	3.500	4.173				
				4.000	4.949	4.000	4.294				
				4.500	5.043	4.500	4.403				
				5.000	5.111	5.000	4.498				

Table A.2: Unary N_2 static equilibrium data on zeolite 13X (0 to 25°C).

0°C		25°C	
p_{N_2} [bar]	$q^*_{N_2}$ [mol/kg]	p_{N_2} [bar]	$q^*_{N_2}$ [mol/kg]
0.0015	0.0010	0.0000	0.0000
0.0052	0.0042	0.0053	0.0021
0.0069	0.0055	0.0069	0.0029
0.0088	0.0073	0.0089	0.0038
0.0109	0.0093	0.0108	0.0052
0.0135	0.0115	0.0135	0.0064
0.0177	0.0149	0.0177	0.0083
0.0224	0.0193	0.0224	0.0105
0.0283	0.0245	0.0283	0.0129
0.0357	0.0308	0.0356	0.0165
0.0451	0.0388	0.0452	0.0208
0.0566	0.0485	0.0570	0.0259
0.0719	0.0621	0.0719	0.0323
0.0910	0.0781	0.0909	0.0405
0.1149	0.0981	0.1149	0.0507
0.1452	0.1233	0.1451	0.0638
0.1836	0.1545	0.1800	0.1000
0.2318	0.1925	0.1836	0.0802
0.2939	0.2402	0.2321	0.1008
0.3720	0.2983	0.2932	0.1263
0.4701	0.3678	0.3741	0.1595
0.5951	0.4519	0.3900	0.1801
0.7530	0.5512	0.4724	0.1987
0.8520	0.6105	0.5900	0.2595
0.9521	0.6671	0.5936	0.2453
1.0134	0.7016	0.7502	0.3039
1.0761	0.7355	0.7900	0.3317
1.2008	0.8009	0.8522	0.3404
		0.9485	0.3729
		0.9900	0.4045
		1.0134	0.3947
		1.0746	0.4162
		1.1900	0.4757
		1.2030	0.4581
		1.3900	0.5403
		1.6000	0.6047
		1.7900	0.6645
		1.9900	0.7226
		2.4900	0.8606
		2.9900	0.9880
		3.5000	1.1034
		4.0000	1.2112
		4.5000	1.3111
		5.0100	1.4042

Table A.3: Unary N_2 static equilibrium data on zeolite 13X (50 to 125°C).

50°C		75°C		100°C		125°C		150°C	
p_{N_2} [bar]	$q^*_{N_2}$ [mol/kg]	p_{N_2} [bar]	$q^*_{N_2}$ [mol/kg]	p_{N_2} [bar]	$q^*_{N_2}$ [mol/kg]	p_{N_2} [bar]	$q^*_{N_2}$ [mol/kg]	p_{N_2} [bar]	$q^*_{N_2}$ [mol/kg]
0.0000	0.0000	0.0000	0.0000	0.0000	0.0000	0.0000	0.0000	0.0000	
0.0016	0.0002	0.0001	0.0016	0.0053	0.0005	0.1800	0.0178	0.1800	0.0088
0.0053	0.0012	0.0015	0.0001	0.0069	0.0006	0.3900	0.0262	0.3900	0.0210
0.0069	0.0016	0.0053	0.0007	0.0088	0.0007	0.5900	0.0395	0.5900	0.0323
0.0088	0.0020	0.0069	0.0009	0.0108	0.0012	0.7900	0.0532	0.7900	0.0415
0.0108	0.0028	0.0088	0.0013	0.0136	0.0013	0.9900	0.0656	0.9900	0.0514
0.0135	0.0037	0.0108	0.0016	0.0203	0.0020	1.1900	0.0787	1.1900	0.0611
0.0178	0.0049	0.0135	0.0020	0.0224	0.0023	1.3900	0.0912	1.3900	0.0702
0.0224	0.0060	0.0178	0.0027	0.0283	0.0030	1.5900	0.1037	1.5900	0.0796
0.0282	0.0077	0.0224	0.0034	0.0357	0.0038	1.7900	0.1178	1.7900	0.0891
0.0358	0.0097	0.0283	0.0044	0.0451	0.0048	1.9900	0.1287	2.0000	0.1001
0.0451	0.0122	0.0358	0.0053	0.0573	0.0061	2.4800	0.1594	2.5000	0.1216
0.0571	0.0151	0.0450	0.0066	0.0720	0.0078	2.9900	0.1890	3.0000	0.1427
0.0719	0.0191	0.0571	0.0084	0.0910	0.0100	3.4900	0.2173	3.5000	0.1653
0.0910	0.0240	0.0720	0.0107	0.1149	0.0126	4.0000	0.2465	4.0000	0.1862
0.1149	0.0303	0.0910	0.0135	0.1452	0.0159	4.5000	0.2730	4.5000	0.2071
0.1453	0.0383	0.1149	0.0170	0.1800	0.0237	5.0100	0.3022	5.0000	0.2286
0.1800	0.0575	0.1453	0.0214	0.1836	0.0202				
0.1835	0.0482	0.1800	0.0276	0.2320	0.0255				
0.2320	0.0603	0.1836	0.0272	0.2935	0.0315				
0.2931	0.0759	0.2320	0.0341	0.3704	0.0398				
0.3740	0.0956	0.2930	0.0426	0.3800	0.0402				
0.3800	0.0987	0.3735	0.0539	0.4729	0.0501				
0.4726	0.1193	0.3800	0.0558	0.5900	0.0563				
0.5900	0.1406	0.4719	0.0681	0.5959	0.0624				
0.5959	0.1478	0.5900	0.0844	0.7523	0.0761				
0.7529	0.1821	0.5955	0.0847	0.7900	0.0759				
0.7900	0.1828	0.7535	0.1059	0.8512	0.0854				
0.8525	0.2045	0.7900	0.1106	0.9485	0.0949				
0.9513	0.2261	0.8515	0.1191	0.9900	0.0924				
0.9900	0.2222	0.9511	0.1322	1.0147	0.1007				
1.0136	0.2392	0.9900	0.1375	1.0756	0.1065				
1.0748	0.2518	1.0148	0.1407	1.1900	0.1088				
1.1900	0.2617	1.0762	0.1485	1.2012	0.1640				
1.2019	0.2787	1.1900	0.1647	1.2028	0.1189				
1.3900	0.3022	1.3900	0.1891	1.4000	0.1250				
1.5900	0.3401	1.5900	0.2134	1.5900	0.1411				
1.7900	0.3771	1.7900	0.2386	1.7900	0.1560				
1.9900	0.4118	1.9900	0.2626	1.9900	0.1735				
2.5000	0.4993	2.4900	0.3208	2.5000	0.2133				
2.9900	0.5817	2.9900	0.3761	3.0000	0.2541				
3.5000	0.6598	3.5000	0.4312	3.5000	0.2912				
4.0000	0.7345	4.0000	0.4834	3.9900	0.3287				
4.5000	0.8056	4.5000	0.5347	4.5000	0.3659				
5.0000	0.8727	5.0000	0.5832	4.9900	0.4020				

A.2 Binary CO_2/N_2 Equilibrium Data

Table A.4: A summary of all competitive CO_2/N_2 experiments on zeolite 13X.

T [°C]	P [bar]	y_{CO_2} [-]	y_{N_2} [-]	$q^*_{CO_2}$ [mol/kg]	$q^*_{N_2}$ [mol/kg]
22.6	0.97	0.05	0.95	2.909	0.14450
22.1	0.97	0.10	0.90	3.461	0.08114
23.1	0.97	0.15	0.85	3.833	0.08006
23.8	0.97	0.50	0.50	4.814	0.03623
23.8	0.96	0.75	0.25	5.375	0.02000
24.4	0.48	0.10	0.90	3.090	0.02805
23.9	0.48	0.20	0.80	3.498	0.01921
24.6	0.48	0.50	0.50	4.200	0.01862
24.1	0.49	0.80	0.20	4.708	0.00815

A.3 Process Studies Parameters

Table A.5: Adsorption and desorption process studies parameters for zeolite 13X [19].

Parameter	Value	Source
Column Properties		
adsorbent mass, m_{ads} [kg]	27.43	assumed
column length, L [m]	1.0	assumed
inner column diameter, d_i [m]	0.289	assumed
outer column diameter, d_o [m]	0.324	assumed
column void fraction, ϵ	0.37	assumed
particle void fraction, ϵ_{p}	0.35	assumed
tortuosity, τ	3	assumed
Properties and Constants		
universal gas constant, R [m^3 Pa mol^{-1} K^{-1}]	8.314	standard value
adsorbent particle density, ρ_{p} [kg m^{-3}]	1130	assumed
column wall density, ρ_{w} [kg m^{-3}]	7800	standard value
specific heat capacity of the gas, $C_{\text{p,g}}$ [J mol^{-1} K^{-1}]	1010.6	NIST database
specific heat capacity of the adsorbed phase, $C_{\text{p,a}}$ [J mol^{-1} K^{-1}]	$C_{p,g}$	assumed
specific heat capacity of the adsorbent, $C_{\text{p,s}}$ [J mol^{-1} K^{-1}]	1070	assumed
specific heat capacity of the column wall, $C_{\text{p,w}}$ [J mol^{-1} K^{-1}]	502.0	standard value
fluid viscosity, μ [kg m^{-1} s^{-1}]	1.720×10^{-5}	standard value
molecular diffusion, D_{m} [m s^{-2}]	1.30×10^{-5}	Chapman-Enskog
effective gas thermal conductivity, K_z [W m^{-1} K^{-1}]	9.03×10^{-2}	assumed
thermal conductivity of column wall, K_{w} [W m^{-1} K^{-1}]	16.0	standard value
internal heat transfer coefficient, h_{in} [W m^{-2} K^{-1}]	8.6	assumed
external heat transfer coefficient, h_{out} [W m^{-2} K^{-1}]	2.5	assumed

A.4 Ideal Adsorbed Solution Theory Calculations

The following equations are solved simultaneously to determine the competitive loading as a function of T, p_i, and fitted single component isotherm equations for each component, q_i^*. The fractional amount of an adsorbed component is the fractional loading, x_i. The sum of all component fractional loadings must be equal to 1.

$$\sum_{i=1}^{n_{\text{comp}}} x_i = 1 \tag{A.1}$$

The equilibrium between the fluid and solid phases, shown in Eqn. A.2, is then described with an expression analogous to Raoult's Law.

$$y_i P = P_i^o(\pi) x_i \tag{A.2}$$

$P_i^o(\pi)$ is defined as the component pressure which all component spreading pressures, π, are the same. This is analogous to the vapor pressure in Raoult's law.

$$\int_0^{P_i^o(\pi)} \frac{q_i^o(p_i)}{p_i} dp_i = \frac{\pi A}{RT} \tag{A.3}$$

To close the overall mass balance the total loading must be determined.

$$\frac{1}{q^{\text{tot}}} = \sum_{i=1}^{n_{\text{comp}}} \frac{x_i}{q_i^o} \tag{A.4}$$

It is important to note these equations can be applied to any number of components in a mixture. For the IAST predictions, the SSL-PP isotherm was used as the single component N_2 isotherm. All of the N_2 fitting procedures predict the single component equilibrium data similarly.

A.5 Competitive CO_2/N_2 Desorption Experiments

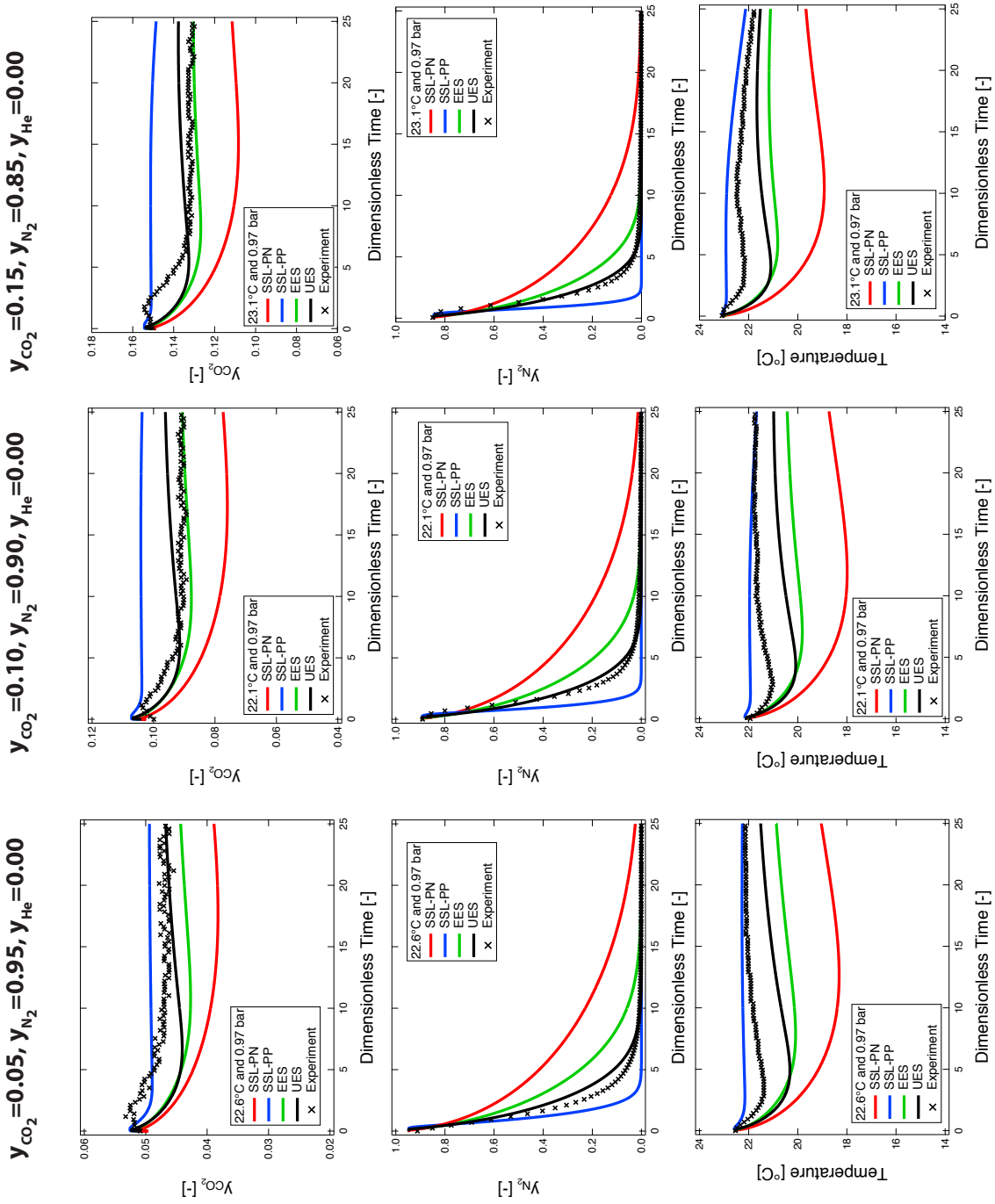

Figure A.1: Competitive CO_2/N_2 concentration (left and middle) and temperature (right) desorption profiles on Zeolite 13X at $\approx 22°C$ and 0.97 bar. Experiments are the markers and simulations are the various lines. The initial concentrations are provided at the top of each column of figures. Temperature is measured at $z = 0.8L$. Desorption was performed using a sweep of He at 50 ccm.

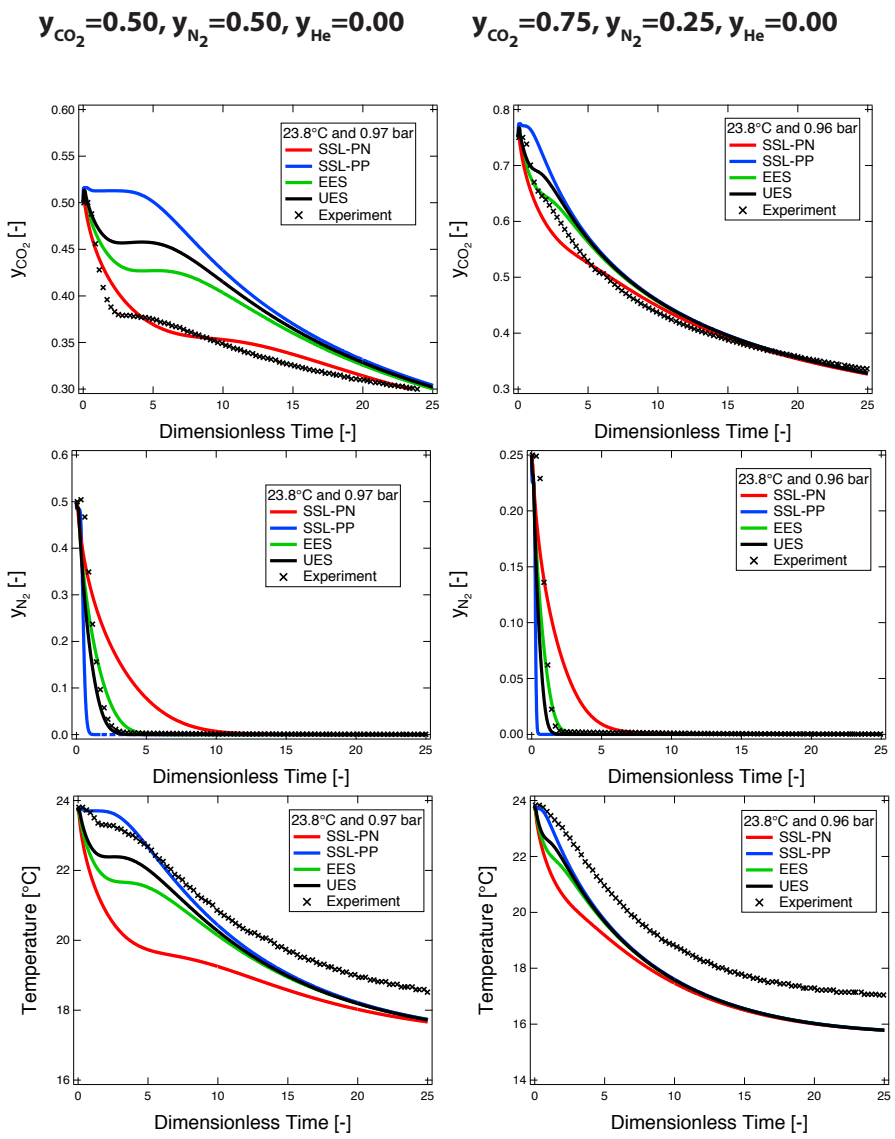

Figure A.2: Competitive CO_2/N_2 concentration (top two rows) and temperature (last row) desorption profiles on Zeolite 13X at $\approx 22°C$ and 0.97 bar. Experiments are the markers and simulations are the various lines. The initial concentrations are provided at the top of each column of figures. Temperature is measured at $z = 0.8L$. Desorption was performed using a sweep of He at 50 ccm.

Appendix B: Supporting Information for "Measurement of competitive CO_2 and H_2O adsorption on zeolite 13X for post-combustion CO_2 capture"

B.1 Single Component H_2O Equilibrium Data

Table B.1: A summary of the single component H_2O equilibrium experiments on zeolite 13X from 22 to 50°C (75 and 100°C in next table).

22°C		30°C		40°C		50°C	
p_{H_2O} [bar]	$q^*_{H_2O}$ [mol/kg]	p_{H_2O} [bar]	$q^*_{H_2O}$ [mol/kg]	p_{H_2O} [bar]	$q^*_{H_2O}$ [mol/kg]	p_{H_2O} [bar]	$q^*_{H_2O}$ [mol/kg]
1.57×10^{-5}	2.019	1.10×10^{-3}	11.464	1.13×10^{-3}	10.886	1.13×10^{-3}	9.597
1.64×10^{-5}	1.009	1.20×10^{-3}	11.485	1.20×10^{-3}	10.865	1.21×10^{-3}	9.820
1.69×10^{-5}	3.028	1.95×10^{-3}	12.536	1.91×10^{-3}	11.840	1.87×10^{-3}	10.882
1.88×10^{-5}	4.037	4.03×10^{-3}	14.625	4.10×10^{-3}	13.826	4.25×10^{-3}	13.073
2.19×10^{-5}	5.046	7.20×10^{-3}	15.430	7.25×10^{-3}	14.521	7.25×10^{-3}	13.737
2.59×10^{-5}	6.055	7.25×10^{-3}	15.301	7.81×10^{-3}	14.531	7.92×10^{-3}	13.723
3.09×10^{-5}	7.064	7.75×10^{-3}	15.330	1.38×10^{-2}	15.317	1.40×10^{-2}	14.629
3.77×10^{-5}	8.073	1.40×10^{-2}	16.160	1.41×10^{-2}	15.385	1.43×10^{-2}	14.543
4.82×10^{-5}	9.081	1.43×10^{-2}	16.057	1.77×10^{-2}	15.624	1.83×10^{-2}	14.945
7.04×10^{-5}	10.089	1.78×10^{-2}	16.449	1.95×10^{-2}	15.769	1.90×10^{-2}	14.989
1.46×10^{-4}	11.094	2.03×10^{-2}	16.592	2.10×10^{-2}	15.704	2.11×10^{-2}	15.000
2.80×10^{-4}	12.302	2.11×10^{-2}	16.497				
4.23×10^{-4}	12.091						
4.99×10^{-4}	12.249						
7.02×10^{-4}	13.021						
7.48×10^{-4}	12.635						
9.98×10^{-4}	12.936						
1.03×10^{-3}	12.101						
1.17×10^{-3}	12.101						
1.25×10^{-3}	13.184						
1.39×10^{-3}	13.720						
1.52×10^{-3}	13.408						
1.75×10^{-3}	13.573						
1.95×10^{-3}	13.207						
2.03×10^{-3}	13.750						
2.08×10^{-3}	14.148						
2.28×10^{-3}	13.883						
2.50×10^{-3}	13.986						
2.76×10^{-3}	14.449						
4.00×10^{-3}	15.549						
4.13×10^{-3}	14.868						
5.00×10^{-3}	14.778						
6.75×10^{-3}	15.394						
7.25×10^{-3}	16.009						
7.56×10^{-3}	15.215						
7.82×10^{-3}	16.009						
9.41×10^{-3}	15.872						
1.23×10^{-2}	16.198						
1.25×10^{-2}	15.882						
1.37×10^{-2}	16.776						
1.39×10^{-2}	16.860						
1.50×10^{-2}	16.187						
1.52×10^{-2}	16.510						
1.71×10^{-2}	16.727						
1.77×10^{-2}	16.565						
1.84×10^{-2}	17.272						
2.02×10^{-2}	16.923						
2.02×10^{-2}	17.534						
2.08×10^{-2}	17.252						
2.12×10^{-2}	17.430						
2.25×10^{-2}	17.426						
2.31×10^{-2}	17.712						
2.34×10^{-2}	17.761						
2.37×10^{-2}	17.809						

Table B.2: A summary of the single component H_2O equilibrium experiments on zeolite 13X from 75 to 100°C (22 to 50°C in previous table).

75°C		100°C	
p_{H_2O} [bar]	$q^*_{H_2O}$ [mol/kg]	p_{H_2O} [bar]	$q^*_{H_2O}$ [mol/kg]
1.08×10^{-3}	6.107	1.20×10^{-3}	4.070
1.18×10^{-3}	5.856	1.22×10^{-3}	4.088
1.93×10^{-3}	7.735	1.83×10^{-3}	4.964
4.23×10^{-3}	10.692	4.23×10^{-3}	7.129
7.69×10^{-3}	11.796	8.23×10^{-3}	8.777
1.44×10^{-2}	12.808	1.43×10^{-2}	10.622
1.71×10^{-2}	13.034	1.73×10^{-2}	11.032
1.90×10^{-2}	13.197	1.88×10^{-2}	11.220

B.2 Binary TGA CO_2/H_2O Equilibrium Data

Table B.3: A summary of all TGA competitive CO_2/H_2O experiments on zeolite 13X. All experiments were performed at 22°C and 0.97 bar total pressure. Relative humidities are reported at 22°C.

RH [%]	y_{H_2O} [-]	y_{CO_2} [-]	$q^*_{H_2O}$ [mol/kg]	$q^*_{CO_2}$ [mol/kg]
4.05	1.07×10^{-3}	0.9989	13.56	0.7457
7.32	1.99×10^{-3}	0.9980	14.23	0.4836
9.24	2.51×10^{-3}	0.9974	14.51	0.1920
13.5	3.66×10^{-3}	0.9963	14.97	0.1375
25.7	6.93×10^{-3}	0.9931	16.09	9.93×10^{-2}
70.9	1.93×10^{-2}	0.9807	16.93	7.41×10^{-2}
72.3	1.96×10^{-2}	0.9804	17.16	5.77×10^{-2}

B.3 Supporting Figures

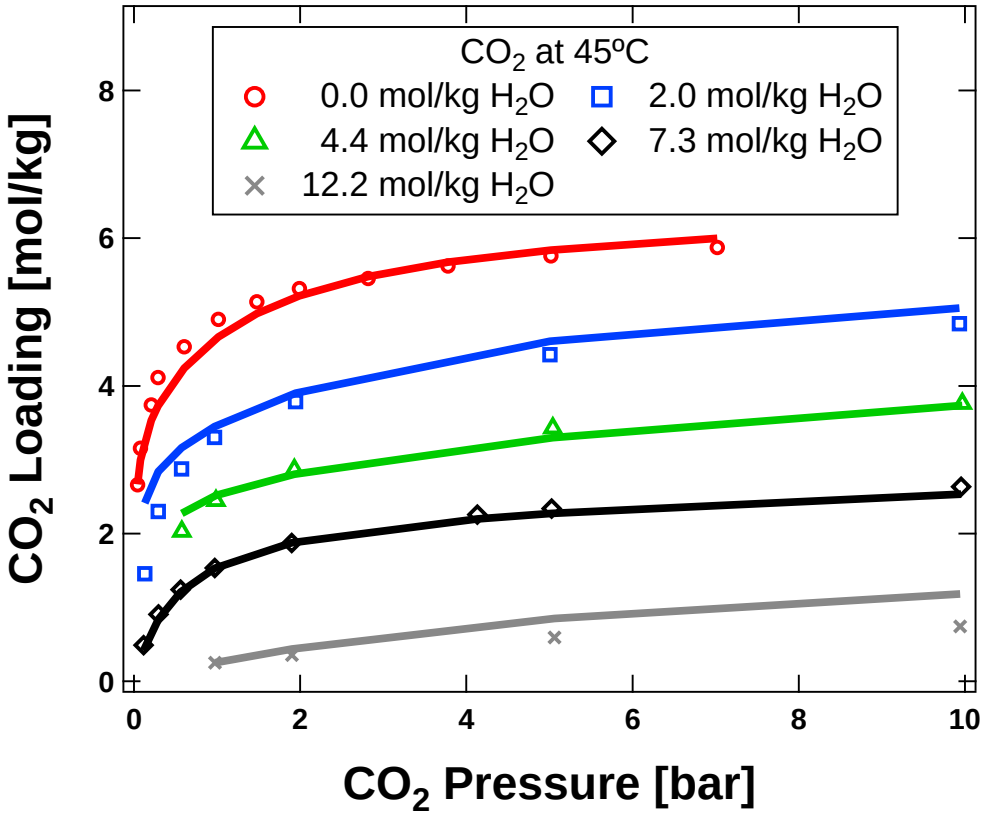

Figure B.1: Competitive CO_2/H_2O equilibrium loadings (markers) from Hefti and Mazzotti with predictions (solid lines) from the modified DSL isotherm [15].

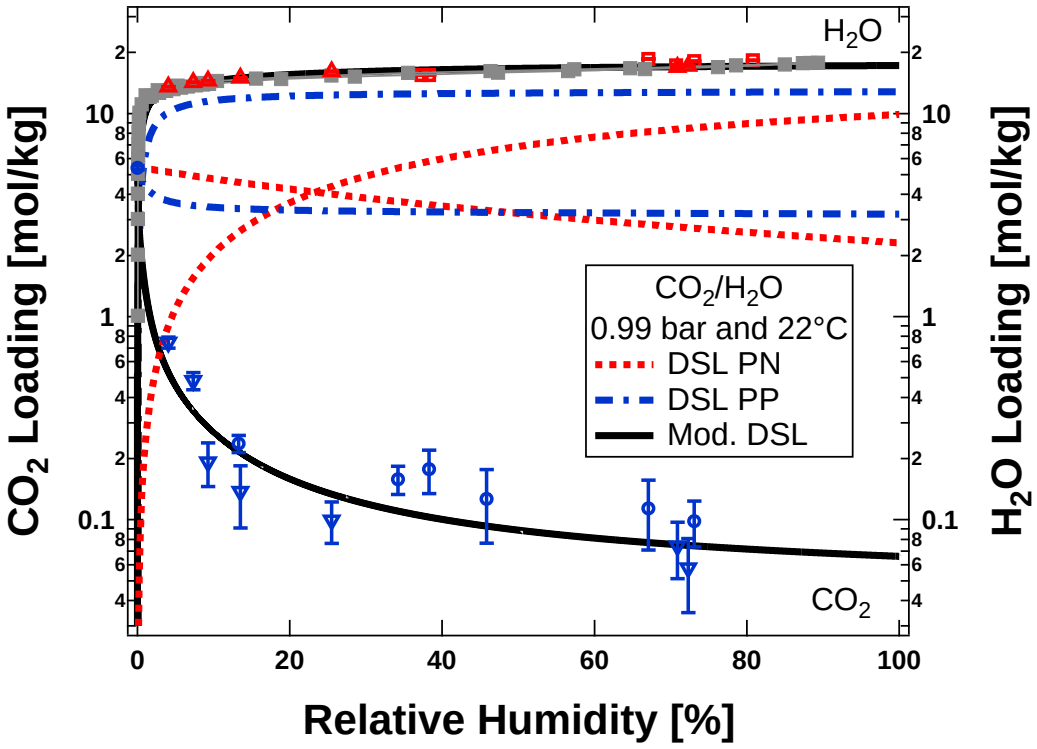

Figure B.2: Competitive CO_2/H_2O equilibrium loadings (circles/squares) from dynamic column breakthrough experiments on Zeolite 13X. Competitive CO_2/H_2O equilibrium points are at a total pressure of 0.99 bar and 22°C. Thermogravimetrically collected competitive CO_2/H_2O equilibrium loadings (up triangles/down triangles) are also shown. For comparison, the single component water vapor loadings are shown as the gray squares. The perfect positive competitive dual-site Langmuir isotherms are shown with the dashed lines. The perfect negative pairing isotherms are shown with dash-dotted lines. The modified dual-site Langmuir isotherms are shown with solid lines.

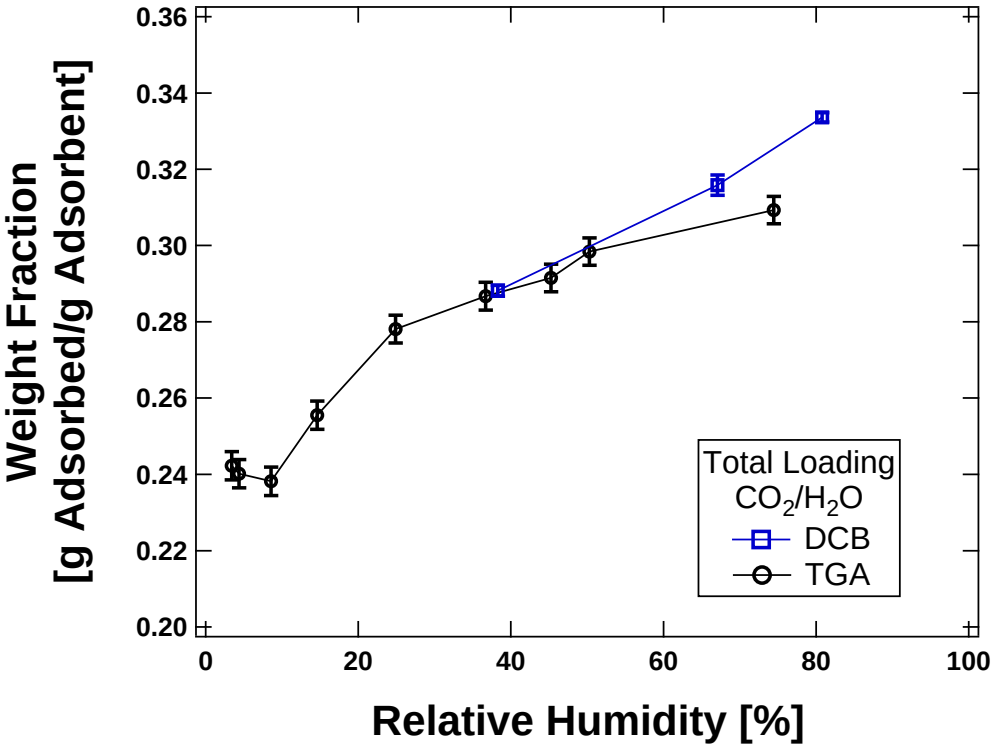

Figure B.3: A comparison of the competitive CO_2/H_2O total loadings for the thermogravimetric and dynamic column breakthrough experiments at 22°C as a function of relative humidity.

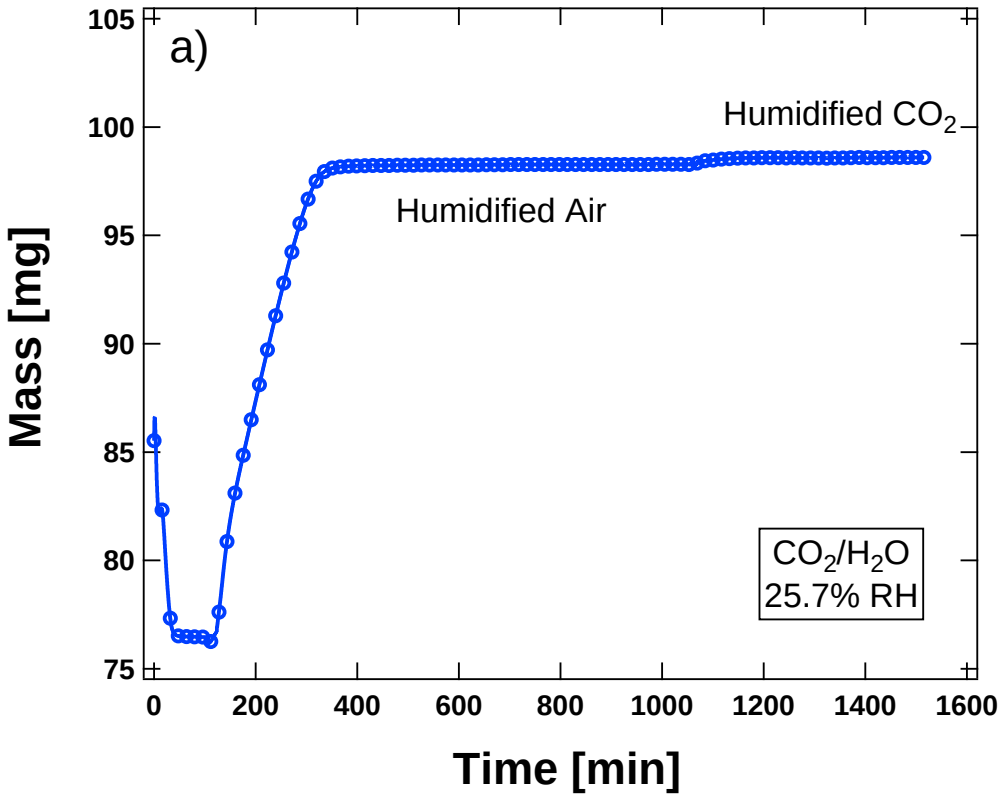

Figure B.4: A thermogravimetric mass uptake curve for a competitive CO_2/H_2O mixture at 22°C and 25.7% relative humidity of H_2O. The experiment was performed by first loading H_2O onto zeolite 13X with air as a carrier then switching to humid CO_2. This allows the easy measurement of the competitive CO_2 loading since the H_2O competitive loading is unaffected by CO_2.

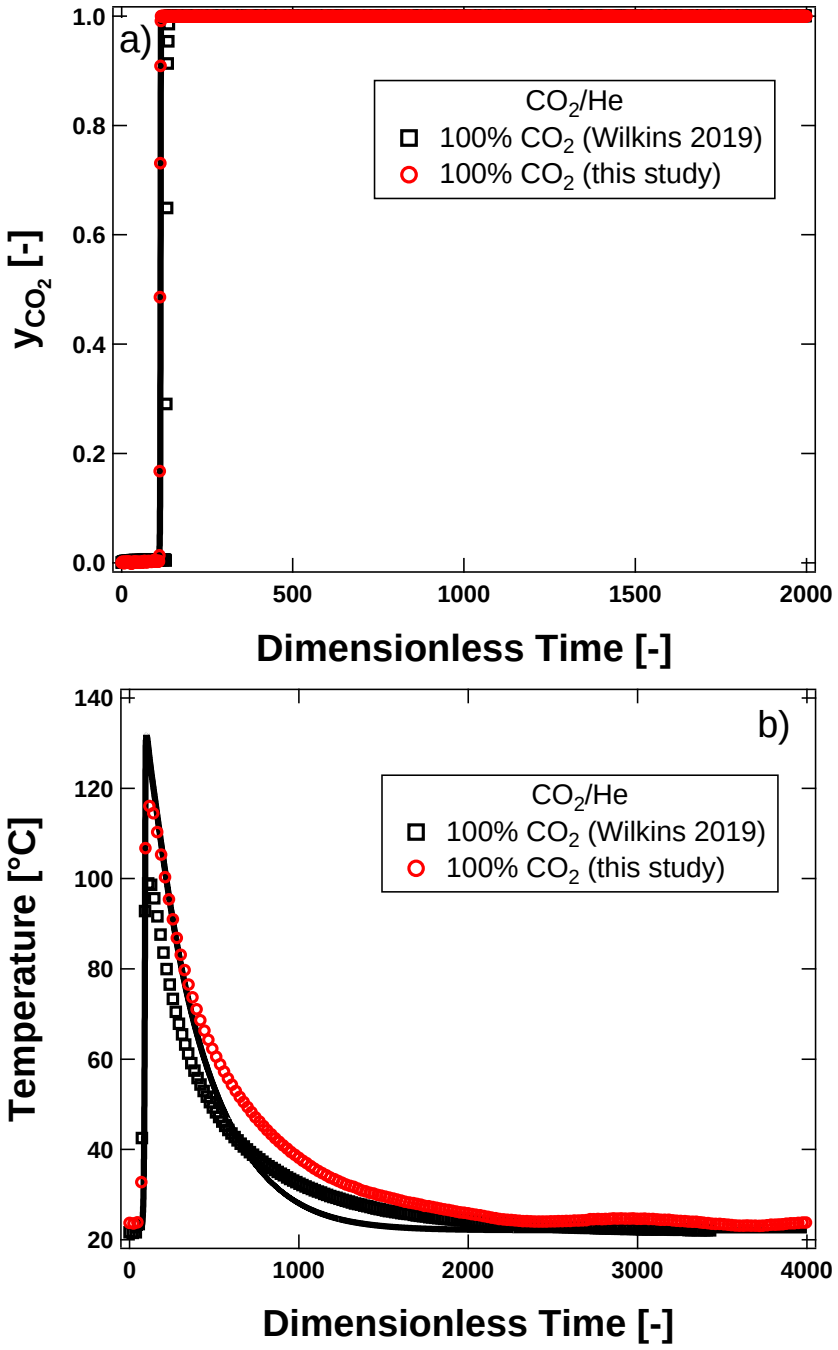

Figure B.5: A single component 100% CO_2 breakthrough experiment at 21.6°C and 0.982 bar. The experiment was performed after all of the competitive CO_2/H_2O breakthroughs were performed. The data is similar with data from our previous study [2]. A CO_2 loading of 5.48 mol/kg was calculated. This is in agreement with the single component CO_2 equilibrium data. This shows that zeolite 13X did not degrade or weaken after repeated exposure to H_2O.

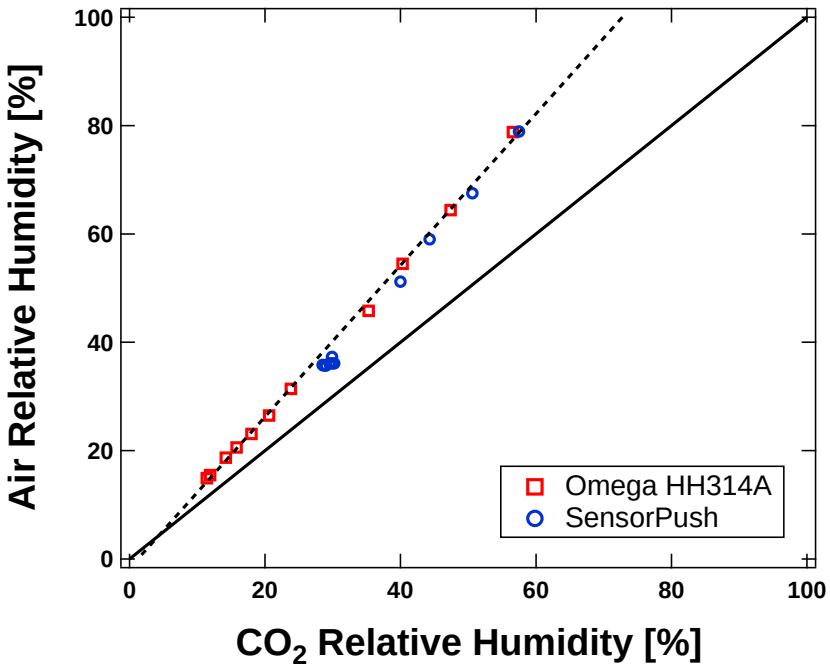

Figure B.6: The calibration curve to correct the relative humidity signal when the carrier gas is CO_2. This fits the equation provided in the main text of the paper.

Appendix C: Supporting Information for "Quantitative microscale dynamic column breakthrough apparatus for measurement of unary and binary adsorption equilibria on milligram quantities of adsorbent"

C.1 Error Analysis Equations for the Column Mass Balance

Error analysis was calculated to estimate the error bars of each equilibrium measurement in this study. The uncertainty (δ) of a given function f with respect to a measured variable γ can be approximated with the following equation:

$$\delta f_\gamma = \left| \left(\frac{\partial f}{\partial \gamma} \right) \delta \gamma \right| \tag{C.1}$$

These uncertainties can be summed for each uncertain variable (γ_i) to determine the total uncertainty (δf_{total}):

$$\delta f_{\text{total}} = \sum_i \left| \left(\frac{\partial f}{\partial \gamma_i} \right) \delta \gamma_i \right| \tag{C.2}$$

For the transient mass balance, the following sum is found:

$$\delta q^*_{\text{total}} = \sum_i \left| \left(\frac{\partial q^*}{\partial \gamma_i} \right) \delta \gamma_i \right| \tag{C.3}$$

There are 8 uncertain variables in calculation for equilibrium loading. These variables are: m_{ads}, T, P, ρ_{sk}, y_{in}, Q_{in}, $y(t)$ and $Q(t)$. The transient mass balance (for adsorption) solved for q^*_{ADS} is shown below:

$$q^*_{\text{ADS}} = \frac{y_{\text{in}} P Q_{\text{in}}}{m_{\text{ads}} RT}\left[\int_0^{t_\infty}\left(1-\frac{y(t)Q(t)}{y_{\text{in}}Q_{\text{in}}}\right)\Bigg|_{\text{comp}} dt - \int_0^{t_\infty}\left(1-\frac{y(t)Q(t)}{y_{\text{in}}Q_{\text{in}}}\right)\Bigg|_{\text{blank}} dt + \frac{m_{\text{ads}}}{\rho_{\text{sk}}Q_{\text{in}}}\right] \tag{C.4}$$

A few abbreviations will be used in this section. Specifically, integrals will be replaced with the mean-residence time definitions where possible:

$$\bar{t}_{\text{ads}} = \int_0^{t_\infty}\left(1-\frac{y(t)Q(t)}{y_{\text{in}}Q_{\text{in}}}\right)\Bigg|_{\text{ads}} dt \tag{C.5}$$

$$\bar{t}_{\text{des}} = \int_0^{t_\infty}\left(\frac{y(t)Q(t)}{y_{\text{init}}Q_{\text{init}}}\right)\Bigg|_{\text{des}} dt \tag{C.6}$$

A derivative of q^*_{ADS} can be made for each uncertain variable, and then multiplied through with the uncertainty of that variable. The uncertainty of m_{ads} in Eqn. C.4 is equal to:

$$\frac{\partial q^*_{\text{ADS}}}{\partial m_{\text{ads}}}(\delta m_{\text{ads}}) = \left|\frac{-y_{\text{in}}PQ_{\text{in}}}{(m_{\text{ads}})^2 RT}\left[\bar{t}_{\text{comp,ads}} - \bar{t}_{\text{blank,ads}}\right]\right|\delta m_{\text{ads}} \tag{C.7}$$

m_{ads} is canceled out in the pyncnometric term, creating a constant that has a derivative of zero. All other terms have $1/m_{\text{ads}}$ as a multiplier. The equivalent function for T is:

$$\frac{\partial q^*_{\text{ADS}}}{\partial T}(\delta T) = \left|\frac{-y_{\text{in}}PQ_{\text{in}}}{m_{\text{ads}}RT^2}\left[\bar{t}_{\text{comp,ads}} - \bar{t}_{\text{blank,ads}} + \frac{m_{\text{ads}}}{\rho_{\text{sk}}Q_{\text{in}}}\right]\right|\delta T \tag{C.8}$$

All terms have a $1/T$ multiplier, which has been previously factored out. The equivalent function for P is:

$$\frac{\partial q^*_{\text{ADS}}}{\partial P}(\delta P) = \left|\frac{y_{\text{in}}Q_{\text{in}}}{m_{\text{ads}}RT}\left[\bar{t}_{\text{comp,ads}} - \bar{t}_{\text{blank,ads}} + \frac{m_{\text{ads}}}{\rho_{\text{sk}}Q_{\text{in}}}\right]\right|\delta P \tag{C.9}$$

All terms have a P multiplier, which has been previously factored out. The derivative of P is equal to 1, so the P is disappears from the numerator with all other terms remaining the same. The equivalent function for ρ_{sk} is:

$$\frac{\partial q^*_{\text{ADS}}}{\partial \rho_{\text{sk}}}(\delta \rho_{\text{sk}}) = \left|\frac{-y_{\text{in}}PQ_{\text{in}}}{RT}\left[\frac{1}{(\rho_{\text{sk}})^2 Q_{\text{in}}}\right]\right|\delta \rho_{\text{sk}} \tag{C.10}$$

The pyncnometric density, ρ_{sk}, is only found in the pyncnometric term. Therefore all other terms are constants and drop out of the equation. The equivalent function for y_{in} is:

$$\frac{\partial q^*_{\text{ADS}}}{\partial y_{\text{in}}}(\delta y_{\text{in}}) = \left| \frac{PQ_{\text{in}}}{RT} \left[\frac{1}{\rho_{\text{sk}} Q_{\text{in}}} \right] \right| \delta y_{\text{in}} \tag{C.11}$$

The inlet mole fraction, y_{in}, is cancelled out in the outlet molar terms and becomes a constant. The inlet terms contain a y_{in}, but the same derivative is found for the blank and composite experiment, with opposite signs. Therefore, the inlet integral terms cancel out. The only term which contains a y_{in} that remains is the pyncnometric term, where the y_{in} goes to one after differentiation. The equivalent function for Q_{in} is:

$$\frac{\partial q^*_{\text{ADS}}}{\partial Q_{\text{in}}}(\delta Q_{\text{in}}) = \left| 0 \right| \delta Q_{\text{in}} \tag{C.12}$$

As with the y_{in} derivatives, the outlet integral terms become constants (Q_{in} cancels out), the inlet terms cancel out due to subtraction, and interestingly, the pyncnometric term also becomes a constant and drops out of the integral yielding no error associated with Q_{in}. The equivalent function for $y(t)$ is:

$$\frac{\partial q^*_{\text{ADS}}}{\partial y(t)}(\delta y(t)) = \left| \frac{y_{\text{in}} PQ_{\text{in}}}{m_{\text{ads}} RT} \left[\int_0^{t_\infty} \left(\frac{Q(t)}{y_{\text{in}} Q_{\text{in}}} \right) \Big|_{\text{comp}} dt - \int_0^{t_\infty} \left(\frac{Q(t)}{y_{\text{in}} Q_{\text{in}}} \right) \Big|_{\text{blank}} dt \right] \right| \delta y(t) \tag{C.13}$$

The inlet integral terms and pyncnometric term cancel out since they are constant, and the $y(t)$ terms are differentiated out for both the composite and blank terms. The equivalent function for $Q(t)$ is:

$$\frac{\partial q^*_{\text{ADS}}}{\partial Q(t)}(\delta Q(t)) = \left| \frac{y_{\text{in}} PQ_{\text{in}}}{m_{\text{ads}} RT} \left[\int_0^{t_\infty} \left(\frac{y(t)}{y_{\text{in}} Q_{\text{in}}} \right) \Big|_{\text{comp}} dt - \int_0^{t_\infty} \left(\frac{y(t)}{y_{\text{in}} Q_{\text{in}}} \right) \Big|_{\text{blank}} dt \right] \right| \delta Q(t) \tag{C.14}$$

The inlet integral terms and pyncnometric term cancel out since they are constant, and the $Q(t)$ terms are differentiated out for both the composite and blank terms. The sum of all of these terms yields the error associated with measurement uncertainty for the adsorption experiment.

The desorption error equations equations are extremely similar. For ρ_{sk}, y_{init}, Q_{init}, $y(t)$ and $Q(t)$, the error terms are equivalent with the "y_{in}" and "Q_{in}" terms changed to "y_{init}" and "Q_{init}". The other error equations include an inlet integral that is not present in the desorption mass balance. The corresponding error equations for m_{ads}, T and P in the desorption mass balance are:

$$\frac{\partial q^*_{\text{DES}}}{\partial m_{\text{ads}}}(\delta m_{\text{ads}}) = \left| \frac{-y_{\text{init}} P Q_{\text{init}}}{(m_{\text{ads}})^2 RT} \left[\bar{t}_{\text{comp,des}} - \bar{t}_{\text{blank,des}} \right] \right| \delta m_{\text{ads}} \tag{C.15}$$

$$\frac{\partial q^*_{\text{DES}}}{\partial T}(\delta T) = \left| \frac{-y_{\text{init}} P Q_{\text{init}}}{m_{\text{ads}} R T^2} \left[\bar{t}_{\text{comp,des}} - \bar{t}_{\text{blank,des}} + \frac{m_{\text{ads}}}{\rho_{\text{sk}} Q_{\text{in}}} \right] \right| \delta T \tag{C.16}$$

$$\frac{\partial q^*_{\text{DES}}}{\partial P}(\delta P) = \left| \frac{y_{\text{init}} Q_{\text{init}}}{m_{\text{ads}} RT} \left[\bar{t}_{\text{comp,des}} - \bar{t}_{\text{blank,des}} + \frac{m_{\text{ads}}}{\rho_{\text{sk}} Q_{\text{init}}} \right] \right| \delta P \tag{C.17}$$

C.2 TCD Calibration Curves for Different Adsorbate Mixtures

This section contains all the calibrations for the thermal conductivity detector (TCD) used in this study. The N_2/He calibrations are shown in the main body of the paper. The calibrations consist two main parts: the trend of an adsorbate's mole fraction with a normalized TCD signal, and the maximum TCD signal to normalize the TCD signal. The maximum TCD signal is a function of flow through the analyzing arm of the TCD. The reference arm was kept at 20 sccm for all experiments. The maximum TCD signal, $I_{i,\mathrm{MAX}}$, was fitted in all cases to a quadratic polynomial of the form:

$$I_{i,\mathrm{MAX}} = aQ_i^2 + bQ_i + c \tag{C.18}$$

where Q_i is the standard flowrate in sccm ($T_{\mathrm{STD}} = 273.15$ K and $P_{\mathrm{STD}} = 1.01325$ bar) of a 100 mol% flow of the analyzing gas i through the TCD cell. The fitting parameters (a, b and c) are shown for all gas mixtures in Table C.1. The mole fraction of the adsorbate, y_i, was a function of the normalized TCD signal, $I_i/I_{i,\mathrm{MAX}}$, and was regressed to one of two empirical equations. The first form is a Langmuir-type equation given below:

$$y_i = \frac{a(I_i/I_{i,\mathrm{MAX}})}{1 + b(I_i/I_{i,\mathrm{MAX}})} \tag{C.19}$$

This fit was used exclusively for the the single-component N_2/He and CH_4/He systems. The second form of fitting equation was a quadratic polynomial:

$$y_i = a(I_i/I_{i,\mathrm{MAX}})^2 + b(I_i/I_{i,\mathrm{MAX}}) \tag{C.20}$$

This form was used for either CH_4/N_2 or CH_4/CO_2 mixtures. The parameters a and b, along with the appropriate form of the equation are shown in Table C.1.

Table C.1: The TCD calibration equation parameters for $f = y_i$ or $I_{i,\mathrm{MAX}}$. The "Eqn. Form" column is for the two empirical equation forms of y_i, explained above. L is for the Langmuir-type and Q is for the quadratic polynomial.

f	Eqn. Form	Gas Mixture	a	b	c
y_i	L	N_2 in He Reference	2.4462	1.4665	-
y_i	L	CH_4 in He Reference	1.4230	0.4452	-
y_i	Q	N_2 in CH_4 Reference	-0.6388	1.6243	-
y_i	Q	CH_4 in N_2 Reference	0.5603	0.4217	-
y_i	Q	CH_4 in CO_2 Reference	0.5543	0.4292	-
y_i	Q	CO_2 in CH_4 Reference	-0.6327	1.1618	-
$I_{i,\mathrm{MAX}}$	-	N_2 in He Reference	-8.9938	-26.9070	903658
$I_{i,\mathrm{MAX}}$	-	CH_4 in He Reference	-3.3091	-34.2999	486988
$I_{i,\mathrm{MAX}}$	-	N_2 in CH_4 Reference	-7.6476	-65.8620	419913
$I_{i,\mathrm{MAX}}$	-	CH_4 in N_2 Reference	-3.8403	-39.2956	-413429
$I_{i,\mathrm{MAX}}$	-	CH_4 in CO_2 Reference	-5.7145	40.8163	-673380
$I_{i,\mathrm{MAX}}$	-	CO_2 in CH_4 Reference	-46.989	-82.4228	693625

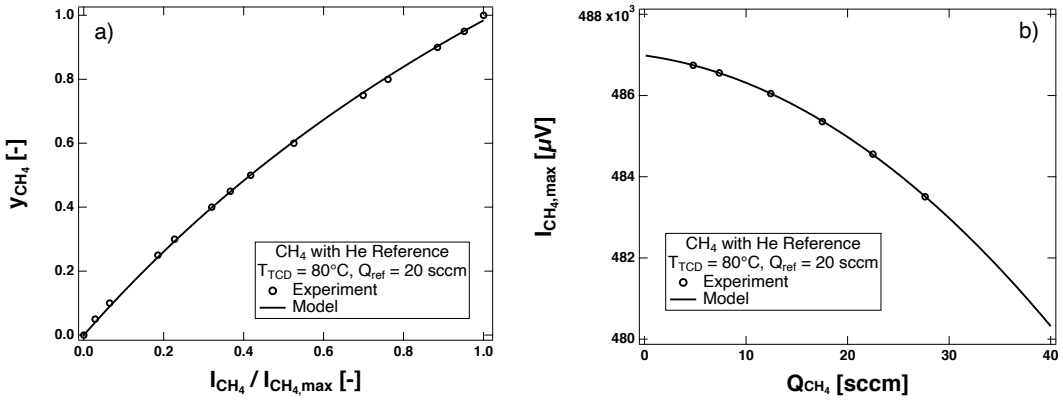

Figure C.1: CH_4/He thermal conductivity detector calibrations at a TCD block temperature of 80°C and a He reference flowrate of 20 sccm. Panel (**a**) shows the mole fraction of CH_4 as a function of the normalized TCD signal. Panel (**b**) shows the effect of analyzing gas flow on the 100% CH_4 TCD signal; this maximum signal is used to normalize the TCD signal in panel (**a**). The markers denote experimentally collected data and the lines are empirical fits.

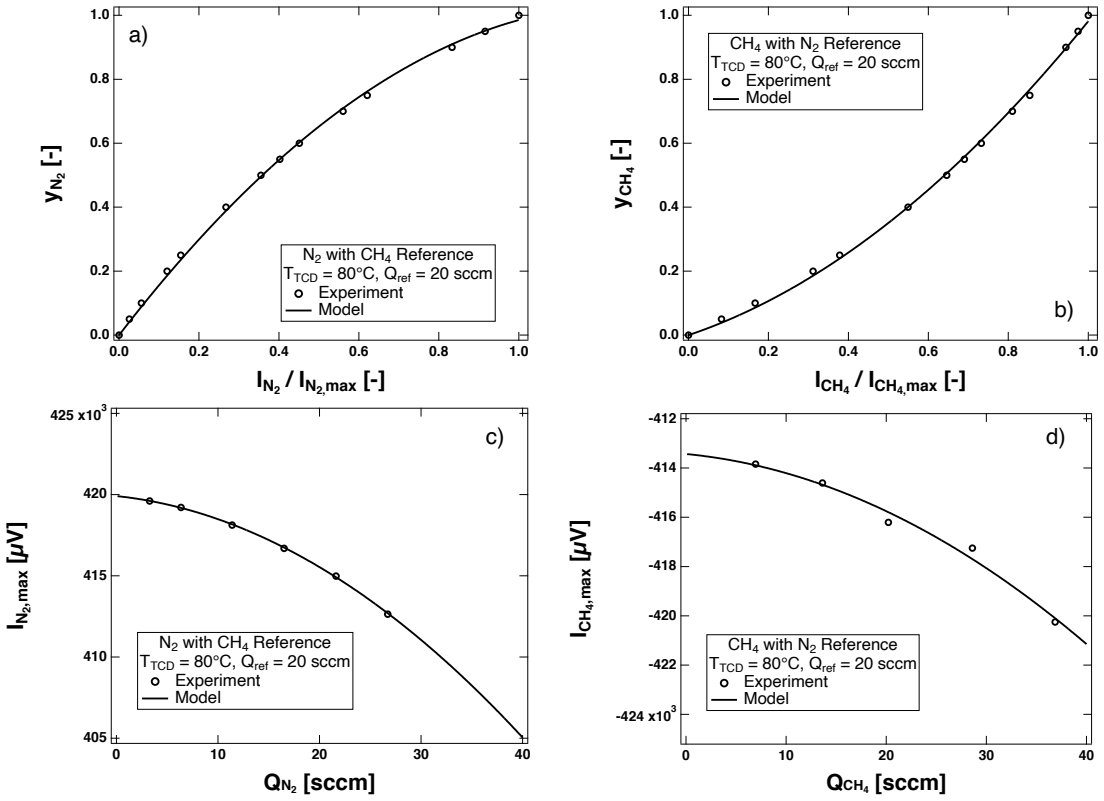

Figure C.2: CH_4/N_2 thermal conductivity detector calibrations at a TCD block temperature of 80°C and either a CH_4 or N_2 reference flowrate of 20 sccm. Panels (**a**) and (**b**) show the mole fraction of N_2 and CH_4 as a function of the normalized TCD signal, respectively. Panels (**c**) and (**d**) show the effect of analyzing gas flow on the 100% N_2 and CH_4 TCD signal, respectively; this maximum signal is used to normalize the TCD signal in panels (**a**) and (**b**). The markers denote experimentally collected data and the lines are empirical fits.

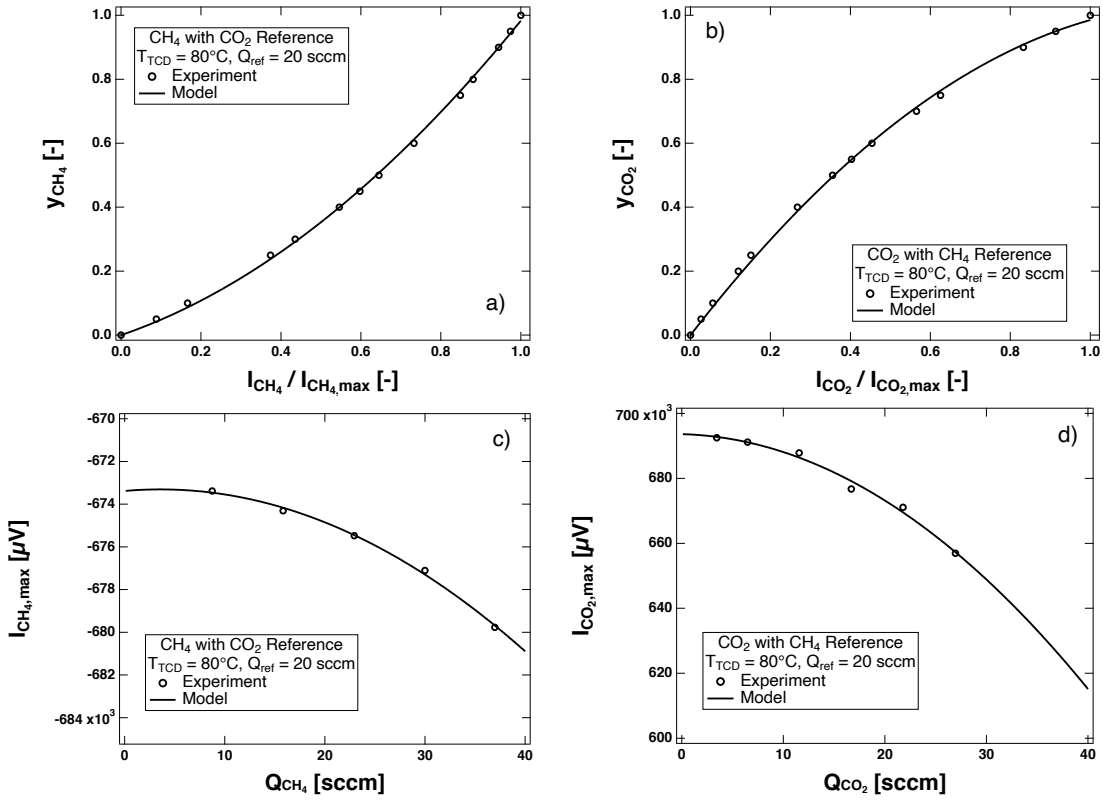

Figure C.3: CO_2/CH_4 thermal conductivity detector calibrations at a TCD block temperature of 80°C and either a CH_4 or CO_2 reference flowrate of 20 sccm. Panels (**a**) and (**b**) show the mole fraction of CH_4 and CO_2 as a function of the normalized TCD signal, respectively. Panels (**c**) and (**d**) show the effect of analyzing gas flow on the 100% CH_4 and CO_2 TCD signal, respectively; this maximum signal is used to normalize the TCD signal in panels (**a**) and (**b**). The markers denote experimentally collected data and the lines are empirical fits.

C.3 Effects of Flow and Composition on the Maximum TCD Signal to Estimate the Effluent Mole Fraction

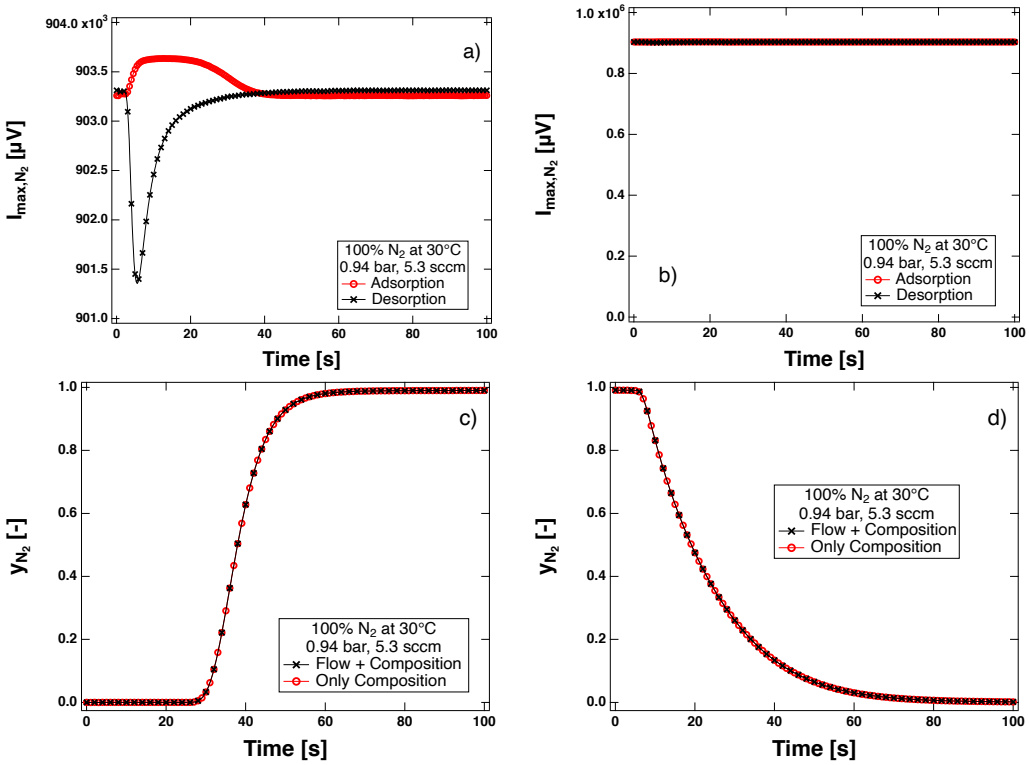

Figure C.4: The effect of effluent flow on the the maximum TCD signal in μV (**a**) for an adsorption/desorption breakthrough experiment of 100 mol% N_2 at 0.94 bar and 30°C on zeolite 13X. The same plot in panel (**a**) is shown over the entire range of recorded signal for the experiment (from zero signal to 100 mol% N_2) in panel (**b**). As seen in panel (**a**), the maximum signal, which is used to normalize the TCD raw signal before converting it to a mole fraction, changes with the effluent flow during an adsorption or desorption experiment. Panel (**b**) shows that this effect is negligible compared to the full signal change observed during the breakthrough experiment (0.0 mol% N_2 is 0.0 μV). The single-component N_2/He adsorption (**c**) and desorption (**d**) composition breakthrough curves at 0.94 bar and 30°C on zeolite 13X. Panels (**c**) and (**d**) include two TCD calibration schemes: the first includes only the change in composition normalized with the inlet flow maximum signal (at 5.3 sccm) and is shown in red; the second allows the maximum signal to change in the denominator of the TCD calibration as the effluent flow changes and is shown in black. The first calibration scheme (in red) is used in this study. As seen, there is no visible difference in the two calibration schemes to estimate the mole fraction from the raw TCD signal. The red curves in (**c**) and (**d**) are the same curves as plotted in Fig. 5.

C.4 Estimates for $Q_{\mathbf{in,max}}$ at 30°C

Table C.2: Estimates for the maximum μDCB inlet flowrate to avoid kinetic control and mass balance inconsistencies.

Adsorbent	Adsorbate	$D_{\mathrm{eff},i}/r_{\mathrm{p}}^2$ at ≈ 30°C [s^{-1}]	H_i at 30°C [-]	$Q_{\mathrm{in,max}}$ [ccm]	Citation
Activated Carbon	N_2	0.071	12.206	12.78	[168]
Activated Carbon	CH_4	0.090	62.071	82.41	[169]
Zeolite 13X	N_2	0.149	22.930	57.84	[170]
Zeolite 13X	CH_4	0.190	36.050	115.96	[169]
Zeolite 13X	CO_2	0.034	10574	6086.6	[170]

C.5 Photos of the μDCB Apparatus

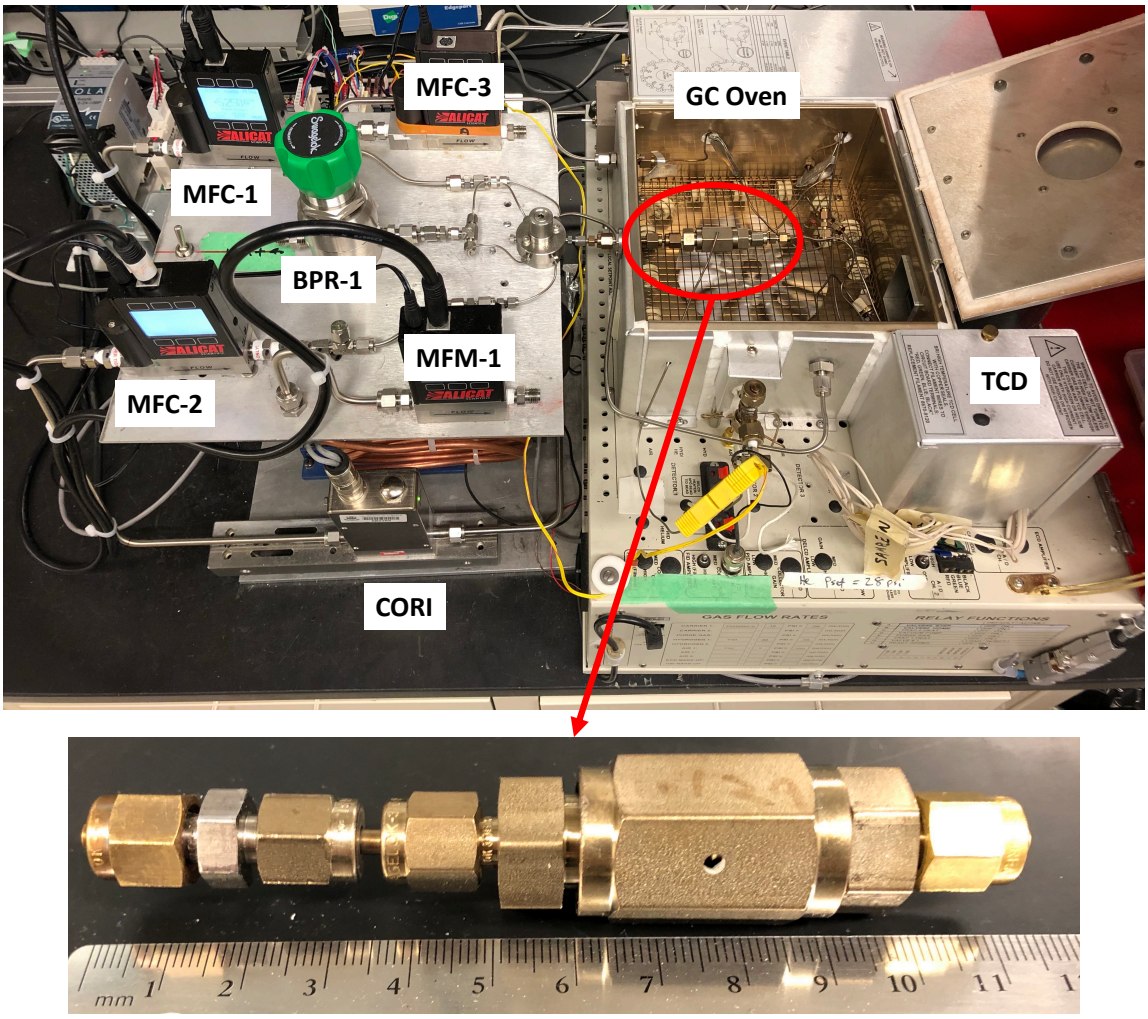

Figure C.5: Photos of the μDCB system used in this study with a VCR column.

C.6 Krishna & van Baten CH_4/CO_2 Equilibrium Data on Zeolite 13X

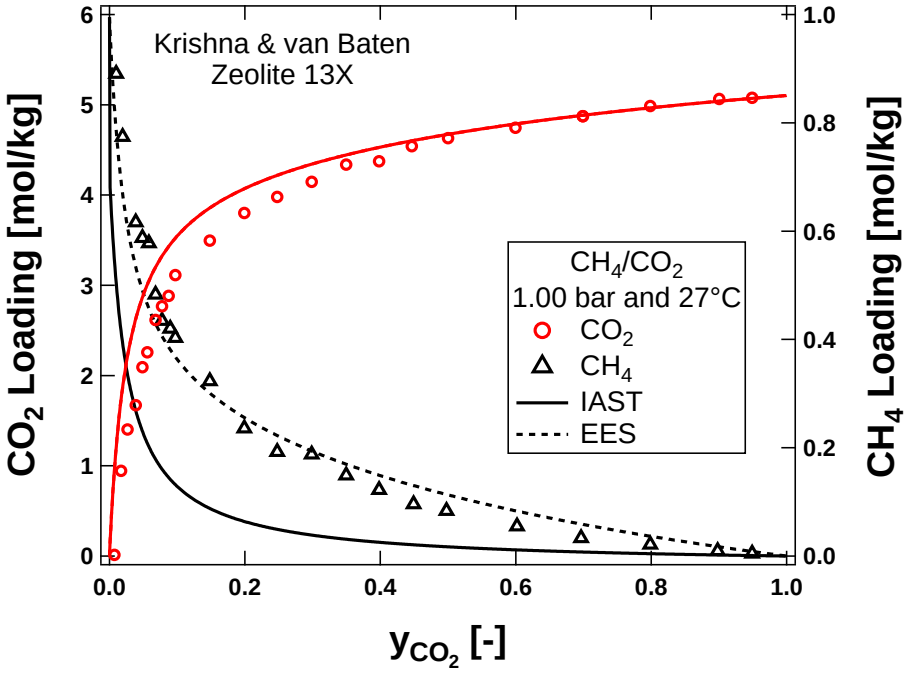

Figure C.6: Multicomponent CBMC simulations for CH_4/CO_2 equilibrium on zeolite 13X by Krishna and van Baten[91] at 27°C and 1.00 bar. DSL isotherm parameters were given in the Supporting Information of the original paper (at 27°C): $q_b^{\text{sat}} = 4.2$ mol/kg, $q_d^{\text{sat}} = 1.7$ mol/kg, $b_{CO_2} = 4.78 \times 10^{-4}$ Pa^{-1}, $d_{CO_2} = 1.39 \times 10^{-5}$ Pa^{-1}, $b_{CH_4} = 2.07 \times 10^{-6}$ Pa^{-1}. The methane b and d constants were refit from the Krishna and van Baten paper to keep q_b^{sat} and q_d^{sat} the same for both species. The equal energy sites (EES) model predicts the CH_4 data well. Markers are CBMC simulations by Krishna and van Baten. Solid lines are ideal adsorbed solution theory predictions and dashed lines are equal-energy sites predictions.

C.7 Single Component Breakthrough Curves on Zeolite 13X

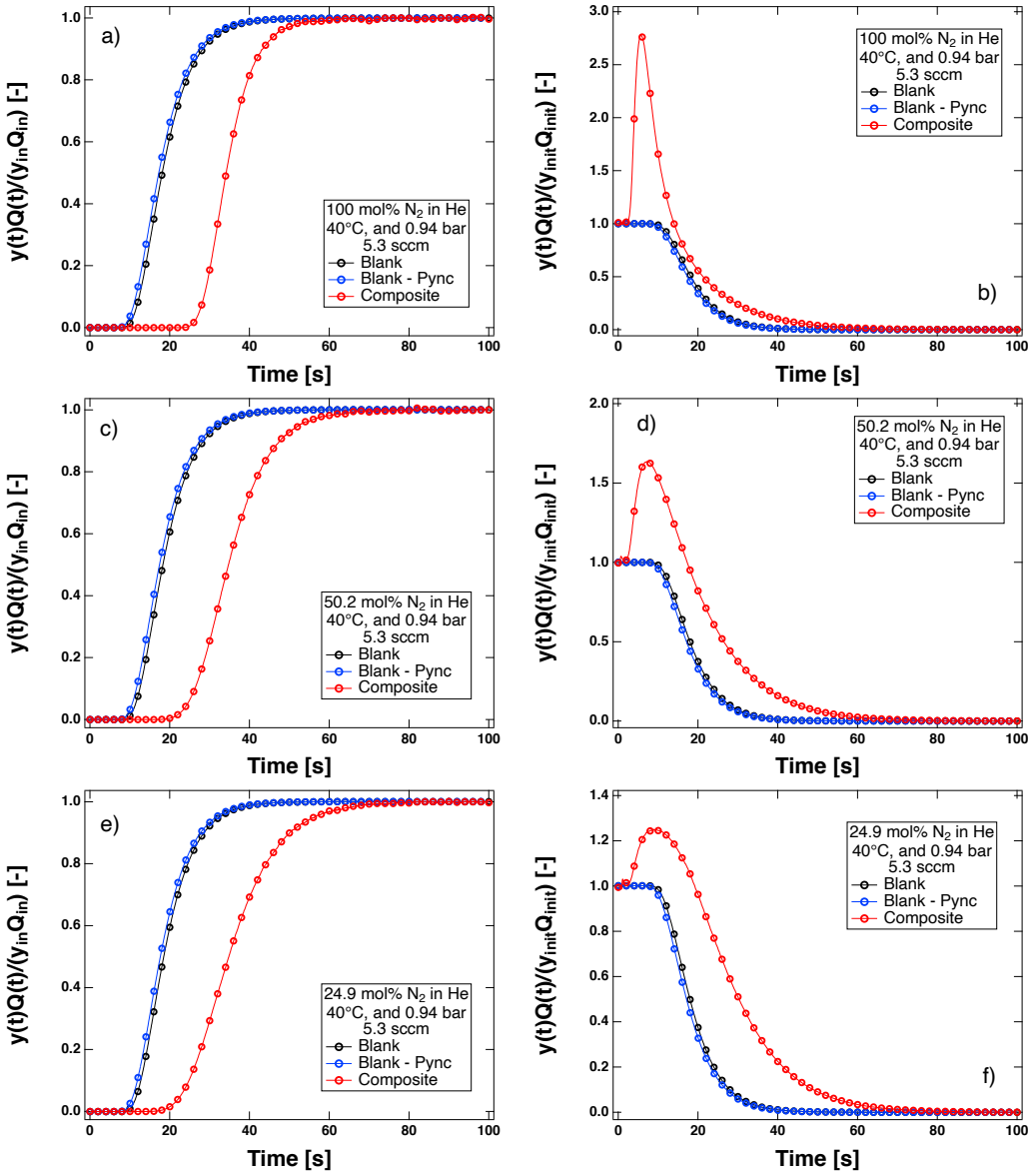

Figure C.7: Single-component N_2/He adsorption (left) and desorption (right) breakthrough curves at 0.94 bar and 40°C on zeolite 13X. Panels (**a**) and (**b**) are at 100 mol% N_2, (**c**) and (**d**) are at 50.2 mol% N_2/He, and (**e**) and (**f**) are at 24.9 mol% N_2/He. The reference gas was He for these experiments. Every tenth point is shown as a marker.

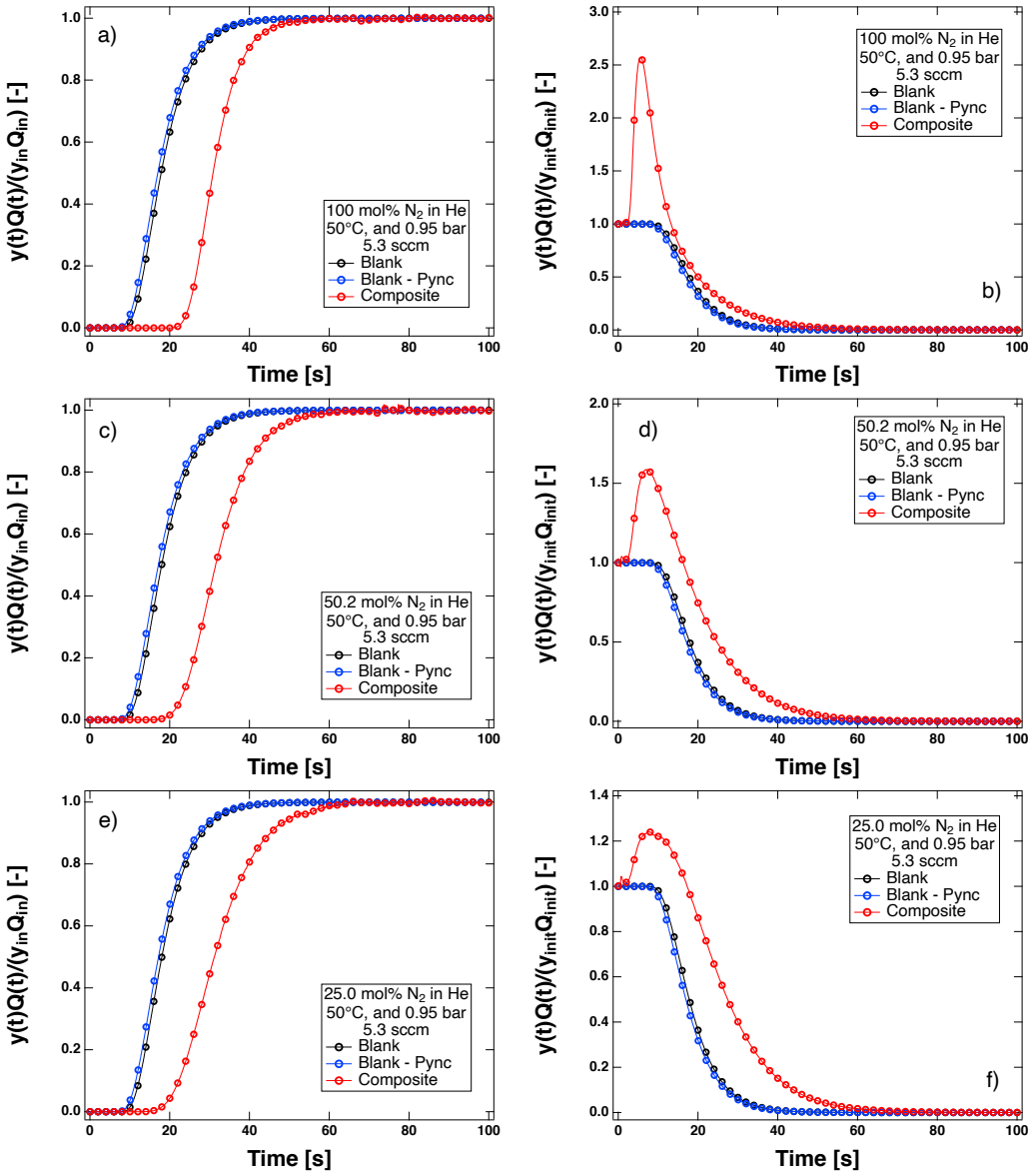

Figure C.8: Single-component N_2/He adsorption (left) and desorption (right) breakthrough curves at 0.95 bar and 50°C on zeolite 13X. Panels (**a**) and (**b**) are at 100 mol% N_2, (**c**) and (**d**) are at 50.2 mol% N_2/He, and (**e**) and (**f**) are at 25.0 mol% N_2/He. The reference gas was He for these experiments. Every tenth point is shown as a marker.

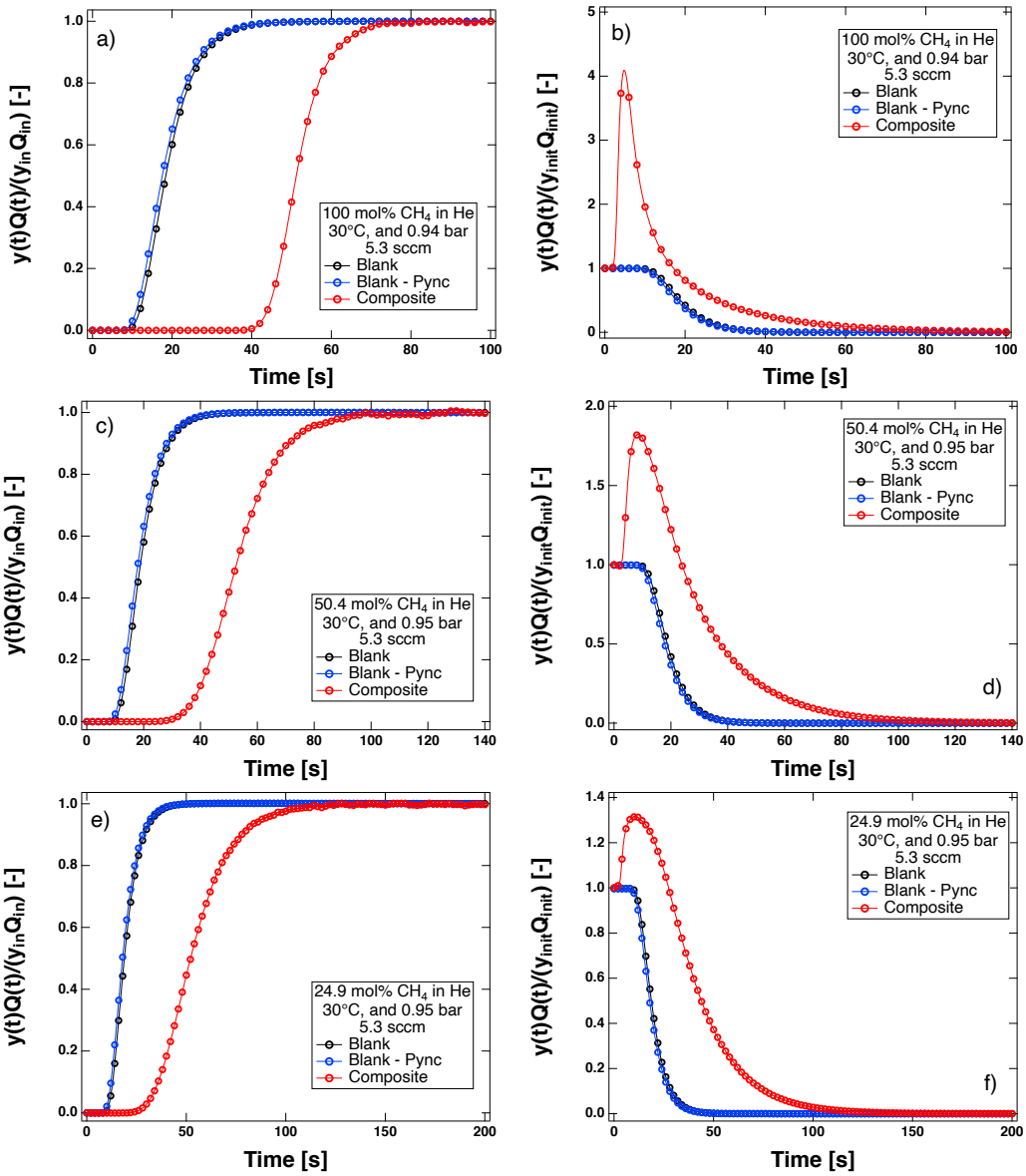

Figure C.9: Single-component CH_4/He adsorption (left) and desorption (right) breakthrough curves at ≈ 0.95 bar and 30°C on zeolite 13X. Panels (**a**) and (**b**) are at 100 mol% CH_4, (**c**) and (**d**) are at 50.4 mol% CH_4/He, and (**e**) and (**f**) are at 24.9 mol% CH_4/He. The reference gas was He for these experiments. Every tenth point is shown as a marker.

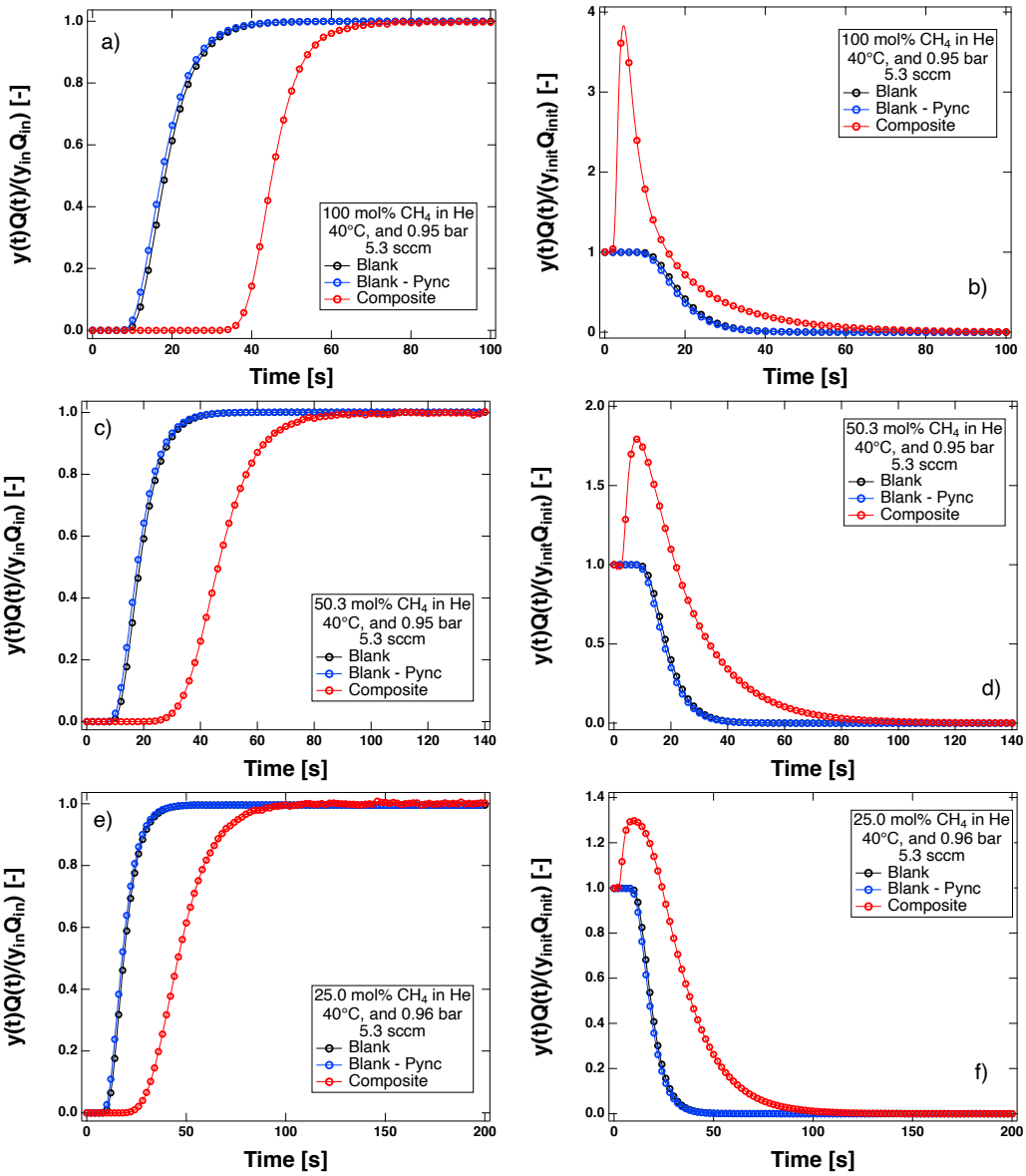

Figure C.10: Single-component CH_4/He adsorption (left) and desorption (right) breakthrough curves at $\approx$ 0.95 bar and 40°C on zeolite 13X. Panels (**a**) and (**b**) are at 100 mol% CH_4, (**c**) and (**d**) are at 50.3 mol% CH_4/He, and (**e**) and (**f**) are at 25.0 mol% CH_4/He. The reference gas was He for these experiments. Every tenth point is shown as a marker.

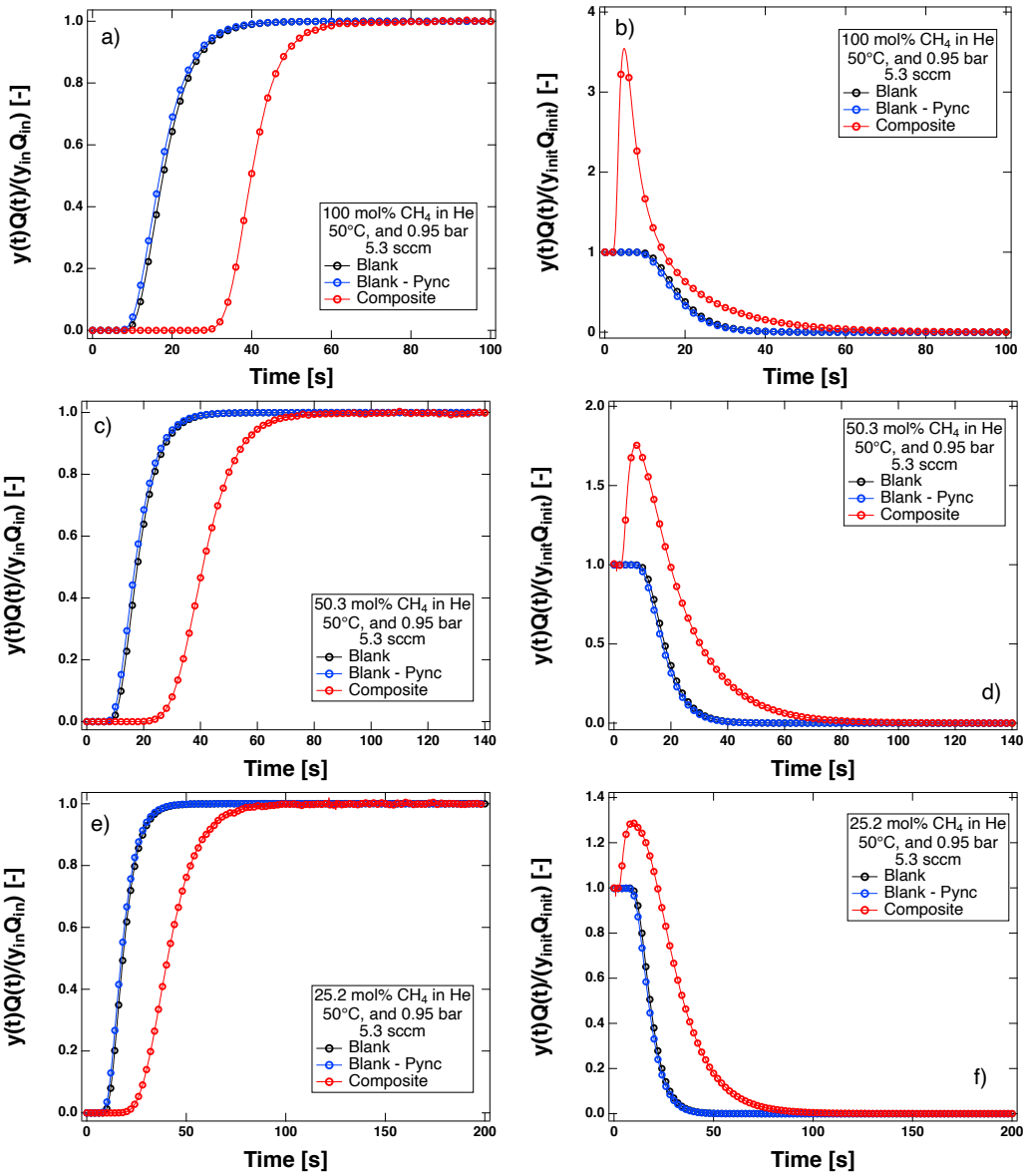

Figure C.11: Single-component CH_4/He adsorption (left) and desorption (right) breakthrough curves at 0.95 bar and 50°C on zeolite 13X. Panels (**a**) and (**b**) are at 100 mol% CH_4, (**c**) and (**d**) are at 50.3 mol% CH_4/He, and (**e**) and (**f**) are at 25.2 mol% CH_4/He. The reference gas was He for these experiments. Every tenth point is shown as a marker.

C.8 Single Component Breakthrough Curves on Activated Carbon

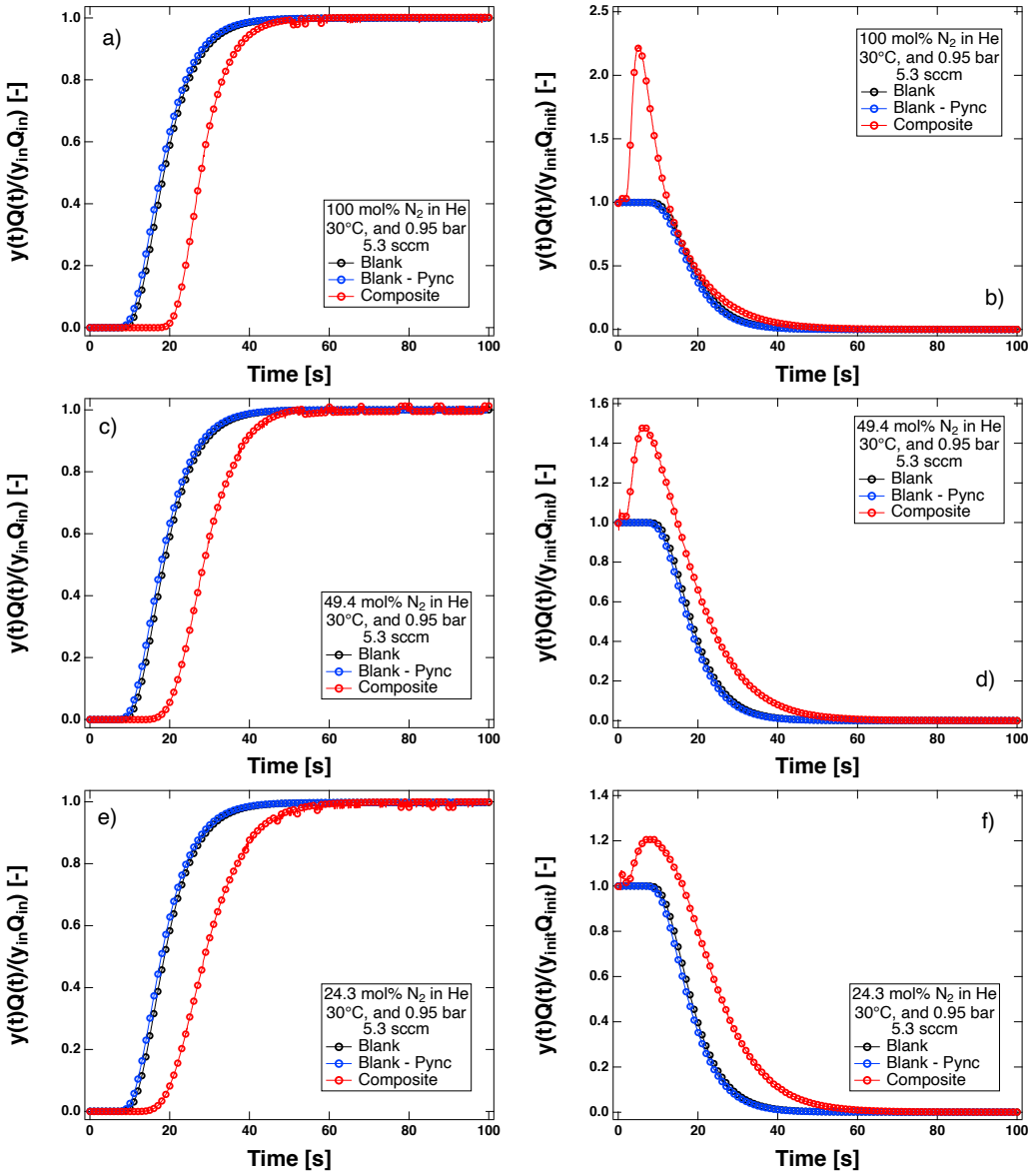

Figure C.12: Single-component N_2/He adsorption (left) and desorption (right) breakthrough curves at 0.95 bar and 30°C on activated carbon. Panels (**a**) and (**b**) are at 100 mol% N_2, (**c**) and (**d**) are at 49.4 mol% N_2/He, and (**e**) and (**f**) are at 24.3 mol% N_2/He. The reference gas was He for these experiments. Every tenth point is shown as a marker.

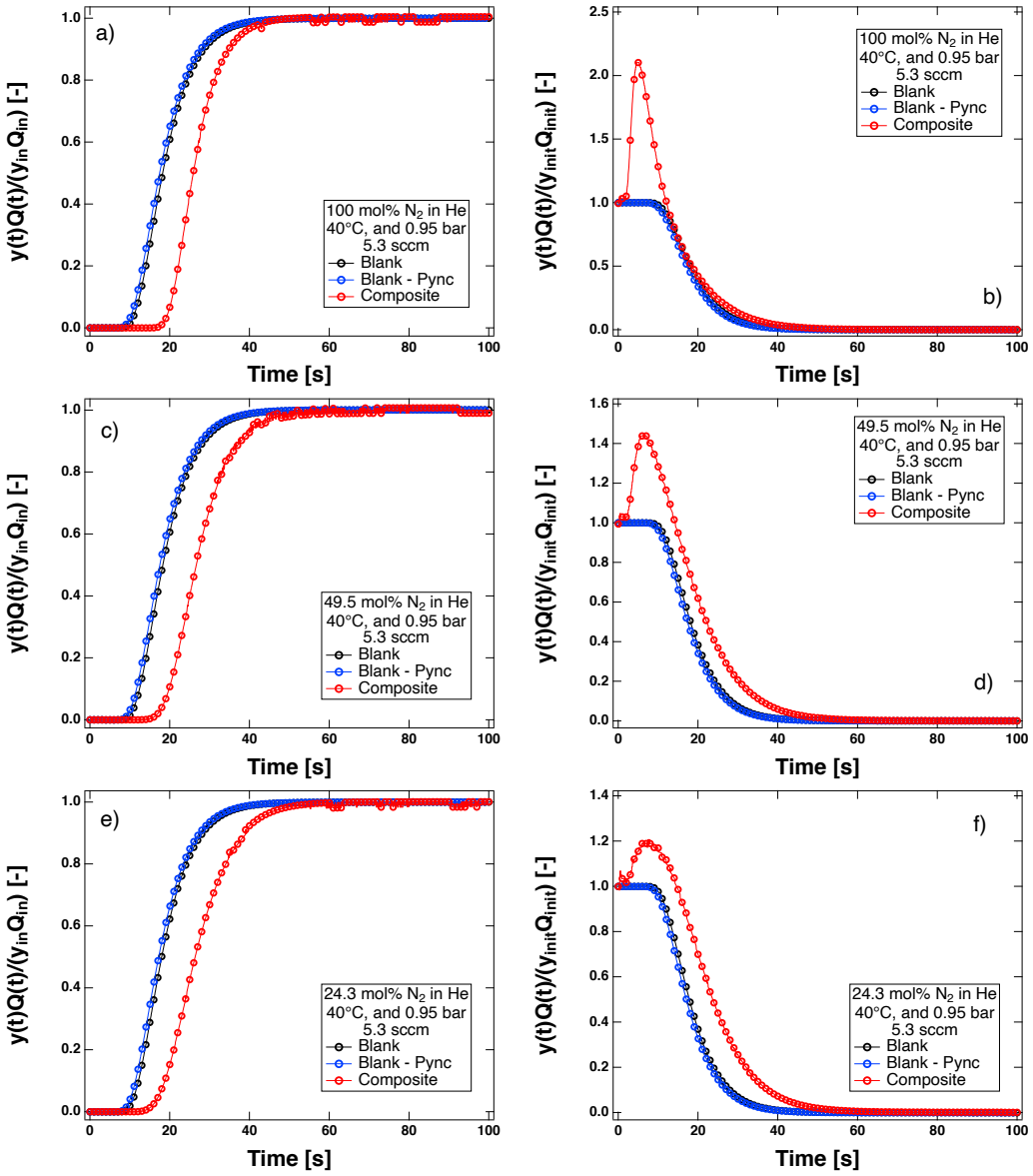

Figure C.13: Single-component N_2/He adsorption (left) and desorption (right) breakthrough curves at 0.95 bar and 40°C on activated carbon. Panels (**a**) and (**b**) are at 100 mol% N_2, (**c**) and (**d**) are at 49.5 mol% N_2/He, and (**e**) and (**f**) are at 24.3 mol% N_2/He. The reference gas was He for these experiments. Every tenth point is shown as a marker.

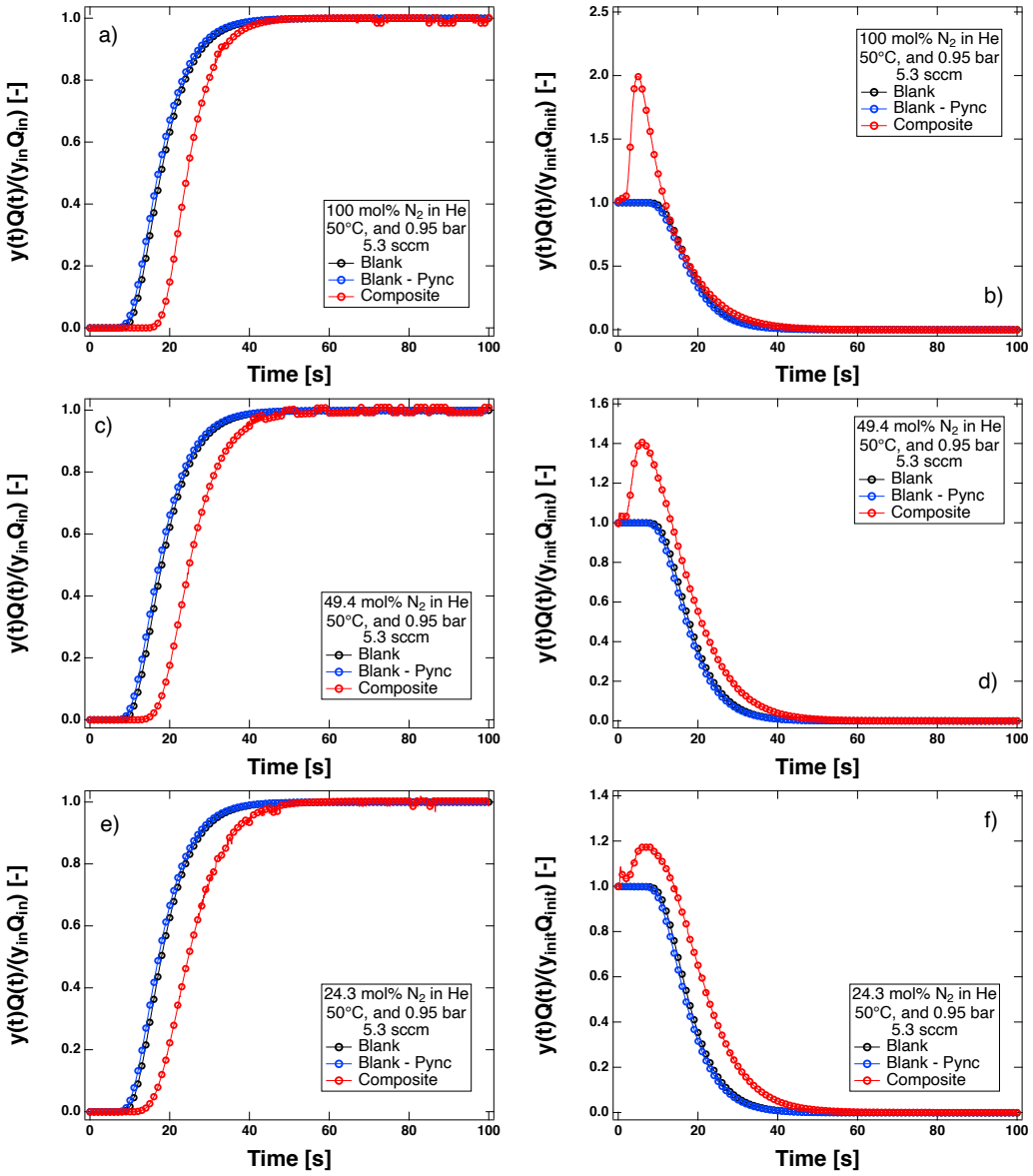

Figure C.14: Single-component N_2/He adsorption (left) and desorption (right) breakthrough curves at 0.95 bar and 50°C on activated carbon. Panels (**a**) and (**b**) are at 100 mol% N_2, (**c**) and (**d**) are at 49.4 mol% N_2/He, and (**e**) and (**f**) are at 24.3 mol% N_2/He. The reference gas was He for these experiments. Every tenth point is shown as a marker.

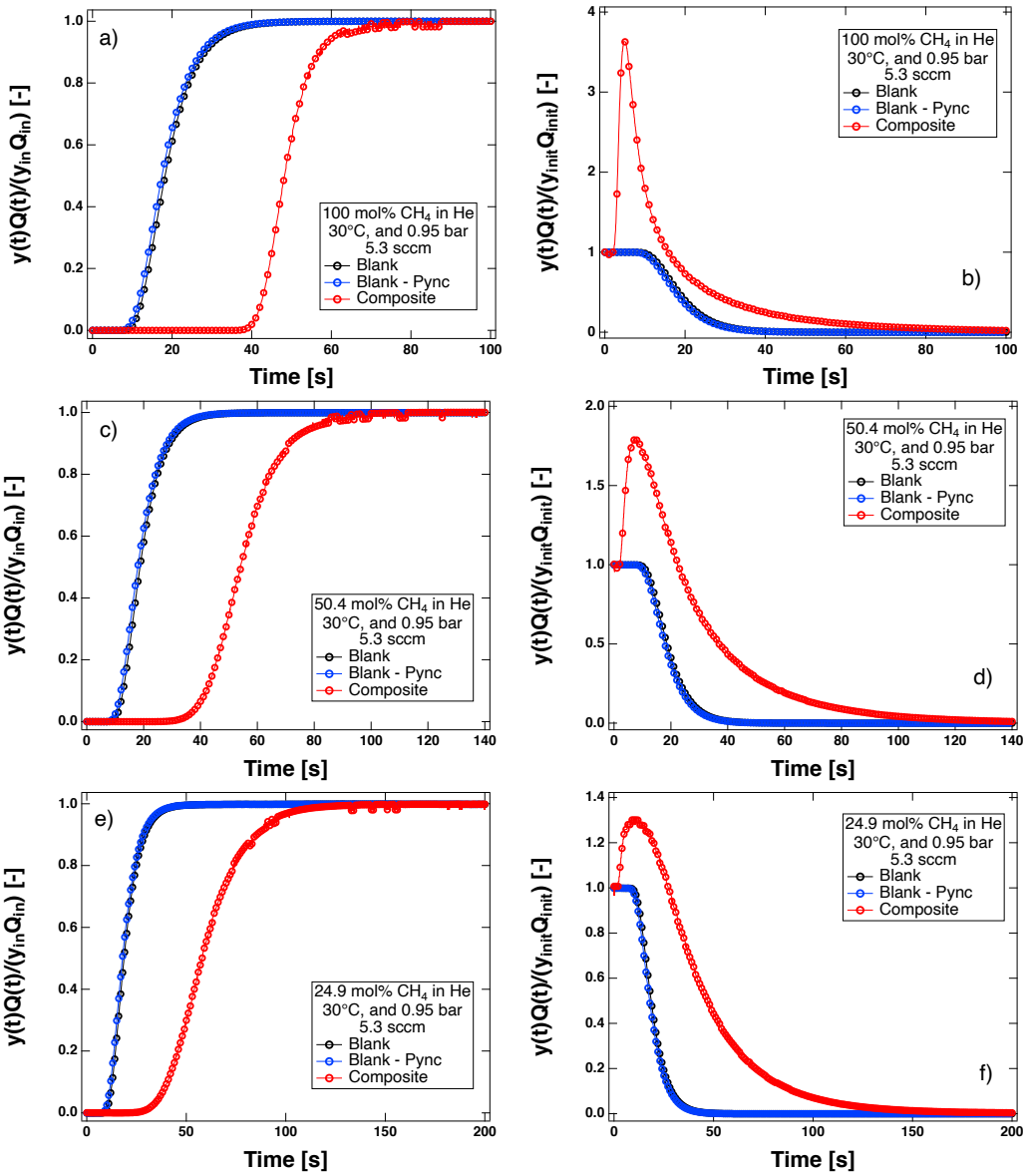

Figure C.15: Single-component CH_4/He adsorption (left) and desorption (right) breakthrough curves at 0.95 bar and 30°C on activated carbon. Panels (**a**) and (**b**) are at 100 mol% CH_4, (**c**) and (**d**) are at 50.4 mol% CH_4/He, and (**e**) and (**f**) are at 24.9 mol% CH_4/He. The reference gas was He for these experiments. Every tenth point is shown as a marker.

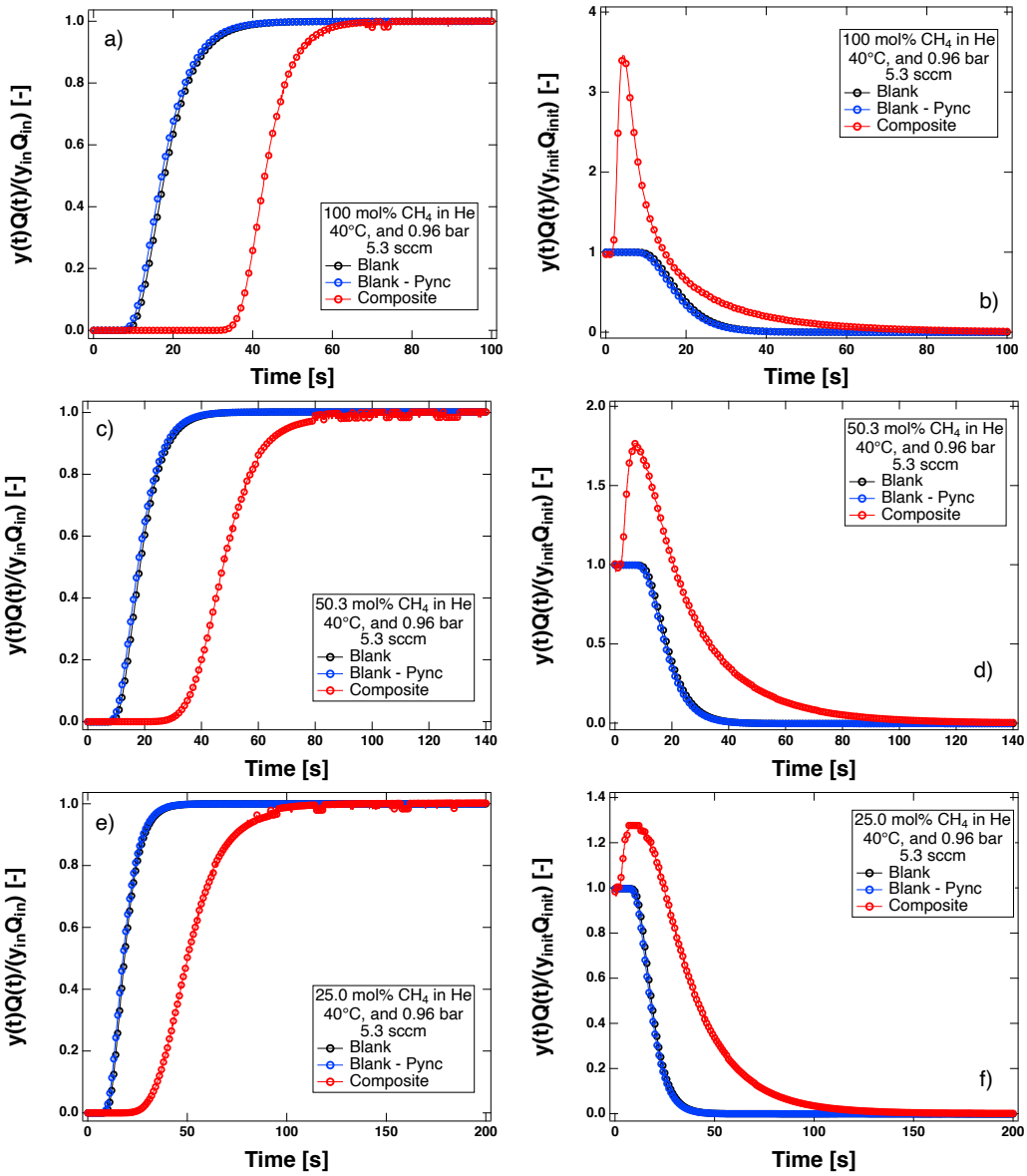

Figure C.16: Single-component CH_4/He adsorption (left) and desorption (right) breakthrough curves at 0.96 bar and 40°C on activated carbon. Panels (**a**) and (**b**) are at 100 mol% CH_4, (**c**) and (**d**) are at 50.3 mol% CH_4/He, and (**e**) and (**f**) are at 25.0 mol% CH_4/He. The reference gas was He for these experiments. Every tenth point is shown as a marker.

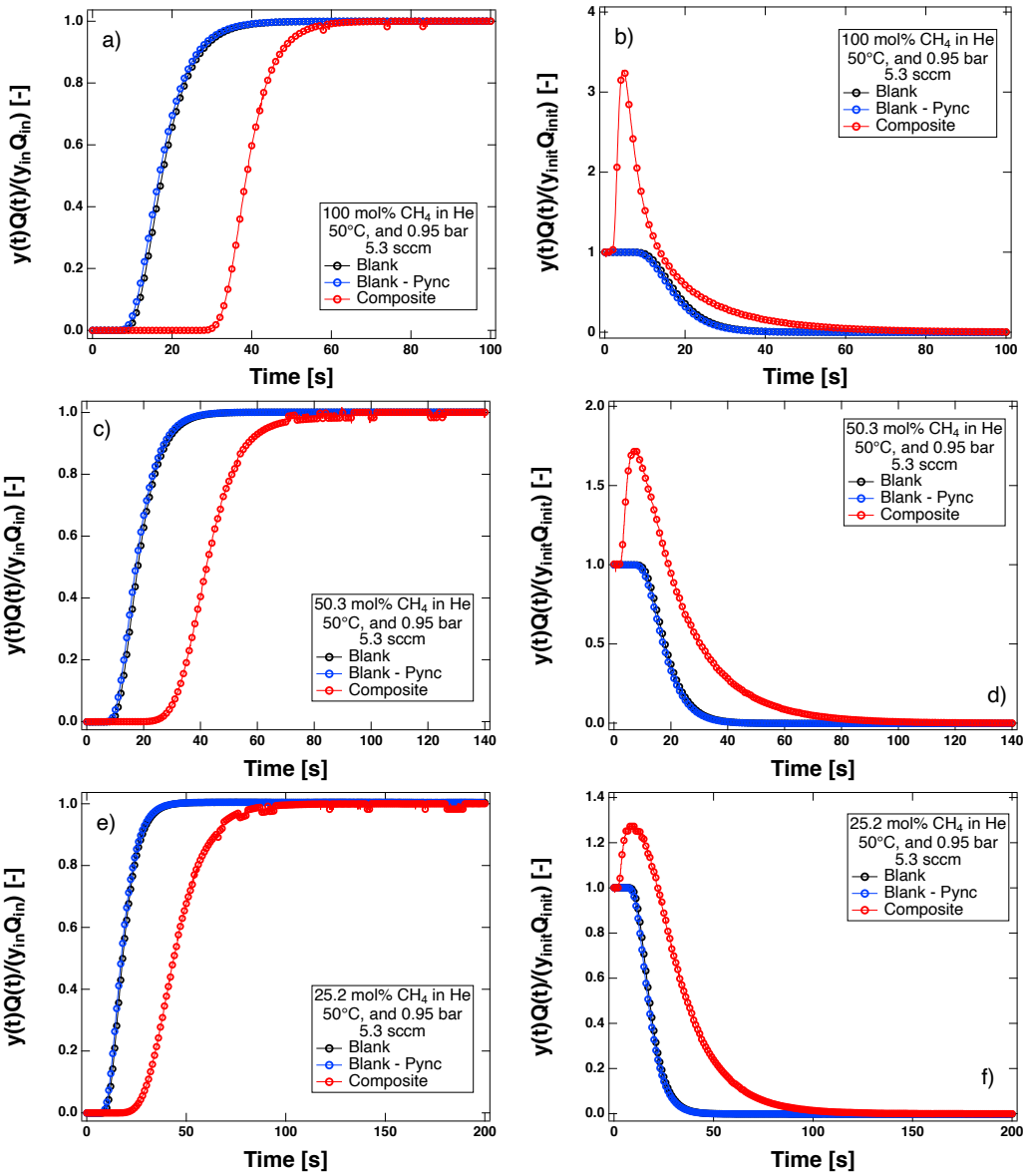

Figure C.17: Single-component CH_4/He adsorption (left) and desorption (right) breakthrough curves at 0.95 bar and 50°C on activated carbon. Panels (**a**) and (**b**) are at 100 mol% CH_4, (**c**) and (**d**) are at 50.3 mol% CH_4/He, and (**e**) and (**f**) are at 25.2 mol% CH_4/He. The reference gas was He for these experiments. Every tenth point is shown as a marker.

C.9 Multicomponent Breakthrough Curves on Activated Carbon

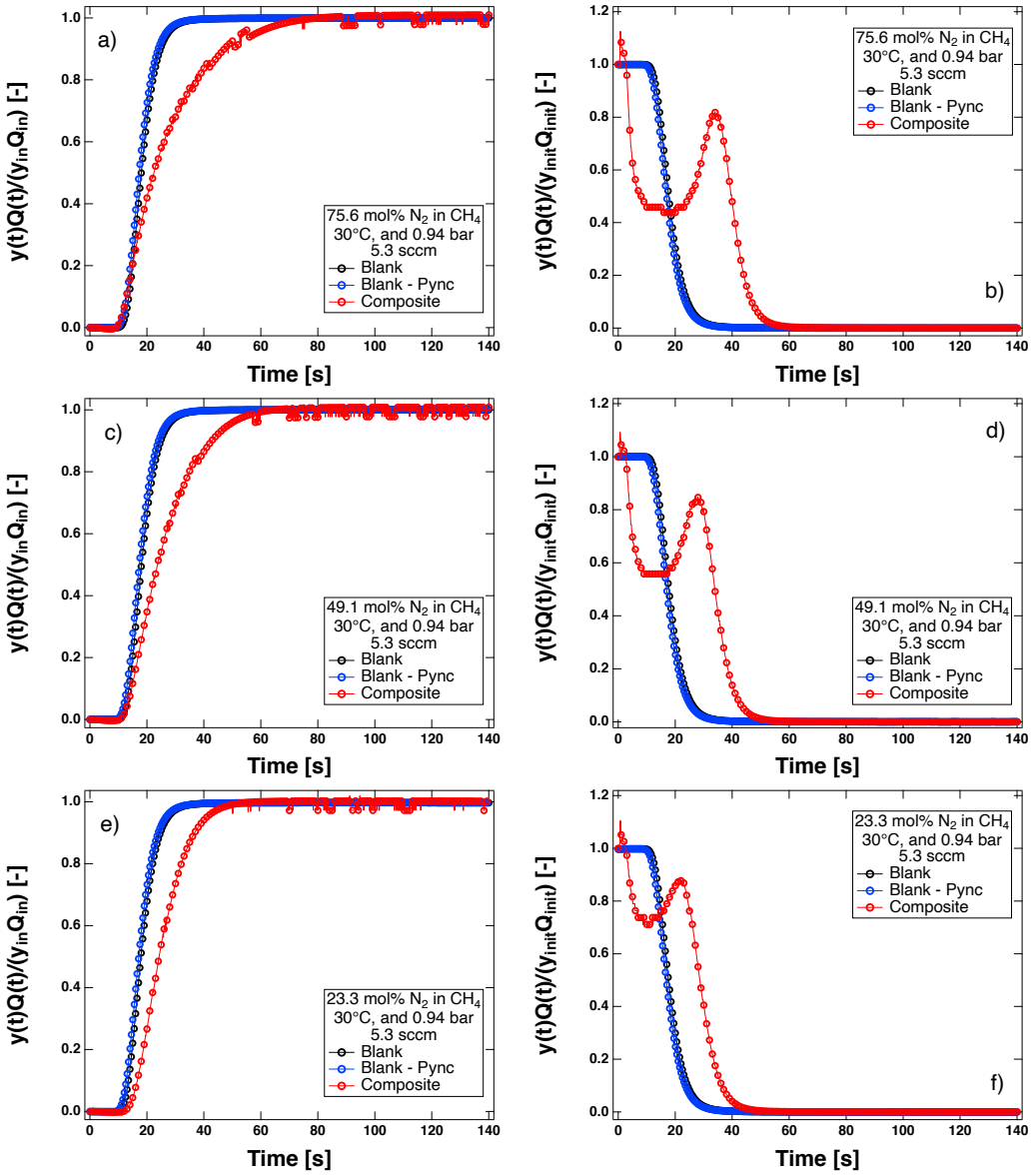

Figure C.18: Multi-component N_2/CH_4 adsorption (left) and desorption (right) breakthrough curves at 0.94 bar and 30°C on activated carbon. Panels (**a**) and (**b**) are at 75.6 mol% N_2/CH_4, (**c**) and (**d**) are at 49.1 mol% N_2/CH_4, and (**e**) and (**f**) are at 23.3 mol% N_2/CH_4. The reference gas was CH_4 for these experiments.

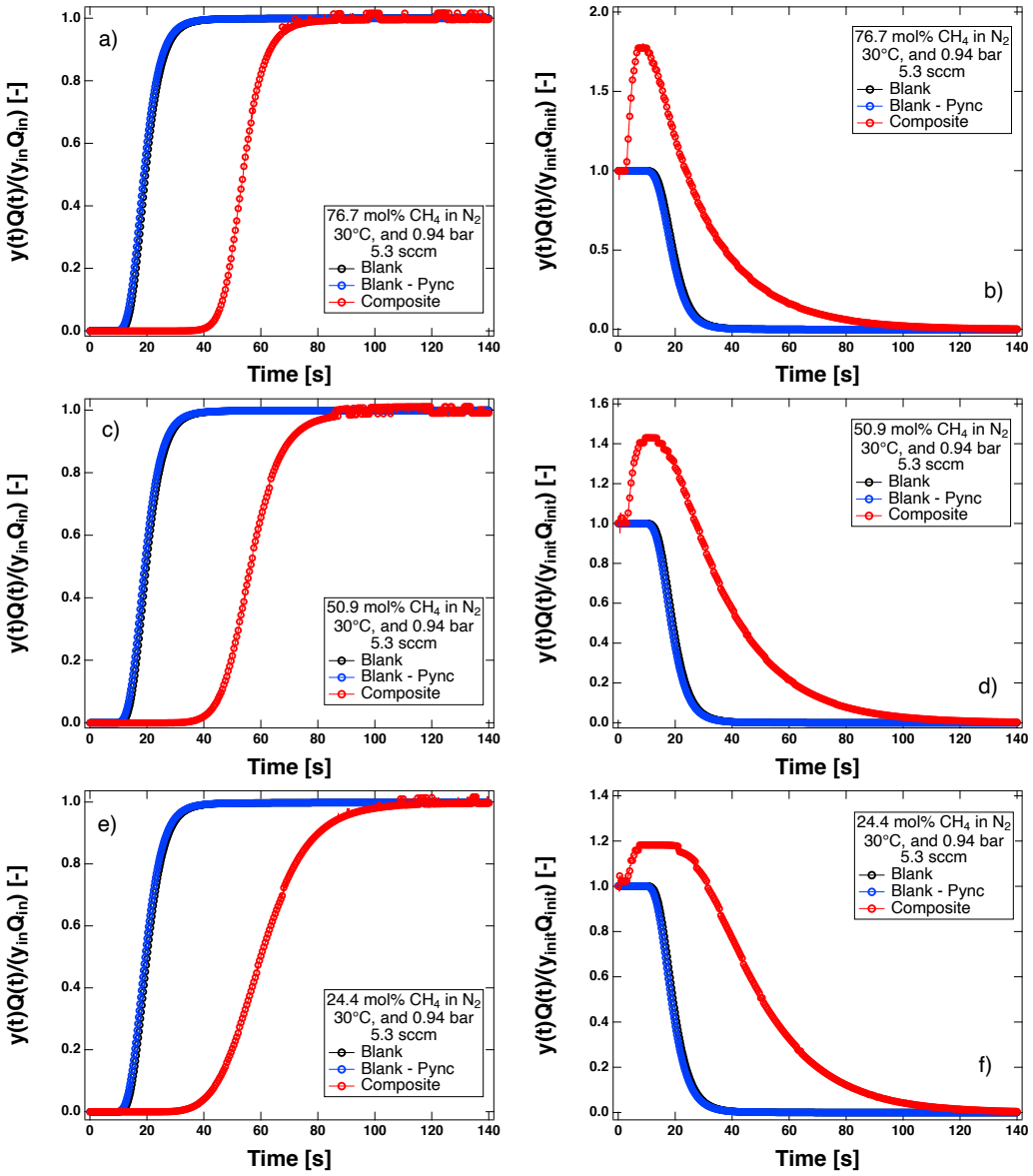

Figure C.19: Multi-component CH_4/N_2 adsorption (left) and desorption (right) breakthrough curves at 0.94 bar and 30°C on activated carbon. Panels (**a**) and (**b**) are at 76.7 mol% CH_4/N_2, (**c**) and (**d**) are at 50.9 mol% CH_4/N_2, and (**e**) and (**f**) are at 24.4 mol% CH_4/N_2. The reference gas was N_2 for these experiments.

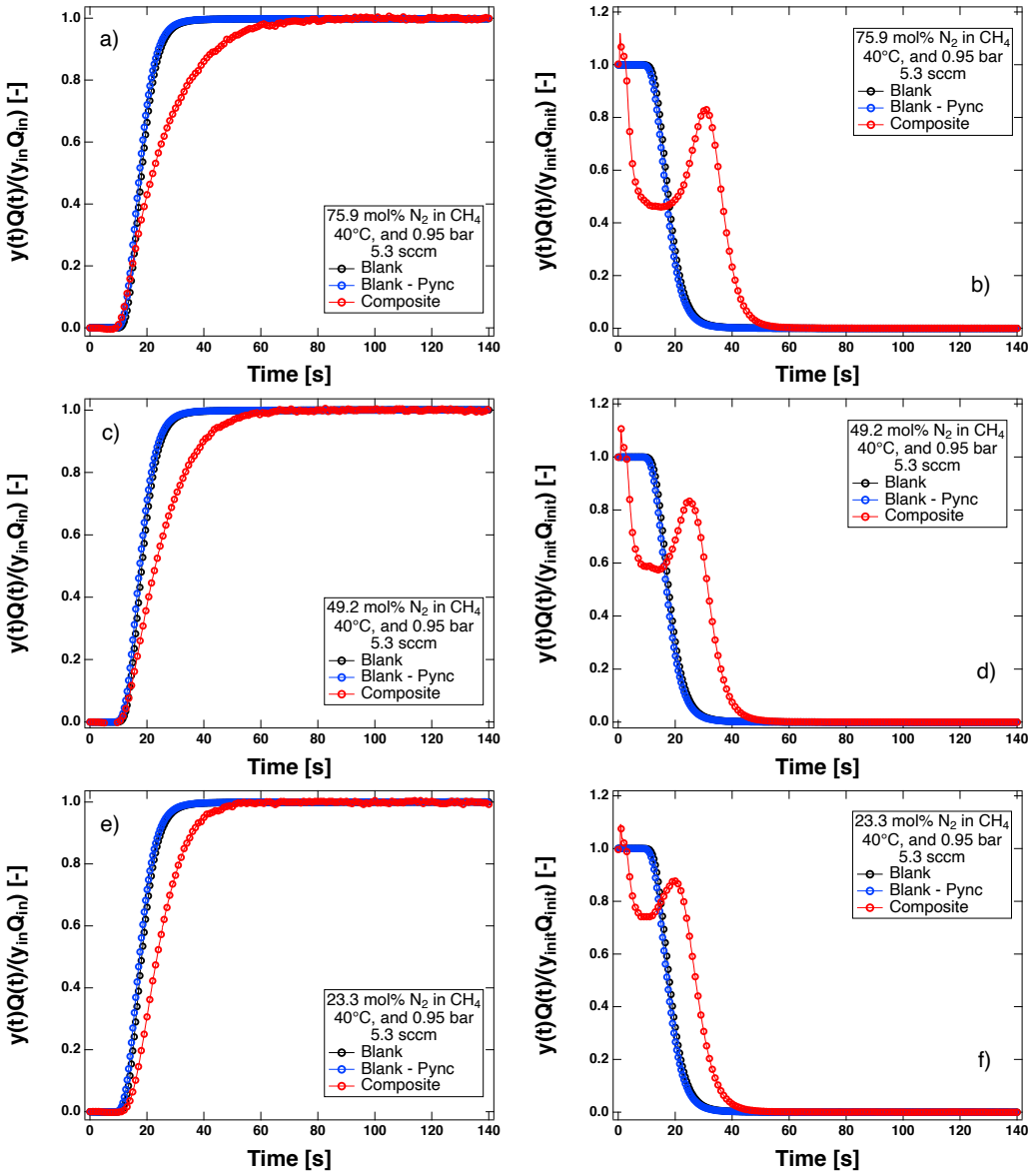

Figure C.20: Multi-component N_2/CH_4 adsorption (left) and desorption (right) breakthrough curves at 0.95 bar and 40°C on activated carbon. Panels (**a**) and (**b**) are at 75.9 mol% N_2/CH_4, (**c**) and (**d**) are at 49.2 mol% N_2/CH_4, and (**e**) and (**f**) are at 23.3 mol% N_2/CH_4. The reference gas was CH_4 for these experiments.

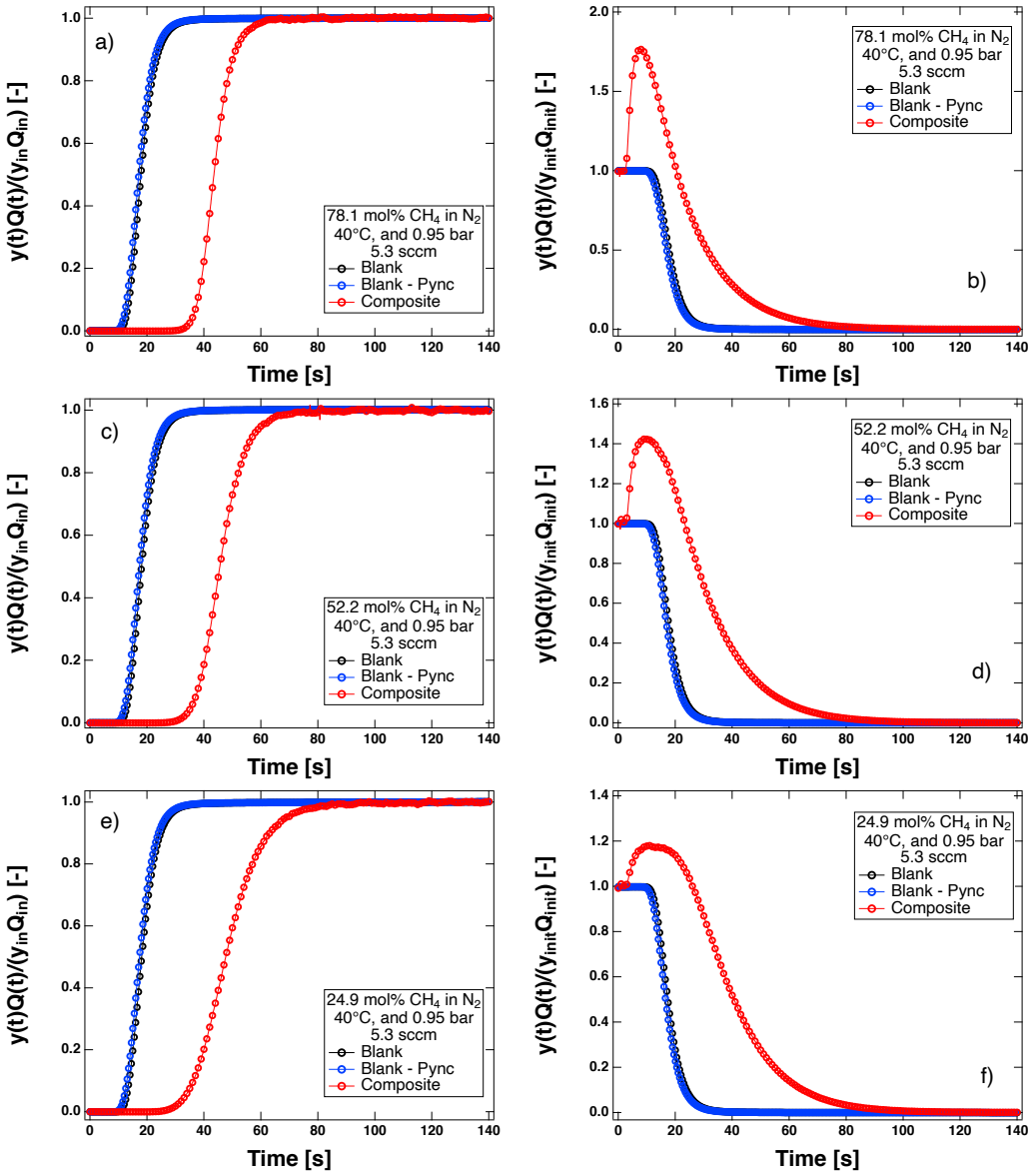

Figure C.21: Multi-component CH_4/N_2 adsorption (left) and desorption (right) breakthrough curves at 0.95 bar and 40°C on activated carbon. Panels (**a**) and (**b**) are at 78.1 mol% CH_4/N_2, (**c**) and (**d**) are at 52.2 mol% CH_4/N_2, and (**e**) and (**f**) are at 24.9 mol% CH_4/N_2. The reference gas was N_2 for these experiments.

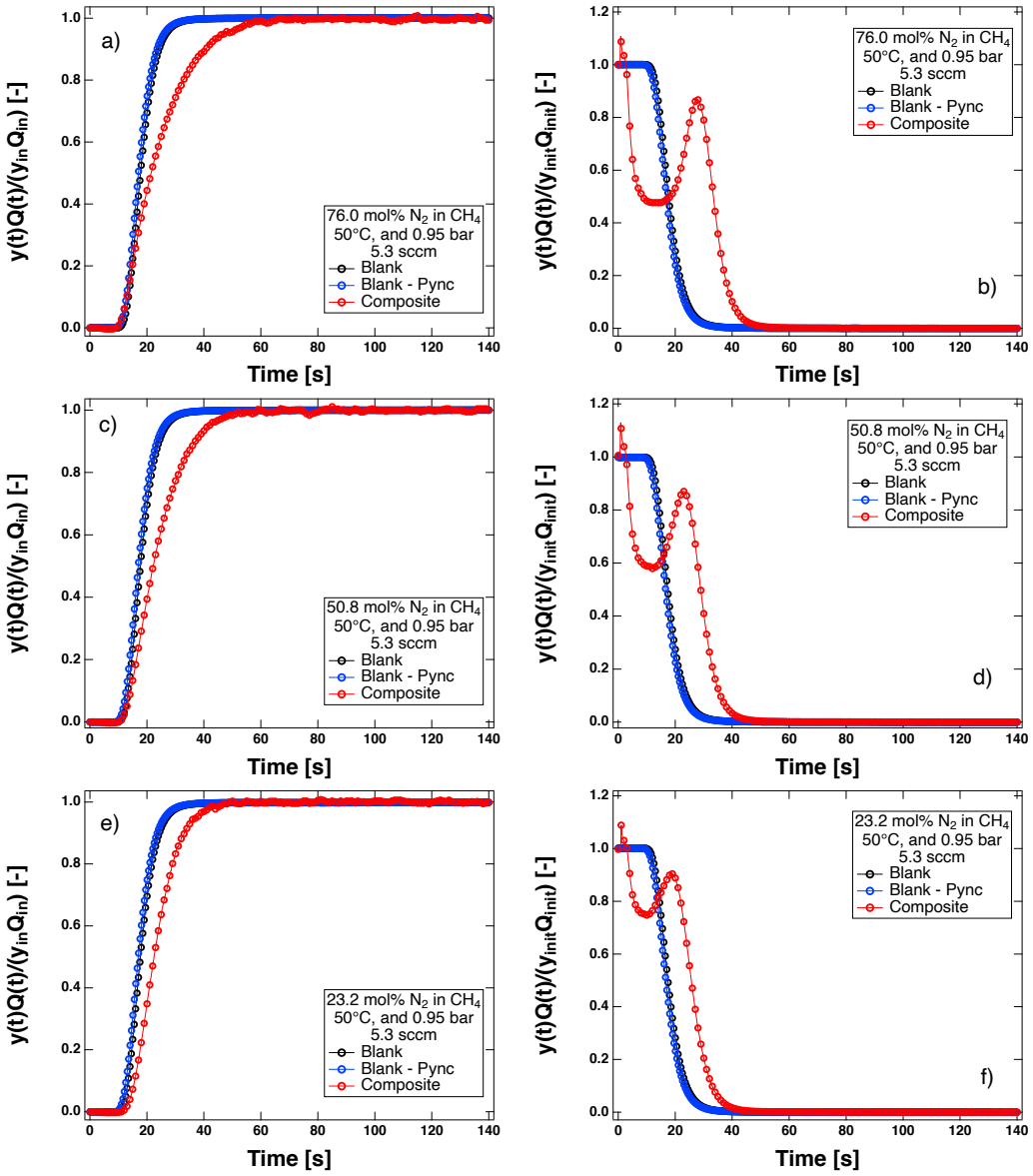

Figure C.22: Multi-component N_2/CH_4 adsorption (left) and desorption (right) breakthrough curves at 0.95 bar and 50°C on activated carbon. Panels (**a**) and (**b**) are at 76.0 mol% N_2/CH_4, (**c**) and (**d**) are at 50.8 mol% N_2/CH_4, and (**e**) and (**f**) are at 23.2 mol% N_2/CH_4. The reference gas was CH_4 for these experiments.

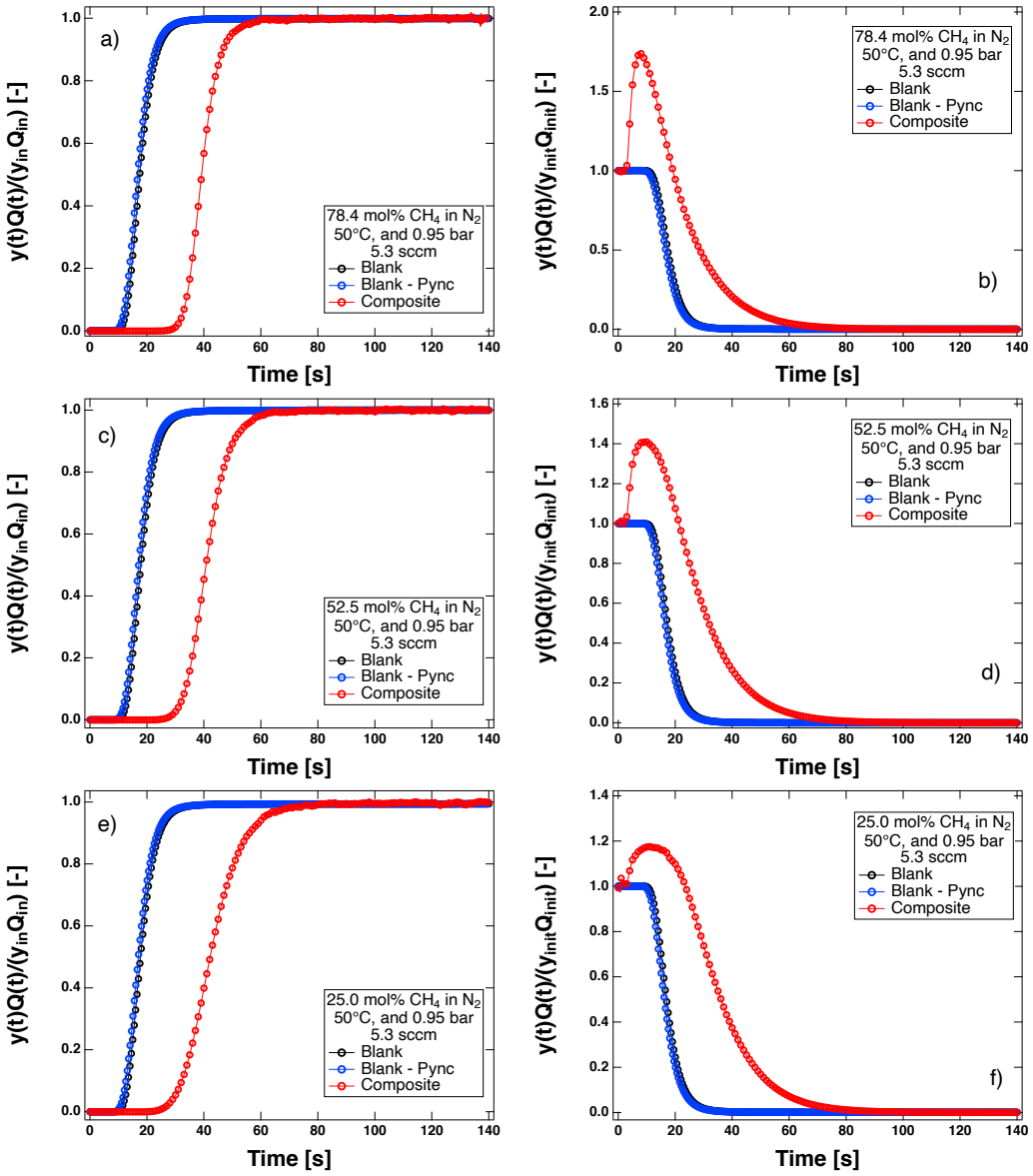

Figure C.23: Multi-component CH_4/N_2 adsorption (left) and desorption (right) breakthrough curves at 0.95 bar and 50°C on activated carbon. Panels (**a**) and (**b**) are at 78.4 mol% CH_4/N_2, (**c**) and (**d**) are at 52.5 mol% CH_4/N_2, and (**e**) and (**f**) are at 25.0 mol% CH_4/N_2. The reference gas was N_2 for these experiments.

C.10 Multicomponent Breakthrough Curves on Zeolite 13X

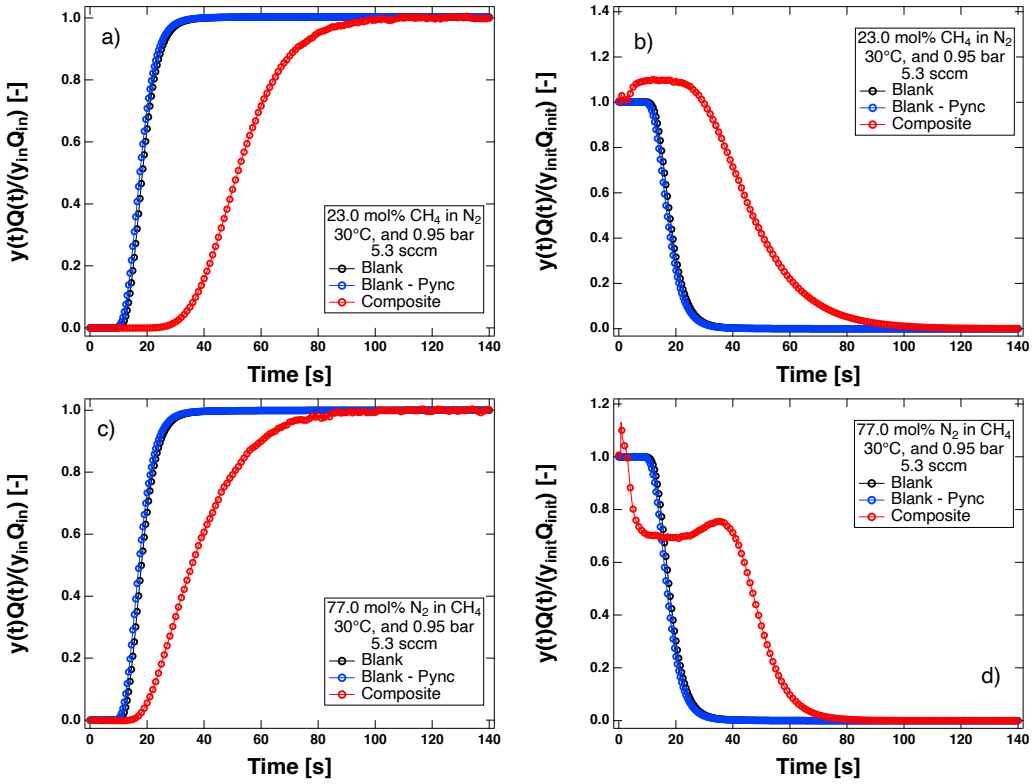

Figure C.24: Multicomponent adsorption (left) and desorption (right) breakthrough curves on zeolite 13X at 0.95 bar and 30°C for a 23.0/77.0 mol% CH_4/N_2 mixture. Panels (**a**) and (**b**) are adsorption and desorption of CH_4, and panels (**c**) and (**d**) are equivalent experiments for N_2. Every tenth point is shown as a marker. Note that the rows denote separate experiments, since the TCD reference changes to detect one gas over the other. The reference gas was N_2 for the CH_4 experiments, and CH_4 for the N_2 experiments.

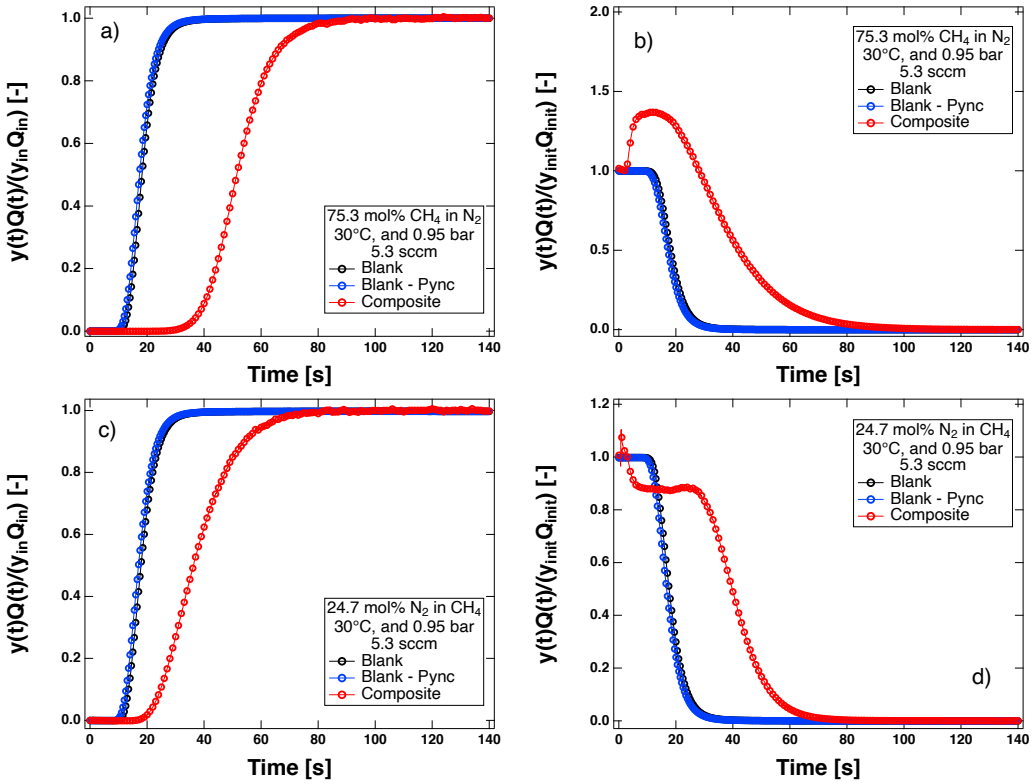

Figure C.25: Multicomponent adsorption (left) and desorption (right) breakthrough curves on zeolite 13X at 0.95 bar and 30°C for a 75.3/24.7 mol% CH_4/N_2 mixture. Panels (**a**) and (**b**) are adsorption and desorption of CH_4, and panels (**c**) and (**d**) are equivalent experiments for N_2. Every tenth point is shown as a marker. Note that the rows denote separate experiments, since the TCD reference changes to detect one gas over the other. The reference gas was N_2 for the CH_4 experiments, and CH_4 for the N_2 experiments.

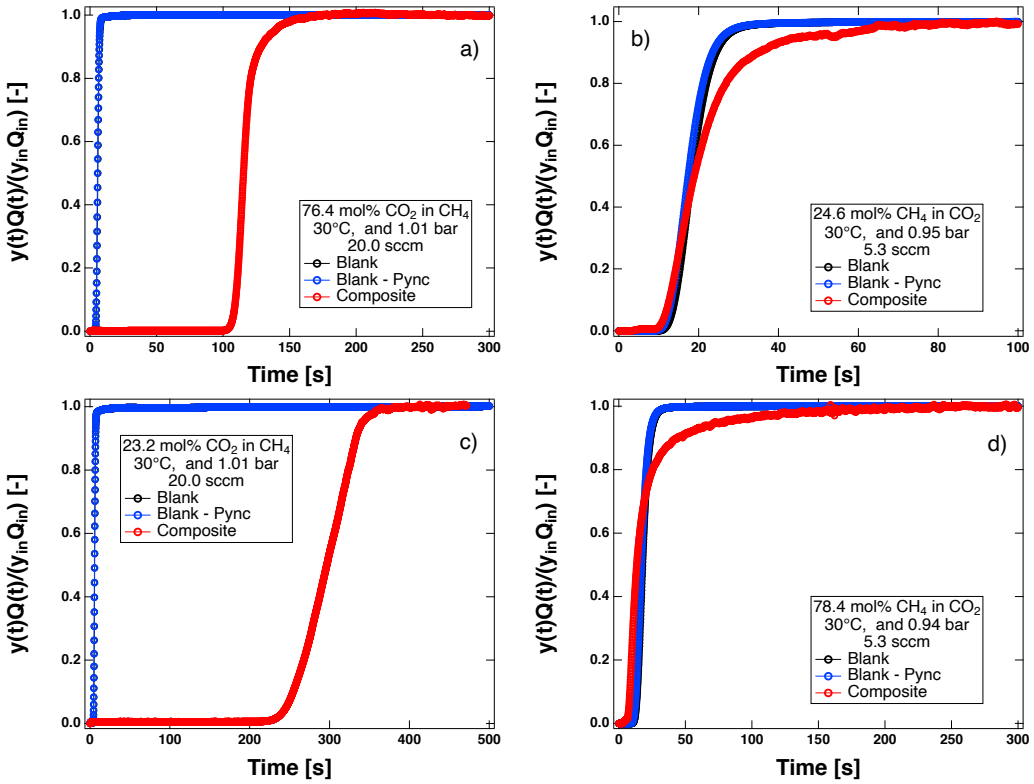

Figure C.26: Multicomponent CO_2/CH_4 adsorption breakthrough curves on zeolite 13X at 30°C. Panel (**a**) adsorption breakthrough of 76.4 mol% CO_2 in CH_4 at 1.01 bar and 20.0 sccm inlet flow. Panel (**b**) adsorption breakthrough of 24.6 mol% CH_4 in CO_2 at 0.95 bar and 5.3 sccm inlet flow. Panel (**c**) adsorption breakthrough of 23.2 mol% CO_2 in CH_4 at 1.01 bar and 20.0 sccm inlet flow. Panel (**d**) adsorption breakthrough of 78.4 mol% CH_4 in CO_2 at 0.94 bar and 5.3 sccm inlet flow. The reference gas was CH_4 for the CO_2 experiments, and CH_4 for the CO_2 experiments. Every second point is shown as a marker.

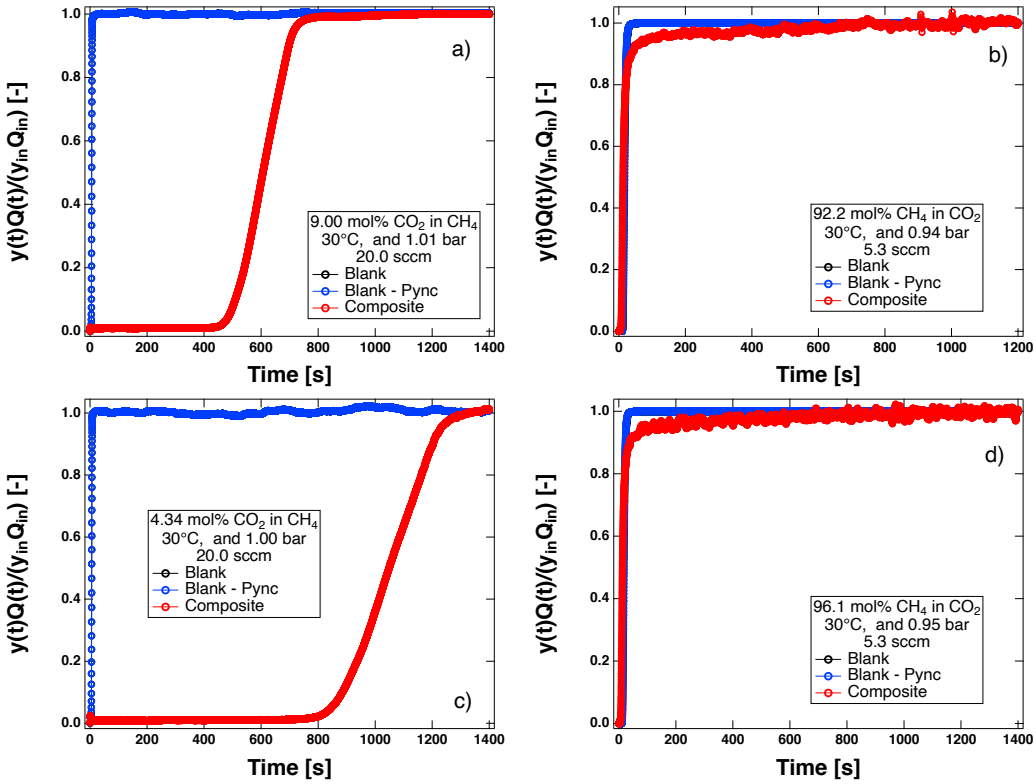

Figure C.27: Multicomponent CO_2/CH_4 adsorption breakthrough curves on zeolite 13X at 30°C. Panel (**a**) adsorption breakthrough of 9.00 mol% CO_2 in CH_4 at 1.01 bar and 20.0 sccm inlet flow. Panel (**b**) adsorption breakthrough of 92.2 mol% CH_4 in CO_2 at 0.94 bar and 5.3 sccm inlet flow. Panel (**c**) adsorption breakthrough of 4.34 mol% CO_2 in CH_4 at 1.01 bar and 20.0 sccm inlet flow. Panel (**d**) adsorption breakthrough of 96.1 mol% CH_4 in CO_2 at 0.95 bar and 5.3 sccm inlet flow. The reference gas was CH_4 for the CO_2 experiments, and CH_4 for the CO_2 experiments. Every second point is shown as a marker.

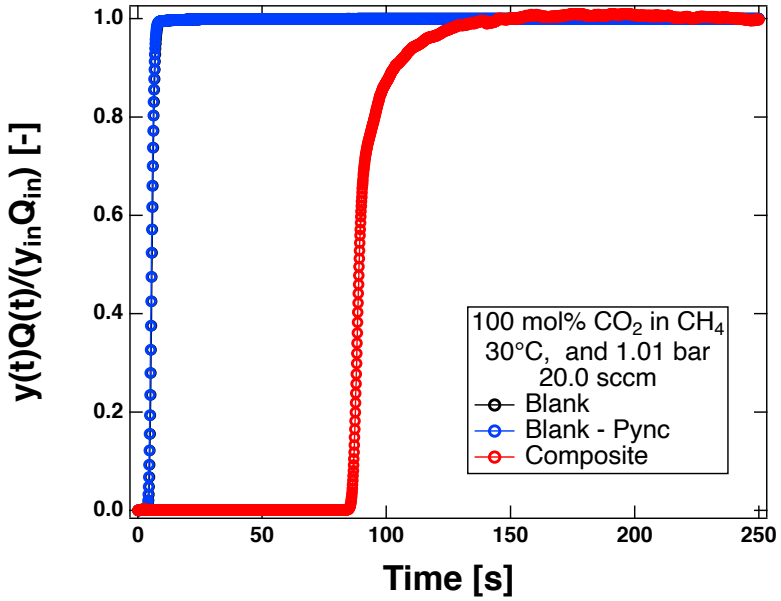

Figure C.28: A 100 mol% CO_2 adsorption breakthrough curve in CH_4 on zeolite 13X at 30°C at 1.01 bar and 20.0 sccm inlet flow. The reference gas was CH_4 for this experiment.

Appendix D: Supporting Information for "Diffusion of CH_4 and N_2 in barium-exchanged reduced pore zorite (Ba-RPZ) and zeolite 4A"

D.1 Determination of the Activation Temperature

The activation temperature is essential to determine accurate equilibrium data. A Q500 thermogravimetric analyzer (TGA) by TA (New Castle, DE USA) was used to quickly screen Ba-RPZ for its thermal stability and an appropriate activation temperature. The TGA profiles for Ba-RPZ crystals are shown in Fig. D.1. As seen in Fig. D.1, Ba-RPZ has a steady decrease in mass to an a final mass value at high temperatures. The mass is non-dimensionalized as in the Chapter 5. This analysis gives a rough idea of what the activation temperature should be, assuming that there is no damage to the adsorbent. For Ba-RPZ crystals, it appears to have lost 95% adsorbed gases (by mass) at 300°C and all trapped gases at 400°C.

To confirm the Ba-RPZ activation temperature, a series of experiments were performed using the Micromeritics ASAP 2020C (Norcross, GA USA) low pressure volumetry unit. A crystalline Ba-RPZ sample was first activated at 250°C before a 30°C N_2 equilibrium experiment. After each 30°C N_2 equilibrium experiment, the activation temperature was raised 25°C until 450°C. The N_2 equilibrium data as a function of activation temperature is shown in Fig. D.1. As seen, the N_2 equilibrium

data is the same for activation temperatures between 250 and 325°C. At 350°C, the N_2 equilibrium loading starts to decrease when compared to the data collected previously (activation temperatures before 350°C). At an activation temperature greater than 375°C, the equilibrium loading of N_2 drops rapidly. This analysis shows that the Ba-RPZ sample is damaged at an activation temperature of 350°C and higher. Since there is no difference of the N_2 equilibrium data at activation temperatures between 250 to 325°C, an activation temperature of 250°C was taken. This temperature has been used for many other titanosilcate adsorbents [66, 171].

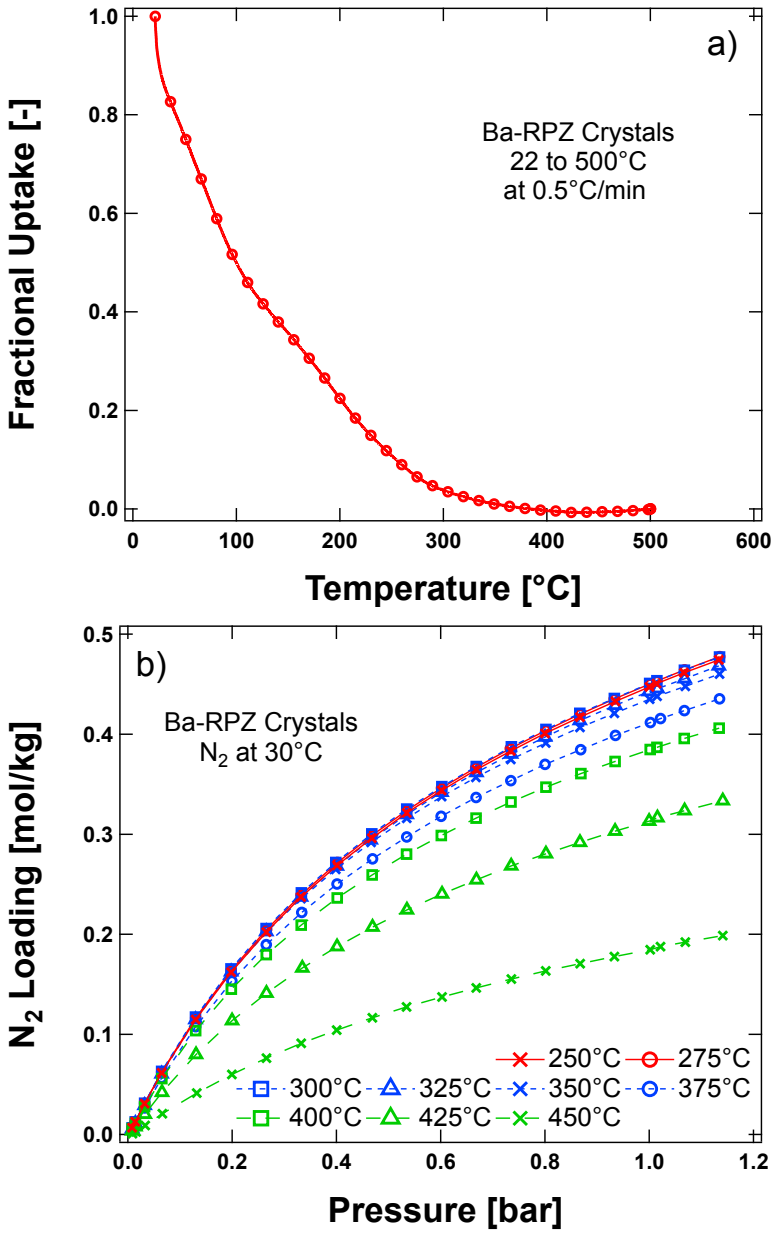

Figure D.1: Thermal activation profiles of Ba-RPZ crystals (**a**). These thermal decays show the loss of mass as a function of temperature. The ramp rate was set to 0.5°C/min from 22 to 500°C in a flow of 200 ccm of Ar. In the second figure (**b**), Ba-RPZ crystals were also tested using the volumetry unit to show repeated N_2 equilibrium experiments as a function of activation temperature.

D.2 SEM Images of Ba-RPZ and Zeolite 4A

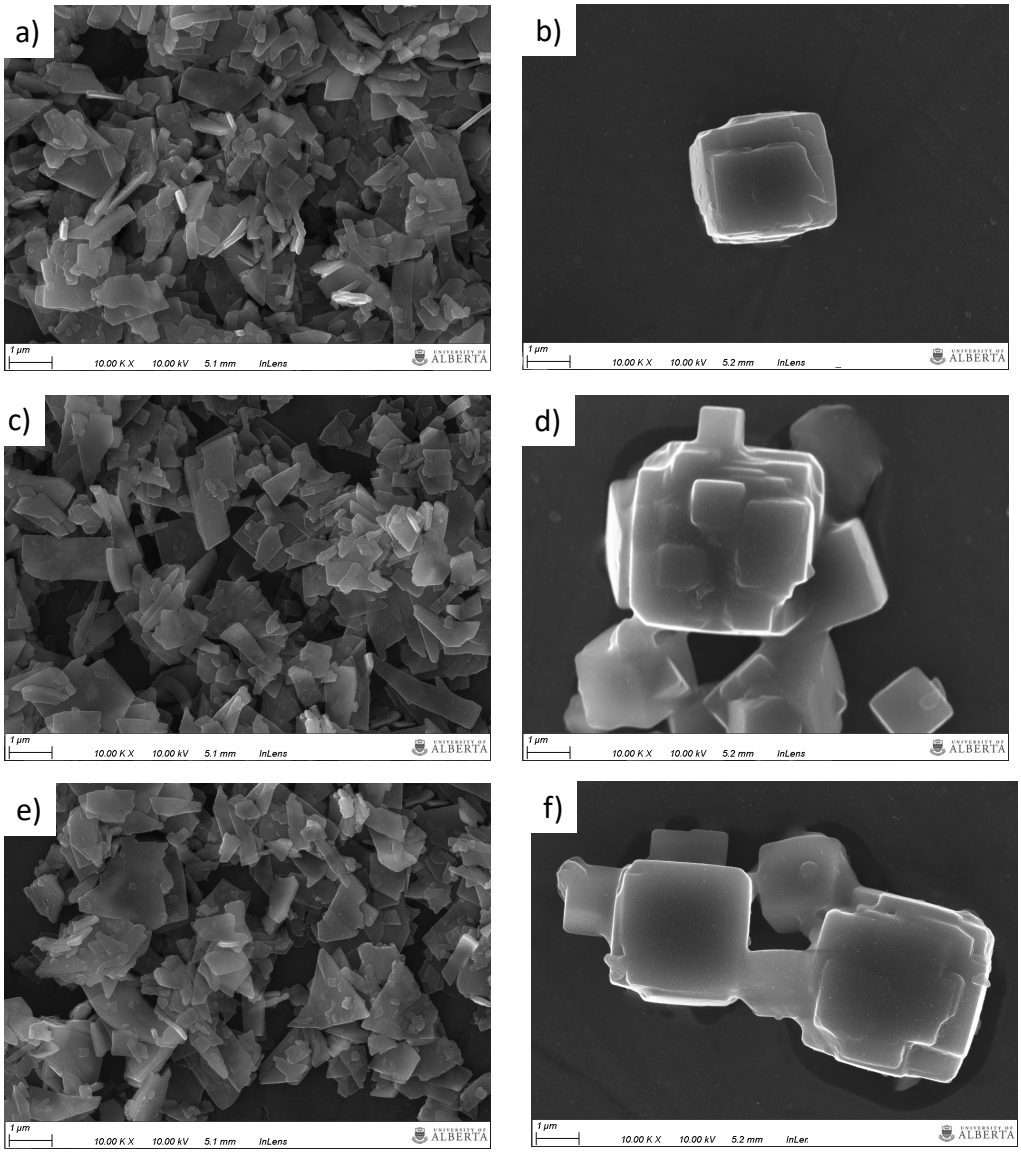

Figure D.2: SEM images of Ba-RPZ crystals (left) and zeolite 4A crystals (right).

D.3 Model Validation with Literature Uptake Curves

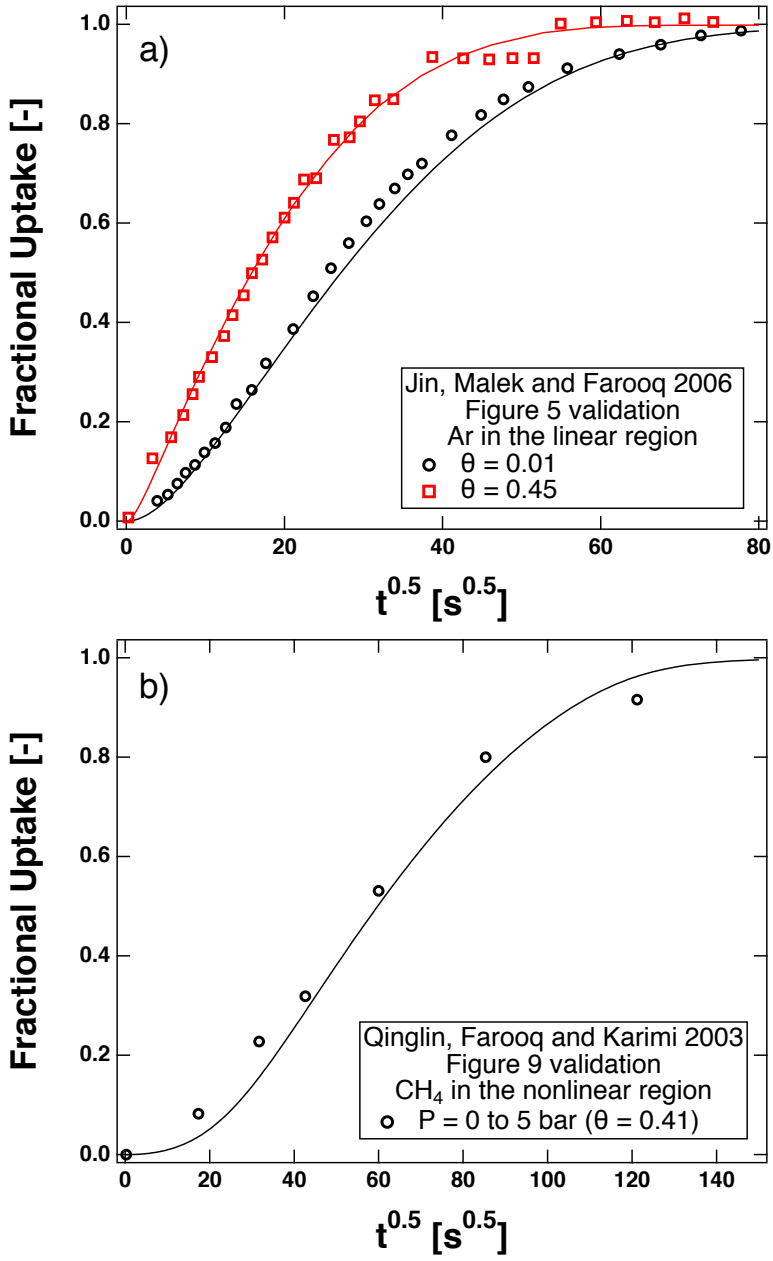

Figure D.3: A comparison of the numerical micropore model (lines) and data from the literature (markers). **(a)** Ar uptake curves on Takeda II CMS in the linear region at two levels of loading [140]. **(b)** Uptake curve of a large dose of CH_4 on a BF-CMS [139].

D.4 High Pressure Ba-RPZ Isotherms

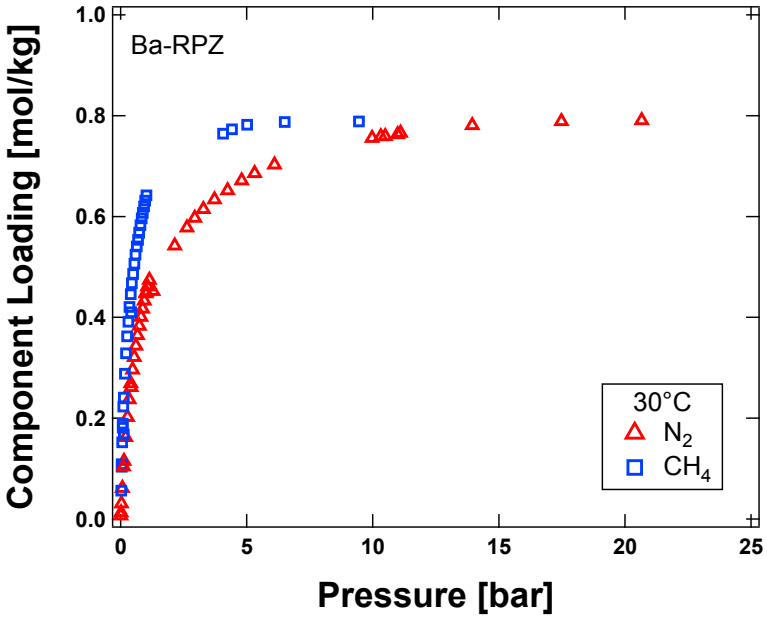

Figure D.4: High pressure equilibrium data at 30°C for N_2 and CH_4 on Ba-RPZ.

D.5 Pressure Uptake Curves (Dosing Cell)

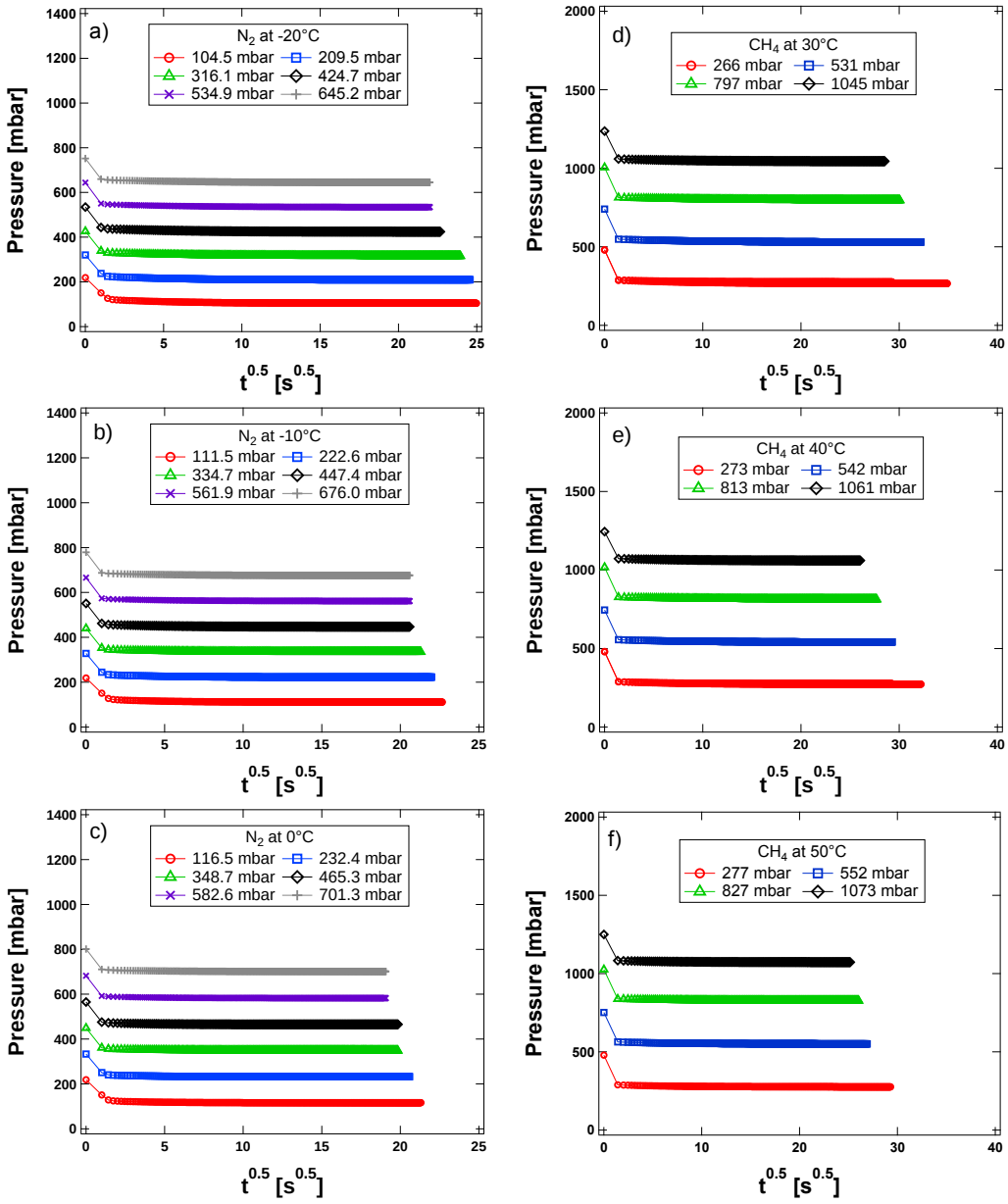

Figure D.5: Pressure transients corresponding to the constant volume experiments for N_2 at (**a**) -20, (**b**) -10 and (**c**) 0°C and CH_4 at (**d**) 30, (**e**) 40 and (**f**) 50°C on zeolite 4A crystals.

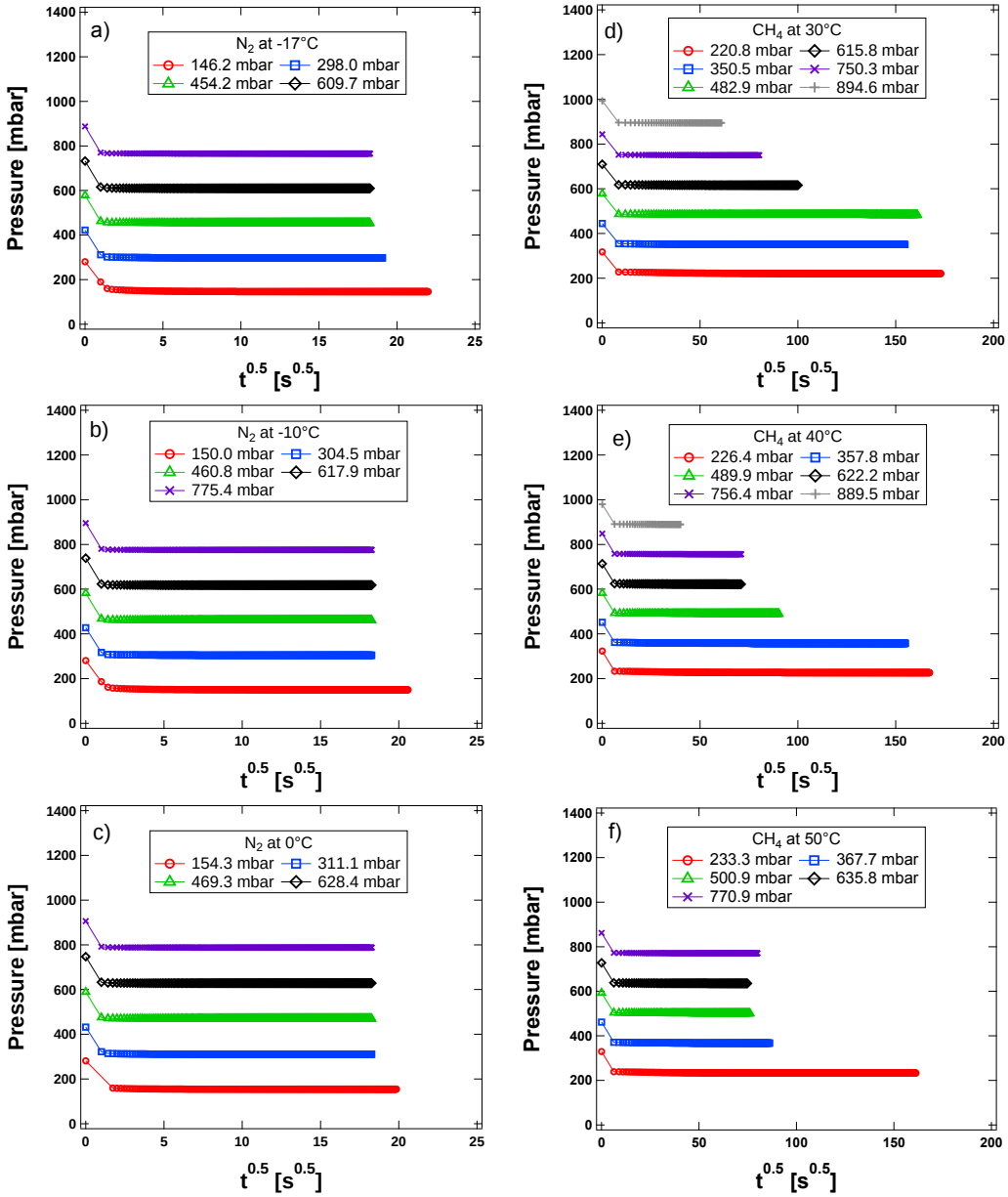

Figure D.6: Pressure transients corresponding to the constant volume experiments for N_2 at (**a**) -17, (**b**) -10 and (**c**) 0°C and CH_4 at (**d**) 30, (**e**) 40 and (**f**) 50°C on Ba-RPZ crystals.

D.6 CH_4 Fitting Sensitivity on Ba-RPZ

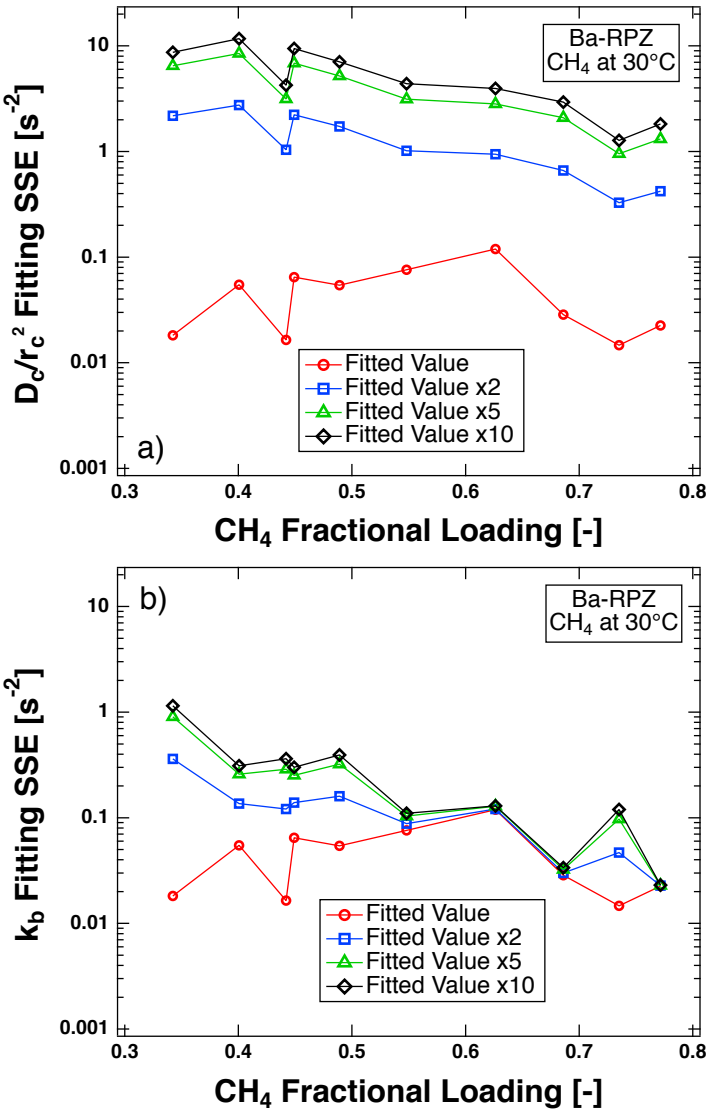

Figure D.7: A sensitivity analysis of the J_2 objective function to minimize squared error between the experimental and model CH_4 uptake curves on Ba-RPZ at 30°C for both the (**a**) pore diffusion time constant and the (**b**) barrier constant. After the value was fitted using J_1, multiples of the fitted diffusivities were tested to see how sensitive J_1 was to a non-fitted value. As seen, there is a much larger change in the calculated sum of squared error for pore diffusion time constant than the barrier constant.

D.7 Barrier Mechanism for CH_4 on Ba-RPZ

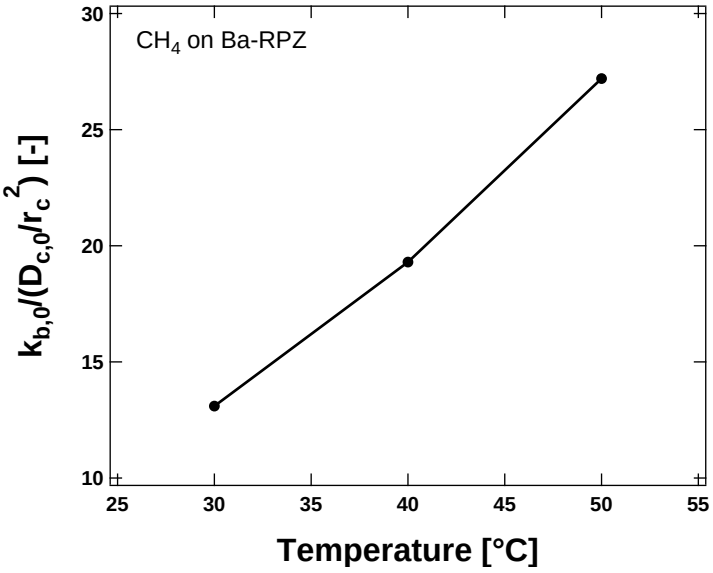

Figure D.8: The ratio of the limiting barrier constant and the pore diffusion time constant as a function of temperature. This quantity increases with temperature, suggesting that the surface resistance mechanism is due to pore narrowing instead of pore blocking.

Appendix E: Supporting Information for "Optimization of pressure-vacuum swing adsorption processes for nitrogen rejection from natural gas streams using a nitrogen selective metal organic framework"

E.1 High Pressure Isotherms on V-MOF

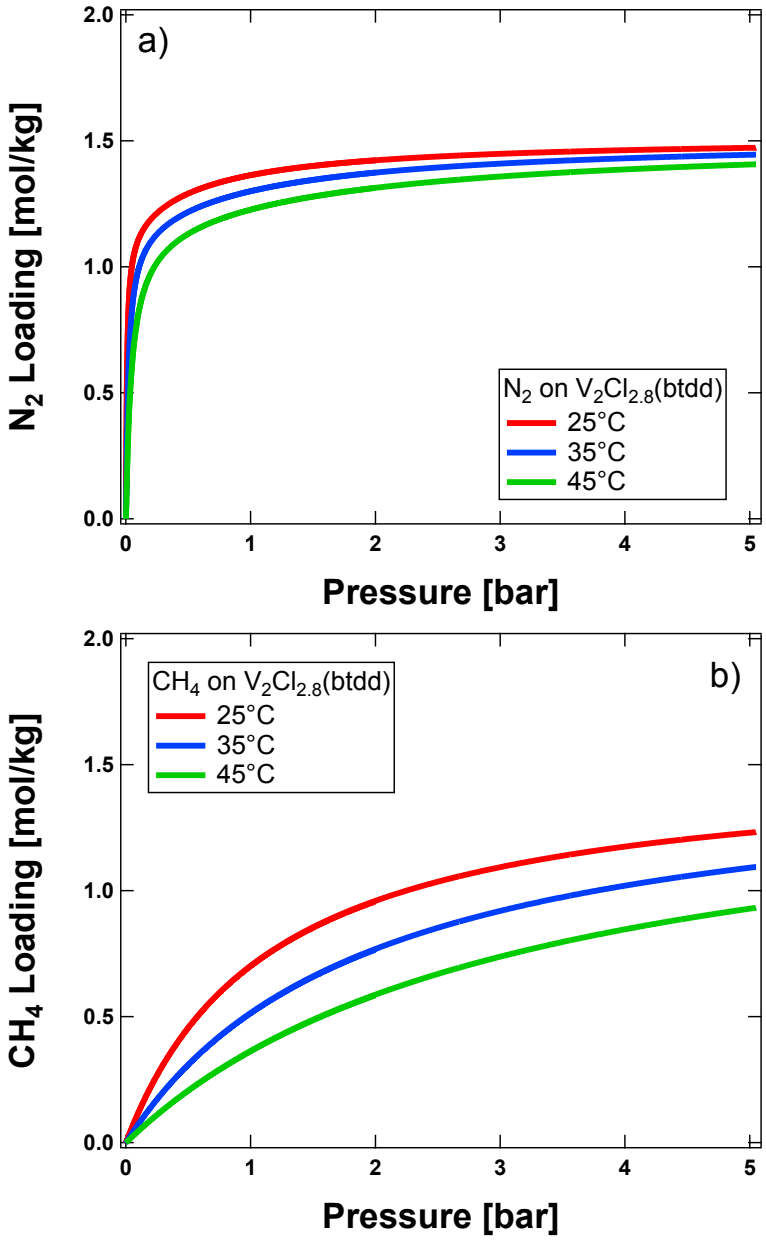

Figure E.1: Dual-site Langmuir isotherm fits used in the detailed process simulations for N_2 (**a**) and CH_4 (**b**) on V-MOF, $V_2Cl_{2.8}$(btdd), at 25, 35 and 45°C from vacuum to 5 bar pressure, including the 25% reduction from the crystalline loading.

E.2 Diversity of Training Data

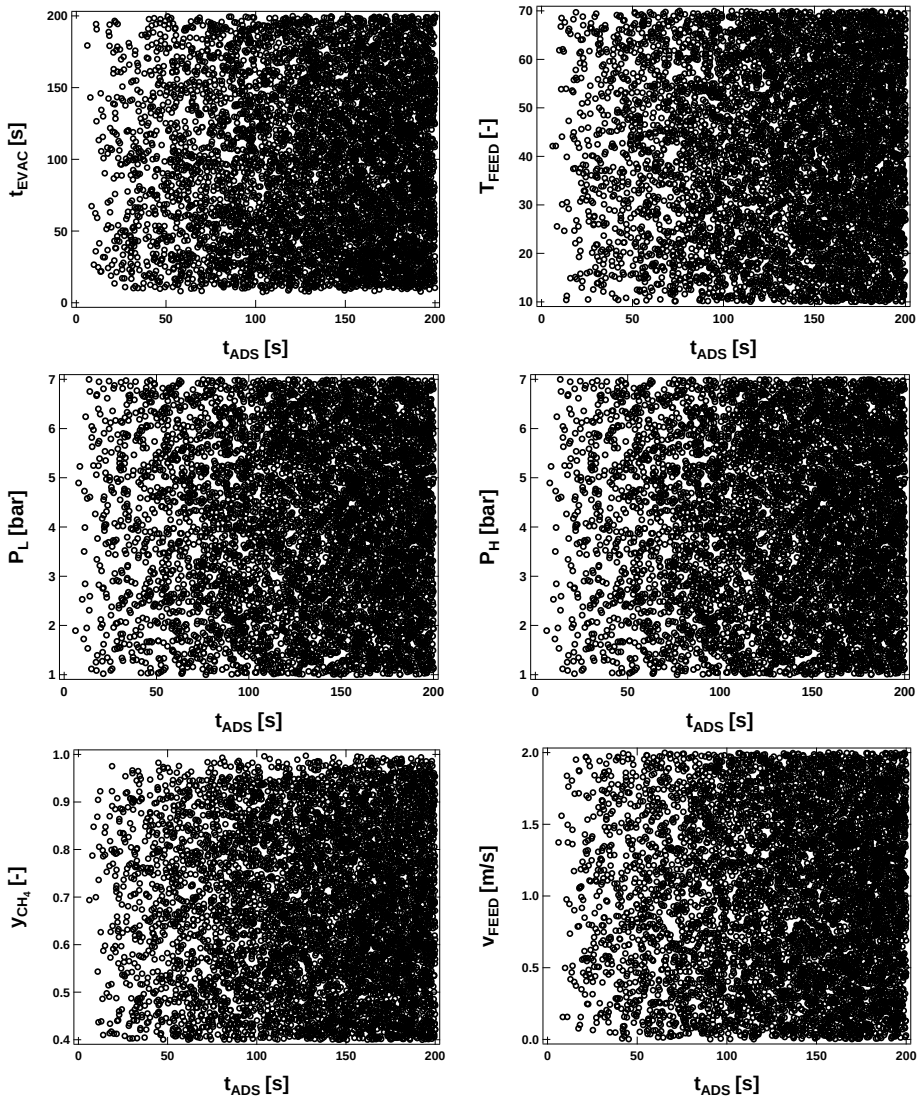

Figure E.2: Samples fed to the 3-step cycle simulations from the Latin hypercube sampling (6325 samples).

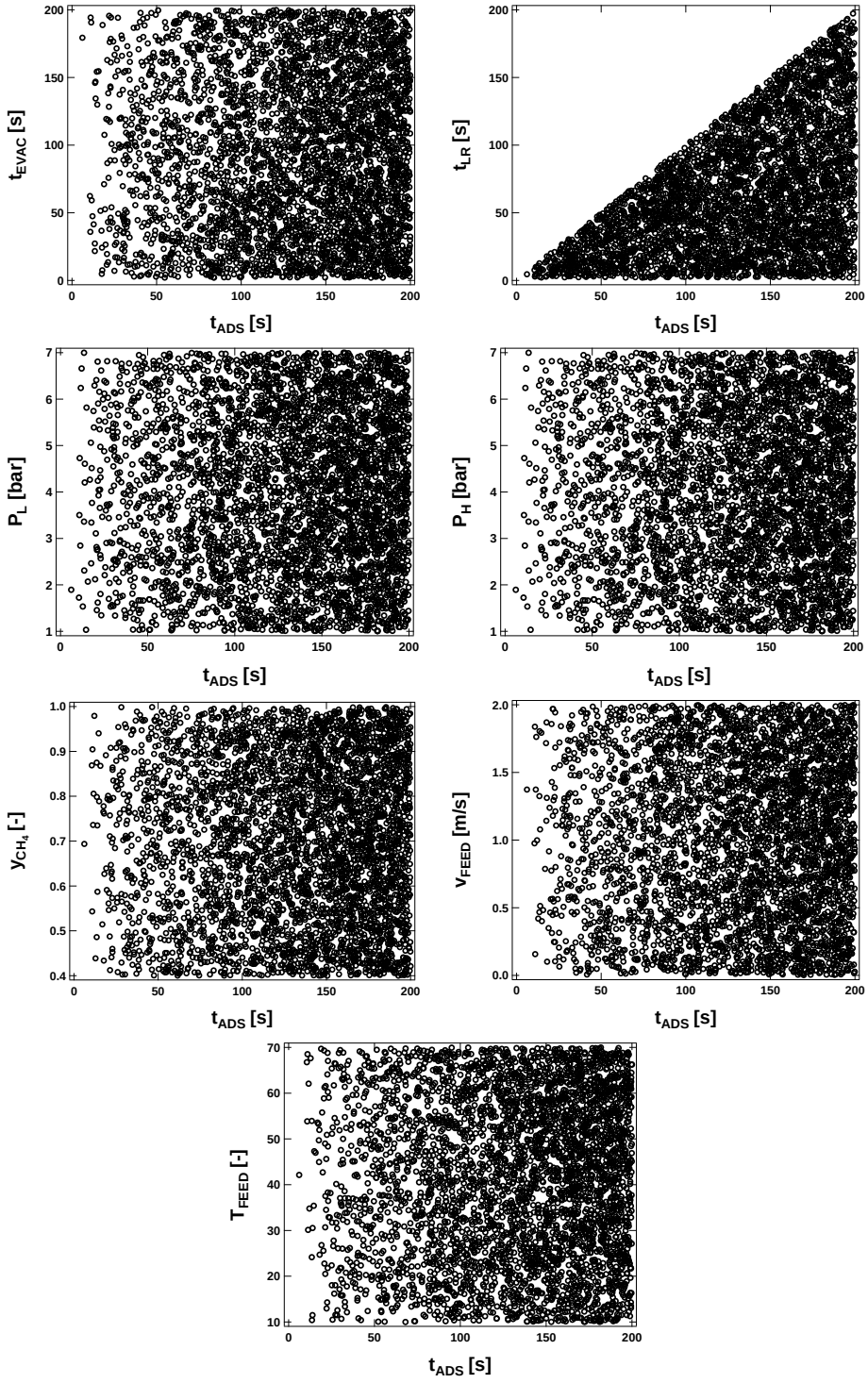

Figure E.3: Samples fed to the Skarstrom simulations from the Latin hypercube sampling (4096 samples).

E.3 Number of Samples Required for ANN Training

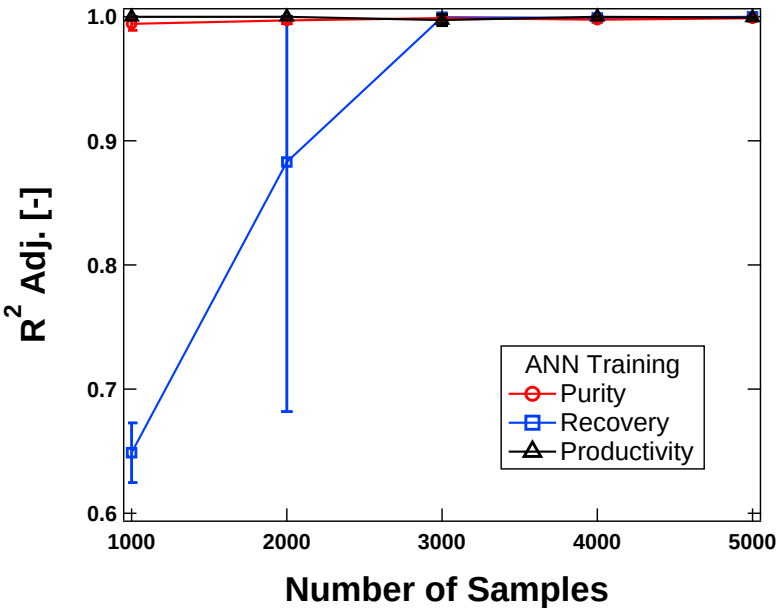

Figure E.4: The effect of sample size on R^2_{adj} for the ANN training of the Skarstrom cycle. These ANN models have eight inputs and one output. 3000 samples are sufficient for each process performance metric to achieve $R^2_{\text{adj}} > 0.99$. The error bars represent the standard error of three repeated ANN model trainings.

E.4 Number of Hidden Layers and Neurons Required for ANN Training

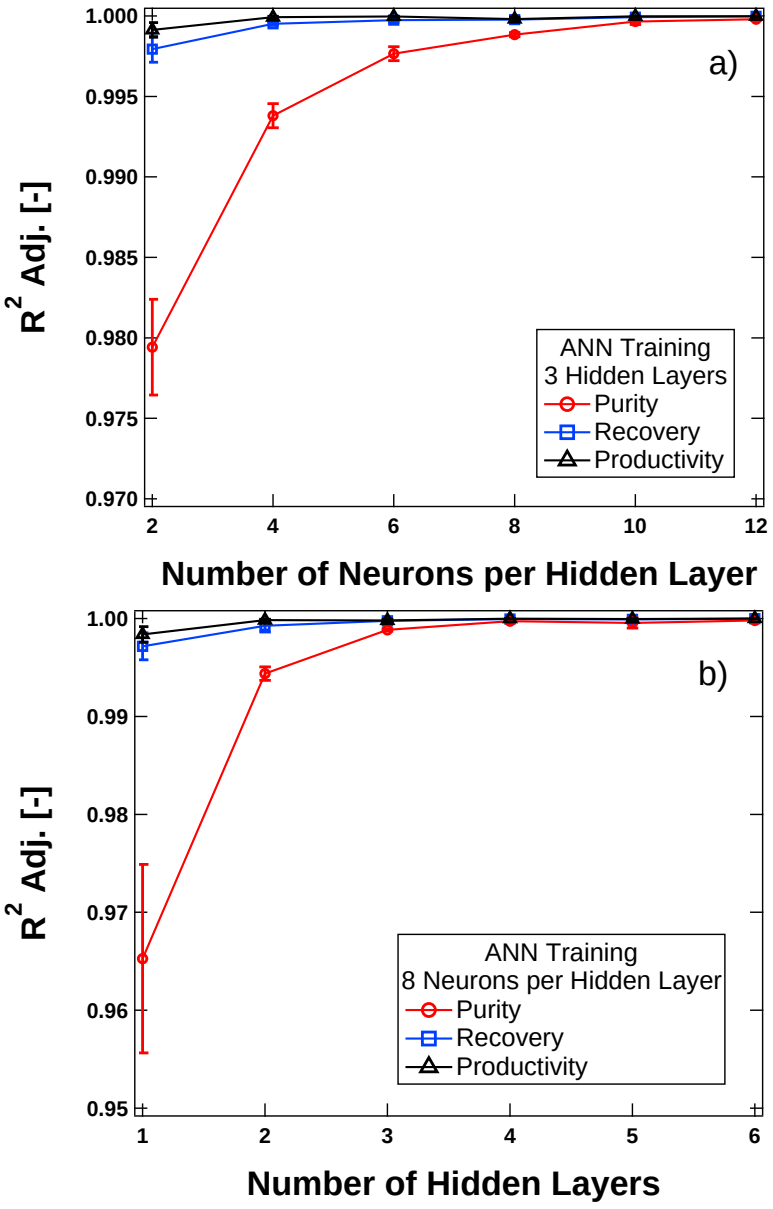

Figure E.5: The effect of (**a**) neurons and (**b**) hidden layers on R^2_{adj} for the ANN training of the Skarstrom cycle. These ANN models have eight inputs and one output. 4096 samples were used in these training routines. The error bars represent the standard error of three repeated ANN model trainings.

E.5 Optimized Adsorption Pressures for High Pressure Optimizations

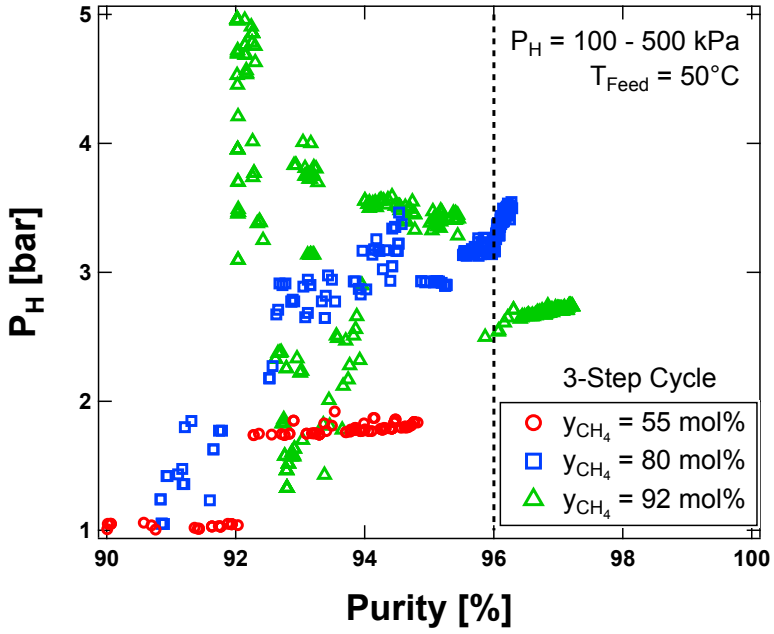

Figure E.6: The optimized adsorption pressures for the $100 - 500$ kPa optimizations in Fig. 7.4(**c**).

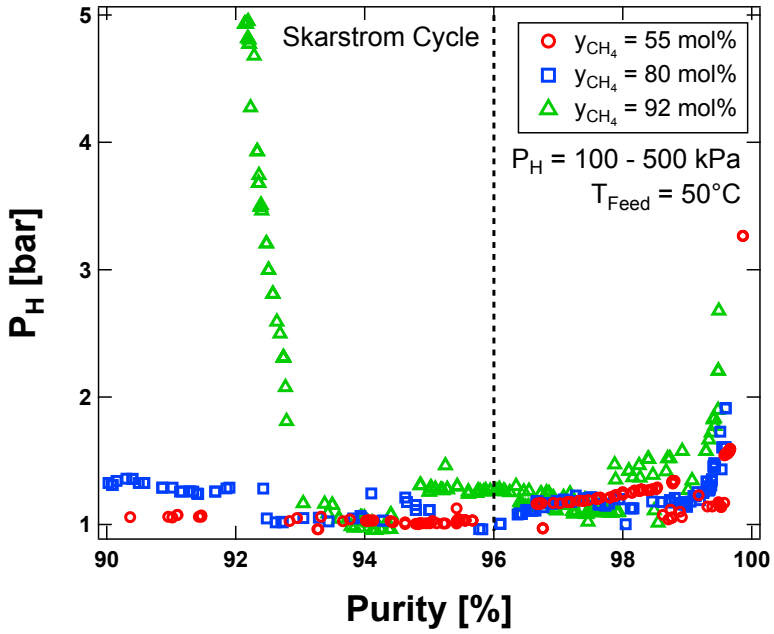

Figure E.7: The adsorption pressures corresponding to the trade-off curve in Fig. 7.6(**c**).